

A Terahertz Spectrometer for the Study of Multilayered Optics & Complex Materials

Akif Ahmed

A Thesis submitted to the Faculty of Graduate Studies of
The University of Manitoba
in partial fulfilment of the requirements of the degree of

MASTER OF SCIENCE

Department of Physics and Astronomy
University of Manitoba
Winnipeg

© Akif Ahmed, 2021

A Terahertz Spectrometer for the Study of Multilayered Optics & Complex Materials

Akif Ahmed

Examining Committee

Dr. Jacob Burgess, Supervisor
(Department of Physics and Astronomy)

Dr. Robert Stamps, Departmental Member
(Department of Physics and Astronomy)

Dr. Arkady Major, External Member
(Department of Electrical and Computer Engineering)

Dedicated to My Family

Abstract

Time domain spectroscopy with terahertz (THz) pulses is a powerful technique in characterizing material properties. THz technology is still developing and many optical components in this electromagnetic spectrum are not yet so economically available. We construct a THz spectrometer utilizing ultrashort laser pulses in nonlinear crystals that allows phase-resolved detection of light in the bandwidth 0.25–2.25 THz. Using our instrument, we examine spectral features of ordinary low loss materials which are later exploited in the study of multilayered dielectric structures designed to serve as low-cost optics for THz light. We develop wideband antireflection (AR) coatings for a variety of substrates with commercially available films and tapes. Utilizing multilayered structures, we propose the design of an economic, yet efficient, THz linear polarizer. In addition, we designed and constructed distributed Bragg reflectors which are incorporated in building a tunable Fabry-Pérot cavity. With the aid of an AR coated electro-optic crystal, high resolution time domain spectroscopy performed on room temperature magnetoelectric multiferroic, BiFeO₃ (BFO), showed the presence of electromagnon resonances in the sub-THz range. BFO is a potential material for the study of strong light matter coupling, which can have a substantial technological impact. We have tried tuning the resonances of BFO with applied electric field and optical heating in order to observe polariton modes. Due to the challenges in tuning BFO magnons, we investigate the design aspects of a high Q cavity for the discovery of a hybrid quasiparticle at room temperature, cavity magnon polariton (CMP), in the promising multiferroic. We have performed calculations showing both frequency and time domain response of the empty cavity system to highlight experimental implications for our apparatus. The tools developed in this thesis will be used in the study of CMP in BFO in a future project alongside other research.

Acknowledgements

During the period of my MSc, I have benefited from many, in both academic sphere and outside. Firstly, I would like to thank my supervisor, Dr. Jacob Burgess, for believing in me as his first graduate student in a new lab. His encouragements have led me to learn various valuable skills throughout the years. Outside of academic work, his advices were of great help to me in a new city. I would like to thank all the members of Ultrafast Microscopy and Magnetism Research Group for their contributions to my research.

I express appreciation to AJ for his assistance and the conversations we had outside of research. I am grateful to you for your accommodating nature and I recognize your passion for memes. I thank Josh for building me the purge box. I am thankful to Sangeev for helping with 3D designs and CNC. The easy communication and feedback from Nils was really useful. Alexander Franzen is acknowledged for making available a collection of optics vector graphics, some of which were used in this project.

The staff at the Department of Physics and Astronomy, University of Manitoba needs to be acknowledged for their support. I thank Susan, Robyn, Aysley for making research life easier for me. I show my gratitude to Peiqing for his swift technical support.

I am indebted to my family members for their moral support over the course of my degree, specifically to my mom. I am grateful to my wife for her constant reminders before important events. I would like to thank Nafi (chotur), Rakibullah (hujur), Moinul, Abdullah, Rafiq (chacha), Mohit (dado), Jaseer Bhai and others for spending fun time with me which helped alleviate my work load.

Contents

Abstract	iii
Acknowledgements	iv
Table of Contents	v
List of Figures	viii
List of Tables	xviii
Abbreviations	xix
List of Variables	xxi
1 Introduction	1
1.1 Optical Spectroscopy	1
1.2 Time Domain Spectroscopy	2
1.3 Terahertz Light	3
1.4 Spectroscopy with THz pulses	4
1.4.1 Normal Materials	4
1.4.2 Magnetoelectric Multiferroic	4
1.5 Multilayered Optics in THz region	5
2 THz Generation and Detection	7
2.1 Introduction	7
2.2 Nonlinear Polarization	7
2.3 Generation Theory	9
2.3.1 Optical Rectification	10
2.3.2 Pulse Front Tilt	12
2.3.3 Determination of Angles & Lens Combination	14
2.4 THz Detection	15
2.4.1 Pockels Effect	16
2.4.2 Phase Matching & Balanced Detection	17

2.5	Experimental Setup	20
2.5.1	Chopper and lock-in setup	23
2.5.2	Nitrogen Purging	24
2.5.3	SNR and DR	25
2.6	Conclusion & Discussion	27
3	Analysis	28
3.1	Introduction	28
3.2	Connecting Time and Frequency Domains	28
3.3	Fast Fourier Transform	30
3.4	Window Function	31
3.5	Optical Parameter Extraction	33
3.6	Fabry-Pérot Effect	36
3.7	Reconstruction of the Signal	38
3.8	Propagation in a Resonant Medium	40
3.9	Discussion & Conclusion	41
4	Spectroscopy of Normal Dielectrics	42
4.1	Introduction	42
4.2	Spectroscopy on Solids	43
4.2.1	Silicon	43
4.2.2	Alumina	46
4.2.3	Quartz Glass	48
4.2.4	Thin Polyimide Film	50
4.3	Discussion & Conclusion	52
5	Anti-Reflection Coating	53
5.1	Introduction	53
5.2	Films for ARC	54
5.3	Application of AR Layers	56
5.4	Calculation & Experiment	57
5.5	Results	60
5.5.1	ARC on Si	61
5.5.2	ARC on Alumina	66
5.5.3	ARC on Quartz Glass	68
5.6	ARC on an Electro Optic Crystal	70
5.7	ARC for Non-Collinear THz Generation	72
5.8	Discussion	74
5.9	Conclusion	74
6	THz Pile-of-Plates Polarizer	75
6.1	Introduction	75

6.2	Polarization Due to Reflection	76
6.3	Construction and Measurement	79
6.4	Results	81
6.5	Improvement in Construction	82
6.6	Calculation on Frequency Domain Response	83
6.7	Discussion & Conclusion	88
7	BFO Spectroscopy & Tunable Cavity	89
7.1	Introduction	89
7.2	Strong Light-Matter Coupling	90
7.3	BFO	93
7.3.1	Basic Properteis	93
7.3.2	THz spectroscopy on BFO	94
7.3.3	Electric Field Tuning	96
7.3.4	Temperature Tuning	99
7.4	Fabry-Pérot Resonator	101
7.4.1	Basic Principle	102
7.4.2	Loss and Photon Lifetime	105
7.4.3	Angle Tuning Fabry-Pérot Modes	106
7.5	Distributed Bragg Reflector	107
7.5.1	Basic Construction	107
7.5.2	Polyimide DBR	108
7.5.3	Silicon DBR	109
7.6	Pulse in Ideal FP Cavity	111
7.7	Response of DBR FP Cavity	114
7.7.1	Transmission Transfer Function	115
7.7.2	Time-domain Response	116
7.8	Result from Cavity Measurement	121
7.9	Discussion	122
7.10	Conclusion	123
8	Conclusions	124
A	Alignment Procedure	128
A.1	Pre-generation Considerations	128
A.2	Generation	128
A.3	Detection	131
B	Matlab Codes	133
	References	154

List of Figures

1.1	Solar absorption lines observed by Fraunhofer, reprinted from Deutsches Museum Munich, Germany and [2] with permission	2
1.2	Fourier Transform connecting time and frequency domain information. In frequency domain all three pulses are centered at the same frequency ν_0	3
1.3	Location of Terahertz light in EM spectrum. Nominal values are given to highlight vacuum properties. The broad interval of far infrared has been omitted. NIR corresponds to near infrared, which is adjacent to visible light.	3
2.1	The frequency components of IR pump pulse, shown on the left, undergo Intra-Pulse DFG inside the nonlinear crystal. The difference between pump's spectral content contribute to the generation of THz pulse, shown on the right. Here axes representing IR and THz are not in the same scale. See [25] for further illustrations.	11
2.2	Illustration of THz generation by non-collinear phase matching in LiNbO ₃ . IR is polarized along the optic axis of LNB. Pulse front and phase front are shown in red and blue.	13
2.3	Setup for PFT in LiNbO ₃ . Only single frequency component is shown	14
2.4	(a) Plot from grating equation. Horizontal gray dash-dot lines indicate the regions where $\alpha - \beta \leq 25^\circ$. Vertical green dashed lines indicate range of allowed β , marked by points A, B. Magenta square showing Littrow condition. (b) Plot of $1/M$ vs allowed β . Dashed horizontal lines correspond to available lens combinations satisfying $1/M$	15
2.5	(a) Pockels effect on the index ellipsoid of EO crystal. Without the presence of THz field, the crystal is isotropic, but incidence of THz field turns the crystal birefringent with altered principal axes [19]. (b) Orientation of GaP and field polarization directions of THz and IR pulse for maximizing EO signal [4].	17
2.6	FSEOS: showing only intensity envelope for probe IR pulse.	18

2.7	IR pulse tracing out THz time-domain electric field	19
2.8	Complete setup for simple transmission mode spectroscopy. Polarization of light and optic axis of LNB are shown by symbols: $\odot, \longleftrightarrow$	21
2.9	Gaussian beam with beam waist $2W_0$ and depth of focus $2z_0$. The dotted curved lines represent radius of curvature of the wavefront $R(z)$	22
2.10	(a) Upper half of beam waist profile scanned with thermopile detector. FWHM ~ 1.5 mm; $\therefore 2W_0 \sim 2.5$ mm, $2z_0 \sim 35$ mm. (b) Image taken using far-infrared camera in the collimated section of THz beam.	23
2.11	180° phase shift between the two balanced signals is evident when sampling peak and trough of the THz pulse. The DC offset in the signals are taken care of by lock-in's AC coupling. The lock-in reference is a square wave sent from the chopper.	24
2.12	Effect of N_2 purging in time and frequency domain. FID due to water vapor is noticeable in the blue waveform.	25
2.13	Pump power ~ 13.5 W at 10 MHz rep rate. (a) 7 time domain sweeps. At peak $SNR \approx 414$, $DR \approx 5473$. (b) Amplitude spectrum of the average waveform. Amplitude noise floor is estimated by dashed line.	26
2.14	(a) Spectral dynamic range. (b) Maximum absorption that can be reliably measured for few values of index, n	26
3.1	Connecting time and frequency domain signals via FT and IFT in LTI systems. The symbols $*$ and \times are used to indicate convolution and multiplication respectively.	29
3.2	FFT extracting amplitude and phase components of a simulated signal: $\text{Sig}(t) = 1 \cdot \cos(2\pi(0.5)t + 1) + 2 \cdot \cos(2\pi(1)t + (-2)) + 1.5 \cdot \cos(2\pi(2.5)t + (2))$	31
3.3	Effect of window functions on N_2 purged experimental waveform. (a) Keeping t_1 fixed and varying t_2 . Resulting waveforms are shown in (b) applying offsets along both axes. Second pulse has been windowed out in \tilde{E}_2, \tilde{E}_3 . (c) Oscillation in spectrum is removed in $ E_2 , E_3 $. Since win-2 is longer than win-3, $ E_3 $ shows weak water vapor signatures which are absent in $ E_2 $	32
3.4	Sample with \bar{n} to be characterized with THz-TDS. Measured signal without the sample is called reference and denoted by \tilde{E}_{ref} . Measured signal with the sample is denoted by \tilde{E}_{smp}	33
3.5	Phase unwrapping is performed in the calculations	35

3.6	These experimental quantities are then used in the simple equation, eq. (3.13), to calculate the optical parameters.	36
3.7	Time and frequency domain simulations from 250 μm thick Si. Waveforms are offset along y-axis for clarity. In this thick sample, the echoes in the waveform can be windowed out.	38
3.8	Time and frequency domain simulations from 40 μm thick Si. Waveforms are offset along both x, y axes for clarity. In this thin sample, the internally reflected echos interfere to produce the output signal in red.	38
3.9	(a) Input signal, (b) resonator $H(\nu)$ with resonance, $\nu_0 = 2$ THz, that would respond to the input pulse.	39
3.10	(a) Output signal from above resonator, fig. 3.9 (b). Top panel shows time-domain ringing which is constructed by following steps highlighted in this section. Bottom panel shows spectral amplitude of the output waveform. (b) Comparison between input and output amplitude spectra due to the resonator.	39
3.11	(a) Transfer function, $H(\nu)$, characterizing a band-stop filter. (b) Output (blue) waveform is the time domain response of the band-stop filter to the input (black) pulse.	40
3.12	Spectrum of portions of time trace distinguishable by color. (a) Osc-b (red) corresponds to the portion of \tilde{E}_2 before the FID, Osc-a (green) corresponds to the FID. (b) Power spectrum calculated with different temporal segments (Osc-a and Osc-b). The black curve is the input and blue is the output considering full time trace of the output waveform, which shows absorption. FID portion of the output waveform showing spectral emission in green. The diminished amplitude in red is the result of the superposition between completely out of phase frequency components.	41
4.1	A THz pulse that has passed through a 500 μm thick wafer of HRFZ-Si (blue) compared to a reference pulse that has not passed through any sample (black)	44
4.2	Transmitted spectra from respective blue and black waveforms above	44
4.3	Ratio of the spectral amplitudes of the pulse that was passed through the HRFZ-Si sample and the reference pulse	45
4.4	Optical parameters extracted from the HRFZ-Si sample. Index of refraction is shown in blue and absorption coefficient in red.	45

4.5	A THz pulse that has passed through a 635 μm thick ceramic alumina (blue) compared to a reference pulse that has not passed through any sample (black)	46
4.6	Transmitted spectra from respective blue and black waveforms above . . .	46
4.7	Ratio of the spectral amplitudes of the pulse that was passed through the ceramic alumina sample and the reference pulse	47
4.8	Optical parameters extracted from the ceramic alumina sample. Index of refraction is shown in blue and absorption coefficient in red.	47
4.9	A THz pulse that has passed through a $\frac{1}{16}$ " thick quartz glass (blue) compared to a reference pulse that has not passed through any sample (black)	48
4.10	Transmitted spectra from respective blue and black waveforms above . . .	48
4.11	Ratio of the spectral amplitudes of the pulse that was passed through the quartz glass sample and the reference pulse	49
4.12	Optical parameters extracted from the quartz glass sample. Index of refraction is shown in blue and absorption coefficient in red.	49
4.13	Left: A THz pulse that has passed through a PI film (blue) compared to a reference pulse that has not passed through any sample (black). Right: Transmitted spectra of respective waveforms from left.	50
4.14	Amplitude ratio and phase difference show FP oscillations for the PI thin film	50
4.15	Effect of inclusion (red) and exclusion (blue) of FP term in calculating amplitude ratio from the PI thin film. Incorporating FP effect, we attempt to manually fit the calculated amplitude ratio (red) to that of experiment (black). Here we have kept the index fixed but approximated κ by a 2 nd order polynomial (shown below) that produces the best fit between red and black curves.	51
4.16	Estimated extinction coefficient (κ) and power absorption coefficient (α) of PI film that allows best fit in fig. 4.15	51
4.17	Time domain reconstruction further shows the merit of the FP term and absorption fitting for the PI thin film. THz pulse that passes through the PI film is shown in black. Waveform simulation including and excluding the FP term is respectively shown in red and blue.	52
5.1	Fresnel loss due to index mismatch between substrate and air.	54
5.2	Configurations for ARC (showing layers only on 1 side of the substrate). Substrate is shown at the bottom and layers on top are the applied polymer films. Violet color denotes adhesive layer.	57

5.3	Multilayered films placed between two media denoted by $\bar{n}_0, \bar{n}_{\text{sub}}$, typically they would denote air and substrate. Layers are ordered from top to bottom, denoted by subscripts. l^{th} layer is characterized by its complex index and thickness.	58
5.4	Transmission through uncoated and coated substrates, (a), (b)	59
5.5	Measured time traces of AR coated Si wafer. Successive waveforms are offset along both axes. Pulses transmitted through samples are on the left side of dashed line. Internally reflected pulses are on the right side of dashed line.	60
5.6	ARC: PI (1 Mil) PDMS (1 Mil) Si (Substrate). Inset in (c) and (d) shows amplitude ratio and waveform of internally reflected pulse, respectively. . .	62
5.7	ARC: PI (1 Mil) PMMA (1.3 Mil) Si (Substrate). Inset in (c) and (d) shows amplitude ratio and waveform of internally reflected pulse, respectively.	62
5.8	ARC: PI (1.85 Mil) PMMA (1.3 Mil) Si (Substrate) Inset in (c) and (d) shows amplitude ratio and waveform of internally reflected pulse, respectively.	63
5.9	ARC: PI (0.5 Mil) PDMS (1 Mil) Si (Substrate). Inset in (c) and (d) shows amplitude ratio and waveform of internally reflected pulse, respectively.	63
5.10	ARC: PE (1.7 Mil) PMMA (0.2 Mil) Si (Substrate). Inset in (c) and (d) shows amplitude ratio and waveform of internally reflected pulse, respectively.	64
5.11	ARC: PE (1.7 Mil) PMMA (0.2 Mil) PI (0.5 Mil) PDMS (1 Mil) Si (Substrate). Inset in (c) and (d) shows amplitude ratio and waveform of internally reflected pulse, respectively.	64
5.12	ARC: PP (1 Mil) PMMA (1.1 Mil) PI (1 Mil) Si (Substrate). Inset in (c) and (d) shows amplitude ratio and waveform of internally reflected pulse, respectively.	65
5.13	ARC: PP (1 Mil) PMMA (1.1 Mil) PI (2 Mil) Si (Substrate). Inset in (c) and (d) shows amplitude ratio and waveform of internally reflected pulse, respectively.	65
5.14	ARC: PE (1.7 Mil) PMMA (0.2 Mil) PI (1 Mil) Si (Substrate). Inset in (c) and (d) shows amplitude ratio and waveform of internally reflected pulse, respectively.	66
5.15	ARC: PI (1 Mil) PDMS (1 Mil) Alumina (Substrate). Inset in (c) and (d) shows amplitude ratio and waveform of internally reflected pulse, respectively.	67
5.16	ARC: PI (1.85 Mil) PMMA (1.3 Mil) Alumina (Substrate). Inset in (c) and (d) shows amplitude ratio and waveform of internally reflected pulse, respectively.	67

5.17	ARC: PE (1.7 Mil) PMMA (0.2 Mil) Alumina (Substrate). Inset in (c) and (d) shows amplitude ratio and waveform of internally reflected pulse, respectively.	68
5.18	Internalaly reflected pulse for the AR coated quartz glass is difficult to locate in the wavefrom. In frequency domain this manifests as greatly reduced FP oscillations. Plots are offset for clarity.	69
5.19	(a) Amplitude of main pulse. (b) Amplitude ratio with respect to reference. (c) ARC: PE (1.7 Mil) PMMA (0.2 Mil) Quartz (Substrate). (d) ARC: PP (1 Mil) PMMA (1.1 Mil) Quartz (Substrate). Inset showing amplitude ratio in (c),(d).	69
5.20	Plots are offset along y-axis. (a) $ FP $ for $\Delta t = 10$ ps, $N = 4$ without any ARC. For comparison $a \sim 0.3$ for GaP, ZnTe. (b) Calculated response of 0.5 mm thick GaP with five internal reflections for uncoated and PI-T1 coated on single and both faces of the crystal.	71
5.21	(a) Experimental spectrum from 1mm thick GaP detection crystal coated with PI-T1 on both sides, where internal reflection shows up after 22 ps. Spectrum in the inset is that of the 1st reflected pulse. Legend indicates time duration of the analyzed waveform. (b) Water vapor absorption spectra from 110 ps long scan using uncoated and coated GaP. High resolution absorption lines are discernable at 0.56, 0.75, 0.99 THz. Clear spectral advantage can be seen in the red curve.	72
5.22	(a) Calculation on THz power outcoupling from LNB, ignoring absorption and dispersion in films. Each ARC's merit can be seen for certain spectral regions and bandwidths. (b) Application of multilayered film on LNB prism.	73
6.1	reflection coefficients for p-polarized (a) and s-polarized (b) light	77
6.2	Ray tracing Fabry-Pérot effect in tilted dielectric film at the Brewster angle. Not showing rays transmitting on the left side for s-polarization	78
6.3	Fabry-Pérot effect in frequency domain from $45\mu\text{m}$ PE film due to transmission of each polarizations. Angles are given in degrees	78
6.4	Increase of plate surface area due to $\theta_i = \theta_B$ for PE, Si, Quartz glass	79
6.5	3D printed and assembled two-axis rotation mount holding many stacks of PE film. The gray cylindrical part rotates about the direction of incidence, while joints holding the PE stacks can be rotated to vary θ_i . Changing polarizer angle from 0° to 90° in (a)–(c)	80
6.6	PE pile of plates polarizer in THz beam at polarization angle 0°	80

6.7	Effect of PE stack number on performance of Brewster Polarizer	81
6.8	Only showing the transmitted light for two configuration of stacking: (a) Beam passing without alteration of aperture size, difficult for compact assembly. (b) Reduction of effective aperture due to stacking plates exactly on top of each-other, can be compacted easily.	82
6.9	Calculated interference effect due to 15 stacks of PE as constructed for experiment on the reflection and transmission transfer function of the system	83
6.10	Calculated transfer functions for a system of 45 μm thick PE stacks with 5 Mil spacing with stack number (a) 5, (b) 10, (c) 15, (d) 20 at $\theta_i = \theta_B$, where 1 Mil = 25.4 μm	84
6.11	Summary of calculated power extinction ratio, ER, and insertion loss, IL, from fig. 6.10 at $\nu = 1.2$ THz	85
6.12	Calculated frequency and time domain response of 10 stack 45 μm PE with 5 Mil spacing	85
6.13	Calculated tuning of transfer function representing 10 stacks of PE film with (a) thickness 45 μm , spacing 3 Mil, (b) thickness 30 μm , spacing 2 Mil, (c) thickness 4 Mil, spacing 10 Mil	86
6.14	Calculated frequency and time domain response due to tuning of stop band for pile-of-plates as described in fig. 6.13. To reiterate, each device is made of 10 layers of PE film with (a) thickness 45 μm , spacing 3 Mil, (b) thickness 30 μm , spacing 2 Mil, (c) thickness 4 Mil, spacing 10 Mil.	87
7.1	Two harmonic oscillators coupled together by spring of coupling strength $\bar{\kappa}$	90
7.2	Assuming $\omega_c/2\pi = 2.5$ THz, we vary the magnon mode so that both resonances may coincide. Calculation was performed using eq. (7.3) with parameters, $\bar{\kappa} = 0.35$, $\gamma_m = 0.011$, $\gamma_c = 0.024$. Polariton modes are represented by solid lines, while uncoupled photon, magnon modes are depicted using dashed lines. (a) Anticrossing polariton branches can be observed. Ω_R is shown with green line. (b) Evolution of mode line width with Δ . Line widths are bound by uncoupled line widths γ_c, γ_m and cross at $\Delta = 0$	92
7.3	(a) Crystal structure with ferroelectric polarization along $\langle 111 \rangle$ shown by the arrow and (111) planes containing spins are shaded, reprinted from [105] with permission from Elsevier, (b) Spin Cycloid structure, reprinted from [108] with permission from Nature Materials	93
7.4	Waveforms are offset along y axis for clarity.	94

7.5	Spectra from time trace before detector reflection to avoid oscillations. Dips after 1 THz are due to weak water vapor absorptions present even after N ₂ purging.	94
7.6	Low and high resolution spectroscopy. Time in legend indicates the time length after the 1 st peak in time domain. 200 ps trace contains many detector reflection which are highly reduced in the region around 0.7 THz due to the AR coating on GaP.	95
7.7	BFO index estimated for two extreme sample thicknesses using etalon reduction technique, from [47] with permission	96
7.8	BFO extinction estimated for two extreme sample thicknesses using etalon reduction technique, from [47] with permission	96
7.9	Polyimide (kapton) tape used to insulate HV electrodes to prevent breakdown. Sample is placed between the electrodes.	97
7.10	Time traces were taken up to 200 ps after the peak. No meaningful change in waveform could be observed.	97
7.11	Transmitted spectrum	98
7.12	Spectrum of the free induction decay (FID) which correspond to the emission of the magnon modes. FWHM of the FID peaks at the modes $\nu \approx 0.53, 0.56, 0.73$ THz are $\Delta\nu \approx 26, 23, 60$ GHz respectively.	98
7.13	Two green laser pointers were used to optically heat the BFO sample. The laser diodes were connected in parallel to an external current limiting power supply for controlled lasing.	99
7.14	Legend indicates total current supplied to two laser diodes in parallel. Higher current implies higher sample temperature.	100
7.15	Spectra using time-trace before echo from detector crystal appears. Increasing temperature is resulting in an increase in transmission loss and decrease in magnon frequency.	100
7.16	Ψ_1 modes tuned by changing diode laser current that induce optical heating in the sample. Frequency shift of 25–30 GHz is observed.	101
7.17	Reflection and transmission coefficients shown for the mirror surface close to the cavity. The other surface is assumed to have no Fresnel loss.	102
7.18	Finesse for an empty cavity made of mirrors with identical reflection coefficients, r	104
7.19	For a cavity with $d = 300\mu m$, varying \mathcal{F}	104

7.20	Magnitude of amplitude transfer functions for reflected and transmitted light for a typical high- \mathcal{F} cavity	105
7.21	Angle tuning ideal resonator with infinite mirror diameter and fixed d . . .	107
7.22	(a) Periodic alteration of high (green) and low (grey) index dielectric constituting a DBR, (b) resonant cavity made with two DBRs	108
7.23	Calculated response of PI DBR varying film number (a) Power reflectance from lossless films (b) amplitude transmission coefficient from lossy films . .	109
7.24	Measured transmission response of PI DBR varying stack number. (a) amplitude spectra, (b) ratio with respect to reference.	109
7.25	Calculated response of Si DBR varying wafer number (a) 40 μm thick Si with 127 μm spacer, (b) 280 μm thick Si with 127 μm air spacer. It is possible to make a DBR that may be utilized to study BFO magnons-polaritons at $\sim 0.55, 0.73$ THz.	110
7.26	Measured transmission spectrum from Si DBR consisting two wafers of thickness 280 μm spaced by 127 μm , sharp absorption dips around 0.55, 0.75 THz correspond to water vapor absorption	110
7.27	Incident Pulse	111
7.28	Cavity length, $d = 1000 \mu\text{m}$, corresponding to $t_r \approx 6.7$ ps. Cavity modes are present in output spectrum (a), but that does not imply we have multiple constructively interfering frequencies (b),(c).	112
7.29	Cavity length, $d = 100 \mu\text{m}$, corresponding to $t_r \approx 0.67$ ps	113
7.30	Cavity length, $d = 50 \mu\text{m}$, corresponding to $t_r \approx 0.33$ ps	114
7.31	Tuning cavity modes by varying L . (a) Each DBR consisting two Si wafers, (b) each DBR consisting three Si wafers.	115
7.32	Air gap, $L = 280 \mu\text{m}$. (a) s-polarization, (b) p-polarization	116
7.33	$L = 550 \mu\text{m}$, Ref is from experiment and Out is calculated. (a) time domain, (b) frequency domain	117
7.34	Calculation with $L = 550 \mu\text{m}$. (a) spectra, (b) waveform.	118
7.35	Spectrogram performed on fig. 7.34 (b) with 50 ps moving window. Top and bottom panels correspond to input and output signals respectively. . .	118
7.36	Calculation with $L = 2800 \mu\text{m}$. (a) spectra, (b) waveform.	119
7.37	Spectrogram performed on fig. 7.36 (b) with 50 ps moving window. Top and bottom panels correspond to input and output signals respectively. . .	120
7.38	Calculated transmission spectra with $L = 2.8$ mm, varying output waveform length that is used for FT.	121

7.39 Cavity made of DBRs consisting three Si wafers each. Due to very low transmission, we could not detect any resonance modes as distance between DBRs are increased. 121

7.40 Cavity made with pair of DBRs each consisting two Si wafers. As cavity length is increased, the number of weak cavity modes can be seen to increase in the reflection region. Due to alignment issues, the modes are not prominent. 122

A.1 (a) 3D printed alignment tool, m denotes the order of diffraction, $m = 1$ is used to pump LNB. (b) 5 axis translation stage PY005 from Thorlabs is used to mount LNB prism. 3 vital axes are labeled according manufacturer specification. 129

List of Tables

2.1	$d_{\text{eff}}, \alpha(\Omega)$ in few nonlinear crystals for OR, from [27, 28]. E_g denotes band gap.	11
2.2	Important properties of few EO crystals belonging to the point group $\bar{4}3m$. Information taken from [4, 35]. λ_0 denotes pump wavelength for phase matching.	18
5.1	Polymer name and parameter $\bar{n} = n - i\kappa$ used for analysis. PDMS-1, PDMS-2 have slightly different κ and correspond to PI-T1, PI-T4 respectively, see table 5.2. n is taken from literature while κ is estimated by fitting.	55
5.2	Tape and film Information. l_1 correspond to film thickness given by supplier. l_2 correspond to film thickness that best fits analysis. 1 Mil = 25.4 μm . PI-T5 is only used for analysis in fig. 5.22	56

Abbreviations

AR	Anti Reflection
ARC	Anti Reflection Coating
BFO	BiFeO ₃ , Bismuth Orthoferrite
BS	Beam Splitter
CMP	Cavity Magnon Polariton
DBR	Distributed Bragg Reflector
DFG	Difference Frequency Generation
DFT	Discrete Fourier Transformation
DR	Dynamic Range
EM	Electromagnetic
EO	Electro Optic
EOS	Electro Optic Sampling
ER	Extinction Ration
FFT	Fast Fourier Tranformation
FID	Free Induction Decay
FIR	Far Infrared
FP	Fabry-Pérot
FSEOS	Free Space Electro Optic Sampling
FT	Fourier Transformation
FTIR	Fourier Transform Infrared
FWHM	Full Width Half Maxima

HRFZ	High Resistivity Float Zone
IFT	Inverse Fourier Transformation
IL	Insertion Loss
IR	Infrared
LNB	LiNbO ₃ , Lithium Niobate
ND	Neutral Density
NIR	Near Infrared
OAPM	Off Axis Parabolic Mirror
OR	Optical Rectification
PC	Polycarbonate
PDMS	Polydimethylsiloxane
PE	Pockels Effect
PE	Polyethylene
PFT	Pulse Front Tilt
PI	Polyimide
PMMA	Polymethyl methacrylate
PP	Polypropylene
PSAT	Pressure Sensetive Adhesive Tape
SCR	Spin Cycloid Resonance
SNR	Signal to Noise Ratio
TDS	Time Domain Spectrometer or Spectroscopy
THz	Terahertz

List of Variables

Variable	Description
c	Speed of light in vacuum
ν	Frequency
ω	Angular frequency $\omega = 2\pi\nu$. In chapter 2, ω is used to denote IR angular frequency.
Ω	Angular frequency of THz light
\tilde{E}	Electric field in time domain
E	Electric field in frequency domain
λ	wavelength
\tilde{P}	Polarization in time domain
P	Polarization in frequency domain. Unless otherwise specified, P denotes the 2 nd order polarization.
$\chi_{ijk}^{(2)}$	2 nd order susceptibility tensor where indices denote 3 Cartesian coordinates
d_{ijk}	$d_{ijk} = \frac{1}{2}\chi_{ijk}^{(2)}$. Can be further contracted to d_{mp} , such that $d_{i(jk)} \rightarrow d_{mp}$, see section 2.2
ω_m	Subscripts m, n is used to distinguish 2 different angular frequencies that take part in nonlinear process
n	Real refractive index
n_g	Group refractive index

\bar{n}	Complex refractive index, $\bar{n} = n - i\kappa$
κ	Extinction coefficient
$\bar{\kappa}$	Coupling strength of spring connecting 2 harmonic oscillators
α	Absorption coefficient. Also used to denote incident angle in grating equation.
β	Diffraction angle in grating equation
E_g	Band gap
v	Phase velocity of light
v_g	Group velocity of light
\vec{k}	Wave vector. $ \vec{k} = k = \frac{2\pi}{\lambda}$
Δk	Phase mismatch. For phase matching condition, $\Delta k = 0$
γ	Tilt angle in pulse front tilt
γ_c, γ_m	Damping factor of cavity, magnon modes, respectively in the coupled harmonic oscillator model of CMP
G	Grating groove density
ϵ_{ij}	Component of dielectric tensor
r_{ijk}	Linear electro optic tensor where indices denote 3 Cartesian coordinates
W_0	Gaussian beam waist is given by $2W_0$
z_0	Rayleigh range of Gaussian beam
\mathcal{W}	Window function. Applied to time domain signal before performing Fourier Transformation.
t_{12}	Transmission coefficient from dielectric medium 1 to 2
\underline{t}	Transmission coefficient of multilayered structure
t_p	Transmission coefficient of p-polarized light
t_s	Transmission coefficient of s-polarized light

r_{12}	Reflection coefficient from dielectric medium 1 to 2
\underline{r}	Reflection coefficient of multilayered structure
r_p	Reflection coefficient of p-polarized light
r_s	Reflection coefficient of s-polarized light
H	Transfer function, $H(\nu) = E_{\text{out}}(\nu)/E_{\text{in}}(\nu)$
Y	Admittance of a medium with complex index \bar{n} , $Y = \bar{n}Y_f$, where admittance of free space, $Y_f = \sqrt{\epsilon_0/\mu_0}$
η_l	Polarization dependent oblique admittance of l^{th} dielectric layer in multilayered structure
δ_l	Phase thickness of l^{th} dielectric layer in multilayered assem- bly
θ_B	Brewster's angle
Δ	Tuning factor in CMP system, $\Delta = \omega_c - \omega_m$
$\tilde{\omega}_{\pm}$	Complex dispersion relation of CMP where $\text{Re}(\tilde{\omega}_{\pm})$ shows anticrossing of polariton branches and $\text{Im}(\tilde{\omega}_{\pm})$ shows evolu- tion of linewidth
C	Cooperativity between cavity photon and magnon. $C > 1$ for strong coupling and $C < 1$ for weak coupling.
g	Coupling strength used in quantum mechanical description of strong coupling
Ω_R	Rabi gap
r_L	Round trip attenuation factor in a cavity resonator
ν_{fsr}	Free spectral range of a cavity
\mathcal{F}	Finesse of a cavity
Q	Quality factor of cavity
τ	Photon lifetime in cavity

Chapter 1

Introduction

1.1 Optical Spectroscopy

There are various methods of uncovering the properties of matter. The principle of spectroscopy is to gain insights about matter by probing it with light. This interaction of light and matter can be observed by transmitting or reflecting light from samples and then observing the dependence of the absorption, transmission, or reflection on the wavelength or frequency of incident light. The decomposition of a given electromagnetic (EM) wave in its constituent frequencies can be demonstrated by a simple dispersive device, like prism or diffraction grating. Newton, in his classic experiment with visible sunlight and a prism, showed how white light's spectral content is made of the well known rainbow pattern of colors [1]. In this case, human eyes act as detectors for this simple spectrometer. As an example of molecular fingerprint, which tells us about materials characteristic vibration, rotation, electronic excitation, etc., we can refer to the absorption lines in solar spectrum, also known as Fraunhofer lines [2] that originate from solar and terrestrial atmosphere, see fig. 1.1.

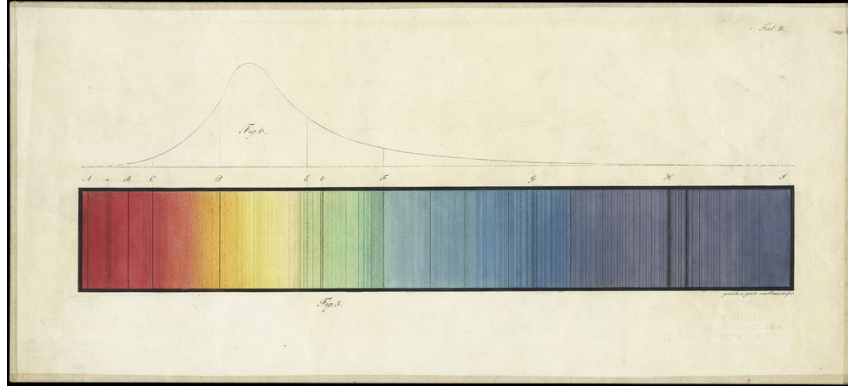


Fig. 1.1: Solar absorption lines observed by Fraunhofer, reprinted from Deutsches Museum Munich, Germany and [2] with permission

1.2 Time Domain Spectroscopy

The above mentioned method of spectral investigation relies on dispersing the components of EM waves based on its frequency by a grating or prism and then detecting each spectral component with the help of appropriate sensors. This conventional method can be categorized under frequency-domain spectroscopy. But there is also a more fundamental means of decomposing light into its frequency elements. That is accomplished by recording the extremely fast oscillating electric field of light, typically using non-linear electro-optic crystals, and then performing Fourier transformation on the temporal waveform which yields the spectral content of light. To observe material response to a broad range of frequency, one requires a light source with necessary bandwidth. Instead of tuning the frequency of light, in time domain, one uses a very short pulse of light which inherently possesses a broad frequency content $\Delta\nu \sim \frac{1}{\Delta t}$ [3]. Thus, coherent light pulses provide a method of spectral analysis which is the backbone of this thesis. Being able to generate and detect extremely short light pulses of the order of ~ 1 ps, we can observe material dynamics directly from measured time-trace which contain both the phase and amplitude response of the substance. Furthermore, in time domain we can distinguish between pulses that result from simple transmission through a sample and the ones that result from internal reflections at the sample-air interface. This feature permits us to selectively analyze certain portions of the waveform which is not possible in frequency domain measurements.

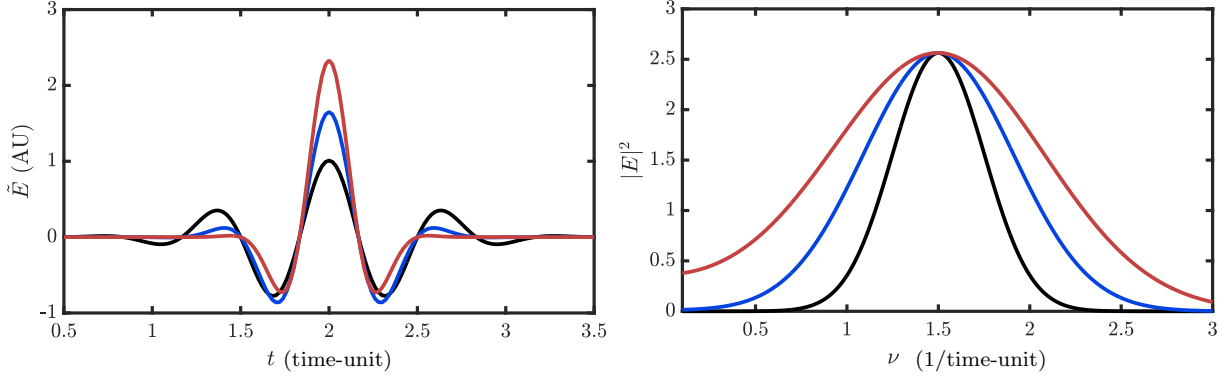


Fig. 1.2: Fourier Transform connecting time and frequency domain information. In frequency domain all three pulses are centered at the same frequency ν_0 .

1.3 Terahertz Light

Terahertz (THz) light is a portion of the electromagnetic (EM) wave between microwave and far-infrared (FIR) that gets its name directly from its temporal frequency, which is around 10^{12} Hz. The spectral range for THz light is loosely defined to be in the interval 0.1–10 THz. Due to the difficulty in generation and detection, this part of the EM spectrum used to be called the ‘Terahertz gap’ [4]. Thus, THz region has been under-exploited and its potentials are being discovered and explored as time advances. A brief summary of some of its optical characteristics in neighboring EM region is illustrated in fig. 1.3.

Vacuum Properties	EM Spectrum		
	Microwave	THz	NIR
ν	1 GHz	1 THz	100 THz
λ	30 cm	0.3 mm	3 μm
$1/\lambda$	3/m	30/cm	300/mm
$h\nu$	4 μeV	4 meV	0.4 eV

Fig. 1.3: Location of Terahertz light in EM spectrum. Nominal values are given to highlight vacuum properties. The broad interval of far infrared has been omitted. NIR corresponds to near infrared, which is adjacent to visible light.

Having low photon energy, this non-ionizing light is used for medical and security imaging and non-destructive testing as an alternative to carcinogenic X-ray, ultrafast wireless communication, etc. to list a few [5–9]. In this project we are interested in the construction of a functional time-domain THz spectrometer for the study of THz dynamics in

magnetic materials, and, in particular, light-matter interaction at THz frequencies in multiferroic BiFeO₃. To accomplish this, we construct a tilted-pulse front Lithium Niobate-based THz-Time Domain Spectrometer (THz-TDS) and develop low-cost multilayered optical components, that can be tuned to specific applications, notably, high resolution spectroscopy.

1.4 Spectroscopy with THz pulses

1.4.1 Normal Materials

In the following chapters we will demonstrate the construction of a terahertz time domain spectrometer (THz-TDS) using an infrared pulsed laser and nonlinear crystals. We will explain the theoretical and practical aspects of generation, detection, and detailed analysis procedure in chapters 2 and 3. We perform spectroscopy on a few different simple low loss dielectric samples and extract their optical parameters in chapter 4. These materials, silicon, alumina, and quartz glass are typically used in THz optics and provide us specifications for future device fabrication. Using the extracted sample properties, we developed optical components that are used in more demanding spectral investigations.

1.4.2 Magnetoelectric Multiferroic

Multiferroic materials have a simultaneous presence of multiple ferroic orders. Magneto-electrics, offer cross-coupling between its electric and magnetic orders which allow control of magnetic behavior via electric field and vice-versa. BiFeO₃ (BFO) exhibits both ferroelectric and antiferromagnetic properties in room temperature, which are coupled together. BFO has been studied extensively for the plethora of potential applications this versatile material offers without requiring low temperature set-up [10–12]. Due to the coupling between electric and magnetic lattice, one is able to observe magnetic dynamics in BFO by incident electric field. The material excitation, electromagnons, of BFO lie in the sub-THz range and can be excited with THz pulses [13, 14]. Presence of observable electromagnons in BFO makes this material a potential candidate for the study of strong light-matter coupling, which has not yet been reported with this magnetoelectric multiferroic.

Two closely spaced electromagnons in BFO lie around 0.55 THz. Using standard time

domain spectroscopy, we are unable to unambiguously resolve these magnon modes. Therefore, for the study of light-matter interaction in BFO, we developed a wide range of antireflection (AR) coatings in chapter 5 for various substrates. With the help of an AR coated detector crystal, we are able to perform high resolution spectroscopy on BFO and resolve the individual magnon modes in chapter 7. Following detection of the magnon modes, attempts were made to detect magnon-photon coupling between the BFO magnons and photons trapped in a rudimentary electromagnetic cavity. Temperature was varied and an external electric field was applied to a polycrystalline BFO slab that acted as a lossy etalon. No signs of coupling could conclusively be detected. However, the development work of custom THz optics performed to upgrade the spectrometer also provided a path forward. Distributed Bragg reflectors (DBRs) were designed and simulated as a basis for the formation of a high quality electromagnetic cavity to replace the sample etalon. A higher quality cavity is expected to make the coupling much easier to detect. Cavity polaritons in the THz regime are still an emerging field and is important for both fundamental science and device applications [15–17]. Based on the DBRs designed in this thesis, examination of the strong coupling between magnons and cavity photons in BFO will be pursued in a future project.

1.5 Multilayered Optics in THz region

THz range has historically been difficult to access, but promising experiments paved the way to THz spectroscopy in the late 20th century [18]. Since its birth, THz technology is developing rapidly, but cost-effective solutions to some optical requirements are still difficult to find. Many widely used technologies in other spectrum are not so conveniently and economically available in the THz range, for example THz light-source, detector, anti-reflection (AR) coating, resonator cavity, large aperture polarizer, etc.

In this thesis, making use of the TDS, we will demonstrate the performance of some low-cost optical components utilizing multilayered dielectric structures. The development of these optics resulted from the experimental demand for the observation of cavity polaritons in BFO. We demonstrate how efficient wide-band AR coatings can be implemented for a variety of substrates using commercially available films and adhesives in chapter 5. We also show that polymer based large area polarizing filters with high extinction ratio can be constructed very economically for a relatively narrow bandwidth in chapter 6. The polarizers are designed to be operated in Brewster’s angle and hence it transmits the

incident light of one polarization while strongly reflects the other polarization due to interference effect arising from carefully layered plastic structure. Availability of an easy to construct polarizer will aid in polarization sensitive experiments. In addition to that, we investigate the characteristics of distributed Bragg reflectors (DBRs) constructed with stacks of low loss dielectrics. Employing two DBRs, we discuss the design aspects of a high Q THz resonator along with its time and frequency response in chapter 7. The prescribed tunable cavity will be applied in the study of THz cavity magnon-polariton in BFO as mentioned in the earlier section.

Chapter 2

THz Generation and Detection

2.1 Introduction

In this Chapter, we describe the theory behind THz generation and detection. Due to technological advances over the years, many methods have been introduced for this purpose. Utilizing optical nonlinearity in electro-optic crystals, we are able to both generate and detect THz light. For generation we will be focusing on Optical Rectification (OR) in a LiNbO₃ (LNB) crystal. For THz detection we will explore Free-Space Electro-Optic Sampling (FSEOS) in GaP crystal. OR in LNB is accomplished by tilting the pulse front of infrared pump beam—a process that is somewhat challenging to optimally implement. In contrast, FSEOS in GaP is much more straightforward. We describe the key practical steps that need to be followed for a functional THz-TDS setup. Once a THz waveform is recorded we can perform spectral investigations using Fourier transformation. We show the effect of water vapor on the THz signal and highlight the requirement for nitrogen purging. Following standard practice in nonlinear optics, we will describe the frequency domain quantities in terms of the angular frequency, ω .

2.2 Nonlinear Polarization

A brief introduction to material nonlinearity is required for the discussion of THz generation. The subject matter can be understood in more detail from [19]. An external electric field, $\tilde{E}(t)$, applied to a dielectric gives rise to electric dipole moments, which collectively

contribute to the material polarization, $\tilde{P}(t)$. Here the tilde symbol ($\tilde{}$) on top of a quantity indicates the oscillating time domain function and the absence of tilde corresponds to the frequency domain function of the same quantity. Under common circumstances in one dimension, a material is characterized by its polarization that varies linearly with external field,

$$\tilde{P}(t) = \epsilon_0 \chi^{(1)} \tilde{E}(t) \quad (2.1)$$

where ϵ_0 is the permittivity of free space and $\chi^{(1)}$ is called linear susceptibility. To describe nonlinear light-matter interaction, the induced polarization is expressed as a power series of external field, assuming instantaneous response:

$$\tilde{P}(t) = \epsilon_0 \left[\chi^{(1)} \tilde{E}(t) + \chi^{(2)} \tilde{E}^2(t) + \chi^{(3)} \tilde{E}^3(t) + \dots \right] \quad (2.2)$$

It should be noted that in numerical value in SI units, $\chi^{(2)}$ is about 10^{12} order smaller than $\chi^{(1)}$ in typical solids ¹. As a result, only for high electric fields do we see the nonlinear susceptibility ($\chi^{(n)}$, $n > 1$) coming into effect. In experiments, we reach high \tilde{E} in a dielectric by focusing pulsed laser light. In our case, we will only take into account the second order nonlinear polarization, i.e., the 2nd term in the series. As a consequence of Fourier transformation, frequency components are allowed to have both positive and negative values. The components of $P^{(2)}$ induced by electric fields with frequencies ω_m and ω_n can be expressed in the frequency domain by eq. (2.3). Here the subscripts m, n represent the different frequencies that may be involved in the nonlinear process. Henceforth we omit the superscript in polarization as we will be only dealing with the 2nd order.

$$P_i(\omega_n + \omega_m) = \epsilon_0 \sum_{jk} \sum_{(nm)} \chi_{ijk}^{(2)}(\omega_n + \omega_m, \omega_n, \omega_m) E_j(\omega_n) E_k(\omega_m) \quad (2.3)$$

Here $\chi_{ijk}^{(2)}$ is a second order susceptibility tensor and i, j, k refer to the Cartesian coordinates. Although ω_m and ω_n are allowed to take any value, $(\omega_m + \omega_n)$ needs be fixed throughout the summation [19]. We notice from eq. (2.3) that for fixed ω_m and ω_n , the resulting single tensor can have 27 components. Ref [19] shows that 12 such tensors are required to provide a complete description of three mutually interacting waves. However, symmetry present in the system help significantly reduce the number of independent components in

¹ $\chi^{(1)}$ is dimensionless and $[\chi^{(2)}] = [\text{length}]/[\text{electric field}]$

the susceptibility tensors. First we define a new tensor d_{ijk} such that:

$$d_{ijk} = \frac{1}{2}\chi_{ijk}^{(2)} \quad (2.4)$$

When dispersion in $\chi^{(2)}$ may be neglected, Klienman's symmetry condition is valid and the d_{ijk} tensor can be represented by a 3×6 contracted matrix d_{mp} , $d_{i(jk)} \rightarrow d_{mp}$, where indices follow [19, 20]:

$jk :$	11	22	33	23,32	31,13	12,21
$p :$	1	2	3	4	5	6

$$d_{mp} = \begin{pmatrix} d_{11} & d_{12} & d_{13} & d_{14} & d_{15} & d_{16} \\ d_{21} & d_{22} & d_{23} & d_{24} & d_{25} & d_{26} \\ d_{31} & d_{32} & d_{33} & d_{34} & d_{35} & d_{36} \end{pmatrix} \quad (2.5)$$

We can further reduce the independent matrix elements by utilizing symmetry present in specific crystal classes [19]. For a fixed crystal orientation, propagation and electric field directions, one can use an effective value of d , d_{eff} , such that polarization can be described in the form of eq. (2.6). d_{eff} is a convenient metric for comparing nonlinear crystals.

$$P(\omega_3) \propto d_{\text{eff}} E(\omega_1) E(\omega_2) \quad (2.6)$$

2.3 Generation Theory

Induced polarization in material acts as a source that drives the generated light. Utilizing this phenomena, we can generate broadband THz light. For nonlinear material selection, some key factors such as d_{eff} , THz absorption coefficient ($\alpha(\Omega)$), and phase matching between pump and THz fields are considered to be of paramount importance. In this project, we chose LiNbO₃ (LNB) as the nonlinear crystal primarily for its high d_{eff} , see table 2.1, and used optical rectification (OR) method for THz generation. LNB also has a higher bandgap of 3.8 eV compared to semiconductor crystals, which aids against multi-photon absorption and as a result LNB can be pumped with higher intensity before reaching saturation in THz output [21]. At room temperature, over 1 THz, LNB has increasing absorption and an optical phonon at 7.7 THz. Despite having relatively higher loss, LNB can produce more intense output pulses than other electro optic crystals. THz

generation efficiencies from GaP, ZnTe, LiNbO₃ pumped with 1035 nm laser can be found in [21]. For optimal generation from LNB, we had to incorporate pulse front tilt (PFT) technique to accomplish velocity matching between the pump IR and THz pulses. The following sections will shed more light on this topic.

2.3.1 Optical Rectification

Considering a monochromatic source of light, it is possible to undergo difference frequency generation (DFG) in a nonlinear crystal with its own components such that [20, 4]:

$$P(0) = \frac{1}{2} \epsilon_0 \sum_{jk} \chi_{ijk}^{(2)}(0, \omega, -\omega) E_j(\omega) E_k^*(\omega) \quad (2.7)$$

This results in a static polarization in the crystal as long as the external fields are applied and known as optical rectification (OR). Now, for a pulsed electric field, $\tilde{E}(t) = \text{Re}[A(t) \exp(i\omega_0 t)]$, where $A(t)$ is a slowly varying envelope and ω_0 the carrier frequency, one can show from [4, 22, 23] the form of induced polarization, $\tilde{P}(t)$, and generated radiation in the far field, $\tilde{E}_{gen}(t)$, in eq. (2.8). Here d_{eff} is assumed to be non-dispersive.

$$\tilde{P}(t) \propto |A(t)|^2, \quad \tilde{E}_{gen}(t) \propto \frac{\partial^2 \tilde{P}(t)}{\partial t^2} \quad (2.8)$$

By observing the nonlinear polarization in frequency domain, eq. (2.9), we can equivalently describe OR due to pulsed excitation as intra-pulse difference frequency generation (IPDFG) [22–25]. Here Ω, ω respectively denote THz and optical frequency and $\omega \gg \Omega$. The components of broadband optical pump pulse undergo difference frequency mixing in the crystal and generate THz frequencies as illustrated in fig. 2.1. A frequency down shift in the IR pump is also observed, also known as the cascading effect, which will be ignored in this discussion. For more details see [24, 25].

$$P(\Omega) \propto \int d\omega E(\omega + \Omega) E^*(\omega) \quad (2.9)$$

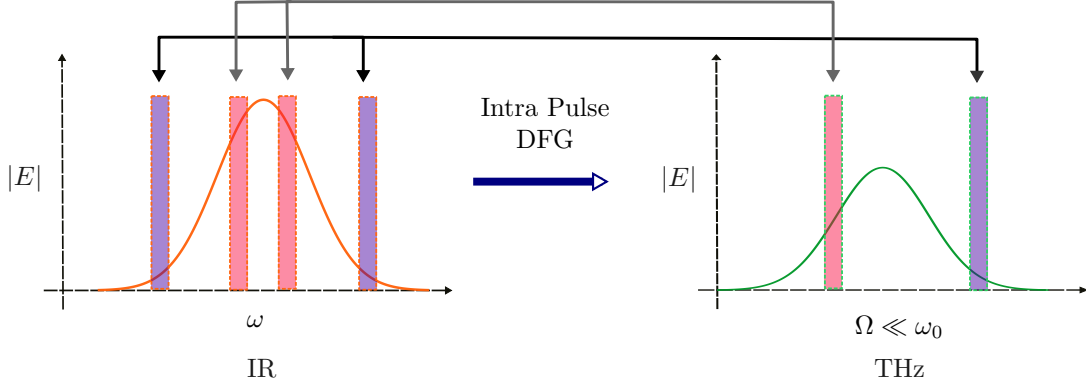


Fig. 2.1: The frequency components of IR pump pulse, shown on the left, undergo Intra-Pulse DFG inside the nonlinear crystal. The difference between pump's spectral content contribute to the generation of THz pulse, shown on the right. Here axes representing IR and THz are not in the same scale. See [25] for further illustrations.

Based on the efficiency of DFG by a pulse of average intensity, I , [26] mentions the following two relations describing efficiency of THz generation predicated upon the effect of THz absorption, $\alpha(\Omega)$, by a crystal of thickness L . It is also highlighted that an effective length of $L_{\text{eff}} = 1/\alpha(\Omega)$ in the crystal participate in THz generation. Hence a thickness of ~ 0.6 mm near the output face of LNB crystal is adequate for broadband generation.

$$\begin{aligned} \eta &\propto d_{\text{eff}}^2 L^2 I, & \alpha(\Omega)L \ll 1 \\ \eta &\propto \frac{d_{\text{eff}}^2 I}{\alpha^2(\Omega)}, & \alpha(\Omega)L \gg 1 \end{aligned} \quad (2.10)$$

Table 2.1: $d_{\text{eff}}, \alpha(\Omega)$ in few nonlinear crystals for OR, from [27, 28]. E_g denotes band gap.

Crystal	d_{eff} (pm/V)	$\alpha(1\text{THz})$ (1/cm)	E_g (eV)
GaAs	65.6	0.5	1.43
GaP	24.8	1.9	2.27 (indirect) 2.48 (direct)
ZnTe	68.5	1.3	2.26
LiNbO ₃	168	17	3.8

2.3.2 Pulse Front Tilt

Velocity matching between the generated (THz) and generating (IR) light waves is of crucial importance in any nonlinear optical phenomenon. Thus, for optimal THz generation, we require that $v_g(\omega_0) = v(\Omega)$, where v, v_g denote phase velocity and group velocity, as defined by eq. (2.11) and ω_0, Ω denote central IR and THz angular frequency. Velocity matching is a consequence of desiring phase mismatch, $\Delta k(\Omega) = 0$. In the case where the pump and THz pulses propagate co-linearly in the crystal we can work in 1D and find $\Delta k(\Omega)$ as shown in eq. (2.12).

$$v_g(\omega) = \frac{d\omega}{dk}, \quad v(\omega) = \frac{\omega}{k} \quad (2.11)$$

$$\begin{aligned} \Delta k(\Omega) &= k(\omega_0 + \Omega) - k(\omega_0) - k(\Omega) \\ &\approx \Omega \frac{dk(\omega_0)}{d\omega} - k(\Omega), \quad [\cdot: \Omega \ll \omega_0] \\ &= \Omega [v_g^{-1}(\omega_0) - v^{-1}(\Omega)] \\ &= [n_g(\omega_0) - n(\Omega)] \frac{\Omega}{c} \end{aligned} \quad (2.12)$$

Where we define group index similar to phase index, $n_g = c/v_g$, where c is the speed of light in vacuum. LNB is a negative uniaxial crystal, hence propagating perpendicular to the optic axis with polarization parallel to that axis, implies that light would experience extraordinary refractive index. In 1 mol% MgO doped stoichiometric LNB we estimate $n(\Omega) \approx 4.92$ [29] and $n_g(\omega_0) \approx 2.21$ calculated from the Sellmeier's equation provided by [30], in room temperature. We used 1035 nm central IR wavelength and 1 THz frequency for the estimation. Unfortunately according to eq. (2.12), $\Delta k(\Omega) = 0$ can not be satisfied in colinear geometry due to the index mismatch resulting in $v_g(\omega_0)/v(\Omega) \sim 2.2$. Hence to accomplish phase matching we are bound to implement a non-colinear geometry where projection of $\vec{v}_g(\omega_0)$ along $\vec{v}(\Omega)$ should equal $v(\Omega)$ [27]. This condition is shown in eq. (2.13), where γ is the angle between $\vec{k}(\omega), \vec{k}(\Omega)$.

$$\begin{aligned} \Delta k(\Omega) &\approx \left[\frac{n_g(\omega_0)}{\cos(\gamma)} - n(\Omega) \right] \frac{\Omega}{c} = 0 \\ v_g(\omega_0) \cdot \cos(\gamma) &= v(\Omega) \end{aligned} \quad (2.13)$$

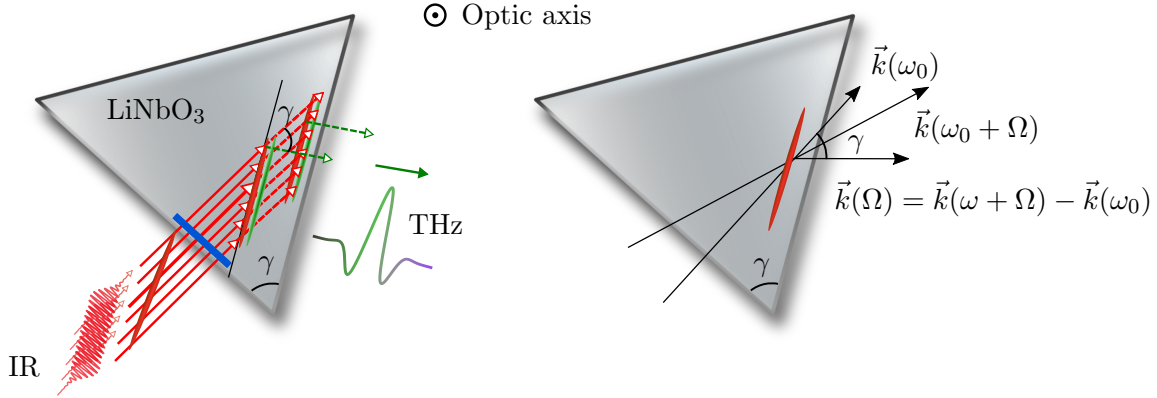


Fig. 2.2: Illustration of THz generation by non-collinear phase matching in LiNbO₃. IR is polarized along the optic axis of LNB. Pulse front and phase front are shown in red and blue.

Experimentally, above mentioned conditions are satisfied by tilting the intensity front of IR pulse by an angle, $\gamma \approx 63.3^\circ$ with respect to the phase front. Pulse front at a given time is defined as the locus of the peak electric field of light beam. Pulse front tilt (PFT) is realized by devices that impart angular dispersion and obeys the following relation, where $\frac{d\beta}{d\lambda}$ quantifies angular dispersion and n is the index of surrounding medium [31]. It should be noted that phase front is perpendicular to the propagation direction of respective wave.

$$\tan \gamma = -\frac{n}{n_g} \lambda_0 \frac{d\beta}{d\lambda} \quad (2.14)$$

We make use of a diffraction grating with 1200 lines/mm to introduce the PFT. The grating equation, eq. (2.15), is used for experimental setup, where G represents grooves per unit length, α, β are incident and diffracted angles measured from grating normal and m is the order of diffraction which in our case, $m = 1$. One criterion for optimal THz generation and beam quality is minimization of IR pulse duration across the pulse front, which is realized by imaging the grating so that grating image coincide with IR pulse front in LNB [28]. Finally the output face of LNB crystal should be cut at the tilt angle to allow THz outcoupling with minimal reflection loss. More on efficient outcoupling can be found in chapter 5.

$$Gm\lambda = \sin(\alpha) + \sin(\beta) \quad (2.15)$$

To reduce the imaging errors a 4f telescope setup was implemented which demagnifies the diffracted light and images the grating in LNB in a small area, see fig. 2.3. Following the grating and telescope setup one can deduce the expression for tilt angle in the crystal, eq. (2.16) [31, 32].

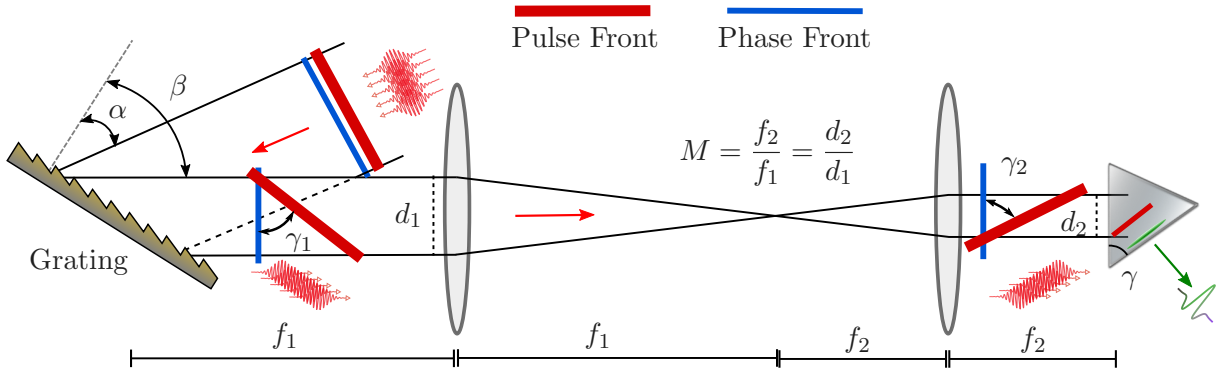


Fig. 2.3: Setup for PFT in LiNbO₃. Only single frequency component is shown

$$\tan(\gamma) = \frac{\lambda_0 G}{n_g(\omega_0) M \cos(\beta)} \quad (2.16)$$

Utilizing the PFT technique, we can find detailed theoretical investigations on THz generation in LNB in [24, 28, 33]. For our project we are concentrating on the experimental applications of the spectrometer.

2.3.3 Determination of Angles & Lens Combination

When using reflection type diffraction grating, in order to maximize power in the diffracted light, the grating is operated in the Littrow configuration where $\alpha = \beta$ [34]. However, this is not practical to implement. Nevertheless, by allowing small deviation from Littrow condition, $\alpha - \beta = 0$, we can achieve an angle, using eq. (2.15), that would still be quite efficient in reflecting incident power. Since $\gamma = 63^\circ$, β is dependent on $M = \frac{f_2}{f_1}$ through eq. (2.16). Because of the availability of multiple lenses, one has to choose the lens combination that allows β to be closest to the Littrow combination. This problem can be graphically solved with the aid of fig. 2.4. Plots were made for $\lambda_0=1035$ nm, $G=1200$ lines/mm and a tolerance of $|\alpha - \beta| \leq 25^\circ$ was used.

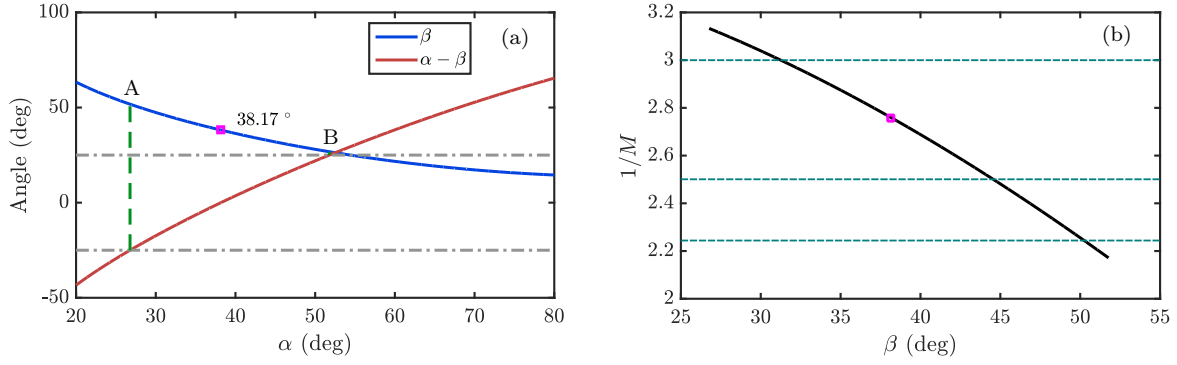


Fig. 2.4: (a) Plot from grating equation. Horizontal gray dash-dot lines indicate the regions where $\alpha - \beta \leq 25^\circ$. Vertical green dashed lines indicate range of allowed β , marked by points A, B. Magenta square showing Littrow condition. (b) Plot of $1/M$ vs allowed β . Dashed horizontal lines correspond to available lens combinations satisfying $1/M$.

For our setup we selected $1/M = 2.5$, that is satisfied by $M = f_2/f_1 = 40 \text{ mm}/100 \text{ mm}$. Additionally, foresight is valuable in choosing focal length combinations: ignoring dispersion and imaging errors, a telescope that is too short may make alignment challenging, while one that is too long may require larger diameter lenses to capture dispersed light.

2.4 THz Detection

In order to detect THz radiation, there are primarily two class of methods employed, coherent and incoherent detection. Coherent detection refers to the phase-resolved measurement of THz waveform, while incoherent method measures the power of incident THz light. Both of these detection methods are utilized for alignment and spectroscopy purpose. Incoherent detection is fairly simple to employ and the detector is primarily a thermal sensor. We utilize a thermopile radiation detector and an far-infrared thermal camera for alignment purposes. In the coherent measurement scheme, we employ the electro-optic (EO) crystal GaP and exploit THz-induced Pockels effect on IR probe pulse. This procedure is also called free space electro-optic sampling (FSEOS). The theory behind Pockels effect is very similar to that of OR. The following sections will highlight key points on FSEOS.

2.4.1 Pockels Effect

The change of material index due to an external static or low frequency electric field is referred to as electro-optic effect [19]. The Pockels effect (PE) or linear electro-optic effect is described as the linear dependence of the change in refractive index due to external static electric field. The origin of this phenomenon lies in the $\chi^{(2)}$ tensor of nonlinear crystals and described by eq. (2.17). The induced polarization at the optical frequency perturbs the index ellipsoid of the crystal and results in a change in crystal birefringence.

$$P_i(\omega) = 2\epsilon_0 \sum_{j,k} \chi_{ijk}^{(2)}(\omega, \omega, 0) E_j(\omega) E_k(0) \quad (2.17)$$

PE is conventionally described in terms of the induced polarization's influence on the dielectric tensor ϵ_{ij} , thus on refractive index ($n^2 = \epsilon$, for linear isotropic dielectric). In general, this relationship can be described as follows [20].

$$\Delta(\epsilon^{-1})_{ij} = \sum_k r_{ijk} E_k(0) \quad (2.18)$$

In eq. (2.18), r_{ijk} is the linear EO tensor, which for lossless materials can be written in a contracted notation and represented by a 6×3 matrix, r_{pm} , where indices follow the same contraction rule as d_{ijk} . Henceforth, r_{pm} would be referred to as the linear EO coefficient for respective crystals. Now, eq. (2.18), can be simplified to eq. (2.19). Moreover, the relation between EO coefficient and $\chi_{ijk}^{(2)}(\omega, \omega, 0)$ are given in eq. (2.20) [20].

$$\Delta(\epsilon^{-1})_p = \Delta\left(\frac{1}{n^2}\right)_p = \sum_n r_{pm} E_m(0) \quad (2.19)$$

$$r_{ijk} = r_{jik} = r_{pm} = -\frac{2\chi_{ijk}^{(2)}(\omega, \omega, 0)}{\epsilon_{ii}\epsilon_{jj}} \quad (2.20)$$

PE can be viewed as the inverse effect of OR. There exists a relationship between the tensors involved. For absorptionless crystals, symmetry in $\chi^{(2)}$ leads to following relationship between coefficients involved in OR and PE [20]:

$$\chi_{kji}^{\text{OR}}(0, \omega, -\omega) = \chi_{ijk}^{\text{PE}}(\omega, \omega, 0) \quad (2.21)$$

In the context of coherent THz pulse detection, the field of THz pulse is approximated as

static in comparison to the much faster oscillating narrow IR pulse field. This is yet another simplification resulting from the condition $\Omega \ll \omega$. For EO sampling we use $\langle 110 \rangle$ cut GaP of 1 mm thickness. The crystal belongs to the point group $\bar{4}3m$ whose members only have one independent EO coefficient, r_{41} . Key properties of popular EO crystals belonging to this group are shown in table 2.2. Moreover, these crystals are optically isotropic in $\chi^{(1)}$ and thus show no birefringence. An external static field, however, gives rise to a fast and slow axes in the index ellipsoid. This results in different speeds for the two polarization components of \tilde{E}_{IR} along the new principal axes. As the two orthogonal polarizations travel along the length of the crystal, L , a relative phase retardation, $\Delta\phi$, builds up which can be expressed as eq. (2.22) for the geometry shown in fig. 2.5 (b) [4].

$$\Delta\phi = (n_y - n_x) \frac{\omega L}{c} = \frac{\omega L}{c} n^3(\omega) r_{41} \tilde{E}_{THz} \quad (2.22)$$

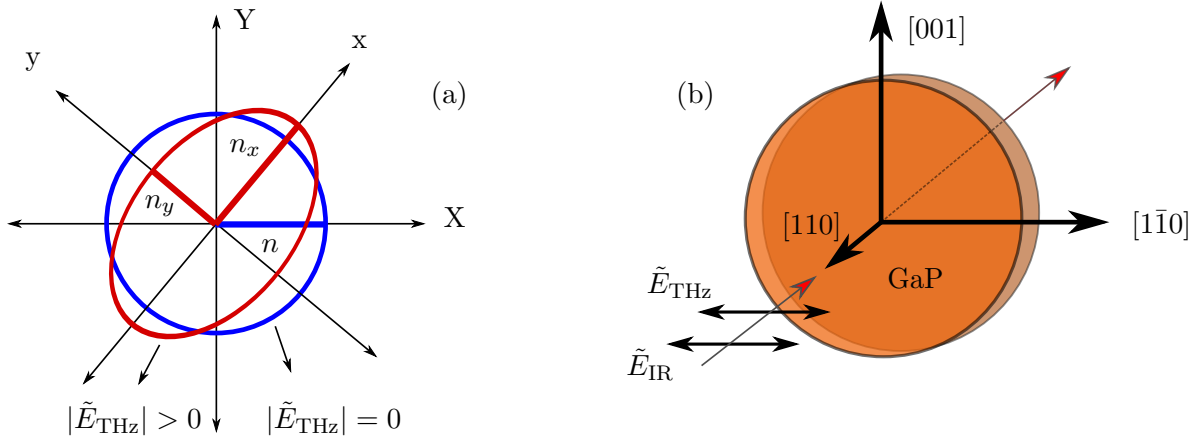


Fig. 2.5: (a) Pockels effect on the index ellipsoid of EO crystal. Without the presence of THz field, the crystal is isotropic, but incidence of THz field turns the crystal birefringent with altered principal axes [19]. (b) Orientation of GaP and field polarization directions of THz and IR pulse for maximizing EO signal [4].

2.4.2 Phase Matching & Balanced Detection

As mentioned in the THz generation section, phase matching is of crucial importance for optimal nonlinear effects. Despite the low EO coefficient of GaP, we still use it since GaP allows colinear phase matching between THz and 1 μm IR pulse. It should be noted that perfect phase matching is not possible for 1035 nm, but the deviation is considerably

smaller than LNB and can be neglected. Additionally, having an optical phonon at 11 THz provides a broader detection bandwidth than other EO crystals, although a thinner crystal is required to that end.

Table 2.2: Important properties of few EO crystals belonging to the point group $\bar{4}3m$. Information taken from [4, 35]. λ_0 denotes pump wavelength for phase matching.

Crystal	r_{41} (pm/V)	λ_0 (μm)	ν_{phonon} (THz)
GaAs	1.43	1.35	8.1
GaP	0.97	1.0	11
ZnTe	4.04	0.8	5.3

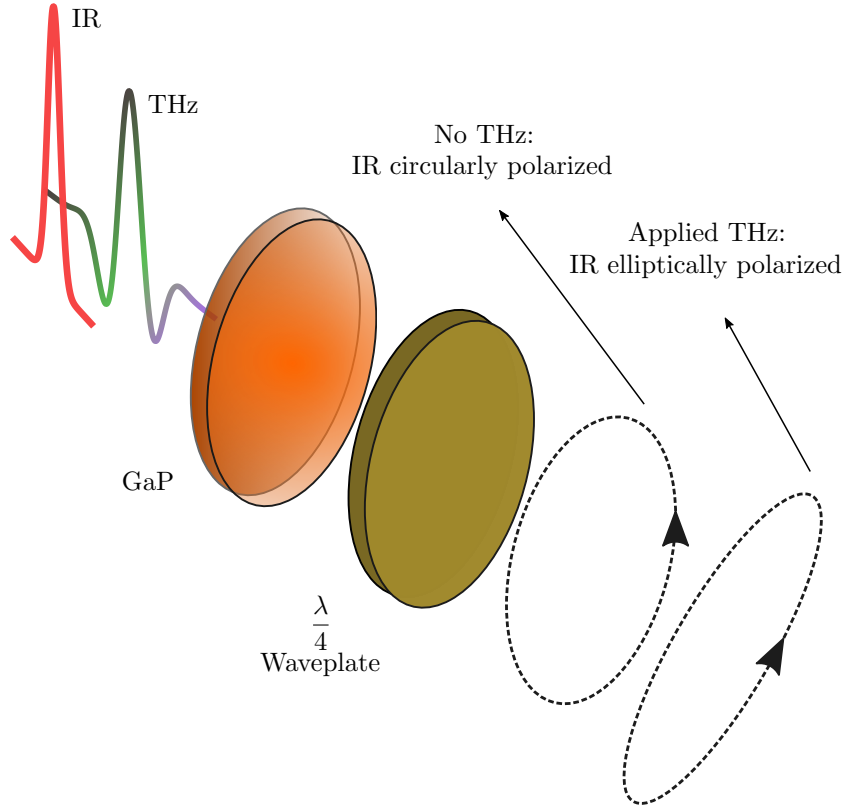


Fig. 2.6: FSEOS: showing only intensity envelope for probe IR pulse.

Figure 2.6 represents a schematic diagram for FSEOS. When no THz pulse is applied, GaP is optically isotropic and does not affect the IR polarization. The quarter ($\lambda/4$) waveplate turns the IR polarization from linear to circular. But applied THz field imparts a phase retardation and turns the IR polarization from circular to slightly elliptical. The probe IR

after the waveplate, is decomposed to its polarization components via a polarizing beam splitter and the intensity difference between two orthogonal components, $I_s = I_y - I_x$ is measured using a balanced photo detector. This intensity difference is proportional to the applied THz field amplitude, eq. (2.24).

At the balanced photo detector, intensities of the two orthogonal beams can be written as, eq. (2.23), where $\Delta\phi \ll 1$ and I_0 is the probe intensity exiting $\lambda/4$ waveplate [4].

$$\begin{aligned} I_x &= \frac{I_0}{2}(1 - \sin \Delta\phi) \approx \frac{I_0}{2}(1 - \Delta\phi) \\ I_y &= \frac{I_0}{2}(1 + \sin \Delta\phi) \approx \frac{I_0}{2}(1 + \Delta\phi) \end{aligned} \quad (2.23)$$

At a given time delay between probe IR and THz pulses, by measuring the intensity difference of the two orthogonally polarized IR beams we can measure the amplitude of the THz field at that time by,

$$I_s \approx I_0\Delta\phi = \frac{I_0\omega L}{c}n^3(\omega)r_{41}\tilde{E}_{\text{THz}} \quad (2.24)$$

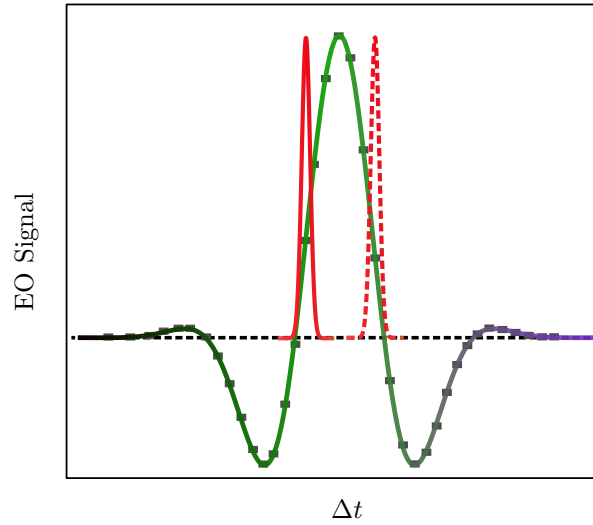


Fig. 2.7: IR pulse tracing out THz time-domain electric field

With the help of a linear delay stage we can introduce time delay, Δt , between THz and IR pulses. At discrete Δt locations we measure I_s which traces out the time domain electric field of THz pulse. This is possible because IR pulse has much smaller duration than THz pulse and at each Δt , the convolution between the two pulses are measured.

2.5 Experimental Setup

For a transmission mode THz-TDS setup see fig. 2.8. We use a Ytterbium (Yb) fiber laser, Y-Fi, that emits pulses <170 fs centered at 1035 nm, with repetition (rep) rates 1–60 MHz with pulse energy of the order of ~ 1 μ J. For the most part we operated the laser at 10 MHz rep rate with an average power from 15–18 Watt. With the help of a 90/10 beam splitter (BS) we split the laser beam into pump and probe. The higher power pump excites LNB that generates THz, while the lower power probe is used for coherent detection. It is interesting to note that the same pulse pair is used for THz generation and detection, ergo we require the pump and probe path to be almost equal.

The pump beam is sent to a delay stage which is used to incorporate time-delay between the pump and probe. A chopper modulates the pump and thus the THz signal. A half waveplate ($\lambda/2$) is used to change IR polarization from vertical to horizontal before impinging on diffraction grating, this enhances efficiency of the grating [34]. The 1st order reflection is sent through a 4f telescope and another $\lambda/2$ waveplate to turn the polarization back to vertical to align with the LNB optic axis. The generated THz is aligned using unprotected gold coated off-axis parabolic mirrors (OAPM) and focused onto the sample to be characterized and then focused on GaP EO crystal for detection.

The low power probe beam goes through appropriate neutral density (ND) filters that attenuate IR power further, well under the damage threshold of balanced detector. A Glan Taylor polarizer is used to ensure no residual horizontal polarization component is incident on GaP. This helps in acquiring good quality signal since the detection scheme is polarization sensitive. An OAPM with hole is used to pass probe through THz focus in GaP, in this step we use a telescope setup (not shown in fig. 2.8) to collimate the probe to a beam diameter comparable to THz spot size. A quarter ($\lambda/4$) waveplate is used to circularly polarize the IR. Finally a polarizing beam splitter, Wollaston prism, is used to decompose the circular/elliptical polarization into two orthogonal components and sent to a balanced photo-detector, Nirvana auto-balanced photoreceiver (model 2007). The output from balanced detector is sent to lock-in amplifier and lock-in output is recorded using data acquisition hardware.

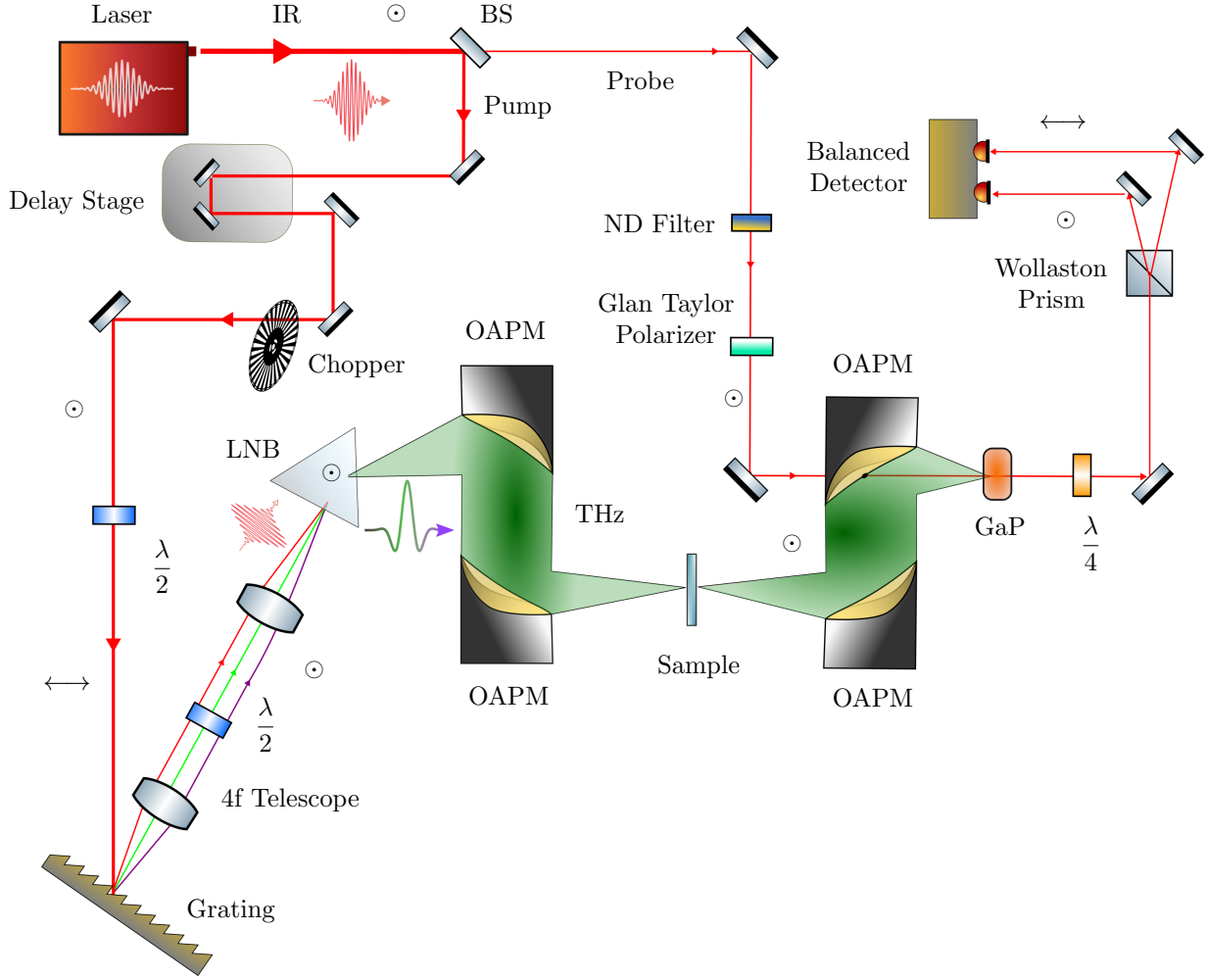


Fig. 2.8: Complete setup for simple transmission mode spectroscopy. Polarization of light and optic axis of LNB are shown by symbols: \odot , \leftrightarrow .

We assume that the THz beam has a Gaussian profile. A Gaussian beam in the cross-sectional plane of propagation axis (z), drops in intensity by a factor of $1/e^2$ at radius $W(z)$, called the beam width [23]. The minimum beam radius, W_0 , is at the beam focus/waist, located at $z = 0$, and $2W_0$ is called the spot size, see fig. 2.9. At $z = 0$, the radius of curvature of wavefront, $R \rightarrow \infty$, i.e., similar to that of plane wave and $R(z)$ slowly decreases to a minimum value at a distance $|z| = z_0$, called the Rayleigh range. The distance $2z_0$ is called the depth-of-focus and related to beam waist via eq. (2.25). Since in analysis we approximate the THz wave as a plane wave, practically, this implies placing the sample of thickness L at the beam waist and satisfying $L \ll 2z_0$.

$$W_0 = \sqrt{\frac{\lambda z_0}{\pi}} \quad (2.25)$$

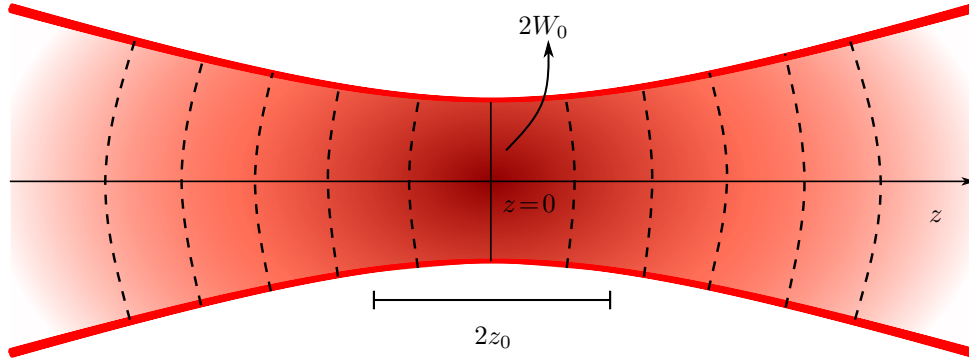


Fig. 2.9: Gaussian beam with beam waist $2W_0$ and depth of focus $2z_0$. The dotted curved lines represent radius of curvature of the wavefront $R(z)$.

For aligning THz beam we have used custom built thermopile sensor with active area $0.51 \times 0.51 \text{ mm}^2$ and silicon (Si) window. This device was utilized in conjunction with lock-in amplifier for THz alignment. Due to the slow response of the sensor, one has to use a low modulation frequency for lock-in detection, we used 23 Hz. With the aid of manual 2D translation stage, we scanned the THz beam-waist with this power detector, see fig. 2.10. Since manually scanning the spot was very demanding, we only scanned one half of the spot and assumed that the other half would be similar.

We also bought 32x32 thermopile array imaging sensor with Si window and complete application set from Boston Electronics, which is a significantly economic alternative to commercial THz detection units. It should be noted that the camera can image only THz beam that are directly incident on its lens. Therefore specular reflection can be imaged while diffused reflection could not be detected. We are unaware of the resistivity of the Si window used and since it is a lens, we could not simply use the camera as a beam profiler. It is possible to increase the THz power transmitted to the imaging array using appropriate AR coating, see chapter 5.

For a step-by-step instruction for THz generation, detection, and alignment, see appendix A.

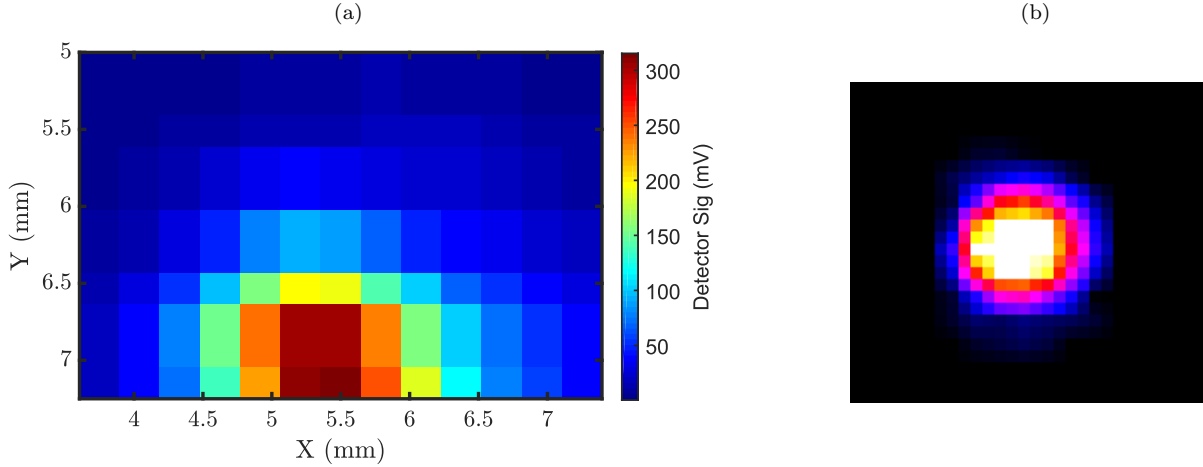


Fig. 2.10: (a) Upper half of beam waist profile scanned with thermopile detector. FWHM ~ 1.5 mm; $\therefore 2W_0 \sim 2.5$ mm, $2z_0 \sim 35$ mm. (b) Image taken using far-infrared camera in the collimated section of THz beam.

2.5.1 Chopper and lock-in setup

Since the Pockels effect induces a small change in the balanced detector output, we extract the signal from a noisy background with the help of lock-in amplifier. Lock-in amplifiers are used to detect small signals of a fixed reference frequency that may be buried in noise. Phase sensitive detection of lock-in allows extraction of both amplitude and phase of the input signal. This significantly improves the signal to noise ration (SNR) in detection. For details on lock-in detection and its application in THz-TDS one can see [36, 37].

For applications in this project, we used SR830 DSP lock-in amplifier. The THz signal was modulated by an optical chopper which we operated at 1 KHz, the highest frequency setting available, to reduce $1/f$ noise. Since our laser has a repetition rate of the order of MHz, the relatively low chopper frequency was not of any concern. The output from balanced detector was sent to lock-in input and the output signal from chopper controller was sent to lock-in reference. At a given time in the THz waveform, see fig. 2.11, we can have three scenarios resulting from modulated balanced signal, I_s . $I_s = 0$, correspond to no THz signal while $I_s > 0$, $I_s < 0$, correspond to the positive or negative polarity of the THz signal. Therefore, ideally the phase difference between the reference and I_s is 0 or π .

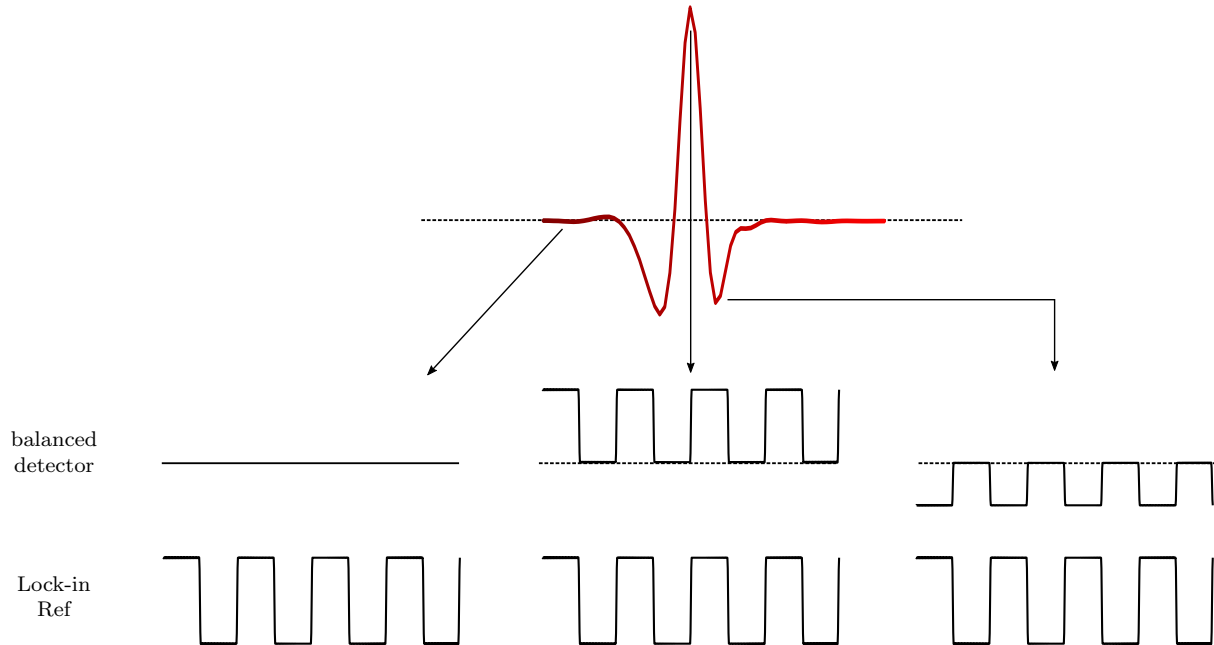


Fig. 2.11: 180° phase shift between the two balanced signals is evident when sampling peak and trough of the THz pulse. The DC offset in the signals are taken care of by lock-in's AC coupling. The lock-in reference is a square wave sent from the chopper.

2.5.2 Nitrogen Purging

In all likelihood the 1st waveform one successfully acquires while building a THz-TDS is influenced by water vapor absorptions. For clear spectroscopy one needs to get rid of the water vapor from THz environment. To that end, we built a box made of aluminum that covers the region where THz is confined and purge air with nitrogen (N_2). Since, in room temperature N_2 does not have any absorption, we get a clear single cycle THz waveform. From fig. 2.12 we see that without purging in time domain, there are oscillations present after the THz pulse peak, which correspond to free induction decay (FID) from the vapor. In the spectrum this shows up as absorption lines. On the contrary, N_2 purging produces a smooth spectrum. We note that there is some vapor we could not get rid of and thus weak absorption features can be noticed even with purging.

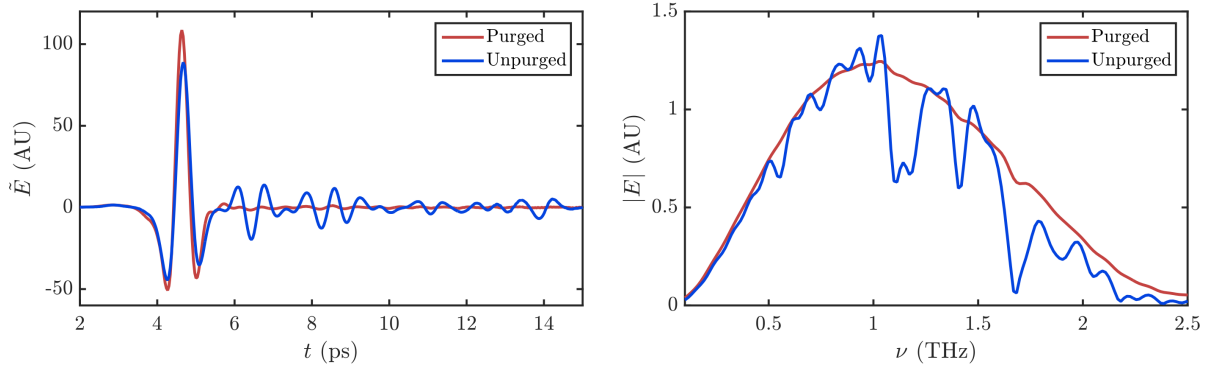


Fig. 2.12: Effect of N₂ purging in time and frequency domain. FID due to water vapor is noticeable in the blue waveform.

2.5.3 SNR and DR

Two most important parameter of the TDS apparatus is signal-to-noise ratio (SNR) and dynamic range (DR). These parameters can be calculated for both time and frequency domains. Ref. [38] points out that since we are dealing with a pulse, DR or SNR calculated in the two domains are not generally the same. This is because in time domain we can calculate these parameters at the peak of THz pulse, but there is no corresponding single point in frequency domain. We use the definitions given in [38] which also shows that in time domain, it is most meaningful to calculate the SNR and DR from the THz peak signal, while for the frequency domain, DR of the full spectrum is easier to follow than SNR. In eq. (2.26), $\overline{\tilde{E}_p}$ denotes the mean value of peak signal, and SD correspond to standard deviation. Here the mean and SD are calculated for the number of sweeps measured under same conditions. The TD noise floor can be measured by blocking the THz beam and measuring the background signal.

$$SNR = \frac{\overline{\tilde{E}_p}}{SD(\tilde{E}_p)} \quad (2.26)$$

$$DR = \frac{\overline{\tilde{E}_p}}{SD(\text{TD noise floor})}$$

For spectral DR calculation, we 1st take the mean time trace and Fourier transform it. By plotting the amplitude spectrum in log-scale we can estimate the spectral noise floor. Using eq. (2.27) we can calculate $DR(\nu)$. $DR(\nu)$ sets the upper limit in material absorption calculation. For simple transmission mode measurement the relationship for sample of

thickness d and index $n(\nu)$ are given by eq. (2.28) [39].

$$DR(\nu) = \frac{|\overline{E(\nu)}|}{\text{amplitude noise floor}} \quad (2.27)$$

$$\alpha_{\max}(\nu)d = 2 \ln \left[DR(\nu) \frac{4n(\nu)}{(n(\nu) + 1)^2} \right] \quad (2.28)$$

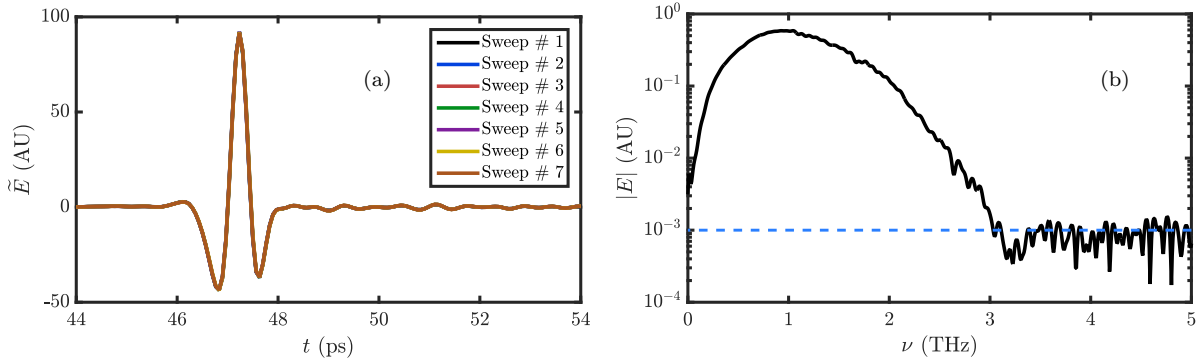


Fig. 2.13: Pump power $\sim 13.5\text{W}$ at 10 MHz rep rate. (a) 7 time domain sweeps. At peak $SNR \approx 414$, $DR \approx 5473$. (b) Amplitude spectrum of the average waveform. Amplitude noise floor is estimated by dashed line.

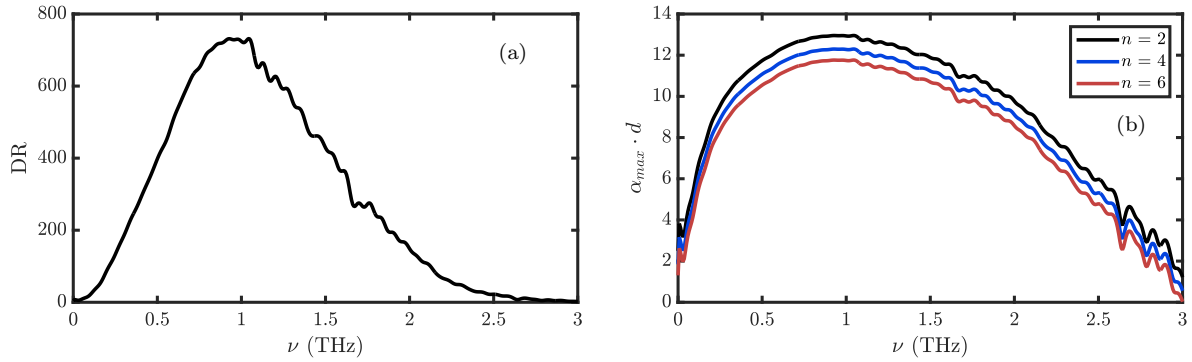


Fig. 2.14: (a) Spectral dynamic range. (b) Maximum absorption that can be reliably measured for few values of index, n .

2.6 Conclusion & Discussion

We have briefly highlighted and illustrated the basic theory of constructing a time domain THz spectrometer exploiting nonlinearity in electro-optic crystals. We have also constructed the fully functional apparatus that incorporates multi axis motion control using micro-controllers that allow characterization of multiple samples without opening the purge box. An improvement in the purge box design would help in faster and more efficient N₂ purging. The small FID present from water vapor in time trace inhibits measuring small signals precisely and often interferes with internally reflected pulses. We also require to calibrate the THz field, for simple linear spectroscopy this was not needed.

In the following chapters we would concentrate on the applications of this spectrometer. It is used to characterize different types of samples and multilayered optics that has technological implications. It is an essential tool in our study of THz light-matter coupling in BiFeO₃. The spectrometer will also be employed in other future projects.

Chapter 3

Analysis

3.1 Introduction

Spectroscopic investigations, by definition, are conducted in the frequency domain. In general, materials or devices that interact with THz pulses have frequency dependent response, hence we are constrained to the frequency space for analysis. Since we acquire data in time domain, Fourier transformation (FT) is an indispensable tool used from the beginning of our analysis. Since THz-TDS preserves the phase of recorded signals, it is superior to another spectroscopic technique, Fourier transform infrared spectroscopy (FTIR), both of which rely on FT. This facilitates THz-TDS to extract material properties without applying Kramers–Kronig relations, which relate the spectral extinction-coefficient to index of refraction and vice-versa. In this chapter we show how one can extract optical properties of optically thick samples. The Fabry-Pérot effect due to echoes in waveform are also addressed. The influence of specimen thickness on calculated absorption coefficient is also highlighted. Finally we illustrate how one can predict the time-domain signal, given spectral information, by virtue of inverse Fourier transformation (IFT).

3.2 Connecting Time and Frequency Domains

While examining the response of linear time invariant (LTI) systems to an input signal, $\tilde{E}_1(t)$, we can view the output, $\tilde{E}_2(t)$, as the convolution of the system's impulse response, $h(t)$, to $\tilde{E}_1(t)$ [23]. In this time domain description, the impulse response characterizes

the system's behavior. Equivalently in the frequency domain, the output spectrum, $E_2(\nu)$, is simply the point-wise product of the input spectrum, $E_1(\nu)$, and transfer function¹, $H(\nu)$. It is insightful to represent the spectrum $E(\nu)$, in polar form which contain both the amplitude and phase spectrum, $|E(\nu)|$, $\phi(\nu)$, as in eq. (3.1). In eq. (3.2) we define FT, IFT and convolution operations.

$$E(\nu) = |E(\nu)|e^{i\phi(\nu)} \quad (3.1)$$

$$\begin{aligned} \text{FT: } E(\nu) &= \mathcal{F}[\tilde{E}(t)] = \int_{-\infty}^{+\infty} dt e^{-2\pi i\nu t} \tilde{E}(t) \\ \text{IFT: } \tilde{E}(t) &= \mathcal{F}^{-1}[E(\nu)] = \int_{-\infty}^{+\infty} d\nu e^{2\pi i\nu t} E(\nu) \\ \text{Conv: } \tilde{E}_1(t) * h(t) &= \int_{-\infty}^{+\infty} d\tau \tilde{E}_1(\tau)h(t - \tau) \end{aligned} \quad (3.2)$$

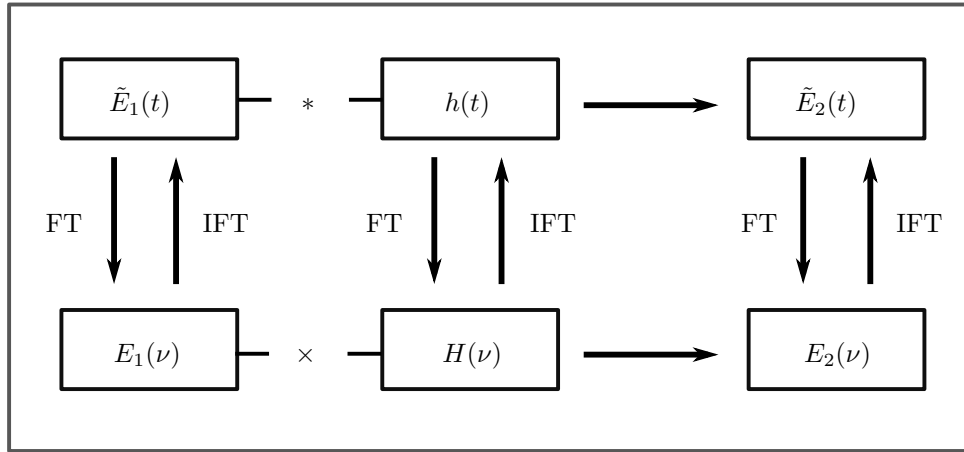


Fig. 3.1: Connecting time and frequency domain signals via FT and IFT in LTI systems. The symbols $*$ and \times are used to indicate convolution and multiplication respectively.

From eq. (3.2), we see that $E(\nu) = \mathcal{F}[\tilde{E}(t)]$ converges if $\tilde{E}(t)$ is absolute integrable, or simply for $|t| \rightarrow \infty$, $|\tilde{E}(t)| \rightarrow 0$. Moreover, FT is defined for both positive and negative frequencies. Interestingly for real valued signals, $\text{FT} : \mathbb{R} \rightarrow \mathbb{C}$, and $E(\nu)$ has Hermitian symmetry: $E^*(\nu) = E(-\nu)$, which leads to useful properties, eq. (3.3), that allow one to represent the full spectrum by $\nu \geq 0$ [40]. The energy contained in the signal in time and

¹ $H(\nu)$ is also called the frequency response of the particular system.

frequency domains are connected via Parseval's theorem eq. (3.4):

$$|E(\nu)| = |E(-\nu)|, \quad \phi(\nu) = -\phi(-\nu) \quad (3.3)$$

$$\int_{-\infty}^{\infty} dt |\tilde{E}(t)|^2 = \int_{-\infty}^{\infty} d\nu |E(\nu)|^2 \quad (3.4)$$

3.3 Fast Fourier Transform

The above definition of FT and IFT are applicable for continuous signals. Since data acquisition is discrete in nature, we rely on the discrete Fourier transform (DFT) for signal processing. However, the inefficiency of DFT lies in requiring extensive computational power. An algorithm called the fast Fourier transform (FFT) significantly speeds up the DFT procedure and was 1st described by Cooley and Tukey in 1965 [40]. While the dimension of the continuous FT spectrum is [sig]/[freq], the dimension of FFT spectrum is [sig]. Knowing spectral dimensions help with interpretation of spectral analysis. In fig. 3.2 we show how FFT can extract the amplitude and phase components of a time-domain signal.

2 important parameters in frequency domain are frequency resolution, $\Delta\nu$ and bandwidth, B. If there are N points in the time trace and total scanned time is T , then $T = (N - 1)\Delta t$. We can define the sampling frequency, $F_s = \frac{1}{\Delta t}$, where Δt is the time step. Given these relations, it is trivial to show that $\Delta\nu$, after FFT follows eq. (3.5) for $\Delta t \ll T$. Therefore, for high resolution time domain spectroscopy², one has to scan longer in time-domain, while still above the noise floor. The bandwidth (B) of a signal is given by Nyquist criterion, eq. (3.6), where $2B$ is called the Nyquist frequency. If $F_s < 2B$, one would encounter aliasing issues. In practice, F_s should be few times greater than $2B$.

$$\Delta\nu = \frac{F_s}{N} \approx \frac{1}{T} \quad (3.5)$$

$$F_s \geq 2B \quad (3.6)$$

²By higher resolution we mean smaller $\Delta\nu$

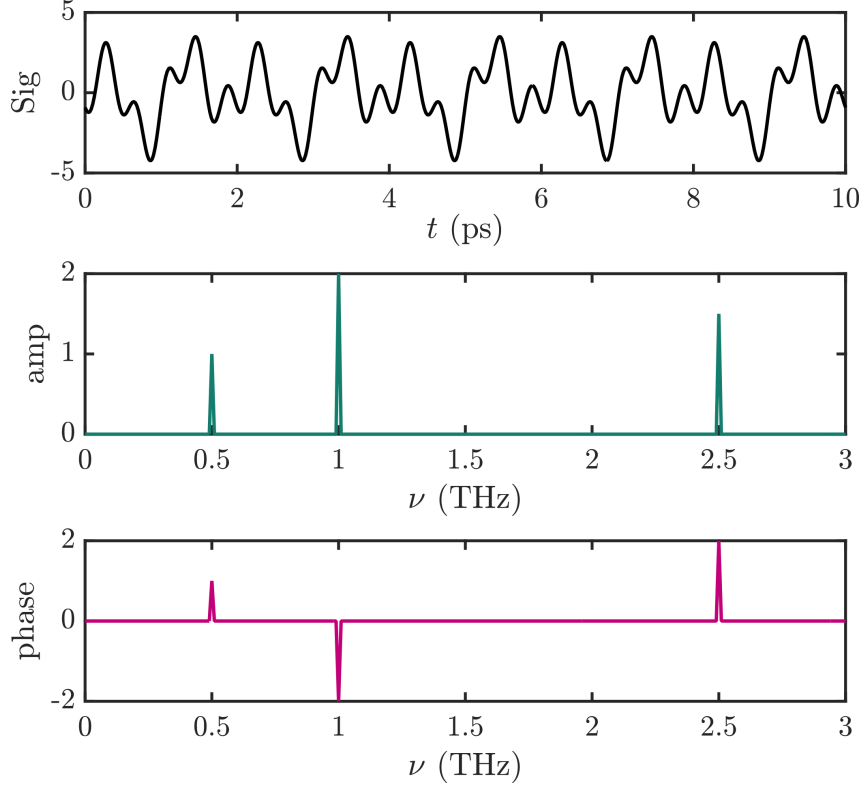


Fig. 3.2: FFT extracting amplitude and phase components of a simulated signal:
 $\text{Sig}(t) = 1 \cdot \cos(2\pi(0.5)t + 1) + 2 \cdot \cos(2\pi(1)t + (-2)) + 1.5 \cdot \cos(2\pi(2.5)t + (2))$

3.4 Window Function

When applying FFT, one has to implement a suitable window function to the waveform so that both ends of the THz time trace gradually go to zero. Abrupt truncation introduces spectral artifacts [40, 41]. Once windowed, the time trace may be zero-padded to increase the data points in frequency domain—this has the effect of smoothing the spectral features but does not provide additional physical information [40, 41].

We use a modified sigmoid function to accomplish the windowing process, see eq. (3.7). We define 2 parameters, t_0, β , where t_0 controls the temporal shift of the function such that at $t = t_0$, $\mathcal{S} = 0.5$ and β controls the steepness of the curve. We construct the window function, \mathcal{W} , where $t_2 > t_1$ and $\beta_1, \beta_2 > 0$. For our analysis, choosing $\beta_1 = \beta_2$ suffices. By setting t_1 some time before the peak signal and t_2 some time after, we can define \mathcal{W} to analyze our region of interest. Note that, $\max(\mathcal{W}) = 1$ and \mathcal{W} stays reasonably flat in the region of interest, but tapers down the waveform at $t < t_1, t > t_2$, see fig. 3.3. Given a

waveform \tilde{E}_0 , we can prepare it for analysis by simple multiplication.

$$\mathcal{S}(t, t_0, \beta) = \frac{1}{1 + \exp(-\beta(t - t_0))}$$

$$\mathcal{W}(t, t_1, t_2, \beta_1, \beta_2) = \mathcal{S}(t, t_1, \beta_1) \cdot \mathcal{S}(t, t_2, -\beta_2) \quad (3.7)$$

$$\tilde{E}_1 = \mathcal{W} \cdot \tilde{E}_0$$

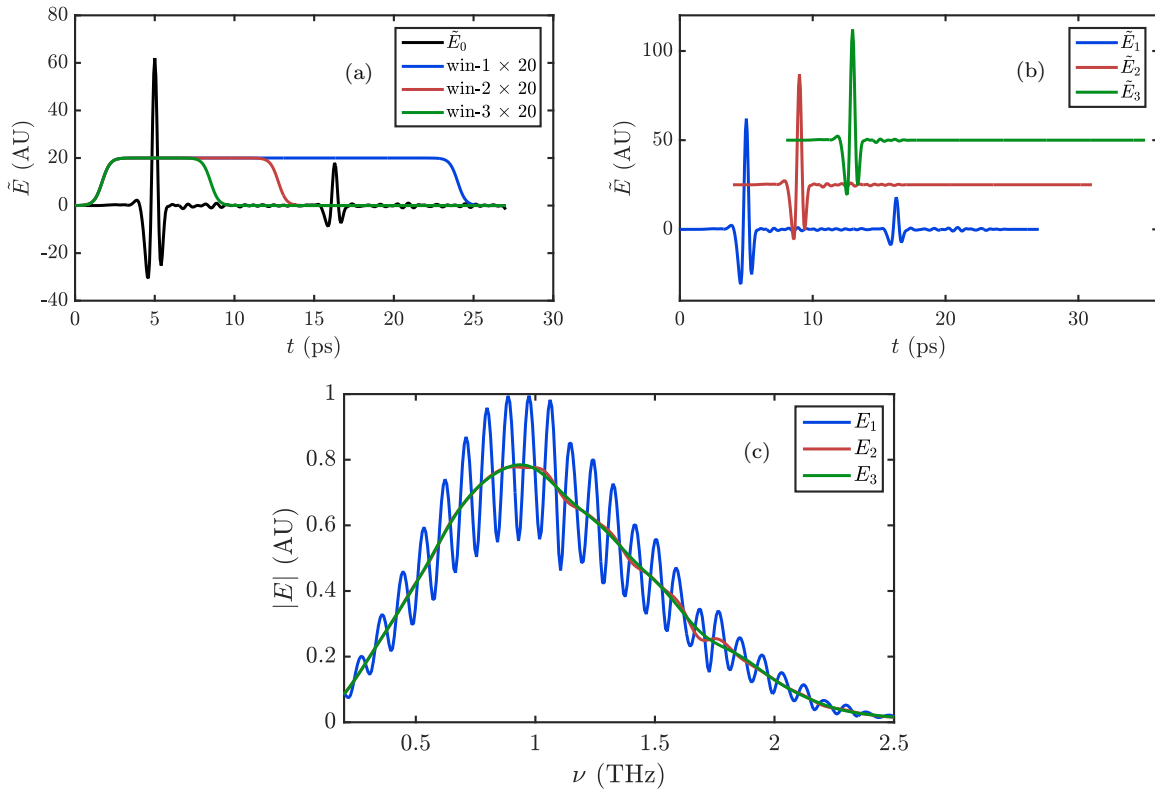


Fig. 3.3: Effect of window functions on N₂ purged experimental waveform. (a) Keeping t_1 fixed and varying t_2 . Resulting waveforms are shown in (b) applying offsets along both axes. Second pulse has been windowed out in \tilde{E}_2, \tilde{E}_3 . (c) Oscillation in spectrum is removed in $|E_2|, |E_3|$. Since win-2 is longer than win-3, $|E_3|$ shows weak water vapor signatures which are absent in $|E_2|$.

A thorough study on the effect of \mathcal{W} on spectrum has not been carried out in this project. If water vapors could completely be eliminated in the experiment, we would not see any FID in the waveform and thus the window functions, win-2 and win-3, would have identical effect on the spectrum in fig. 3.3.

3.5 Optical Parameter Extraction

We make some assumptions before describing a simple theory for optical parameter extraction. The dielectric samples are assumed to be in the shape of a slab of rectangular cross-section. The two faces of the sample allow multiple internal reflections to propagate toward the detector, giving rise to Fabry-Pérot (FP) effect. Hence, the sample of interest should be optically thick enough so that it is possible to separate the echoes from the main transmitted pulse, which allows FP contributions to be ignored. We assume that the incident light can be approximated as a plane wave at normal incidence, since sample of appropriate thickness is placed in the Rayleigh range of focused THz. Additionally we assume that scattering and diffraction losses are negligible. We define complex refractive index, $\bar{n} = n - i\kappa$, where n and κ respectively correspond to the real refractive index and extinction coefficient, which quantifies the absorption in material.

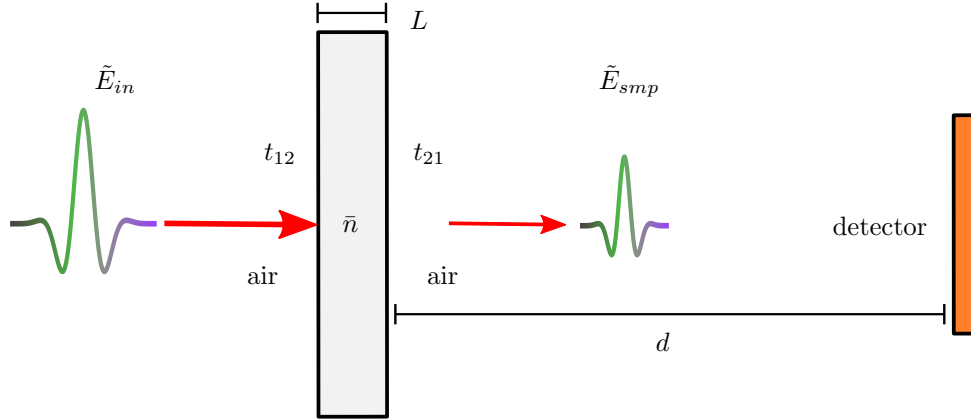


Fig. 3.4: Sample with \bar{n} to be characterized with THz-TDS. Measured signal without the sample is called reference and denoted by \tilde{E}_{ref} . Measured signal with the sample is denoted by \tilde{E}_{smp} .

In principle, time domain spectroscopy is straightforward. One has to record two time traces, one without any sample, labeled \tilde{E}_{ref} , and another with sample inserted in the path of light, labeled \tilde{E}_{smp} . For air medium $\bar{n}_{air} = 1$, hence in the frequency domain we have:

$$\begin{aligned}
 E_{ref}(\nu) &= E_{in}(\nu) \cdot e^{-i(2\pi\nu)L/c} \cdot e^{-i(2\pi\nu)d/c} \\
 E_{smp}(\nu) &= E_{in}(\nu) \cdot t_{12}(\nu)t_{21}(\nu)e^{-i(2\pi\nu)\bar{n}L/c} \cdot e^{-i(2\pi\nu)d/c}
 \end{aligned}
 \tag{3.8}$$

Where $e^{-i(2\pi\nu)d/c}$ is the propagation factor common to both spectra and cancels out upon division. Transmission coefficients, t_{12}, t_{21} , are functions of \bar{n}, θ_1 [23]. Here the first subscript denotes the air-sample interface and the second subscript denotes the sample-air

interface. At normal incidence, $\theta_1 = 0$, when light travels from $\bar{n}_1 \rightarrow \bar{n}_2$ and $\bar{n}_2 \rightarrow \bar{n}_1$, we get:

$$\begin{aligned} t_{12}(\nu) &= \frac{2\bar{n}_1}{\bar{n}_1 + \bar{n}_2} \\ t_{21}(\nu) &= \frac{2\bar{n}_2}{\bar{n}_1 + \bar{n}_2} \end{aligned} \quad (3.9)$$

For notational simplicity, henceforth, we denote reference and sample by subscripts 1 and 2, instead of ref and smp, respectively. The transfer function $H(\nu)$ that relates output signal to the reference one in frequency domain is defined in eq. (3.10).

$$H(\nu) = \frac{E_2(\nu)}{E_1(\nu)} = \frac{4\bar{n}(\nu)}{(1 + \bar{n}(\nu))^2} \exp\left(-i\frac{(2\pi\nu)}{c}L(\bar{n}(\nu) - 1)\right) \quad (3.10)$$

In the case of low absorption such that, $\kappa \ll n$, we can simplify the factor coming from the transmission coefficients by replacing $\bar{n} \rightarrow n$ in the quotient and thereby de-couple index and extinction-coefficient. Since, $H(\nu) = |H(\nu)| \exp(i\phi_H(\nu))$, we unwrap the phase $\phi_H(\nu)$ and write:

$$\begin{aligned} |H(\nu)| &= \frac{4n(\nu)}{(1 + n(\nu))^2} \exp\left(-\frac{(2\pi\nu)}{c}L\kappa(\nu)\right) \\ \phi_H(\nu) &= \frac{(2\pi\nu)}{c}L(1 - n(\nu)) \end{aligned} \quad (3.11)$$

We explicitly write the transfer function in terms of the amplitude and phase spectra of sample and reference fields which are experimentally evaluated.

$$\frac{E_2(\nu)}{E_1(\nu)} = \frac{|E_2(\nu)|}{|E_1(\nu)|} \exp(i(\phi_2(\nu) - \phi_1(\nu))) \quad (3.12)$$

We first need to obtain index, $n(\nu)$, which would be used to calculate absorption coefficient $\alpha(\nu) = 2\kappa(\nu)(2\pi\nu)/c$. From eqs. (3.11) and (3.12) we deduce:

$$\begin{aligned} n(\nu) &= 1 - \frac{c}{2\pi\nu L} (\phi_2(\nu) - \phi_1(\nu)) \\ \alpha(\nu) &= -\frac{2}{L} \ln\left(\frac{(1 + n(\nu))^2 |E_2(\nu)|}{4n(\nu) |E_1(\nu)|}\right) \end{aligned} \quad (3.13)$$

As an illustration of the parameter extraction, we show the time and frequency domain information of two pulses: reference and a non-dispersive sample. Where the time delay (Δt) results from the optical path difference. In frequency domain this is equivalent to a phase shift as illustrated in fig. 3.5, since $(\phi_1 - \phi_2) = 2\pi\nu\Delta t$, where $\phi_2(\nu) < \phi_1(\nu)$. Once the amplitude and phase spectra are calculated, we can determine the quantities shown in fig. 3.6 and finally extract the optical parameters.

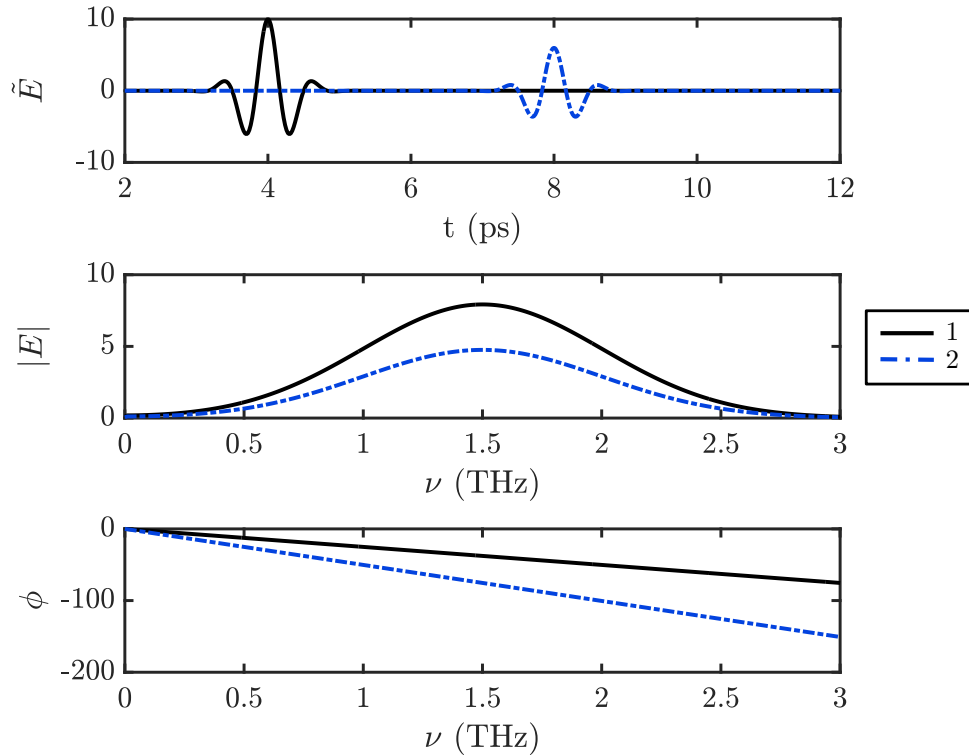


Fig. 3.5: Phase unwrapping is performed in the calculations

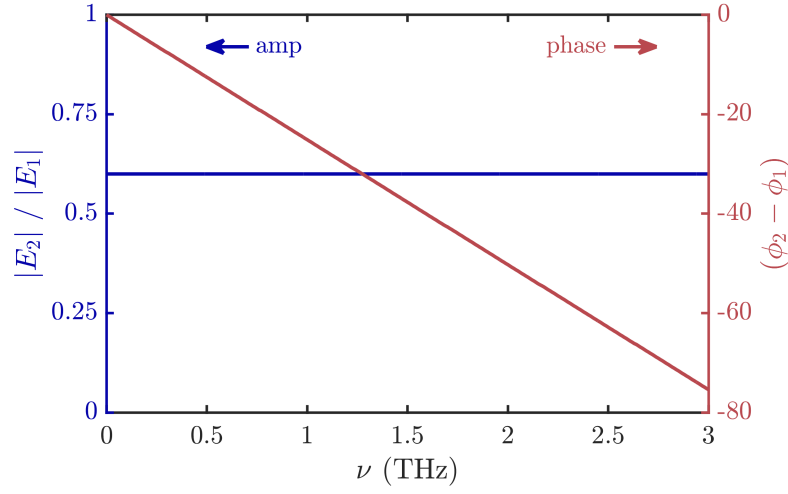


Fig. 3.6: These experimental quantities are then used in the simple equation, eq. (3.13), to calculate the optical parameters.

However for real signals, the presence of noise hinders accurate parameter extraction. Due to the phase noise at low frequencies, one has to calculate the phase from complex spectrum and unwrap it in the spectral region where $\phi(\nu)$ has high SNR and using these data points linearly fit the low frequency region such that at $\phi(\nu=0) = 0$ [42]. Uncertainty in sample thickness further impacts the error in optical parameters. Concerning sample thickness, one has to be between two extremes. If sample is too thick, then the plane wave assumption will breakdown, see fig. 2.9. Moreover, thick lossy samples set an upper limit to $\alpha(\nu)$ based on the dynamic range (DR) of apparatus [39]. On the other hand, if the sample is too thin, the spectrometer would become less sensitive to the sample's response. For a given uncertainty in ϕ_H , the uncertainty in index increases like, $\Delta n \propto 1/L$ [43]. There is an optimal frequency dependent thickness that solves the issues resulting from sample thickness [44]. There are other accurate, iterative procedure for parameter estimation [45, 46].

$$\alpha_{\max}(\nu)d = 2 \ln \left[\text{DR}(\nu) \frac{4n(\nu)}{(n(\nu) + 1)^2} \right], \quad L_{\text{opt}}(\nu) = \frac{2}{\alpha(\nu)} \quad (3.14)$$

3.6 Fabry-Pérot Effect

In section 3.5 we strategically avoided the echoes that arise from internal reflections within the sample and travel to the detector. A waveform containing echoes in time domain

correspond to oscillations in frequency domain, resulting from the shifting property of FT. The magnitude of the oscillations depend on the the internal reflection coefficient, r_{21} , when light travels from sample to air. At normal incidence r_{21} is polarization independent and given by eq. (3.15) [23].

$$r_{21}(\nu) = \frac{n_2(\nu) - n_1(\nu)}{n_2(\nu) + n_1(\nu)} \quad (3.15)$$

Since subsequent echoes travel an extra distance of $2L$, they are temporally delayed by $\delta t = 2nL/c$. This results in a spectral oscillation of $1/\delta t$. The above consequences are called the Fabry-Pérot (FP) effect. The output pulse in eq. (3.8) is corrected by including N echoes after the main pulse in eq. (3.16).

$$E_2(\nu) = E_1(\nu) \cdot t_{12}(\nu)t_{21}(\nu)e^{-i(2\pi\nu)\bar{n}L/c} \sum_{k=0}^N [r_{21}(\nu)e^{-i(2\pi\nu)\bar{n}L/c}]^{2k} \quad (3.16)$$

The term in the summation is called the FP term. The FP effect hinders accurate high resolution measurements using THz-TDS, which can be mitigated by appropriate antireflection coatings by satisfying $r_{21} \rightarrow 0$. one can see [47] for high resolution parameter extraction using thick samples taking into consideration the multiple echoes. Moreover, extracting optical parameters from thin samples is a major hurdle caused by the FP term since the echoes can no longer be singled out and special treatment is required to that end [48]. On a positive note, FP effect is utilized in constructing cavity resonators.

In figs. 3.7 and 3.8 we illustrate the effect of FP term in optically thick (relative to the wavelength of light) and thin silicon (Si) samples. We consider a non-dispersive index $n = 3.417$ and $\alpha = 0$, which is reasonable description of high resistivity float zone Si. Calculations were performed with $N = 25$ reflections. However, if the samples had antireflection coating, we could highly reduce the FP oscillations.

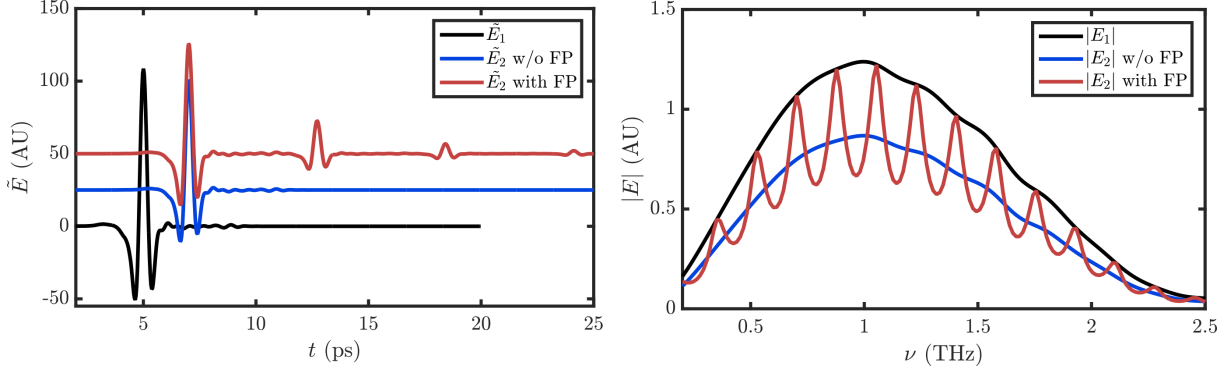


Fig. 3.7: Time and frequency domain simulations from 250 μm thick Si. Waveforms are offset along y-axis for clarity. In this thick sample, the echoes in the waveform can be windowed out.

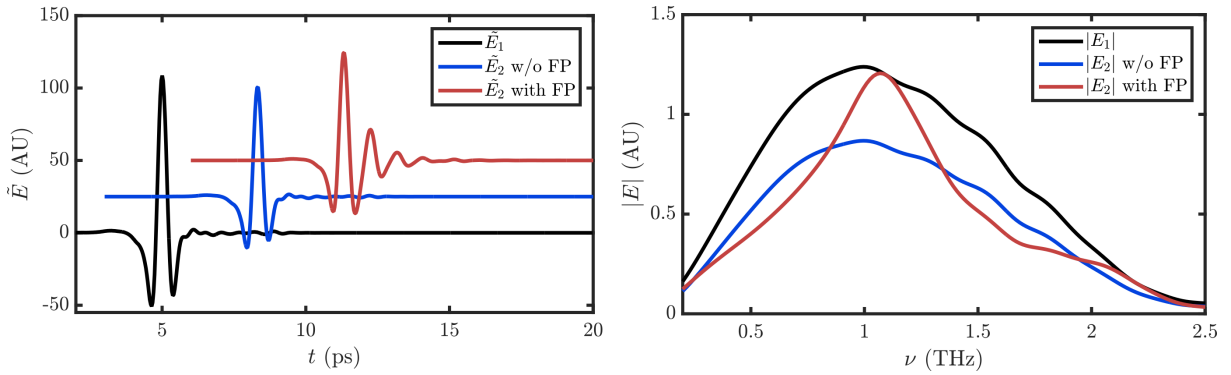


Fig. 3.8: Time and frequency domain simulations from 40 μm thick Si. Waveforms are offset along both x, y axes for clarity. In this thin sample, the internally reflected echos interfere to produce the output signal in red.

3.7 Reconstruction of the Signal

While for real waveforms it is possible to represent the spectrum using only one-sided FT by considering $\nu \geq 0$, one has to consider both negative and positive frequencies to apply IFT to reconstruct the waveform. Due to the symmetry of the FT (see eq. (3.3)), it is possible to rearrange the spectral components to obtain the two-sided representation from one-sided spectrum. This allows spectral analysis using only the non-negative frequencies, but care has to be taken when switching between the two representations.

For an input waveform, given a transfer function, $H(\nu)$, we briefly mention the steps required to construct the output waveform, the order of operation is also shown in fig. 3.1 :

- (1) Calculate input spectrum: $E_1(\nu) = \mathcal{F}[\tilde{E}_1(t)]$
- (2) Calculate output spectrum: $E_2(\nu) = E_1(\nu) \cdot H(\nu)$
- (3) Calculate output waveform: $\tilde{E}_2(t) = \mathcal{F}^{-1}[E_2(\nu)]$

$H(\nu)$ can correspond to a cascade of LTI systems, such that $H(\nu) = H_1(\nu)H_2(\nu)H_3(\nu)\dots$. For a simple cavity resonator the above process is illustrated in figs. 3.9 and 3.10.

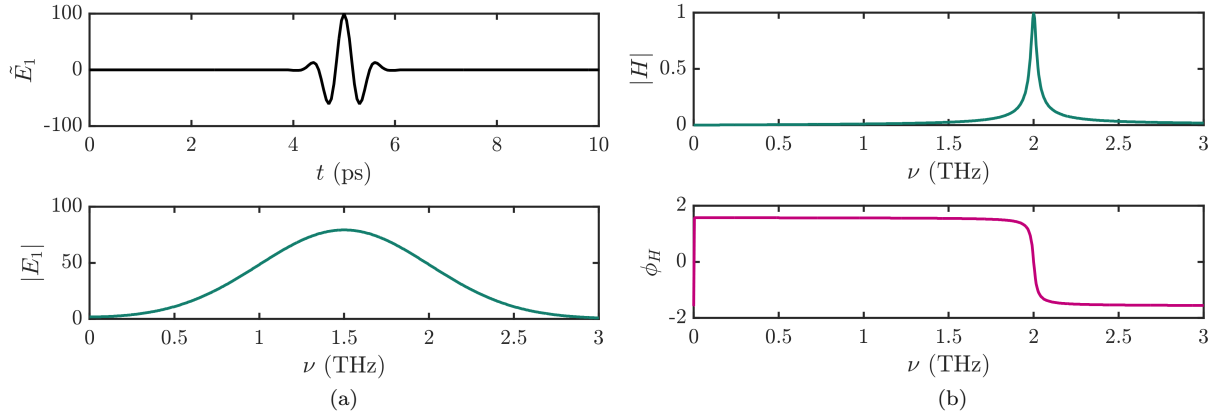


Fig. 3.9: (a) Input signal, (b) resonator $H(\nu)$ with resonance, $\nu_0 = 2$ THz, that would respond to the input pulse.

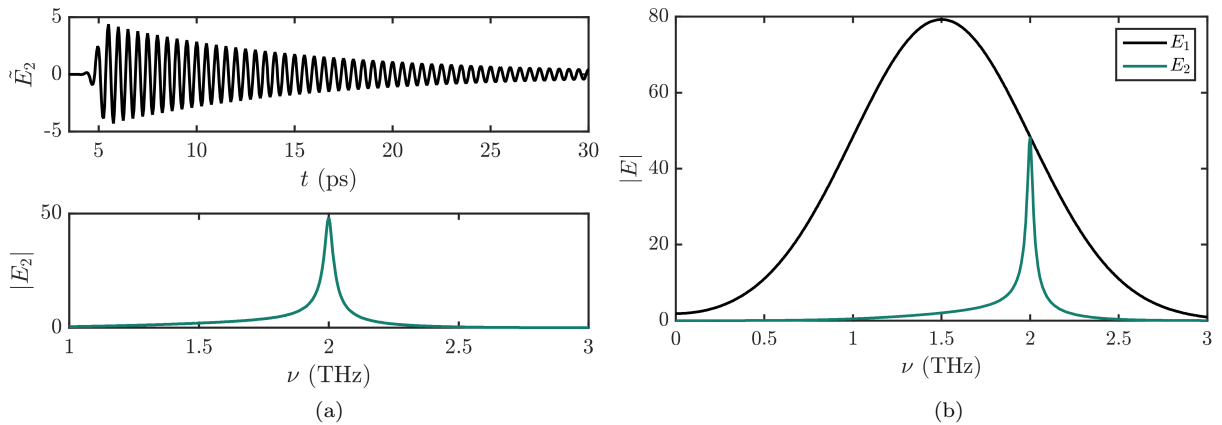


Fig. 3.10: (a) Output signal from above resonator, fig. 3.9 (b). Top panel shows time-domain ringing which is constructed by following steps highlighted in this section. Bottom panel shows spectral amplitude of the output waveform. (b) Comparison between input and output amplitude spectra due to the resonator.

3.8 Propagation in a Resonant Medium

Light matter interaction in a dielectric that possesses an electric dipole resonance in the bandwidth of incident light can be described by Lorentz oscillator model [49, 3]. The model predicts that at resonance the oscillator is $\pi/2$ phase delayed with respect to the input field, \tilde{E}_1 . The oscillating dipoles will then radiate secondary waves. Considering a sheet of driven dipoles, one can show that at a finite distance there is another additional phase lag of $\pi/2$ in the emitted secondary waves. Hence at $\nu = \nu_0$, the phase difference between \tilde{E}_1 , and the secondary scattered field is π and they destructively interfere to produce the output field \tilde{E}_2 [3]. The emitted light from the dipoles are also called free induction decay (FID).

The bare bones of this effect can be illustrated by considering a sharp band-stop filter of infinitesimal physical thickness and loss with $\nu_0 = 1.5$ THz, as in fig. 3.11. The decayed oscillation portion in \tilde{E}_2 will correspond to FID. The filter, in fact, produces an oscillation π out of phase relative to \tilde{E}_1 which interferes with \tilde{E}_1 ; the resultant waveform, \tilde{E}_2 , when analyzed over the full time trace would produce a dip in transmitted spectrum.

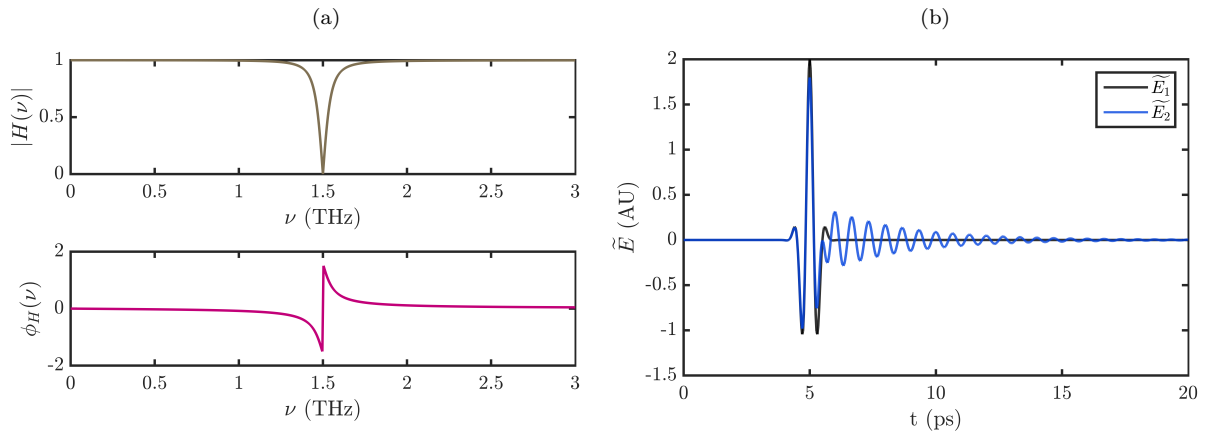


Fig. 3.11: (a) Transfer function, $H(\nu)$, characterizing a band-stop filter. (b) Output (blue) waveform is the time domain response of the band-stop filter to the input (black) pulse.

In fig. 3.12 we show the waveform and power spectrum of two time domain segments of the output signal, one that appears prior to the FID and another that is the FID. Plotting the spectrum of temporal segments along with the full input and output spectrum, we get a clearer picture of the band-stop filter's behavior. Indeed, completely out of phase emission can produce spectral absorption if the full length of time trace is considered.

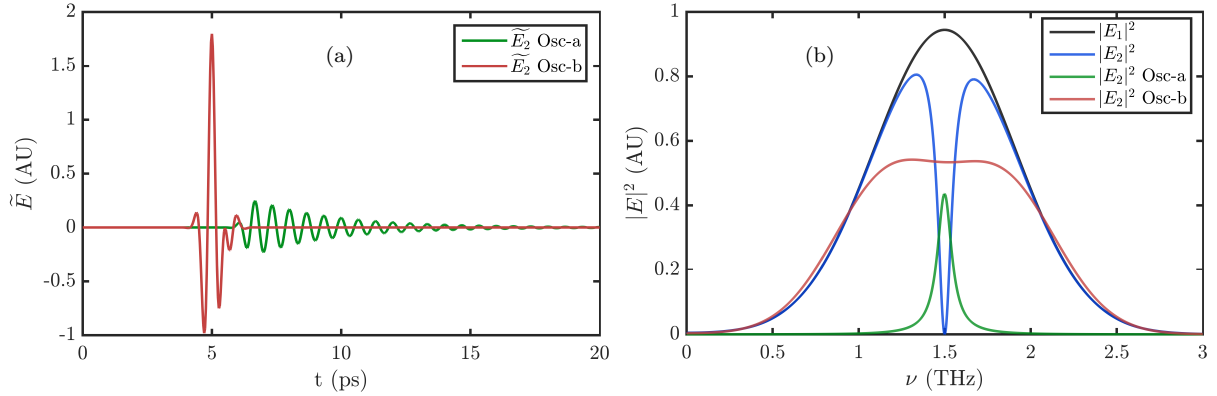


Fig. 3.12: Spectrum of portions of time trace distinguishable by color. (a) Osc-b (red) corresponds to the portion of \tilde{E}_2 before the FID, Osc-a (green) corresponds to the FID. (b) Power spectrum calculated with different temporal segments (Osc-a and Osc-b). The black curve is the input and blue is the output considering full time trace of the output waveform, which shows absorption. FID portion of the output waveform showing spectral emission in green. The diminished amplitude in red is the result of the superposition between completely out of phase frequency components.

3.9 Discussion & Conclusion

The basic mathematical foundation for data analysis has been described. The concepts mentioned here will be used in subsequent chapters. Waveform reconstruction technique is utilized in simulating the time domain response of AR coated substrates and cavity resonators, which facilitate our study of strong coupling in BFO. The effect of sample thickness on analysis technique is illustrated. A rigorous code, based on the references cited above, would help in more accurate parameter extraction for samples of various thicknesses. The FID spectrum would provide us insight when analyzing resonant light-matter interaction. As illustrated in section 3.8, one should not be surprised to find spectral emission after analyzing the FID.

Chapter 4

Spectroscopy of Normal Dielectrics

4.1 Introduction

Material characterization in the THz regime is the main purpose of the constructed time-domain spectrometer (TDS). Using our THz-TDS we extract the optical parameters of a few different dielectrics. In this chapter we will investigate the transmission spectrum of relatively low loss dielectrics which do not possess any resonance modes in our accessible bandwidth. Except for one, all the samples are optically thick, so Fabry-Pérot (FP) effect in optical parameters was avoidable by windowing out the internally reflected pulses in time-domain. Therefore we only analyze the main transmitted pulse and ignore the reflections. Finally, we demonstrate the merit of incorporating FP term in analyzing optically thin samples. Materials characterized in this chapter are widely used for THz applications. Their spectral properties will be used to determine specific technological applications they offer. The multilayered optics developed in this project will rely on material properties determined in this chapter. We extracted parameters in the range 0.3–2.25 THz; regions outside of this did not have sufficient SNR for reliable analysis. Furthermore, spectroscopy of these materials allow us to test the performance of the spectrometer by comparing results to those reported in literature.

4.2 Spectroscopy on Solids

We will perform spectral investigations on silicon wafer, ceramic alumina, quartz glass, and thin polyimide (kapton) film; being optically thin, polyimide film could not be fully characterized. Optical parameters of a sample seem to have some dependence on its supplier. Oftentimes, suppliers do not provide specifications (spec) for these materials, and sometimes the spec is not accurate. Hence, we require to characterize the dielectrics purchased for THz applications. THz optics tend to be bulky and expensive, compared to other optical regions. Ergo, there is an increasing demand for producing low loss optics that are cost-effective. The samples analyzed here are used as substrates for a variety of anti-reflection (AR) coatings, see chapter 5. Thin stacks of Si wafers are used for the design of efficient tunable reflector and THz cavity resonator, see chapter 7. Other than the film, the solids mentioned above are ideal for THz windows and possess distinctive qualities that make them advantageous for specific environment. The THz-TDS will be a light source for cryogenic instruments in ultrahigh vacuum, hence appropriately AR coated low loss windows will enhance performance of the involved equipment.

4.2.1 Silicon

Among the semiconductors, silicon (Si) is extensively used for THz applications. But to reduce material absorption one has to choose a sufficiently high resistivity float zone silicon (HRFZ-Si). HRFZ-Si is one of the most transparent materials for THz light. Its high refractive index and optical isotropy make it very useful for THz optics. The HRFZ-Si sample used for the following measurement is 500 μm thick, purchased from MTI Corp with rated resistivity 15 $\text{k}\Omega\text{-cm}$. We expected negligible loss from the sample, but the absorption at higher frequencies in fig. 4.4 suggest that the quoted resistivity of the wafer may not be accurate.

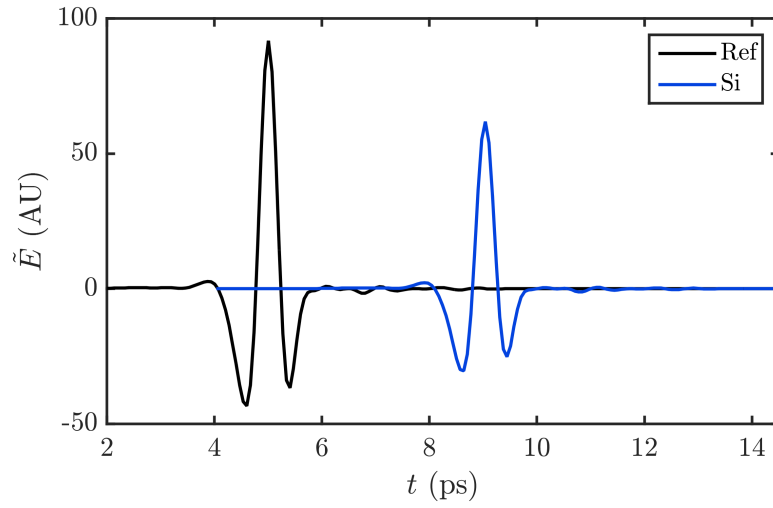


Fig. 4.1: A THz pulse that has passed through a 500 μm thick wafer of HRFZ-Si (blue) compared to a reference pulse that has not passed through any sample (black)

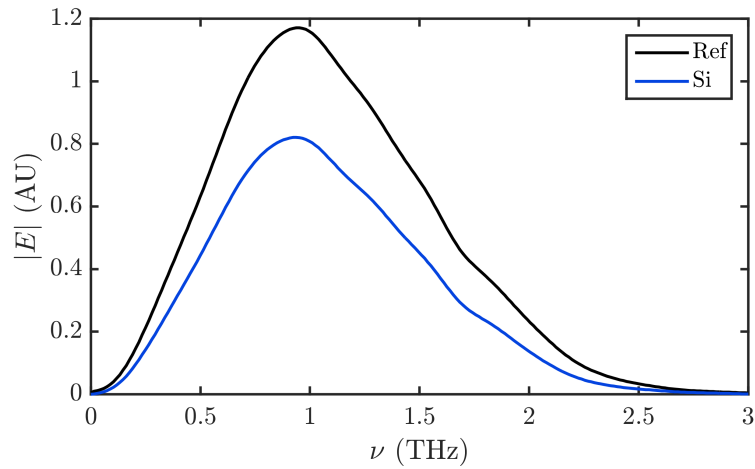


Fig. 4.2: Transmitted spectra from respective blue and black waveforms above

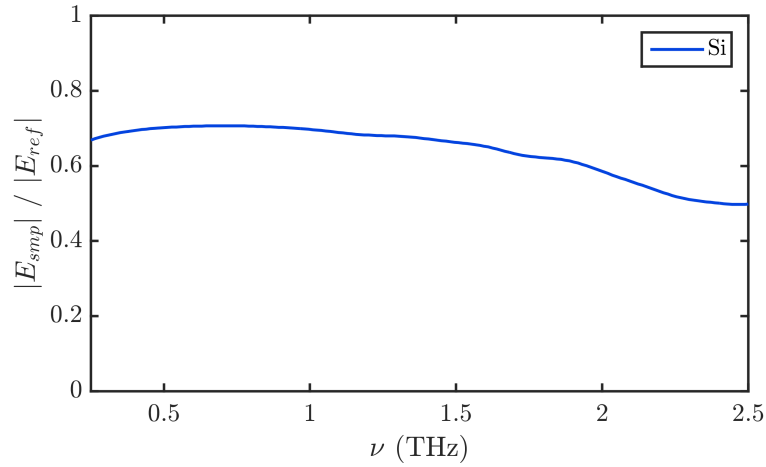


Fig. 4.3: Ratio of the spectral amplitudes of the pulse that was passed through the HRFZ-Si sample and the reference pulse

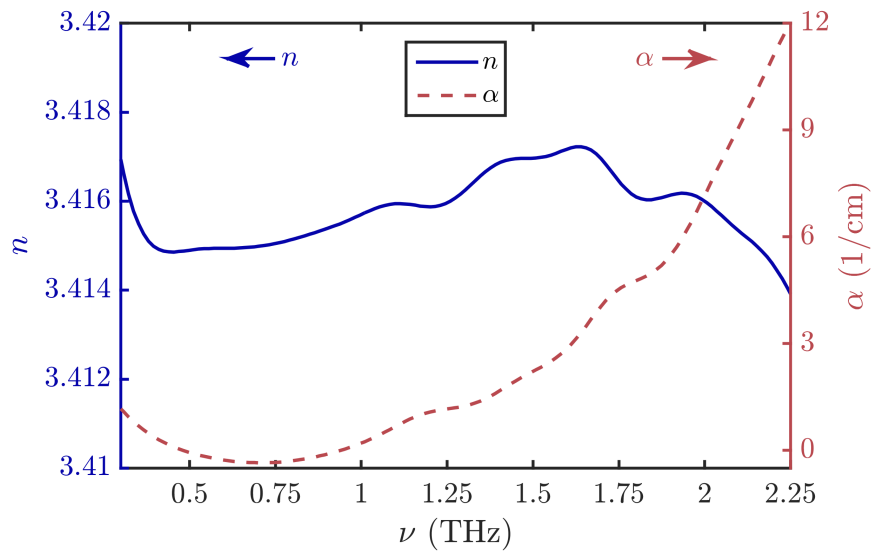


Fig. 4.4: Optical parameters extracted from the HRFZ-Si sample. Index of refraction is shown in blue and absorption coefficient in red.

Reported optical parameters for HRFZ-Si can be found in [50, 51], the index is in agreement with the ones reported but the absorption at higher end of the bandwidth would require further investigation. Si wafers would be used in construction of reflector and resonator designed for the sub-THz region. The characterized wafers are also extensively used for empirical evaluation of developed AR coatings.

4.2.2 Alumina

Ceramic Alumina is typically made of fine powder of Al_2O_3 crystals mixed with impurities such as glass. Despite being an electrical insulator, alumina has an impressive thermal conductivity. Crystal Al_2O_3 is birefringent with reported index $n_e \approx 3.07$, $n_o \approx 3.39$ [52]. The Alumina sample used in following measurements was purchased from McMaster-Carr with advertised thickness $0.025'' \pm 0.003''$, which correspond to $635 \pm 76 \mu\text{m}$.

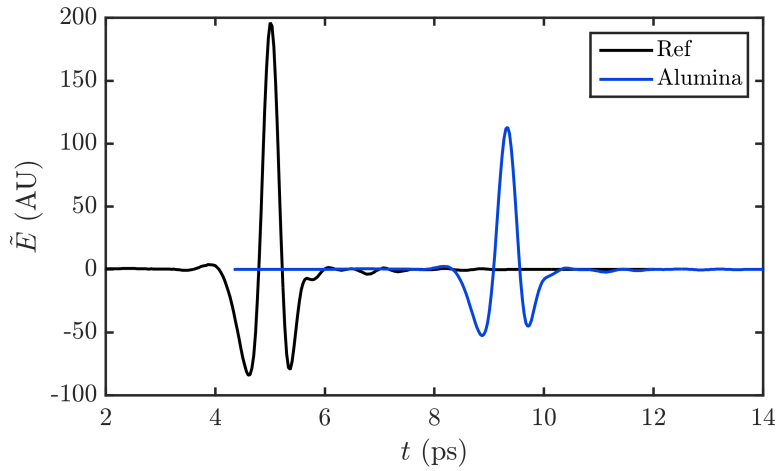


Fig. 4.5: A THz pulse that has passed through a $635 \mu\text{m}$ thick ceramic alumina (blue) compared to a reference pulse that has not passed through any sample (black)

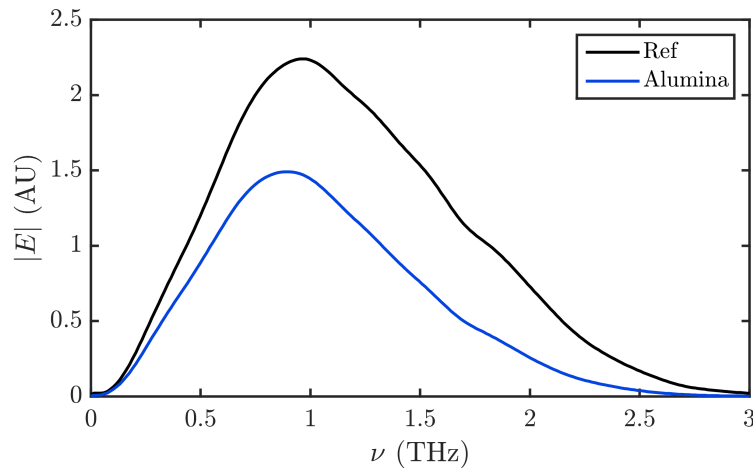


Fig. 4.6: Transmitted spectra from respective blue and black waveforms above

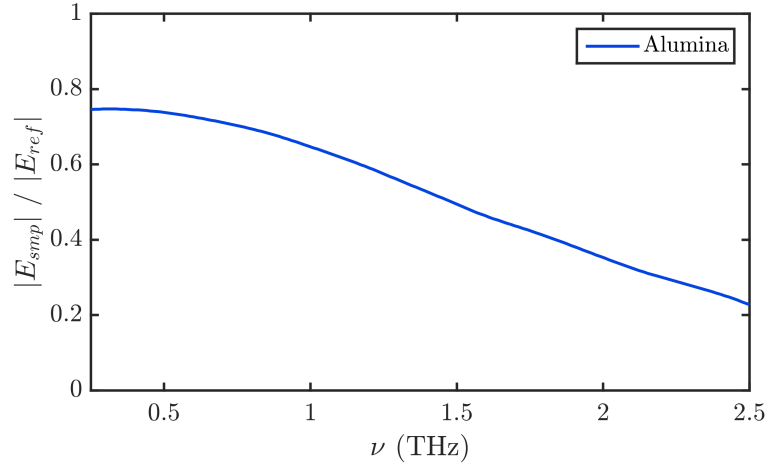


Fig. 4.7: Ratio of the spectral amplitudes of the pulse that was passed through the ceramic alumina sample and the reference pulse

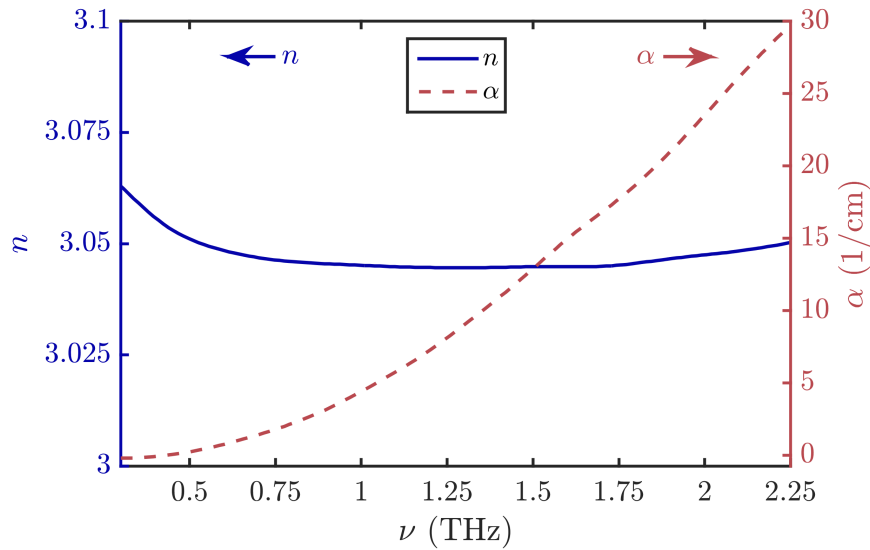


Fig. 4.8: Optical parameters extracted from the ceramic alumina sample. Index of refraction is shown in blue and absorption coefficient in red.

A broadband spectroscopy on ceramic Alumina with two different purities can be found in [53]. The index calculated with our spectrometer is in agreement with the article, which show very small index dependence on impurity, but a significant impurity dependent absorption. Our measurements suggest that for sub-THz frequencies Alumina would be a good low-cost window material if used with proper anti-reflection (AR) coating. In situation where temperature of a specific sample is required to be tuned, alumina would offer a great solution by simultaneously being the window and thermal conductor.

4.2.3 Quartz Glass

Quartz glass is amorphous and composed of SiO_2 (silica), one of the most abundant compounds found on earth. Quartz glass has high transparency over a broad range of frequencies from infrared to ultraviolet. It is relatively inexpensive due to wide availability. The sample used for characterization was purchased from McMaster-Carr and has thickness $\frac{1}{16}'' = 1587.5 \mu\text{m}$.

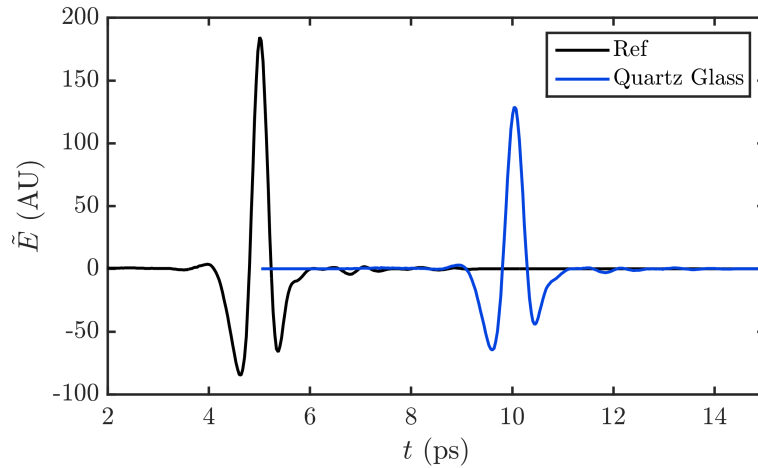


Fig. 4.9: A THz pulse that has passed through a $\frac{1}{16}''$ thick quartz glass (blue) compared to a reference pulse that has not passed through any sample (black)

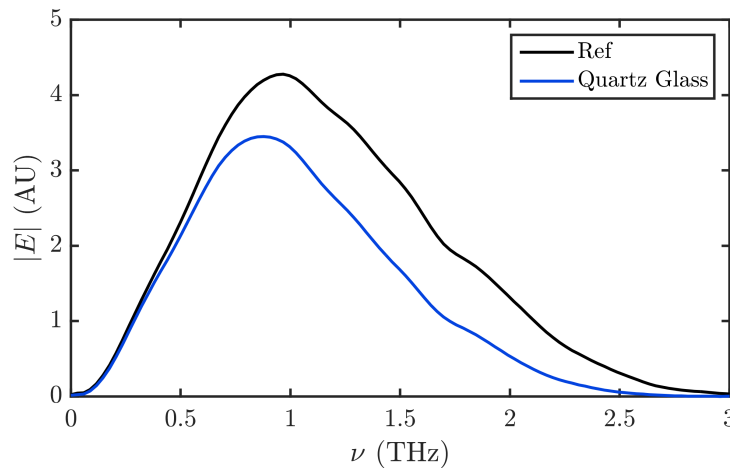


Fig. 4.10: Transmitted spectra from respective blue and black waveforms above

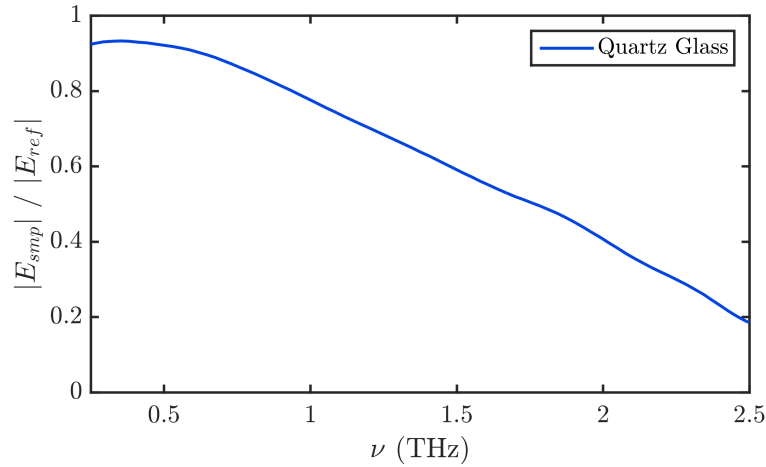


Fig. 4.11: Ratio of the spectral amplitudes of the pulse that was passed through the quartz glass sample and the reference pulse

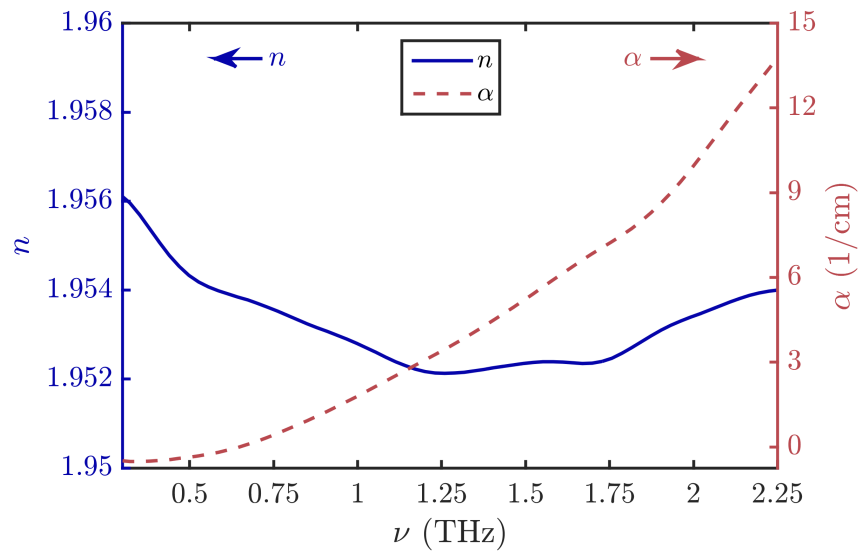


Fig. 4.12: Optical parameters extracted from the quartz glass sample. Index of refraction is shown in blue and absorption coefficient in red.

The measured index is in well agreement with ones reported in [54, 55], while both index and absorption seem to agree with [55]. The relatively low index, $n \approx 1.95$, reduces the Fresnel loss due to transmission and the low material absorption further makes quartz glass a very good candidate for THz window without the need for AR coatings. Transparency in the visible frequency serves as an additional alignment advantage and provides an option for broadband window material. Since FP effects are minimal in quartz glass, one can use a thin uncoated window for THz applications.

4.2.4 Thin Polyimide Film

Polyimide (PI) film or better known as kapton film of thickness 3 Mil was purchased from McMaster Carr, where 1 Mil = 25.4 μm . Due to being so thin we can not window out the etalon reflections in our analysis. Therefore, we observe Fabry-Pérot (FP) oscillations imposed on the main pulse, which makes spectral analysis much difficult compared to the thick samples. Due to having a low index ~ 1.87 [56], we have a weak etalon oscillation in the amplitude and phase, as can be seen in fig. 4.14. In this case, simultaneous determination of the index and absorption would require special iterative calculations as illustrated in [48]. However, since the n has already been reported by [56] which looks reasonably dispersionless up to 3 THz, we can make use of this fact and try fitting the extinction coefficient, κ .

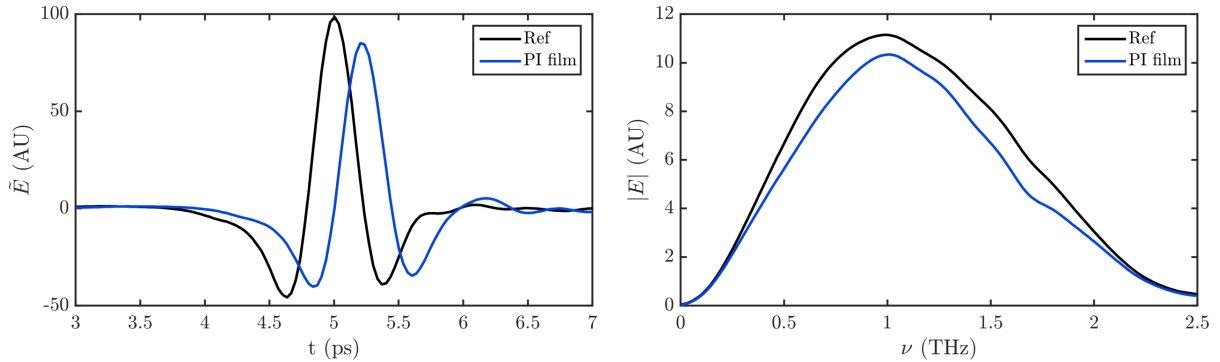


Fig. 4.13: Left: A THz pulse that has passed through a PI film (blue) compared to a reference pulse that has not passed through any sample (black). Right: Transmitted spectra of respective waveforms from left.

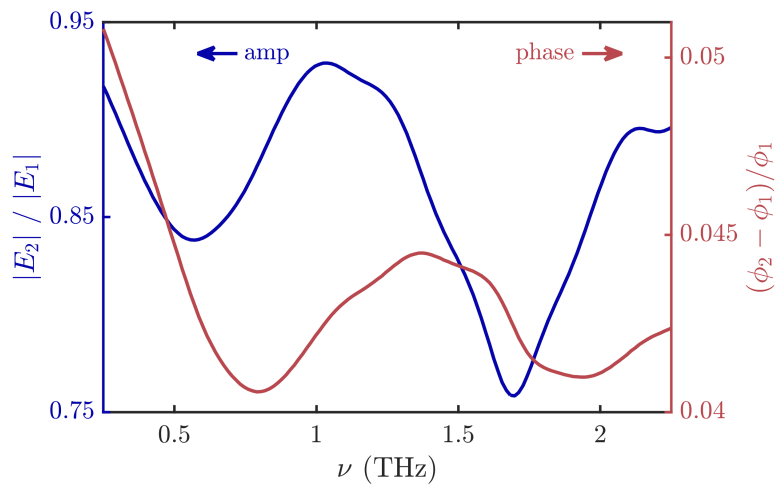


Fig. 4.14: Amplitude ratio and phase difference show FP oscillations for the PI thin film

The oscillations in the amplitude ratio is dependent on the optical thickness nd of the film. Since $n = 1.87$, $d = 2.85$ Mil best fits the experiment. The calculated ratio $|E_2|/|E_1|$ was manually fit to the experimental one by approximating κ by a 2nd order polynomial of ν . In figs. 4.15 and 4.17, we show the effect of incorporating the FP term in frequency and time domain.

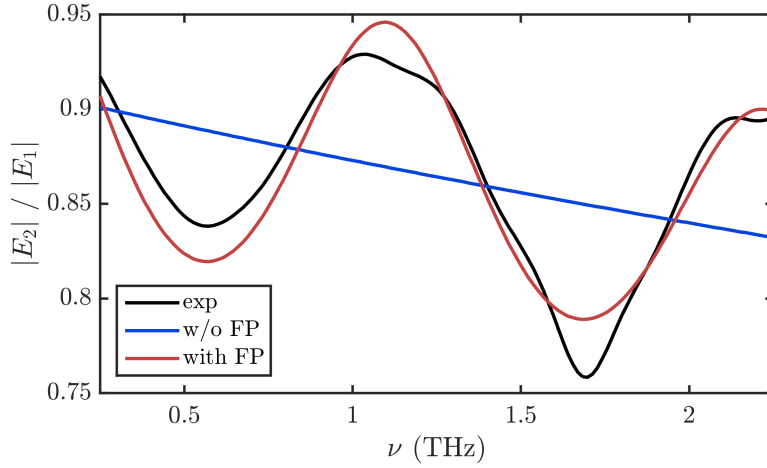


Fig. 4.15: Effect of inclusion (red) and exclusion (blue) of FP term in calculating amplitude ratio from the PI thin film. Incorporating FP effect, we attempt to manually fit the calculated amplitude ratio (red) to that of experiment (black). Here we have kept the index fixed but approximated κ by a 2nd order polynomial (shown below) that produces the best fit between red and black curves.

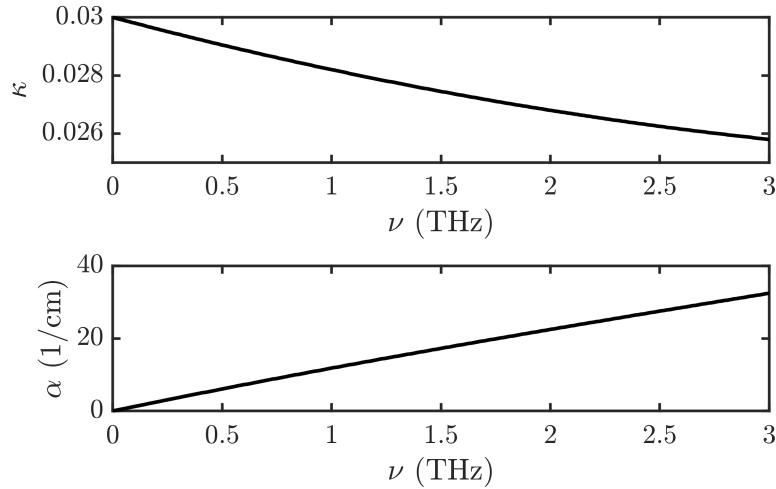


Fig. 4.16: Estimated extinction coefficient (κ) and power absorption coefficient (α) of PI film that allows best fit in fig. 4.15

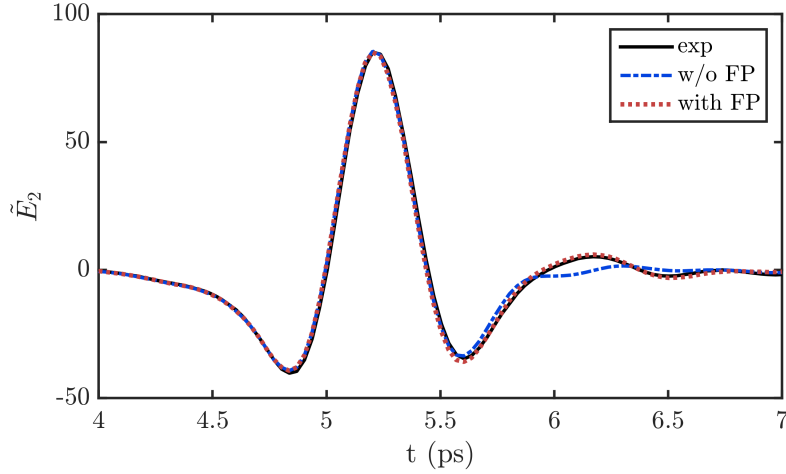


Fig. 4.17: Time domain reconstruction further shows the merit of the FP term and absorption fitting for the PI thin film. THz pulse that passes through the PI film is shown in black. Waveform simulation including and excluding the FP term is respectively shown in red and blue.

4.3 Discussion & Conclusion

We have performed spectroscopy of HRFZ-Si, ceramic alumina, and quartz glass employing our THz-TDS. Careful observation of the samples' absorption spectra reveals a small negative absorption in the low frequency end for the low loss materials. Realistically, this is not meaningful. Such phenomenon has been reported previously in [57–59]. This may be explained by not having sufficient sample thickness for longer wavelengths in transmission measurements, which results in lower frequency end becoming less sensitive to the presence of sample material [60]. The Gouy phase shift in tightly focused Gaussian pulse may also lead to some discrepancy [61]. For complete thin film characterization, proper code has to be developed based on the reference cited. Taking a constant index of refraction from literature, we have attempted to estimate the absorption of polyimide thin film. In extraction of optical parameters, we also require to incorporate uncertainties that may result from the different components of our apparatus. Overall, the spectroscopy performed on above materials provide us useful information that will be taken into account in developing future optical components.

Chapter 5

Anti-Reflection Coating

5.1 Introduction

When light travels from one medium to another, it is accompanied by reflection loss at the interface dictated by the Fresnel equations [3]. Impedance matching between the two media serves to minimize this loss and it is accomplished by anti-reflection coating (ARC). The text book example for ARC is the quarter wavelength thick film between the two media satisfying the refractive index relation $n_f^2 = n_1 n_2$, where the subscripts denote the film and two media respectively. Destructive interference causes electric field of light to vanish on the reflected medium, while a boost in electric field on the transmitted medium results from constructive interference. Since the single layer coating has a narrow bandwidth, it is in general not suitable for broadband sources. In the THz regime finding the right material and technique for applying a functional ARC can be very challenging. Many different methods have been employed to create suitable ARCs which include thin multilayered films, metallic absorptive coating, intricate surface structures, etc. [62–65]. Besides their pros and cons, all such techniques rely on very careful implementation of the AR structure, which does not provide a low-cost solution to the problem.

We apply pressure sensitive adhesive tapes (PSAT) and films made of low-loss polymers of appropriate thicknesses on Si wafer, ceramic alumina, quartz glass, and GaP electro-optic (EO) crystal. The procedure is similar to [66, 67], where polyimide (Kapton) and fused quartz were respectively glued to semiconductor substrates and their performance were recorded in frequency domain. In those cases, the thicknesses of both adhesive and

polyimide/quartz had to be carefully monitored for optimal performance. In contrast, we use commercially available tapes and films with given thicknesses, along with their combination on substrates and record their response in the time-domain. This allows one to see both the transmitted THz pulse and internally reflected pulse. We compare experimental and calculated performance both in time and frequency domain, which allows us to reconstruct the signals post analysis. With some combination of thin films, we are able to reduce Fresnel loss on a wide range of frequency with drastically low cost, in room temperature and pressure.

5.2 Films for ARC

From Fresnel equations we have seen in chapter 3 that for normal incidence on a rectangular slab of dielectric, the total transmission coefficient is given by $t_1 t_2$, where subscripts denote air-substrate, substrate-air interface eq. (5.1). Hence, if we take the ratio of output fields without considering internal reflections, between two identical slabs, one with no Fresnel loss (E_0) and the other with usual loss (E_n), we get the following relation. One purpose of ARC for a given substrate index, n , is to approach E_0 , see fig. 5.1.

$$t_1 t_2 = \frac{4n}{(1+n)^2}, \quad \frac{E_0}{E_n} = \frac{1}{t_1 t_2} \quad (5.1)$$

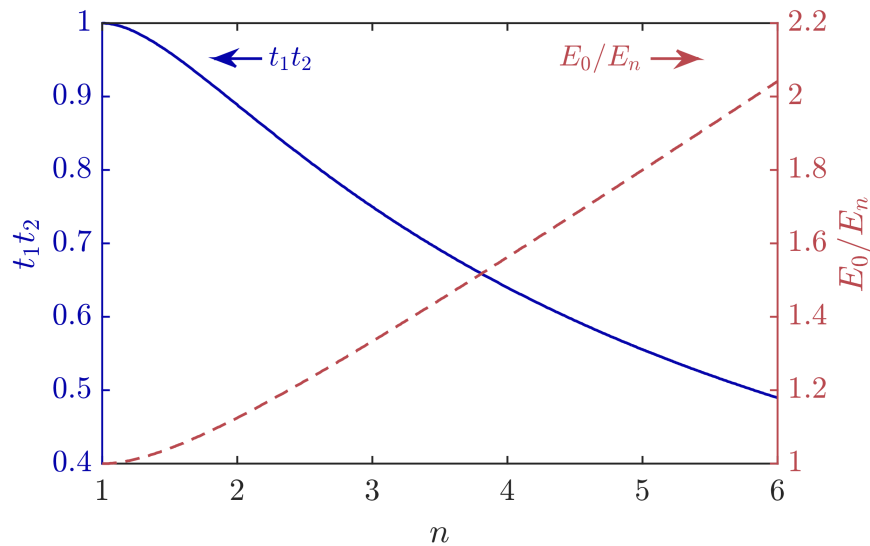


Fig. 5.1: Fresnel loss due to index mismatch between substrate and air.

We performed our measurements with polyimide (kapton), polyethylene, polypropylene single-sided PSAT. Each of such tape is composed of a polymer adhesive layer, a backing film, and a release coating on the backing film. The purpose of release coating is to help unwind the tape against its own adhesive and this coating is significantly thinner than the other two layers, typically $<1 \mu\text{m}$, or sometimes $<0.1 \mu\text{m}$ [68]. We have ignored the effect of this thin coating in analysis. We have used the properties of PMMA and PDMS to represent respectively the adhesive layers acrylic and silicone mentioned by the suppliers. The THz optical properties of these polymers vary specimen to specimen and we can see more deviation in the reported α than n , as summarized in [69]. The real index, n , for each material used in our calculation listed in table 5.1, is taken from [56, 70, 71]. We also note from literature that in the bandwidth 0.2–3 THz, PE and PP are very low in absorption, nominally $\alpha < 1 \text{ cm}^{-1}$, while PI has much higher, monotonically increasing, absorption which is bounded by $\alpha < 25 \text{ cm}^{-1}$ [56]. From [72] we see that PDMS is slightly more absorptive than PMMA below 1.5 THz, while above 1.5 THz PMMA becomes more lossy and both of them satisfy $\alpha < 10 \text{ cm}^{-1}$ below 1 THz. However as mentioned above, there is a noticeable variation in absorption for a each polymer, which prompted us to estimate α for each layer from our experiment.

Table 5.1: Polymer name and parameter $\bar{n} = n - i\kappa$ used for analysis. PDMS-1, PDMS-2 have slightly different κ and correspond to PI-T1, PI-T4 respectively, see table 5.2. n is taken from literature while κ is estimated by fitting.

Polymer	Complex index \bar{n}	$\alpha(1\text{THz}) \frac{1}{\text{cm}}$
Polyethylene (PE)	$1.52 - i \cdot 0.002$	0.84
Polypropylene (PP)	$1.50 - i \cdot 0.005$	2.10
Polyimide (PI)	$1.87 - i \cdot 0.031$	12.99
Polymethyl methacrylate (PMMA)	$1.60 - i \cdot 0.035$	14.67
Polydimethylsiloxane (PDMS)-1	$1.55 - i \cdot 0.03$	12.58
Polydimethylsiloxane (PDMS)-2	$1.55 - i \cdot 0.032$	13.41

In analyzing the measured data, we assumed that all dielectrics involved are non-dispersive and κ was estimated by fitting calculation to experiment. For the thickness of the polymer layers we are using the unit Mil, where $1 \text{ Mil} = 25.4 \mu\text{m}$, which is a standard commercial unit for film/tape thickness. Our thicknesses of individual AR layers range from 0.15–2Mil,

i.e., about 3.8–50.8 μm . We noticed that after good application of PSAT on substrate, the total thickness of the films is thinner than advertised, which was confirmed by physically measuring the thickness of 20 layers of tape with a vernier calipers. Thicknesses can also be slightly reduced by stretching the polymers due to Poisson effect. Taut film is a requirement for air-bubble free application of PSAT. In table 5.2 we enlist the polymer films used in our work.

Table 5.2: Tape and film Information. l_1 correspond to film thickness given by supplier. l_2 correspond to film thickness that best fits analysis. 1 Mil = 25.4 μm . PI-T5 is only used for analysis in fig. 5.22

Label	Material		l_1 (Mil)		l_2 (Mil)		Supplier
	Film	Adhesive	Film	Adhesive	Film	Adhesive	
PE-T	PE	PMMA	1.8	0.2	1.6–1.8	0.15–0.2	McMaster-Carr
PP-T	PP	PMMA	—	—	1	1.1	Walmart
PI-T1	PI	PDMS	1	1.5	1	1–1.1	Thorlabs
PI-T2	PI	PMMA	1	1.5	1	1.3	Caplinq
PI-T3	PI	PMMA	2	1.5	1.85	1.3	Caplinq
PI-T4	PI	PDMS	0.5	1	0.5	1–1.1	McMaster-Carr
PI-T5	PI	PDMS	0.5	0.5	—	—	Caplinq
PI-F1	PI	—	1	—	0.9–1	—	McMaster-Carr
PI-F2	PI	—	2	—	2	—	McMaster-Carr

5.3 Application of AR Layers

We have used three configurations of AR coating on both sides of the substrates to maximize the effect of the coating. In fig. 5.2 (a), we have a simple one-sided PSAT attached on the substrate. In (b), first a film of relatively high index polymer, in our case PI film, is placed on the substrate and then a PSAT with relatively low index layers is applied on top of them holding the film tightly in place. In (c), we first apply a tape with

higher index backing film on the substrate, in our case a PI tape, and then on top of that we apply a tape with lower index backing film.

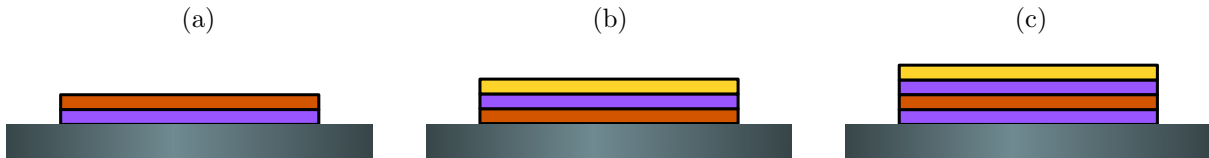


Fig. 5.2: Configurations for ARC (showing layers only on 1 side of the substrate). Substrate is shown at the bottom and layers on top are the applied polymer films. Violet color denotes adhesive layer.

We first firmly attached the substrate on a fixed petri dish. When directly applying tape on the substrate, we attached one end of the PSAT on the substrate and held the tape taut while slowly and carefully applying pressure along the PSA film in order to eliminate or minimize air bubbles that form between the substrate and adhesive layer.

To apply non-adhesive film as the first layer, as in configuration (b), we first place a PSAT with adhesive side pointing upwards and backing film attached on a fixed petri dish. Then we carefully apply our high index polymer film of surface area smaller than the PSAT, on top of the adhesive layer. Then we apply the three layered structure on top of the substrate as shown above. There would unavoidably be a very thin air layer between the film and the substrate which had a negligible effect on the AR performance. Using this method for larger substrates, the thickness of air layer was no longer negligible and performance disruption was noticed. To completely remove the unwanted effect of air film, we replaced the 1st polymer film with a PSAT as in configuration (c). This 2-tape structure works well with all sizes of substrate but adds additional absorptive layer.

5.4 Calculation & Experiment

To calculate the frequency response of multilayered structures, we used the matrix method described in [3, 73], corresponding to fig. 5.3. Here underlined variables, $\underline{r}(\nu)$, $\underline{t}(\nu)$, are used to denote the reflection and transmission coefficients of the layered structure.

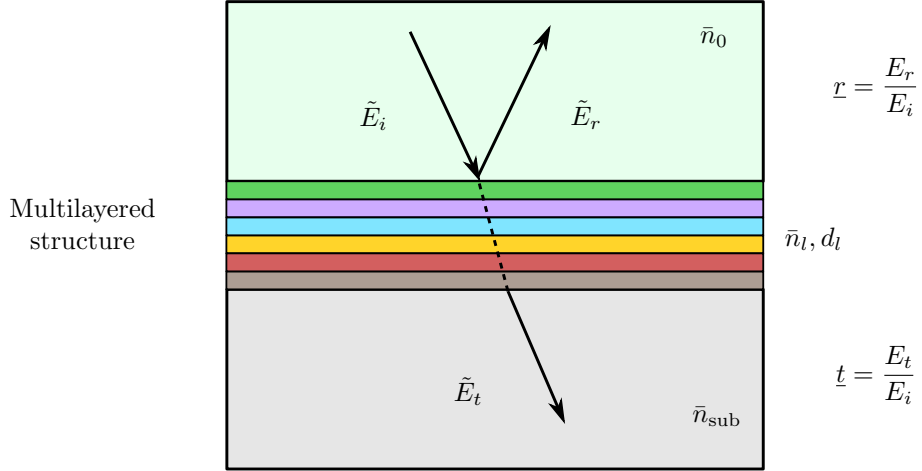


Fig. 5.3: Multilayered films placed between two media denoted by $\bar{n}_0, \bar{n}_{\text{sub}}$, typically they would denote air and substrate. Layers are ordered from top to bottom, denoted by subscripts. l^{th} layer is characterized by its complex index and thickness.

Following the procedure outlined in [73], we first define the admittance of free space, $Y_f = \sqrt{\epsilon_0/\mu_0}$. At normal incidence, the admittance of a medium with complex index \bar{n} is $Y = \bar{n}Y_f$. But for oblique incidence one has to take into consideration the s, p polarizations of light. Consequently for a transmission angle θ , the oblique admittance for a medium \bar{n} is given in eq. (5.2) by η , where the subscript denote polarization. Later we will use subscripts to identify the dielectric layer of interest for a given polarization.

$$\begin{aligned}\eta_s &= Y \cos(\theta) \\ \eta_p &= \frac{Y}{\cos(\theta)}\end{aligned}\tag{5.2}$$

The consequence of layered dielectric is the relative phase change between multiple beams resulting from the optical thickness of each layer. For a given wavelength, λ , this is characterized by phase thickness, δ_l , for the l^{th} layer of thickness, d_l and index, \bar{n} .

$$\delta_l = \frac{2\pi\bar{n}_l d_l \cos(\theta_l)}{\lambda}\tag{5.3}$$

Now, for a given polarization and transmission angle, each layer of the multilayered dielectric structure can be characterized by a matrix with two parameters δ, η . For an assembly of N layers the characteristic matrix of the system is given by the product of the matrices, eq. (5.4). Given the admittance of the incident medium and substrate, $\eta_0, \eta_{\text{sub}}$,

respectively, one can calculate the amplitude reflectance and transmission of the layered structure by following equations, where B, C are used to determine the transfer functions:

$$\begin{bmatrix} B \\ C \end{bmatrix} = \left\{ \prod_{l=1}^N \begin{bmatrix} \cos \delta_l & (i \sin \delta_l) / \eta_l \\ i \eta_l \sin \delta_l & \cos \delta_l \end{bmatrix} \right\} \begin{bmatrix} 1 \\ \eta_{\text{sub}} \end{bmatrix} \quad (5.4)$$

$$\begin{aligned} \underline{r} &= \frac{E_r}{E_i} = \frac{\eta_0 B - C}{\eta_0 B + C} \\ \underline{t} &= \frac{E_t}{E_i} = \frac{2\eta_0}{\eta_0 B + C} \end{aligned} \quad (5.5)$$

In a nitrogen purged environment, the AR coated and uncoated samples are placed in the THz focus for recording the time traces, $\tilde{E}(t)$, in transmission mode. The Fourier transformed spectra, $E(\nu)$, from them are then compared. We also assume focused THz pulse to be plane wave at normal incidence. We construct the time-domain transmitted signal due to AR coating using inverse Fourier transform for comparison. For a single substrate we analyzed both the main pulse and twice internally reflected pulse, a feature offered by TDS. For these pulses the amplitude ratios in the frequency domain are respectively given by eq. (5.6), where t_1, t_2 denote the transmission coefficients at the air-sample, sample-air interface and r is the reflection coefficient from sample-air. Underlined co-efficients denote the corresponding functions for AR coated sample.

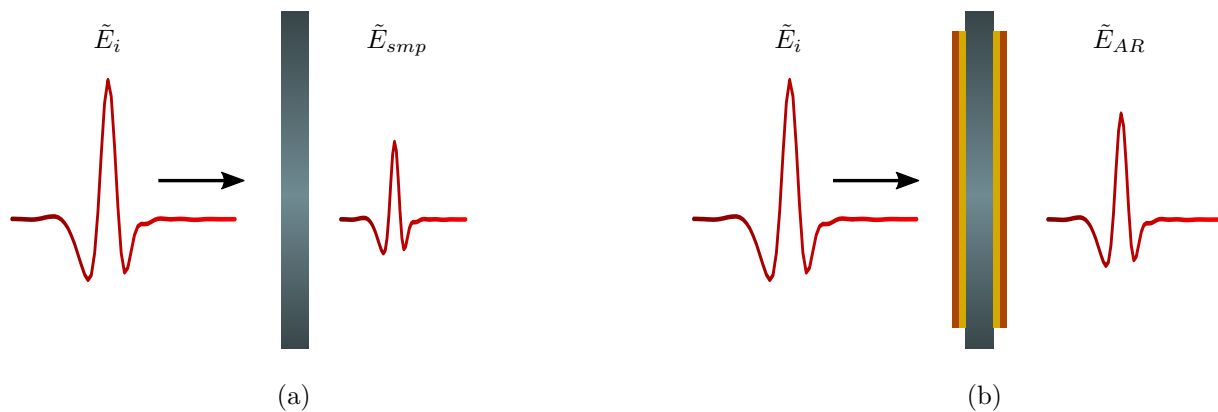


Fig. 5.4: Transmission through uncoated and coated substrates, (a), (b)

$$\left(\frac{|E_{AR}|}{|E_{smp}|}\right)_t = \frac{|t_1 t_2|}{|t_1 t_2|} \quad (5.6)$$

$$\left(\frac{|E_{AR}|}{|E_{smp}|}\right)_r = \frac{|t_1 t_2 \cdot r^2|}{|t_1 t_2 \cdot r^2|}$$

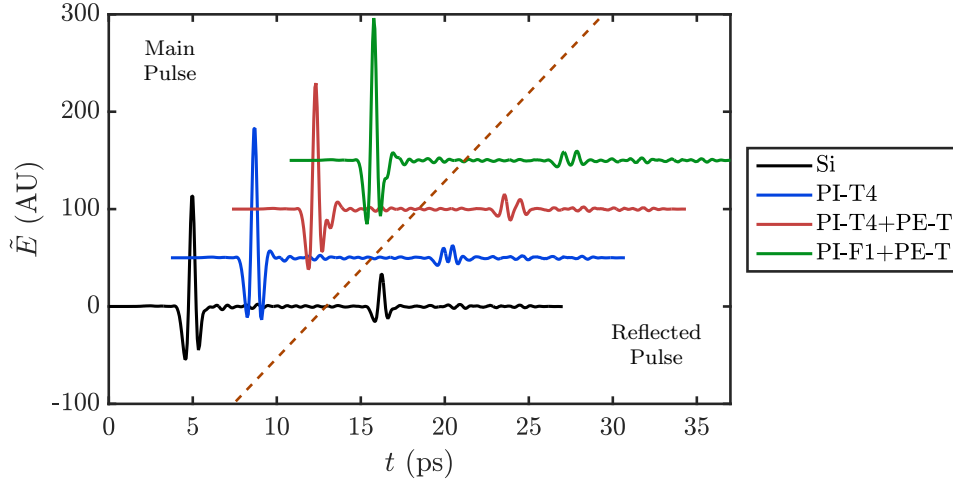


Fig. 5.5: Measured time traces of AR coated Si wafer. Successive waveforms are offset along both axes. Pulses transmitted through samples are on the left side of dashed line. Internally reflected pulses are on the right side of dashed line.

5.5 Results

Before presenting the results, it is worth while to describe the fitting method used in comparing calculated curve to experiment. Due to the many unknown variables in each layer, we employed a heuristic approach for fitting curves outlined below. We did not incorporate dispersion in calculation and therefore satisfactory fitting of the curves for the complete bandwidth was not possible for all ARCs.

- We took the real index for each film, n , from literature, tabulated in table 5.1. Since multiple films are involved, we first worked with a coating configuration having the least number of films, fig. 5.2 (a).
- Using the advertised thicknesses and no absorption, we plotted the calculated and experimental curves of $|E_{AR}|/|E_{smp}|$ on the same figure.
- The spectral oscillation, which is primarily a horizontal feature, is a result of film thickness. We kept the backing thickness fixed and varied the adhesive thickness to

align the horizontal features of the curves. If required we slightly varied the backing film thickness.

- Next we made educated guess on the absorption coefficient from literature and adjusted the imaginary part of \bar{n} , which vertically aligns the calculated curve to experiment.
- Using above steps we acquired estimates of the thickness (d) and extinction coefficient (κ) of films that are later used in more complex configurations with unknown film parameters. This approach is then applied on those films to estimate their parameters.

This process of fitting allowed us to consistently estimate κ, d for each coating. We only found slight variation between the κ in PDMS adhesive for two different tapes, see table 5.1. Lastly, we constructed the time-domain signal. In figure-captions, we mention nominal value of best-fit thickness for each film material employed in each ARC.

5.5.1 ARC on Si

500 μm thick, HRFZ-Si with resistivity $>15\text{k}\Omega\text{-cm}$ from MTI Corporation was used as the sample. The measured index was $n \approx 3.42$. In the following 9 figures, transmitted spectra of main pulse is in (a), frequency domain ratios are in (b), (c) and time domain trace is shown in (d). Both (c), (d) show experimental and calculated response of both main and reflected pulse (inset). In the ideal case of no Fresnel loss from Si substrate, $E_{AR}/E_{smp} \approx 1.43$.

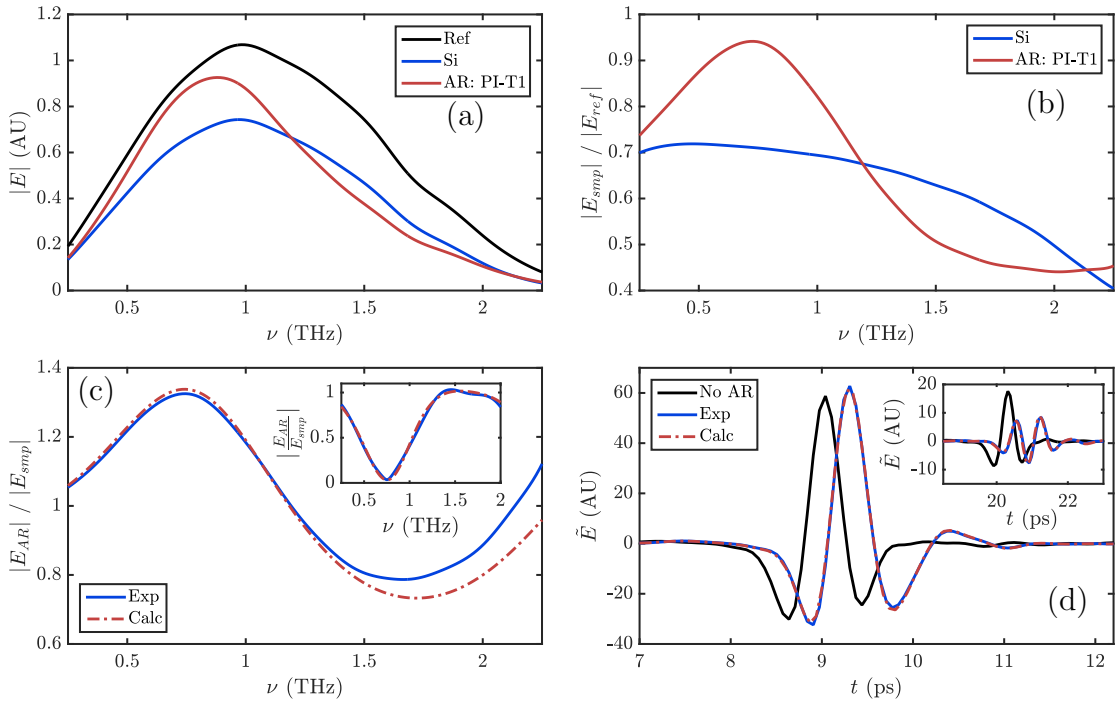


Fig. 5.6: ARC: PI (1 Mil)| PDMS (1 Mil)| Si (Substrate). Inset in (c) and (d) shows amplitude ratio and waveform of internally reflected pulse, respectively.

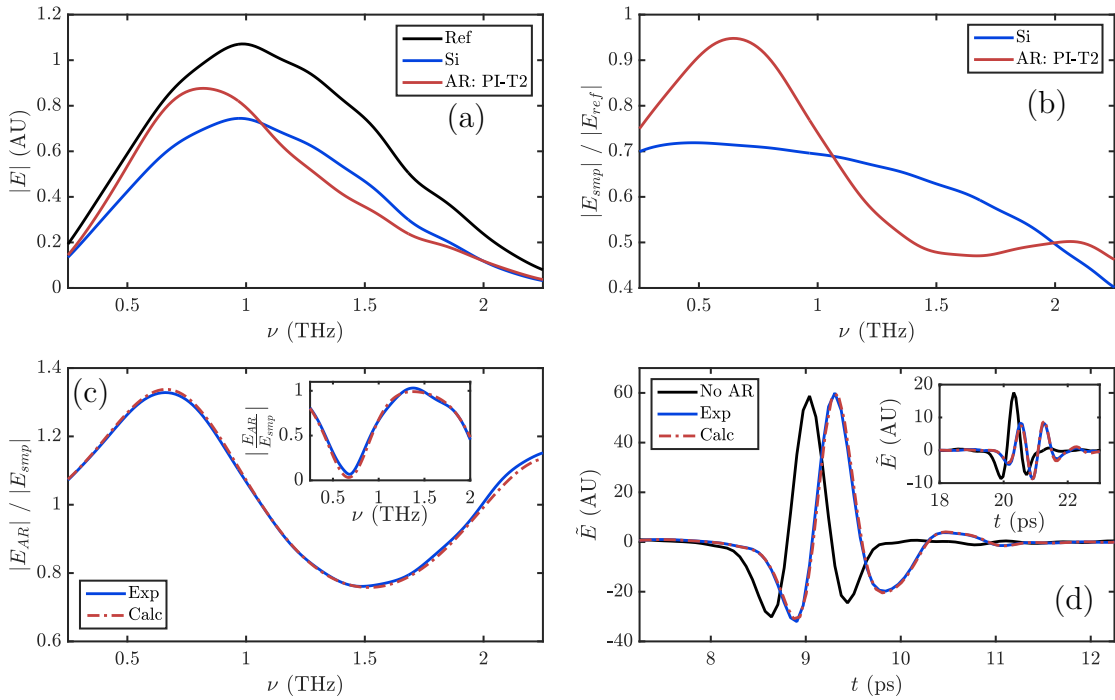


Fig. 5.7: ARC: PI (1 Mil)| PMMA (1.3 Mil)| Si (Substrate). Inset in (c) and (d) shows amplitude ratio and waveform of internally reflected pulse, respectively.

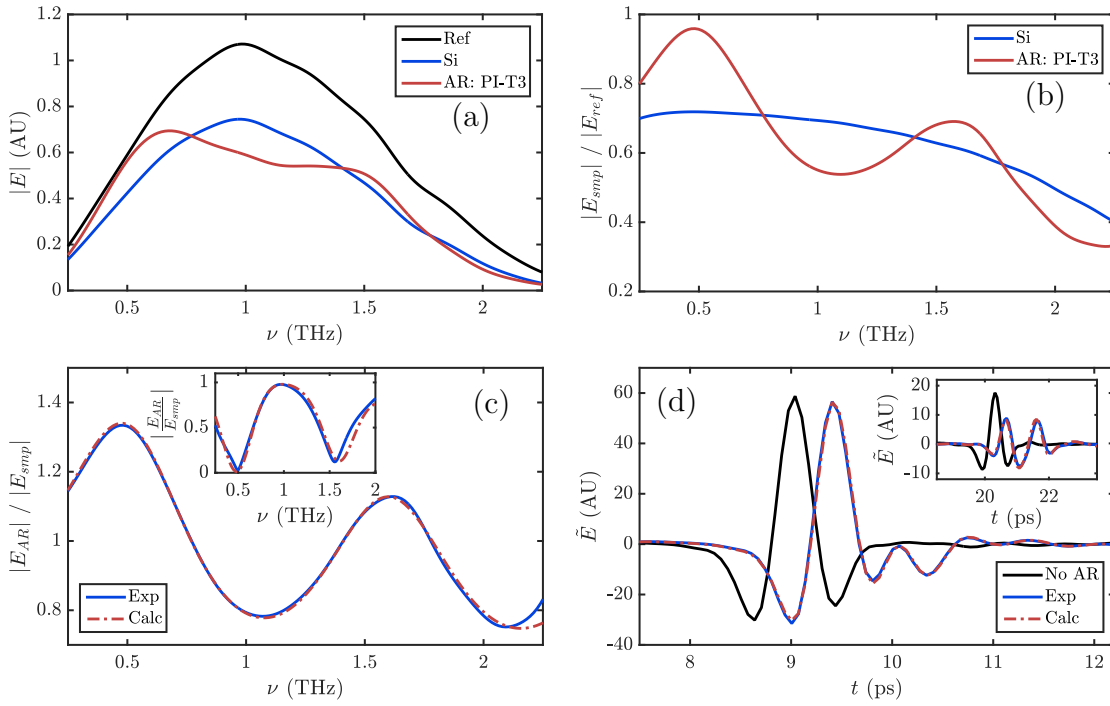


Fig. 5.8: ARC: PI (1.85 Mil)| PMMA (1.3 Mil)| Si (Substrate) Inset in (c) and (d) shows amplitude ratio and waveform of internally reflected pulse, respectively.

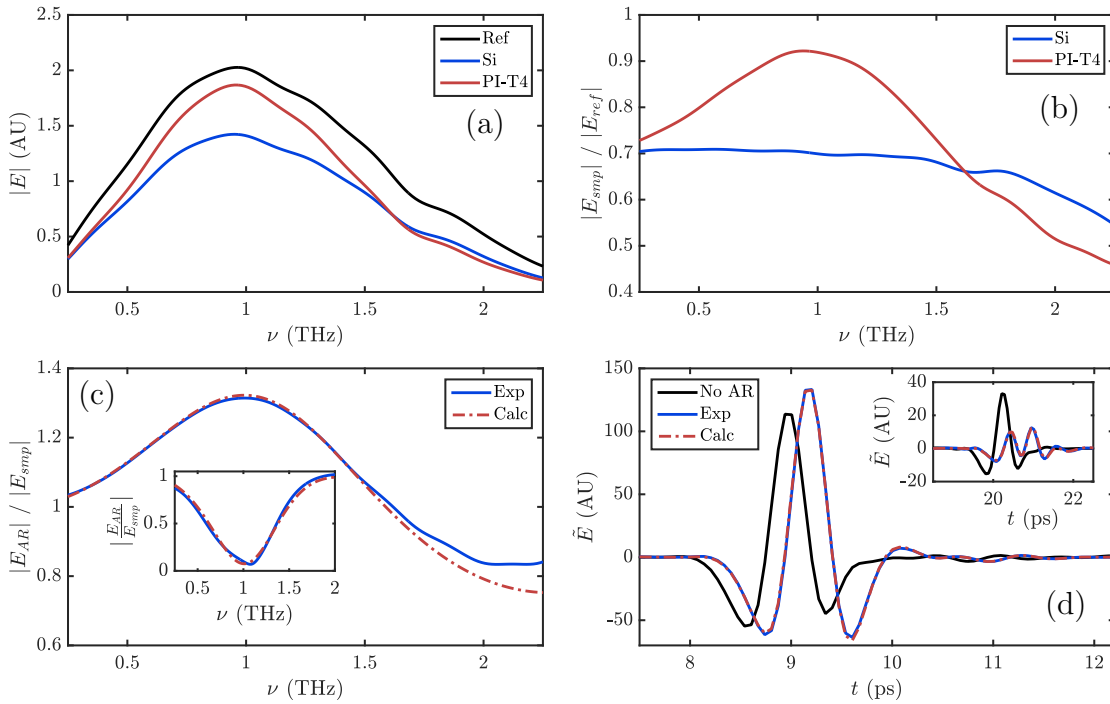


Fig. 5.9: ARC: PI (0.5 Mil)| PDMS (1 Mil)| Si (Substrate). Inset in (c) and (d) shows amplitude ratio and waveform of internally reflected pulse, respectively.

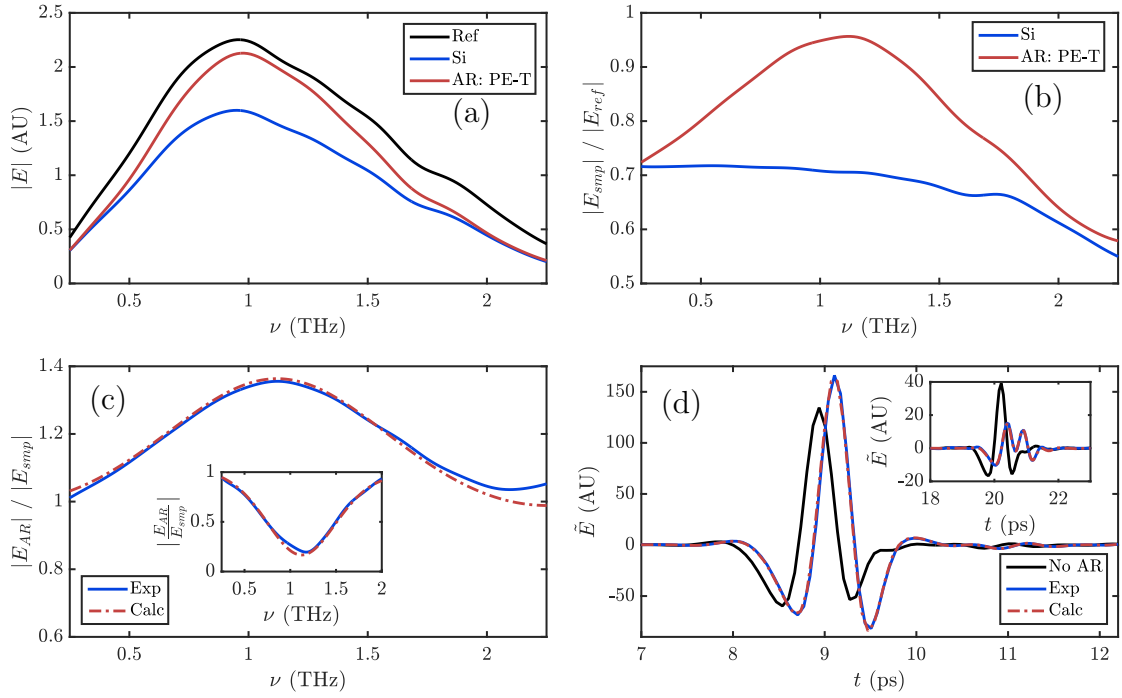


Fig. 5.10: ARC: PE (1.7 Mil) | PMMA (0.2 Mil) | Si (Substrate). Inset in (c) and (d) shows amplitude ratio and waveform of internally reflected pulse, respectively.

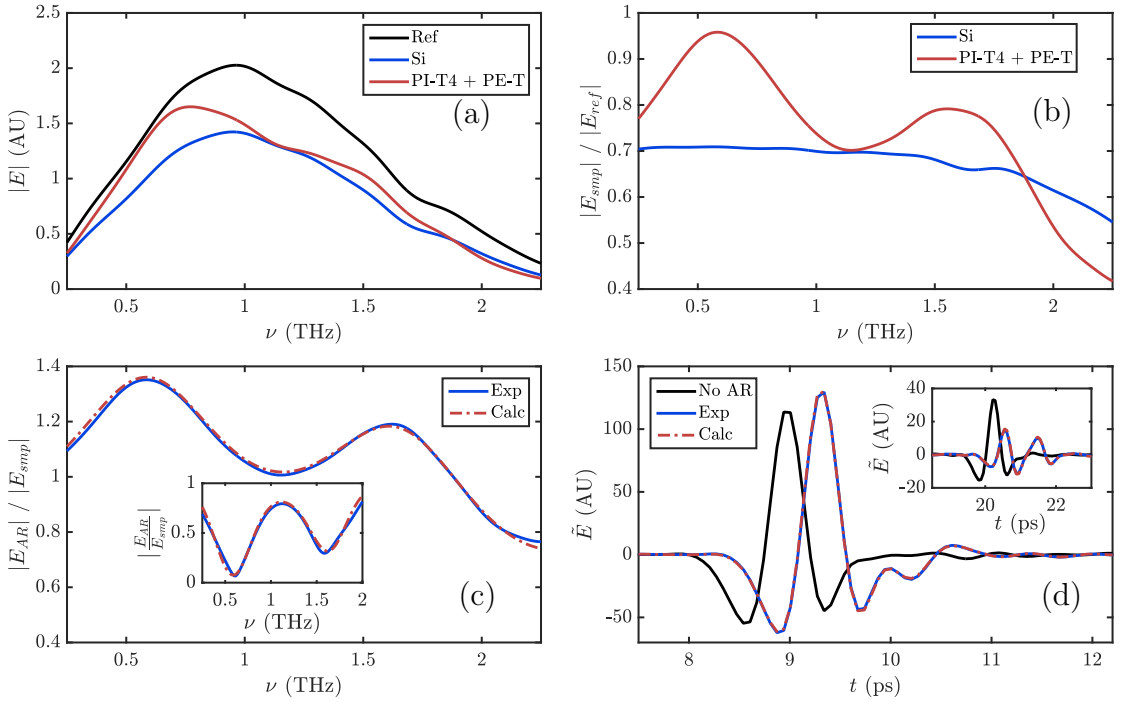


Fig. 5.11: ARC: PE (1.7 Mil) | PMMA (0.2 Mil) | PI (0.5 Mil) | PDMS (1 Mil) | Si (Substrate). Inset in (c) and (d) shows amplitude ratio and waveform of internally reflected pulse, respectively.

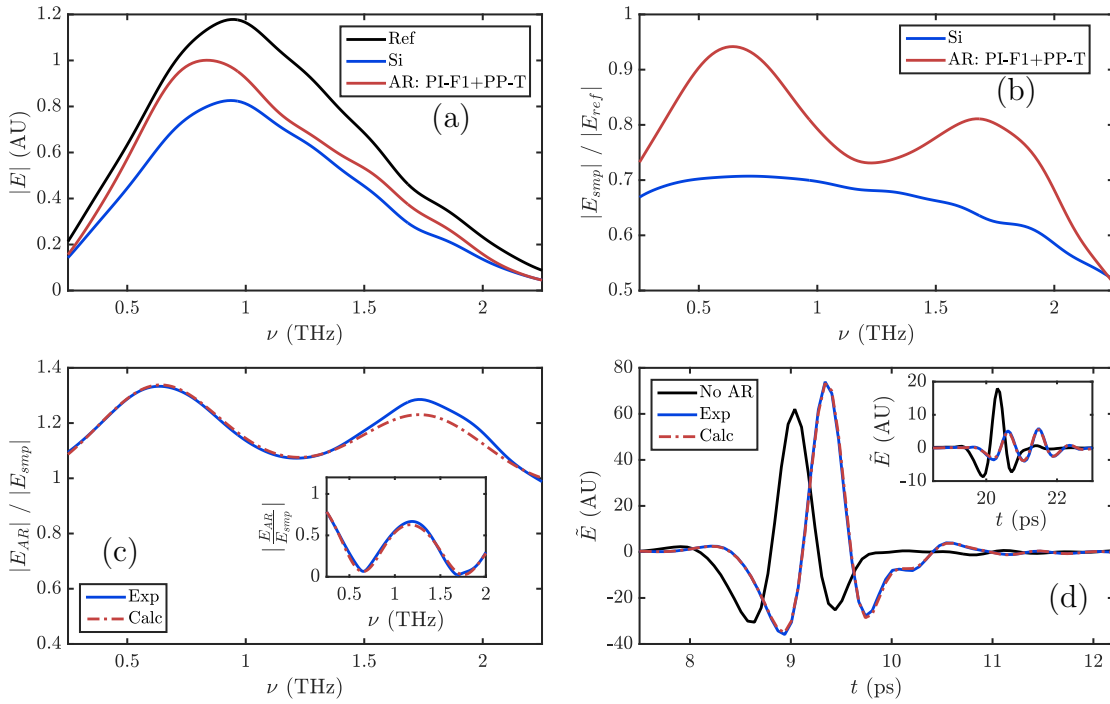


Fig. 5.12: ARC: PP (1 Mil)| PMMA (1.1 Mil)| PI (1 Mil)| Si (Substrate). Inset in (c) and (d) shows amplitude ratio and waveform of internally reflected pulse, respectively.

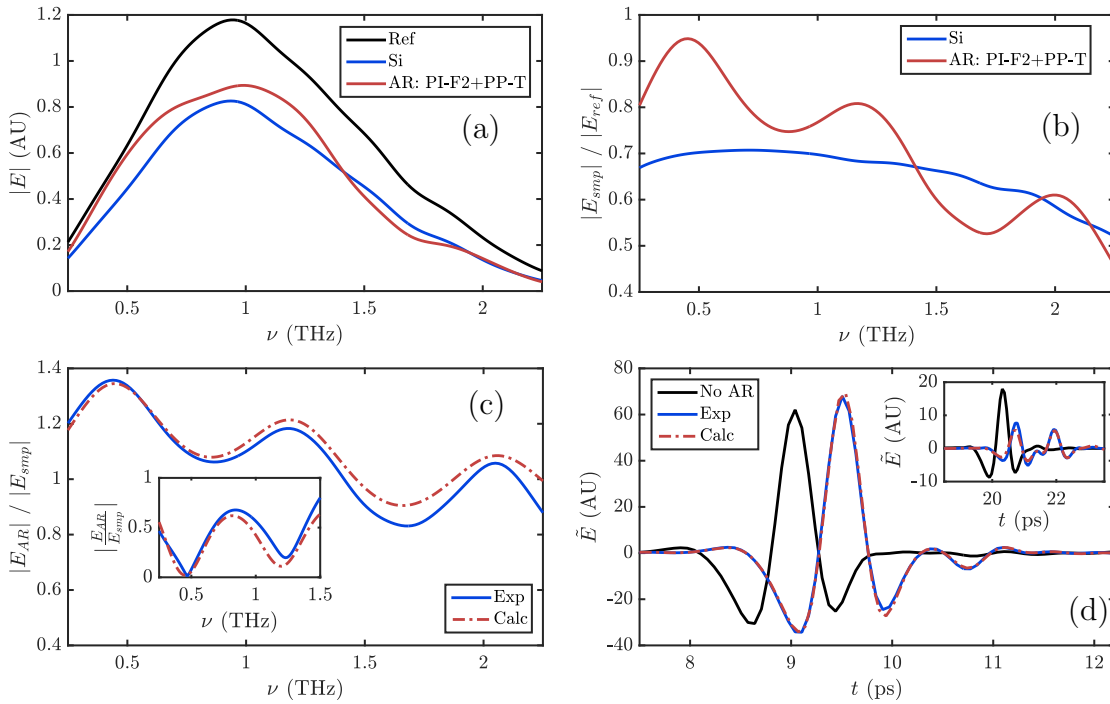


Fig. 5.13: ARC: PP (1 Mil)| PMMA (1.1 Mil)| PI (2 Mil)| Si (Substrate). Inset in (c) and (d) shows amplitude ratio and waveform of internally reflected pulse, respectively.

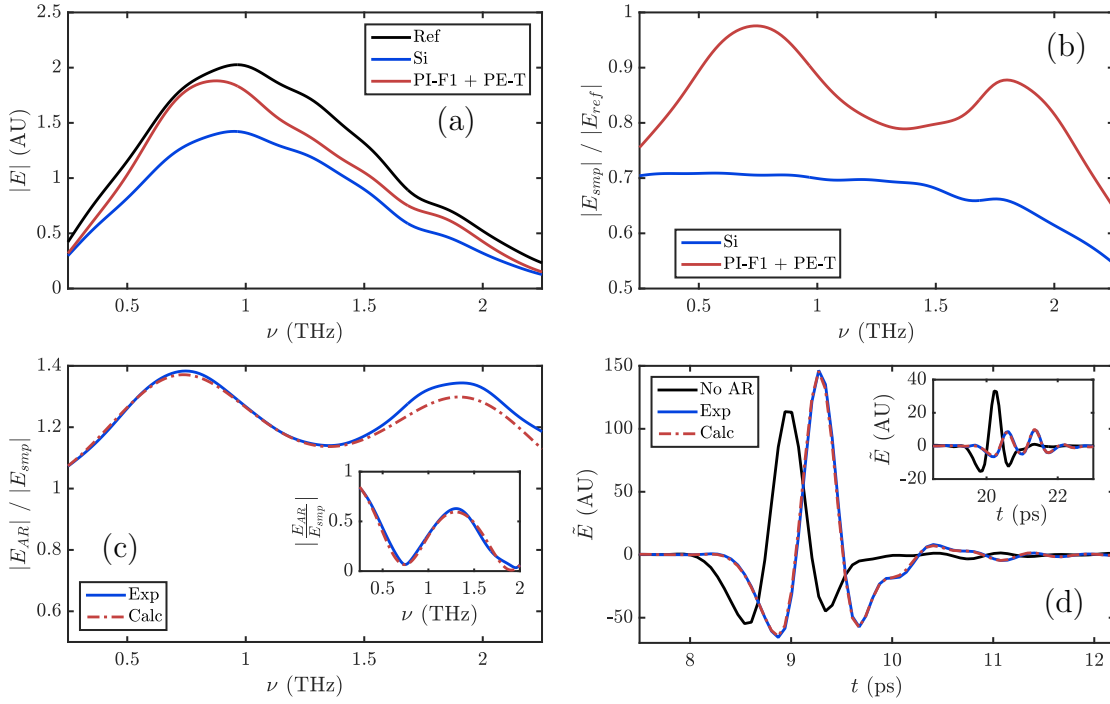


Fig. 5.14: ARC: PE (1.7 Mil)| PMMA (0.2 Mil)| PI (1 Mil)| Si (Substrate). Inset in (c) and (d) shows amplitude ratio and waveform of internally reflected pulse, respectively.

5.5.2 ARC on Alumina

Ceramic alumina (Al_2O_3) of thickness 6.35 mm from McMaster Carr was used as the second substrate for measurements. We measured the samples index, $n \approx 3.05$. Due to higher absorption than HRFZ-Si and much thicker substrate, the internally reflected pulse could reasonably be analyzed up to 1.5 THz. We performed fewer measurements with this sample than Si. In the next three figures, transmitted spectra of main pulse is in (a), frequency domain ratios are in (b), (c) and time domain trace is shown in (d). Both (c), (d) show experimental and calculated response of both main and reflected pulse (inset). In the ideal case of no Fresnel loss from alumina substrate, $E_{AR}/E_{smp} \approx 1.34$.

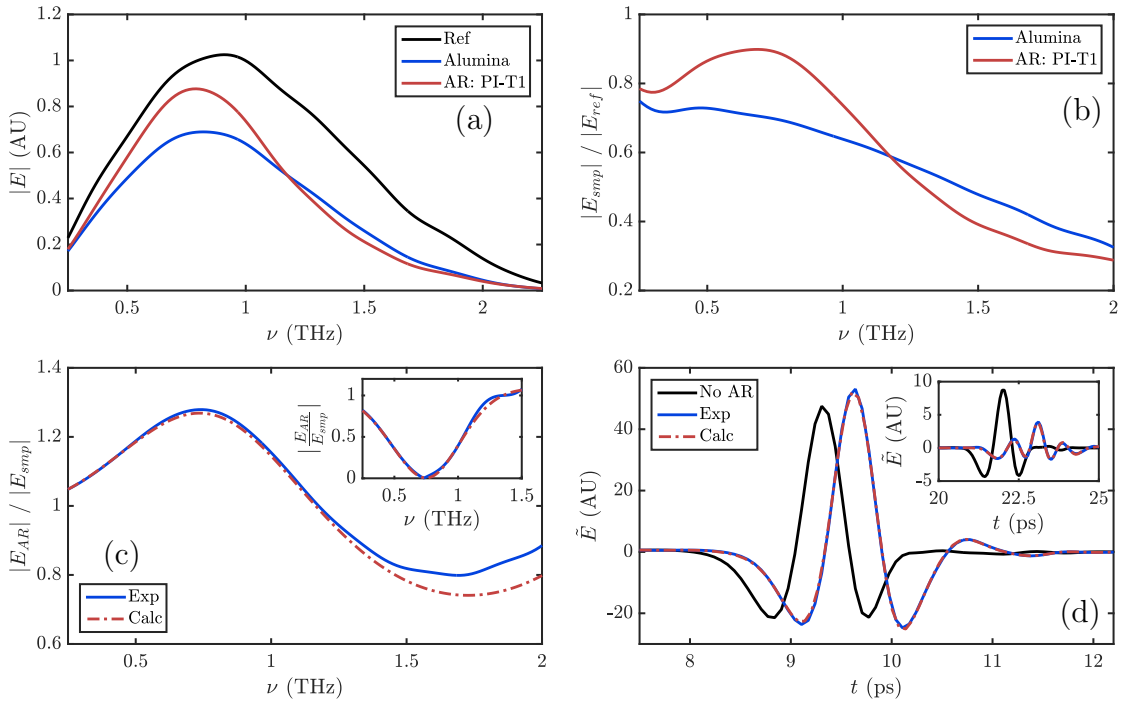


Fig. 5.15: ARC: PI (1 Mil)| PDMS (1 Mil)| Alumina (Substrate). Inset in (c) and (d) shows amplitude ratio and waveform of internally reflected pulse, respectively.

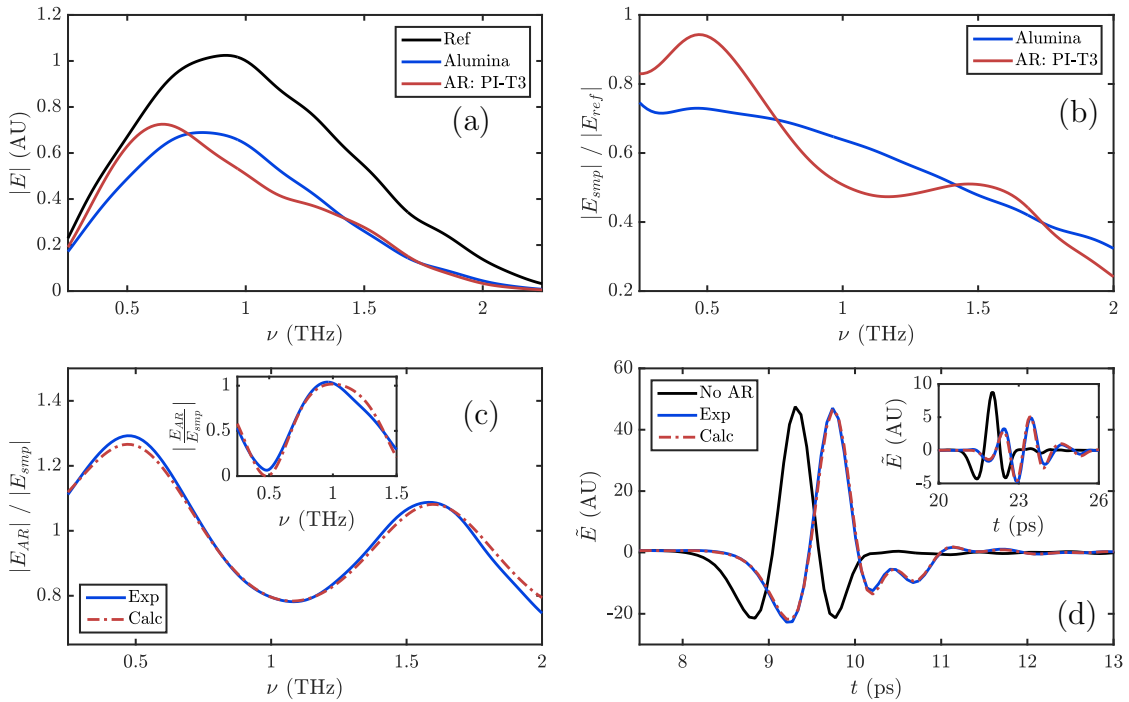


Fig. 5.16: ARC: PI (1.85 Mil)| PMMA (1.3 Mil)| Alumina (Substrate). Inset in (c) and (d) shows amplitude ratio and waveform of internally reflected pulse, respectively.

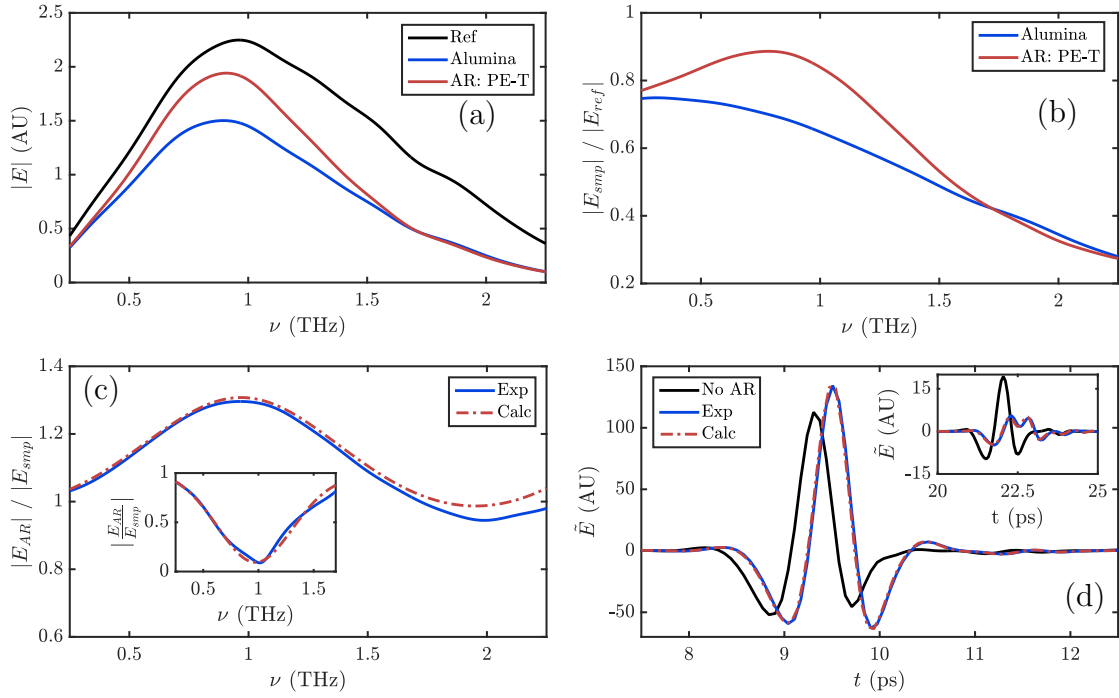


Fig. 5.17: ARC: PE (1.7 Mil)| PMMA (0.2 Mil)| Alumina (Substrate). Inset in (c) and (d) shows amplitude ratio and waveform of internally reflected pulse, respectively.

5.5.3 ARC on Quartz Glass

$\frac{1}{16}$ " thick quartz glass from McMaster Carr was used as a substrate. The index was measured to be, $n \approx 1.95$. Due to the relatively low index, we see a very weak reflected pulse in the time domain, which almost vanishes due to AR coating. We only analyze the main pulse for this substrate. In the ideal case of no Fresnel loss from quartz substrate, $E_{AR}/E_{smp} \approx 1.12$.

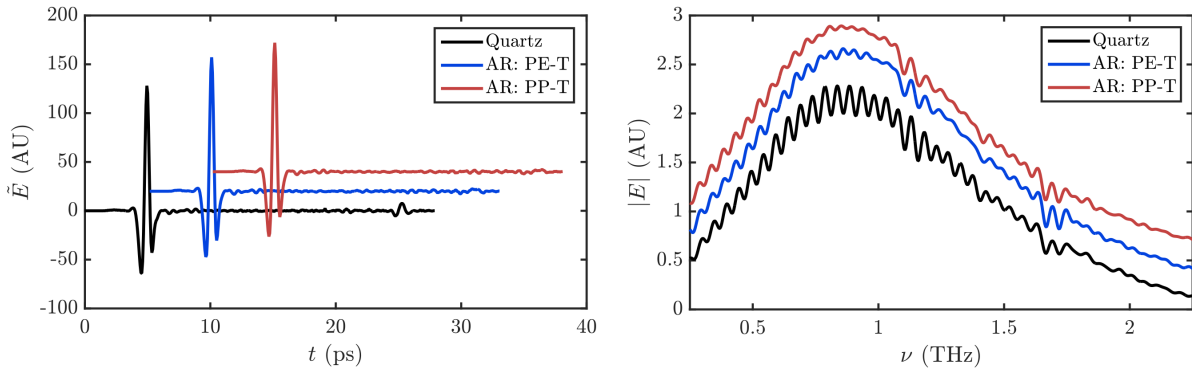


Fig. 5.18: Internalaly reflected pulse for the AR coated quartz glass is difficult to locate in the waveform. In frequency domain this manifests as greatly reduced FP oscillations. Plots are offset for clarity.

ARC on quartz glass offers slight enhancement of output field. Therefore, for the purpose of a window material, quartz glass may not require any coating. Nevertheless, the attenuation of internal reflection can be useful in certain applications. Moreover, we are able to demonstrate in fig. 5.19 the advantage of PE-T over PP-T, keeping in mind that PP-T has a much thicker adhesive layer than PE-T.

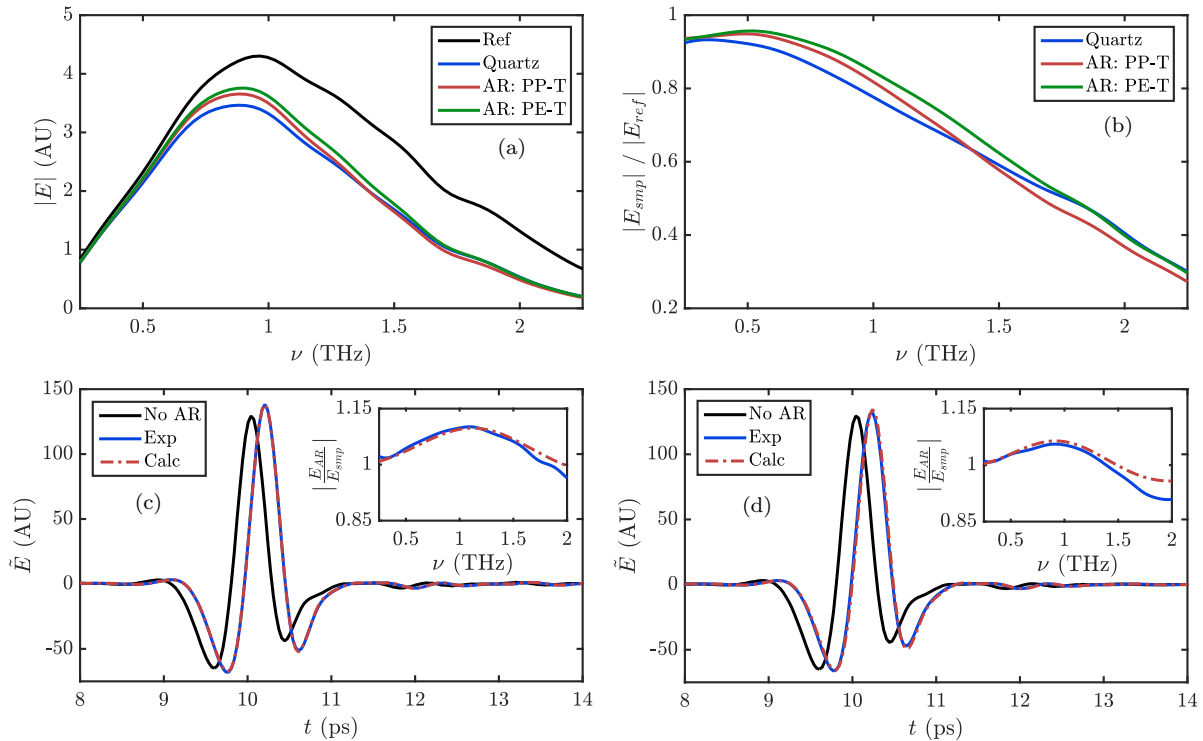


Fig. 5.19: (a) Amplitude of main pulse. (b) Amplitude ratio with respect to reference. (c) ARC: PE (1.7 Mil) | PMMA (0.2 Mil) | Quartz (Substrate). (d) ARC: PP (1 Mil) | PMMA (1.1 Mil) | Quartz (Substrate). Inset showing amplitude ratio in (c),(d).

5.6 ARC on an Electro Optic Crystal

To perform high resolution frequency domain measurements from THz-TDS, one requires a long temporal signal. The criterion for this is set by FFT, $\Delta\nu \approx 1/T$, where T is the total length of the signal. In free space electro-optic (EO) sampling, we use an EO crystal for coherent detection of THz waveform, see chapter 2. Due to the finite thickness of the crystal, THz light reflects off of the two crystal-air interfaces which introduce Fabry-Pérot (FP) oscillations in frequency domain. Thus uninterrupted long scans are not possible and we are limited in spectral resolution. One solution to this problem is to use a thick EO crystal to sufficiently time-delay the reflected signal. But increasing crystal thickness reduces detection bandwidth and increases cost.

Samples that do not possess any resonance, has smooth transmission spectra and having high spectral resolution for detection is of no practical benefit. On the contrary, samples with resonance(s) require high resolution spectroscopy to determine the resonance frequency and its linewidth. Moreover, for closely spaced resonances, higher resolution is a must to resolve individual material signatures. Since material resonances of interest are usually located in a certain region of signal bandwidth, we can utilize a narrow-bandwidth ARC optimized for the target region for the EO crystal. This significantly reduces the amplitude of internal reflections and thus attenuate the FP effects in frequency domain. Additionally, the PSAT based ARC developed in this chapter can be removed from the detector crystal and another ARC, tailored for a different target frequency, can be applied. This makes our low-cost ARC very versatile for a wide range of spectral analysis.

To show the oscillatory term that appears in calculation, we represent the trapped light in the EO crystal, in frequency domain by eq. (5.7). For simplicity we assume negligible dispersion and absorption in the crystal. In that case, transmission and reflection coefficients entirely depend on the real index. The round-trip time is given by $\Delta t = 2nL/c$, where L is the length of the crystal and c is speed of light in vacuum. N denotes the number of internally reflected pulse considered, t_1 is the transmission coefficient of the incoming interface and r_1, r_2 are the internal reflection coefficients for the two crystal-air interface.

$$E_{EO}(\nu) = E_i(\nu)t_1(\nu)e^{-i2\pi\nu(\frac{\Delta t}{2})} \sum_{k=0}^N [r_1(\nu)r_2(\nu)e^{-i2\pi\nu\Delta t}]^k$$

$$|E_{EO}(\nu)| = |E_i(\nu)| \cdot (|t_1(\nu)||FP(\nu)|) \quad (5.7)$$

$$|FP(\nu)| = \left| \frac{1 - [r_1(\nu)r_2(\nu)e^{-i2\pi\nu\Delta t}]^{(N+1)}}{1 - [r_1(\nu)r_2(\nu)e^{-i2\pi\nu\Delta t}]} \right|$$

Oscillation in the amplitude spectrum is a consequence of $|FP(\nu)|$ term. For the uncoated crystal, $r_1(\nu) = r_2(\nu) = r(\nu)$. Writing $a(\nu) = r^2(\nu)$, we can derive eq. (5.8) which explicitly shows the oscillatory term. Minimizing $a(\nu)$ in the spectral region of interest, would reduce oscillations in that region allowing high resolution measurements.

$$|FP(\nu)| = \left[\frac{1 + |a(\nu)|^{2(N+1)} - 2|a(\nu)|^{(N+1)} \cos(2\pi(N+1)\Delta t \cdot \nu)}{1 + |a(\nu)|^2 - 2|a(\nu)| \cos(2\pi\Delta t \cdot \nu)} \right]^{1/2} \quad (5.8)$$

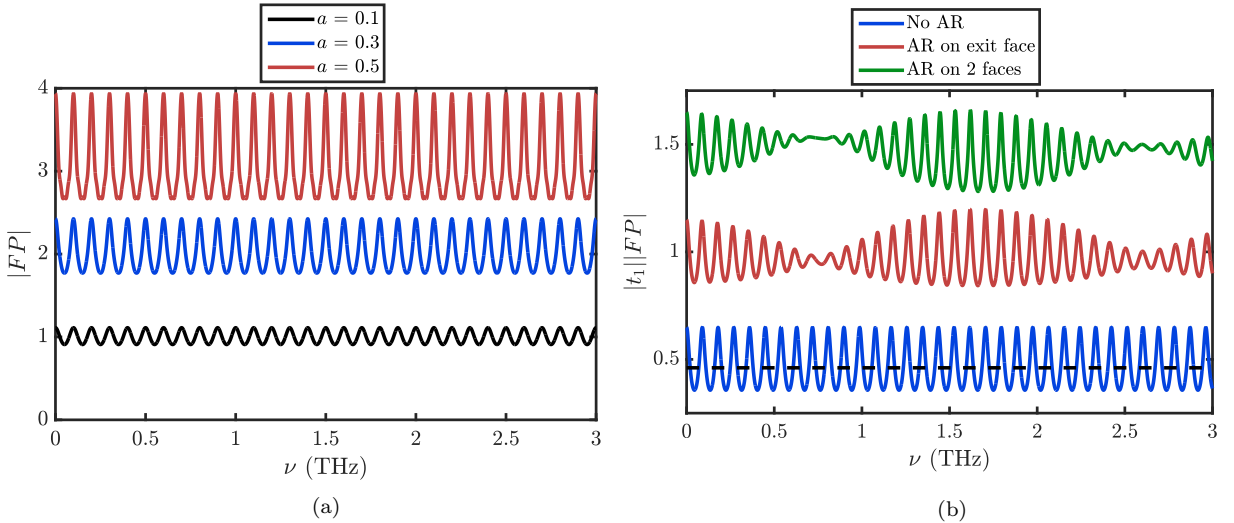


Fig. 5.20: Plots are offset along y-axis. (a) $|FP|$ for $\Delta t = 10$ ps, $N = 4$ without any ARC. For comparison $a \sim 0.3$ for GaP, ZnTe. (b) Calculated response of 0.5 mm thick GaP with five internal reflections for uncoated and PI-T1 coated on single and both faces of the crystal.

Our multilayered ARC suppresses $a(\nu)$ in the target region. As an additional advantage, there is reduced Fresnel loss when coupling light from air to EO crystal. Depending on the index of crystal and target detection frequency, our ARC can be applied on various EO crystals, given the films do not substantially reduce probe beam intensity. We use GaP for EO sampling which has $n \approx 3.34$, close to that of Si ($n \approx 3.42$) [27]. Qualitative the results from ARC on Si can be utilized in determining the suitable layered structure for

GaP. In this thesis, we are interested in the high resolution study of multiferroic BiFeO_3 (BFO) which has resonant frequencies in the region 0.5–0.75 THz. Since the resonances of BFO are reported to be tunable via external electric field and temperature, we have a plan to tune the resonances to higher frequencies, where we have greater dynamic range and SNR chapter 7. Considering current and possible future requirements, we employed ARC: PI-T1 with films PI (1 Mil)| PDMS (1 Mil)| GaP (substrate), which has a target frequency around 0.75 THz, fig. 5.20 (b). We had some transmission loss for the IR probe and also some distortion to the probe beam profile due to scattering after the tape-coated GaP crystal. These effects on the probe beam were reduced by appropriately adjusting neutral density filters and placing a lens with long focal length before balanced detector.

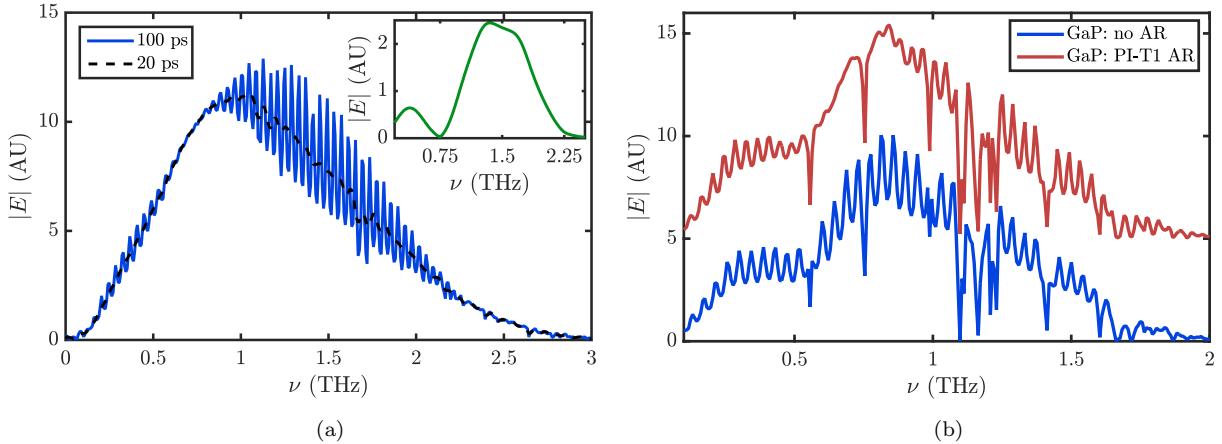


Fig. 5.21: (a) Experimental spectrum from 1mm thick GaP detection crystal coated with PI-T1 on both sides, where internal reflection shows up after 22 ps. Spectrum in the inset is that of the 1st reflected pulse. Legend indicates time duration of the analyzed waveform. (b) Water vapor absorption spectra from 110 ps long scan using uncoated and coated GaP. High resolution absorption lines are discernable at 0.56, 0.75, 0.99 THz. Clear spectral advantage can be seen in the red curve.

5.7 ARC for Non-Collinear THz Generation

Intense THz pulses can be generated using pulse-front-tilt in MgO doped LiNbO_3 (LNB), in a non-collinear fashion where IR and THz propagate in different directions, see chapter 2. In room temperature typical bandwidth attainable with this technique may go up to 2.5–3 THz. But due to refractive index mismatch between the extraordinary index in THz range ($n_e \sim 5$) of LNB and air, we have a power reflectance loss, $R \sim 44\%$. To circumvent this Fresnel loss, there has been a few attempts with AR coating. LNB was coated with

100 μm thick fused silica in [74], while in [75], it was coated with three stacks of PI-T1 tape. Both such technique provide a narrow band solution. We reproduce their calculated performance in the fig. 5.22 (a), using dashed lines which are absent in the respective articles for the wide bandwidth considered here. Based on the ARCs developed in this chapter, we propose wider-bandwidth solution to the problem. ARC has the additional advantage of increasing the critical angle, θ_c , for THz inside the LNB crystal. For LNB-air interface $\theta_c \approx 11.5^\circ$, but after coating with films mentioned in this article one can get $\theta_c \approx 18^\circ$, which can further prevent losses.

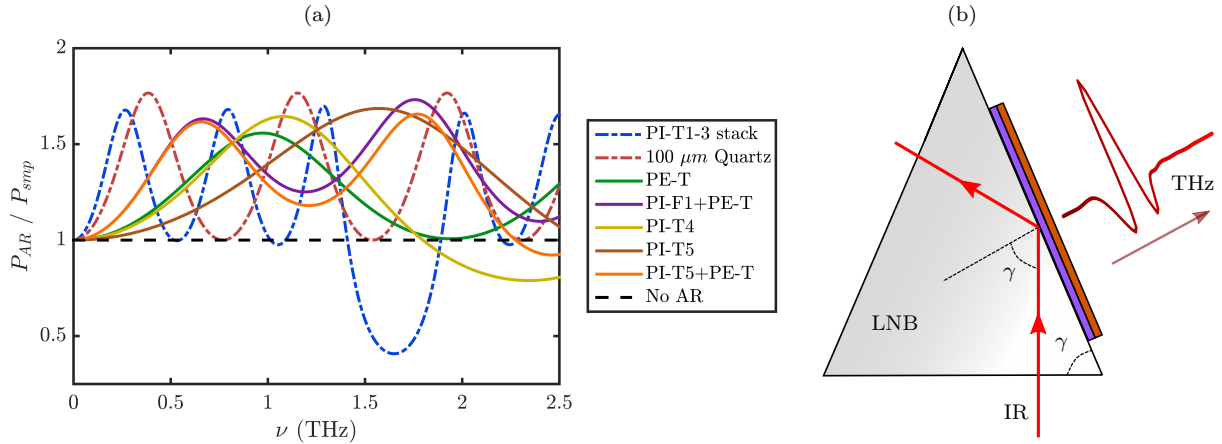


Fig. 5.22: (a) Calculation on THz power outcoupling from LNB, ignoring absorption and dispersion in films. Each ARC's merit can be seen for certain spectral regions and bandwidths. (b) Application of multilayered film on LNB prism.

Due to the desired tilt-angle, $\gamma \approx 63^\circ$, the LNB prism is designed to accommodate γ , fig. 5.22 (b). This ensures that IR light is total internally reflected and leaves the prism from another face and ideally both input and output faces are AR coated for IR. For MgO doped LNB, $n_{IR} \approx 2.15$ at wavelength $\sim 1 \mu\text{m}$ [76], thus one can safely attach a film with $n_{IR} < 1.9$ onto LNB to operate above the θ_c , which guarantees that IR power is not transferred to the films.

For broadband ARC on LNB, we propose that films of PDMS, PMMA, PI be in contact with LNB. According to [77], the IR indices $n_{PDMS} < 1.42$, $n_{PMMA} < 1.49$. PI on the other hand, has slightly higher index which according to [78, 79], $n_{PI} < 1.9$. We placed 1, 2 Mil PI film in the IR probe path and by observing the time shift of THz pulse we can estimate $n_{PI} \approx 1.8$. Therefore, we can safely attach the polymer layers considered in this chapter on LNB prism. By tuning the thickness of films we can attain a coating tailored for a maximizing THz pulse's peak electric field.

5.8 Discussion

Our elaborate testing shows that it is possible to utilize commercially available polymer films and adhesives to create relatively broadband and economic ARC. Both experiment and calculation along with their agreement in both time and frequency domains bolster the assertion. The substrates considered in this chapter has a range of index, $n= 2-5$. Multilayered film structures can be adapted to any specific frequency region by adjusting film thickness, but best suited for $\nu < 1.5$ THz due to absorptions at higher frequency. The realizable broadband performance with simple removable films sets the layered structure apart from the ones found in literature. A myriad of possible applications can be found with our ARCs that require reduction of Fresnel loss and FP effect. Application to window materials, Si, alumina, and quartz glass show enhanced performance at desired frequency region. The application to high resolution spectroscopy with EO crystal, GaP, is also demonstrated. The calculation for THz ARC on LNB in tilted pulse front geometry indicates that an increase in THz peak power by a factor of ~ 1.5 would be possible with appropriate combination of films.

5.9 Conclusion

We have performed thorough evaluation of commercially available tapes and films for THz AR coating applications. Time domain spectroscopy has accommodated us to separately analyze main transmitted pulse and internally reflected pulse. By tuning the thickness and index of polymer films, one can tune the region and efficacy for ARC. We note that for higher frequencies PDMS adhesive was less lossy than PMMA and we could not fit experimental curve by ignoring dispersion. As a rule of thumb, applying thin PE tape on substrates with $n > 2$, would significantly reduce Fresnel loss in the THz region. The method for ARC application outlined in this chapter is well suited for flat substrates. Applying the AR coated GaP crystal, we perform high resolution spectroscopy of BFO in chapter 7, where we are able to resolve the closely spaced magnon modes around ~ 0.55 THz. Moreover, the higher resolution should aid in the unambiguous detection of Rabi splitting, which is characteristic of cavity-polaritons. Overall, the economic ARC solution presented here is expected to have a positive impact on THz technology.

Chapter 6

THz Pile-of-Plates Polarizer

6.1 Introduction

Natural light, or radiation from ordinary sources are randomly polarized, i.e., it lacks a predictable directionality of the electric field vector of the EM wave. Polarized light on the other hand, has a well-defined electric field direction and can be primarily considered to be elliptically polarized¹, which in special cases fall into linear and circular polarization states. Regardless of its polarization, electric field of light can be decomposed into two mutually orthogonal linear states, both of which are normal to the direction of propagation. Working with these linear states is simple because of their fixed plane of oscillation.

A linear polarizer is a device that has a fixed direction called transmission axis, and when light is incident on it, only the component of electric field parallel to the transmission axis will be allowed to transmit, while the field perpendicular will be blocked. The rejection of the orthogonal state can be accomplished by selective absorption, reflection, or refraction [3, 23]. This allows a mechanical way of altering the output power of a polarized light source. The transmission intensity of a linearly polarized light as a function of polarization angle θ , the angle between electric field and transmission axis, for an ideal polarizer is given by Malus's law [3]:

$$I(\theta) = I_0 \cos^2(\theta) \tag{6.1}$$

¹There is also axially symmetric polarization, i.e., radial and azimuthal polarization.

Where I_0 is the maximum incident intensity when $\theta = 0$. Due to unavoidable losses present in practical polarizers, for comparison purpose, we would let I_0 represent intensity of the transmitted light so that $\cos^2(\theta)$ proportionality can be inspected.

We will explore a simple linear polarizer configuration in the THz frequency range based on reflection mechanism, called pile-of-plates polarizer. The available polarizers for THz light are quite expensive and a review of this technology can be found in [80]. We will investigate on improvement on an economic design targeted for far-infrared region [81, 82] made of polyethylene (PE) films. Our design will aim to significantly enhance the extinction ratio and reduce insertion loss, but will operate on a narrower bandwidth than typical THz pulse.

6.2 Polarization Due to Reflection

When light impinges from one dielectric medium to another, the transmission and reflection coefficients, t and r are given by Fresnel equations. The Fresnel equations, eq. (6.2), can be found in any text-book on optics and electro-dynamics, which essentially is derived from the boundary conditions of electric and magnetic fields, see for example [3, 23, 83]. The subscripts, s and p, denote s-polarized or TE light and p-polarized or TM light respectively. The polarization direction is measured with respect to the plane of incidence. If the electric field lies parallel to this plane, the light is called p-polarized and if it is perpendicular, the light is called s-polarized. The subscripts 1, 2 denote incident and transmission media.

$$\begin{aligned} r_s &= \frac{n_1 \cos \theta_1 - n_2 \cos \theta_2}{n_1 \cos \theta_1 + n_2 \cos \theta_2}, & t_s &= 1 + r_s \\ r_p &= \frac{n_1 \cos \theta_2 - n_2 \cos \theta_1}{n_1 \cos \theta_2 + n_2 \cos \theta_1}, & t_p &= (1 + r_p) \frac{\cos \theta_1}{\cos \theta_2} \end{aligned} \quad (6.2)$$

For absorptive dielectrics, in the above set of equations one typically replaces the index n by the complex index $\bar{n} = n - i\kappa$ and uses complex angles in Snell's law. For a detailed analysis on Fresnel equations for lossy material, one can see [84, 85].

From the reflection coefficients when light travels from air to dielectric, in fig. 6.1 we find there exists an incident angle $\theta = \theta_B$, for which $|r_p| = 0$. This angle is called Brewster's

angle and can be calculated as follows:

$$\tan(\theta_B) = \frac{n_2}{n_1} \quad (6.3)$$

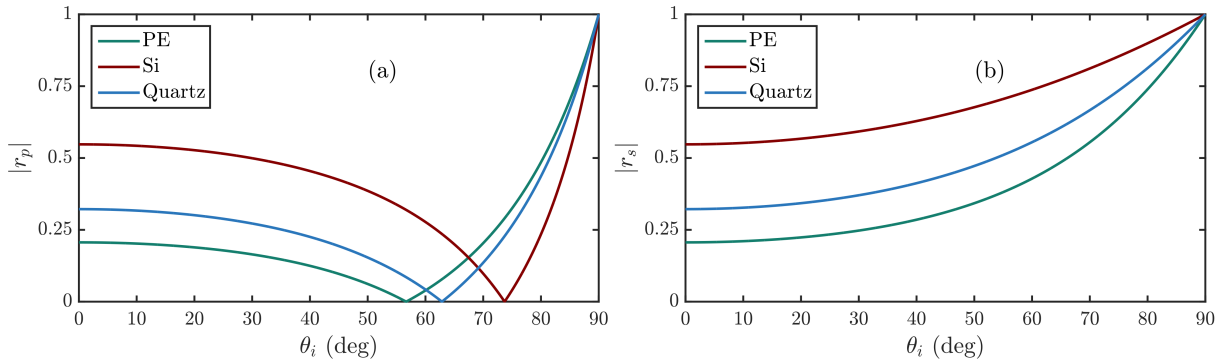


Fig. 6.1: reflection coefficients for p-polarized (a) and s-polarized (b) light

At Brewster's angle, s-polarization is partially reflected and partially transmitted while p-polarization is completely transmitted. Using Stokes relations [3] eq. (6.4), one can show that for a slab with two parallel faces (where light enters and exits) if $\theta_1 = \theta_{B1}$, then $\theta_2 = \theta_{B2}$. As a result both reflection coefficients r_1 and r_2 would vanish, and there would be no Fresnel loss in transmission. So, it suffices to consider only $\theta_{B1} = \theta_B$ for flat dielectrics.

$$\begin{aligned} r_2(\theta_2) &= -r_1(\theta_1) \\ t_1(\theta_1)t_2(\theta_2) &= 1 - r_1^2(\theta_1) \end{aligned} \quad (6.4)$$

A stack of dielectrics at the Brewster's angle will continue to reflect s-polarized light until it vanishes. Such a polarizer configuration is known as pile-of-plates. As a result of non-zero r_s , one has to consider the Fabry-Pérot effect present in the system. Although easy to construct, such polarizers are bulky and need to be operated on collimated beam.

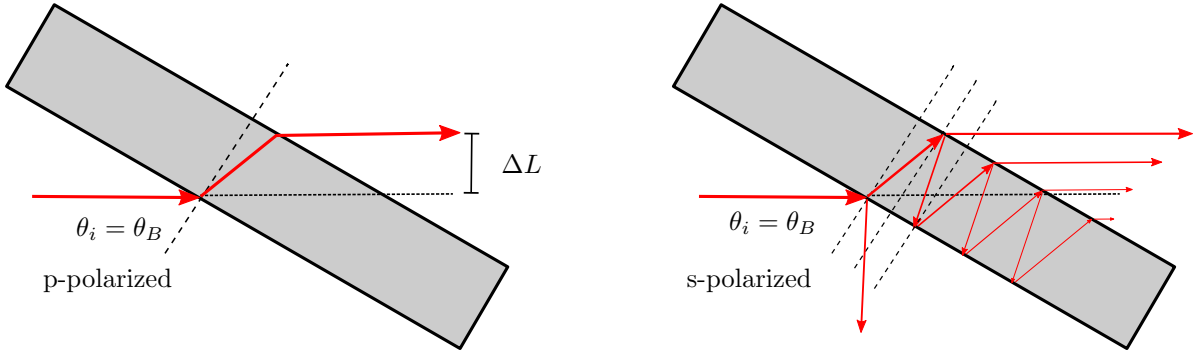


Fig. 6.2: Ray tracing Fabry-Pérot effect in tilted dielectric film at the Brewster angle. Not showing rays transmitting on the left side for s-polarization

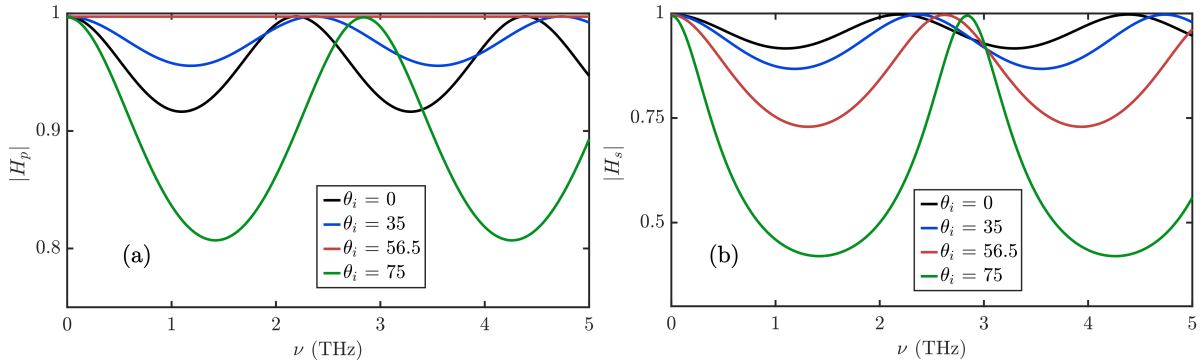


Fig. 6.3: Fabry-Pérot effect in frequency domain from $45\mu\text{m}$ PE film due to transmission of each polarizations. Angles are given in degrees

For the ideal material, one wants to use as lowest absorptive dielectric as possible. For THz light, it is known that from the commonly used materials, HRFZ-Si and PE have significantly low loss and between the two HRFZ-Si is substantially more transparent. But due to high θ_B for Si, one requires a large surface area wafer. From a practical point of view, this makes the polarizer quite expensive. Four stacks of 100 mm diameter HRFZ-Si was used in [86], where they have spaced the Si wafers such that inter-wafer reflections do not transmit out of the polarizer. Since, Fabry-Pérot effect will be contributed from individual plates, there has to be a non-flat frequency response of such a system, which was not described in the article. Although lossy, one big advantage of PE film is that we are not limited by the beam-diameter. Commonly, THz beam is diameter ≥ 25 mm, as a result an increase of dielectric area is unavoidable to satisfy the required beam size. Another advantage for is the relatively slow change of $r_p(\theta_i)$ in the neighborhood $\theta_i = \theta_B$, which reduces difficulty involved in misalignment of incidence angle, see fig. 6.1.

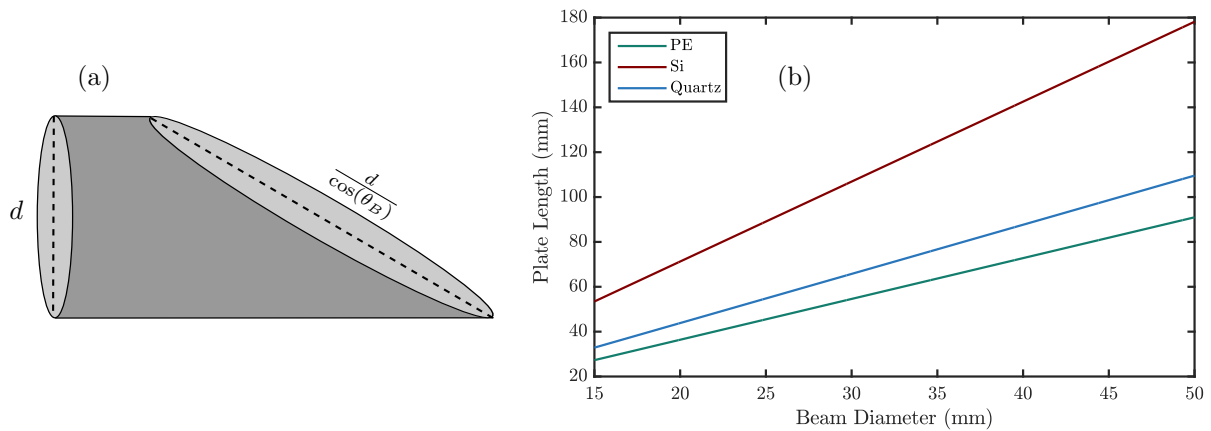


Fig. 6.4: Increase of plate surface area due to $\theta_i = \theta_B$ for PE, Si, Quartz glass

We define two parameters that are commonly used to characterize the performance of a polarizer, power extinction ratio (ER) and power insertion loss, where P_T is the power transmitted with no polarizer placed.

$$ER = \frac{P_p}{P_s}, \quad IL = \frac{P_T}{P_p} \quad (6.5)$$

6.3 Construction and Measurement

As a proof of concept, we built the first version of our polarizer unoptimized for performance. A unique feature we implemented in order to keep a flat plastic film, is we used PE shrink-wrap films. Thin rectangular frames of thickness 0.7 mm were 3D printed using polycarbonate (PC) based filament (Polycarbonate Copolyester blend) for its excellent heat resistance. Then we applied double sided tapes to attach the shrink-wraps on to the frames. We then used a heat-gun to heat-shrink the plastics until they were flat. The measured thickness was between 40–45 μm .

All other parts for this prototype is printed with PLA. The PC frames were attached to a thick frame that keeps them flat. For the purpose of rotation, one big mount with angle marks was printed (blue) which would hold a cylindrical part (gray) using set-screws. The cylinder can be rotated about its axis, which would allow us to vary the polarization angle. Attached to the cylinder are two arms that connect with the PC frames via screws which allow rotation along axis perpendicular to the propagation direction of light. This allows us to change the angle of incidence and satisfy $\theta_1 = \theta_B \sim 55^\circ$.

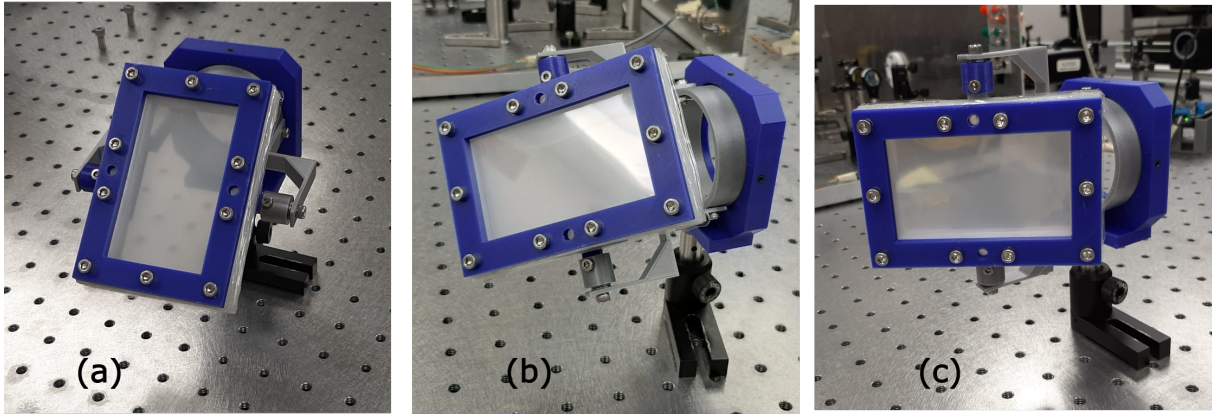


Fig. 6.5: 3D printed and assembled two-axis rotation mount holding many stacks of PE film. The gray cylindrical part rotates about the direction of incidence, while joints holding the PE stacks can be rotated to vary θ_i . Changing polarizer angle from 0° to 90° in (a)–(c)

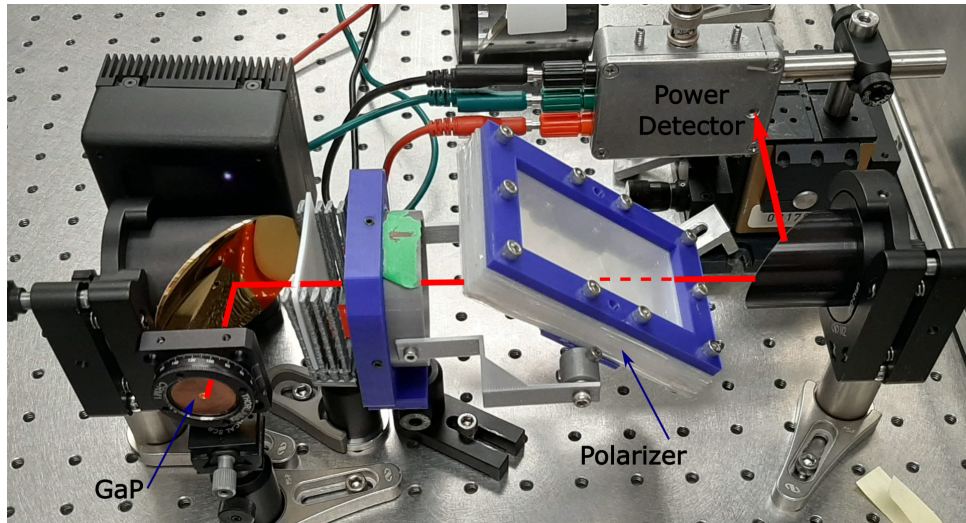


Fig. 6.6: PE pile of plates polarizer in THz beam at polarization angle 0°

Initial characterization was performed using thermopile power detector. The THz emitter was a 0.3 mm thick GaP pumped using ~ 100 fs IR pulse at 1035 nm. The generated THz has a bandwidth up to 5 THz. In fig. 6.6 the off-axis parabolic mirror (OAPM) right after GaP has a hole that allows most of the IR to exit while THz light is collimated and sent along the red arrow on to another OAPM to be focused on the detector. A white teflon sheet is placed to further filter residual IR from entering the power detector. Our polarizer is placed in the collimated section for measuring out-put power as a function of polarization angle. The emitted THz has a polarization parallel to the pump IR, although the degree of polarization may be questionable. Ultimately, 1 standard polarizer and 1 test polarizer are required to test the functionality of the latter device. So for initial

measurements we did not use a standard polarizer to check parallel and cross polarization with our device.

6.4 Results

For stack number 15, 18, and 22 we obtained the following curves in fig. 6.7 for angles 0° – 90° . A full 360° could not be measured due to the aperture size effect mentioned in section 6.5. It is incorrect to compare the data directly to Malus's law because we have not yet measured the frequency response of the polarizer, as will be shown from calculation in fig. 6.9. We still show the Malus's law to compare the data to a broad-band high extinction ratio device. For the stacks for full input bandwidth we respectively find power extinction ratio and insertion loss, $ER \approx 4.6, 6.4, 6.4$ and $IL \approx 1.23, 1.27, 1.33$. The fact that ER does not increase significantly with stack number is in fact not a bad sign. Calculations indicate that at certain narrow frequency regions, the ER should be appreciable while in others almost equal to unity. Nevertheless, this version of the device is good enough to verify the direction of polarization of the incoming light.

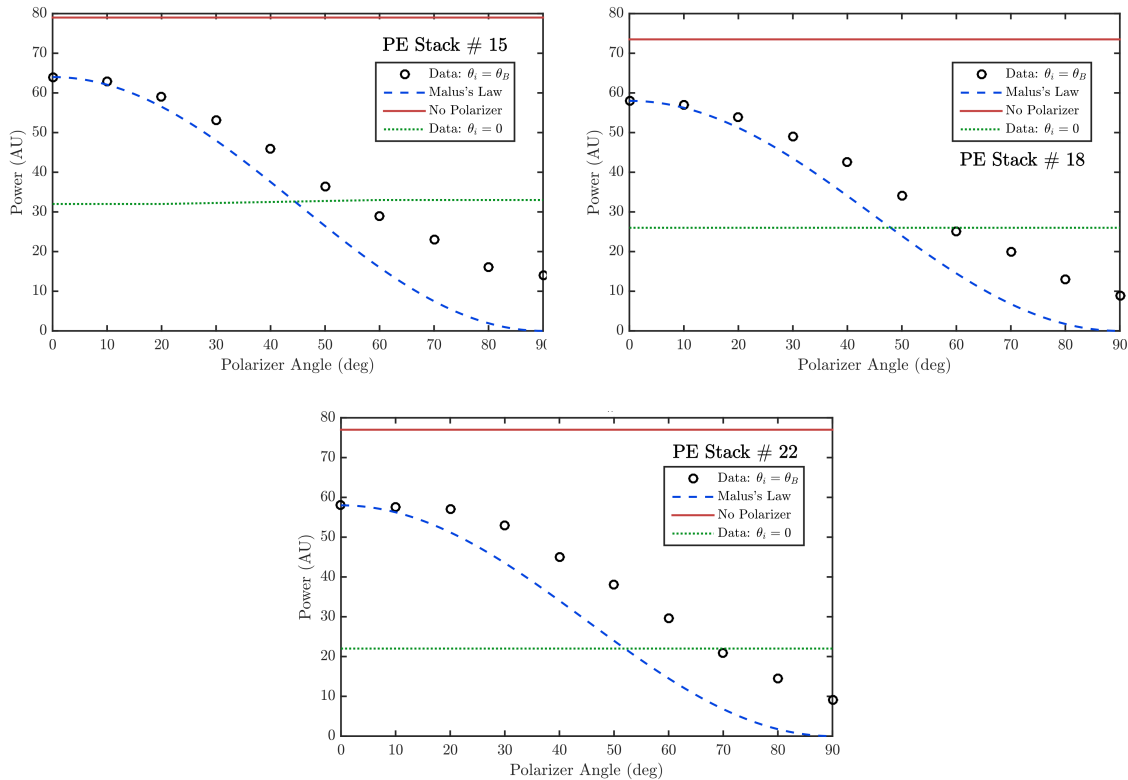


Fig. 6.7: Effect of PE stack number on performance of Brewster Polarizer

6.5 Improvement in Construction

We propose an improved version of the polarizer that would be narrowband but compact and impressive in performance. For the optimized polarizer, we should further reduce the thickness between the PE films to get more space-efficient, which will also reduce the aperture size issue shown in fig. 6.8. More importantly, utilizing the gap between PE films, we can create a distributed Bragg reflector (DBR) optimized for a certain band of frequency. Thus, for our bandwidth of operation, p-polarized light will transmit without any Fresnel loss, while s-polarized light will be reflected off by the DBR. By tuning the thickness of film and spacing we can also tune the stop-bands for s-polarization.

Each PE film must be much bigger than the effective aperture size, so we do not run into the issue illustrated in fig. 6.8. Also the edges of the heat-shrunk plastic are not perfectly flat. The mounts also require some modifications. For example, there should be a fixed mount designed so that when the stacks of PE are attached to it $\theta_i \approx 56.5^\circ$. Note that, for PE there is some relaxation in the uncertainty in this angle, i.e., 55° – 57° would work well, with higher angles more desirable.

To utilize the interference effects rising from the assembled 1D photonic crystal, one should use commercial sub-mm metal shims with suitable aperture. Appropriate thickness shims need to be placed between plastic films and then all them should be pressed on to a rigid frame before heat-shrinking.

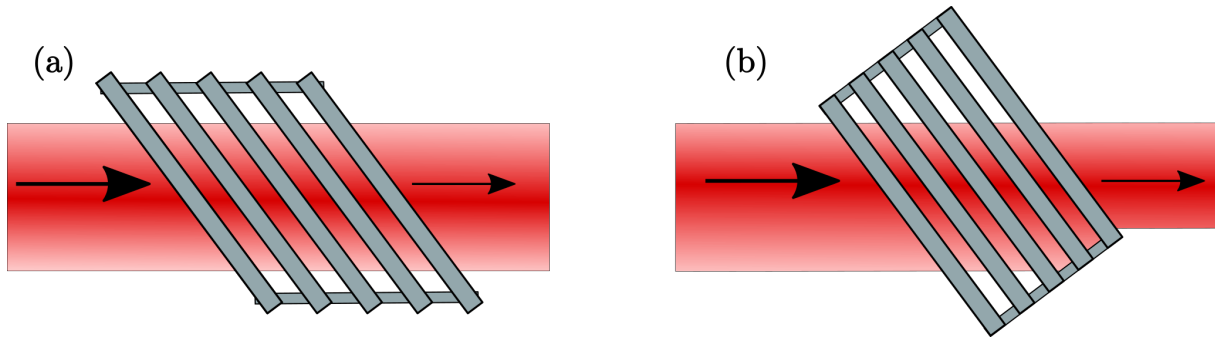


Fig. 6.8: Only showing the transmitted light for two configuration of stacking: (a) Beam passing without alteration of aperture size, difficult for compact assembly. (b) Reduction of effective aperture due to stacking plates exactly on top of each-other, can be compacted easily.

6.6 Calculation on Frequency Domain Response

For our prototype, the PC frame along with double sided tape was around $850 \mu m$ thick. So a stack of $45 \mu m$ films would have a transfer function similar to fig. 6.9. Changing the stack number would only substantially affect the stop bands as illustrated in fig. 6.10. Calculations were performed using [3, 73] as described in chapter 5, where we have assumed a non-dispersive PE with $n = 1.52$, $\kappa = 0.003$, which correspond to $\alpha = 1 \frac{1}{cm}$ at 1 THz. The reported variation in α at 1 THz can be seen from to vary sample to sample from $0.3\text{--}2.2 (\frac{1}{cm})$ [69]. We used $\theta_i = 56.5^\circ$ for calculation instead of exact value of $\arctan(1.52)$.

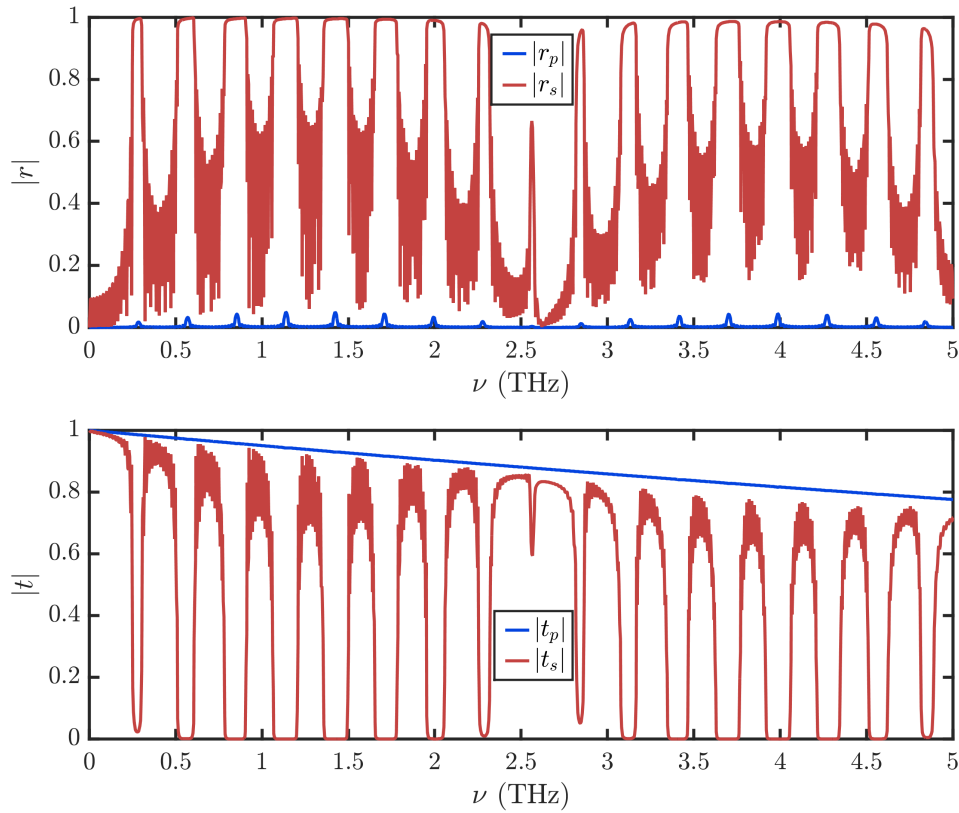


Fig. 6.9: Calculated interference effect due to 15 stacks of PE as constructed for experiment on the reflection and transmission transfer function of the system

For optimized performance, one needs to broaden the stop-bands for s-polarization. We show the calculated transfer functions for both polarizations while varying both the stack number fig. 6.10 and associated thicknesses fig. 6.13.

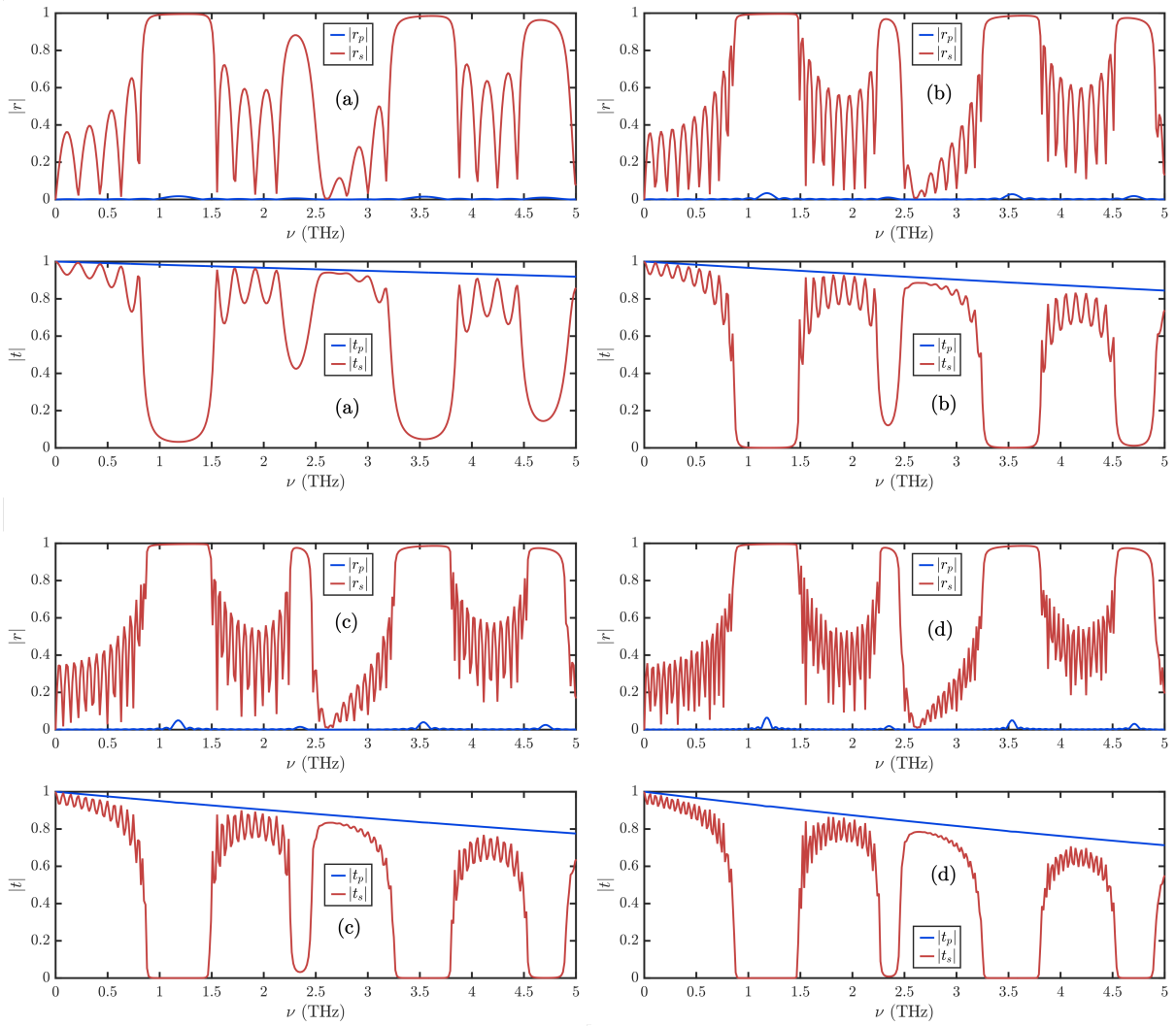


Fig. 6.10: Calculated transfer functions for a system of $45 \mu\text{m}$ thick PE stacks with 5 Mil spacing with stack number (a) 5, (b) 10, (c) 15, (d) 20 at $\theta_i = \theta_B$, where 1 Mil = $25.4 \mu\text{m}$

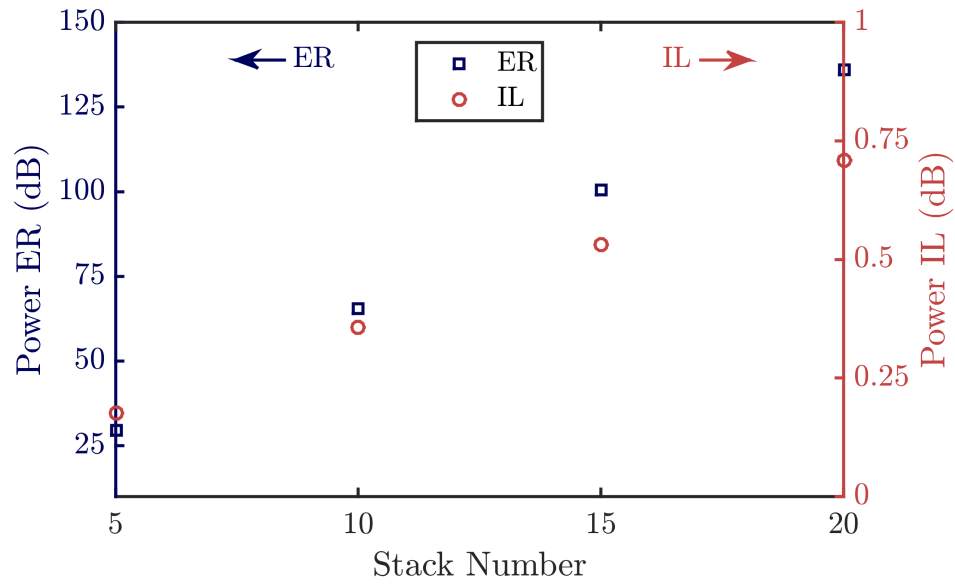


Fig. 6.11: Summary of calculated power extinction ratio, ER, and insertion loss, IL, from fig. 6.10 at $\nu = 1.2$ THz

With the help of inverse Fourier transform we can construct the time-domain signal as a result of the photonic crystal. The calculation was performed using a reference pulse from LiNbO₃ crystal.

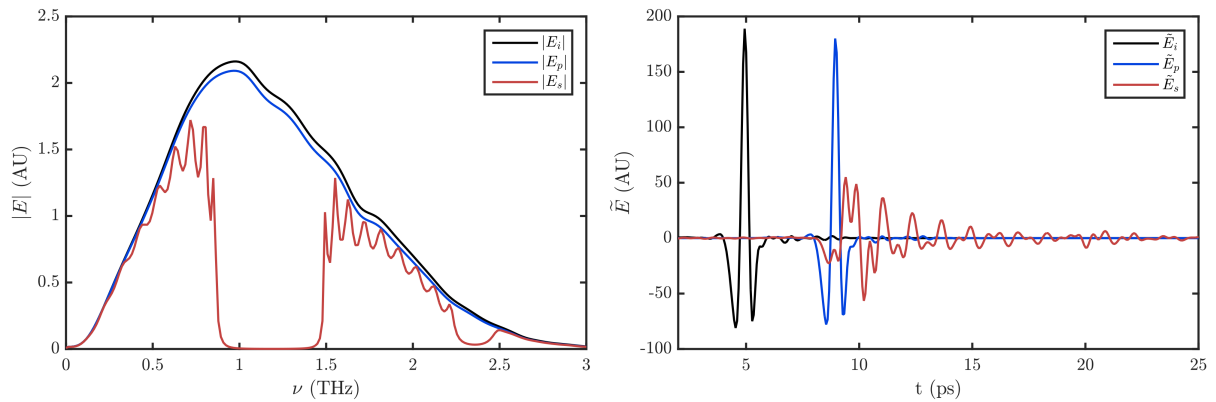


Fig. 6.12: Calculated frequency and time domain response of 10 stack 45 μm PE with 5 Mil spacing

Tuning of the stop bands for DBR are shown for three other regions of interest in figs. 6.13 and 6.14.

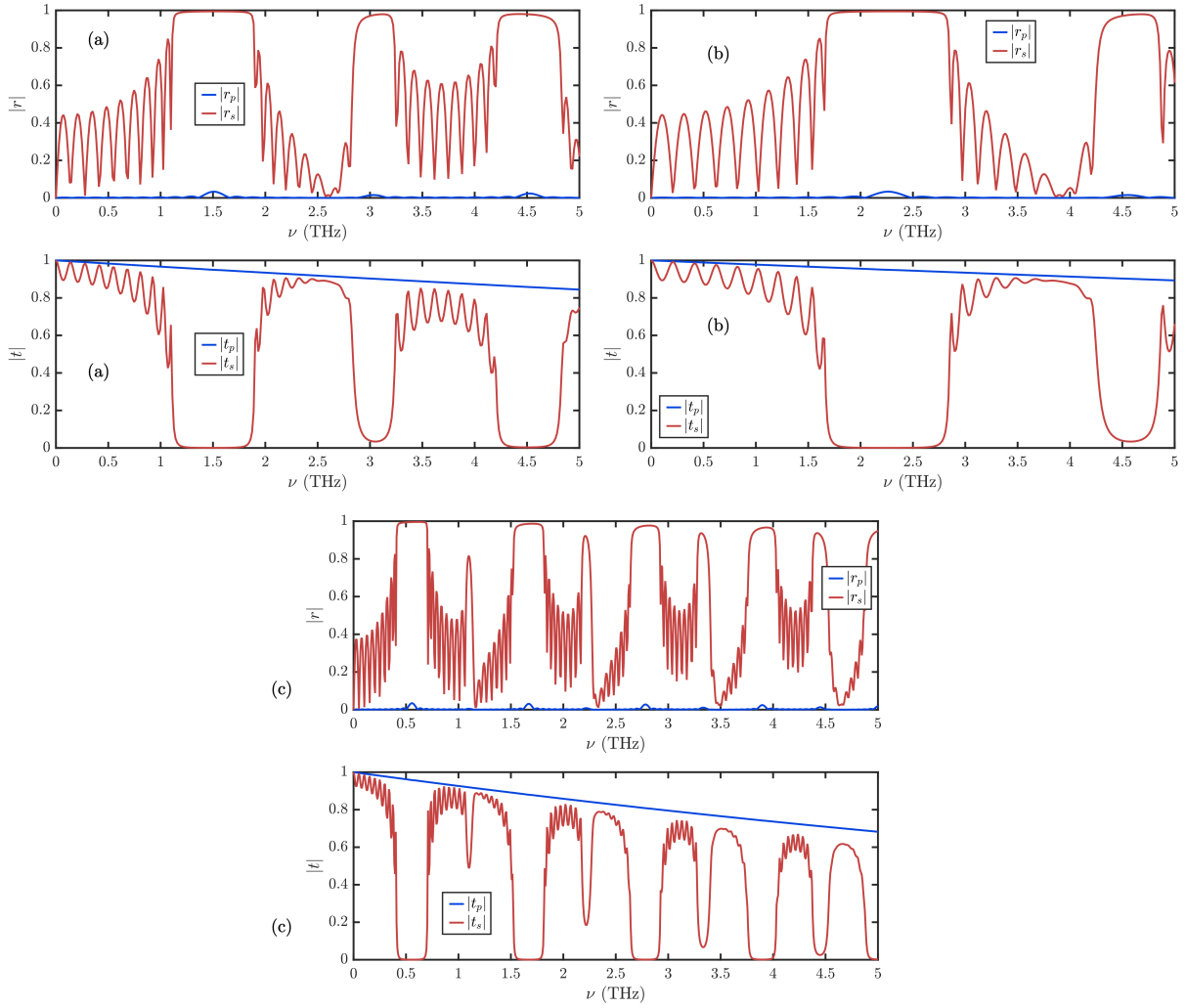


Fig. 6.13: Calculated tuning of transfer function representing 10 stacks of PE film with (a) thickness $45 \mu\text{m}$, spacing 3 Mil, (b) thickness $30 \mu\text{m}$, spacing 2 Mil, (c) thickness 4 Mil, spacing 10 Mil

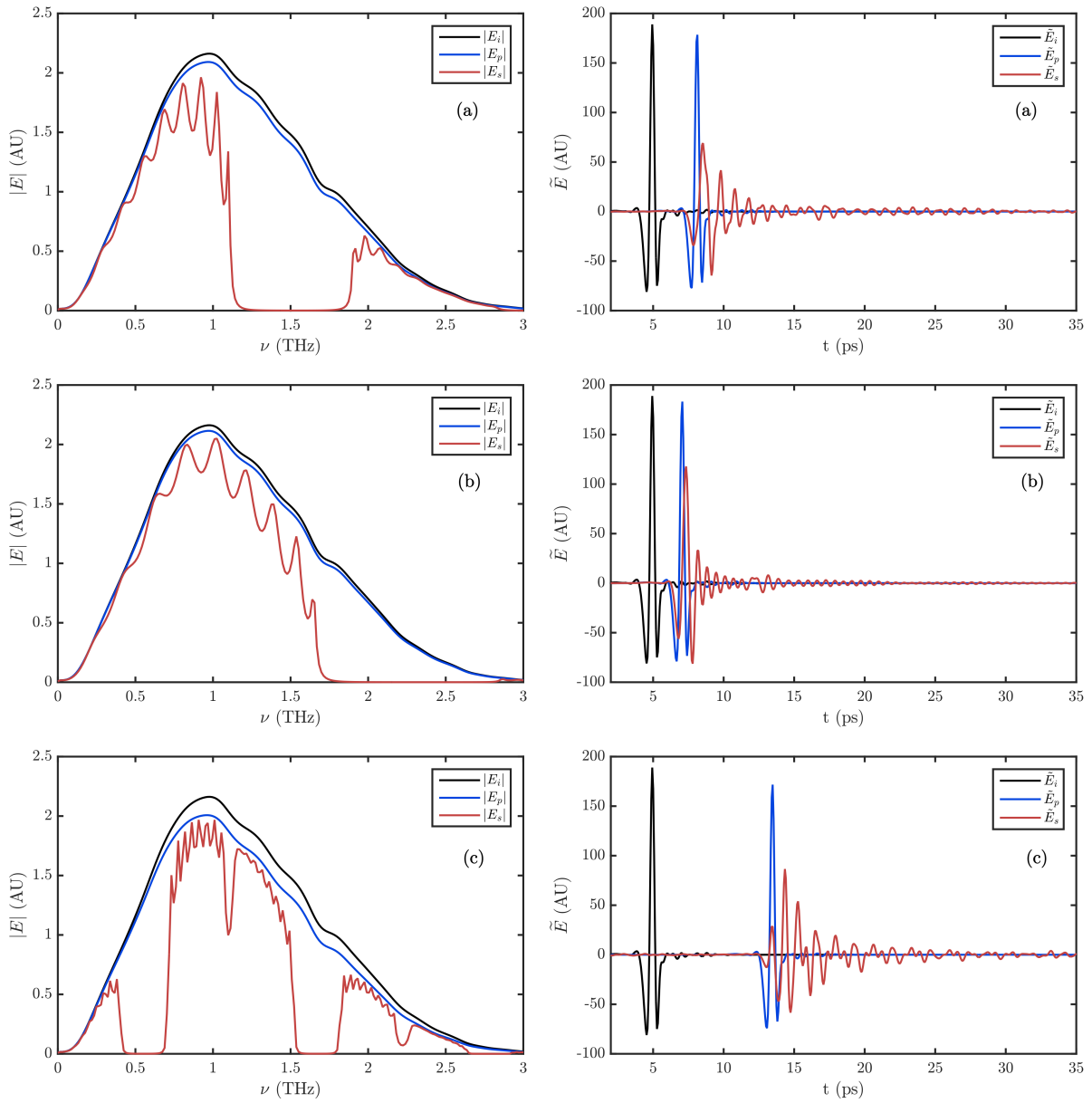


Fig. 6.14: Calculated frequency and time domain response due to tuning of stop band for pile-of-plates as described in fig. 6.13. To reiterate, each device is made of 10 layers of PE film with (a) thickness $45 \mu m$, spacing 3 Mil, (b) thickness $30 \mu m$, spacing 2 Mil, (c) thickness 4 Mil, spacing 10 Mil.

6.7 Discussion & Conclusion

We built a prototype linear polarizer with multilayered PE films and showed that it allows us to identify the plane of polarization of THz light, although not very efficiently. We propose an improved and more compact design for the device which is constructed but could not be tested during this thesis. We showed the frequency and time domain calculations which illustrate that the upgraded polarizer would function as a high performance DBR in certain frequency intervals for s-polarized light while transmit all light for entire relevant THz range. The device would be a very cost-effective solution to polarization sensitive experiments and can be simply constructed with commercial shrink wraps. By modifying the design, we can also construct a narrowband beam splitter with desirable splitting ratio.

Chapter 7

BFO Spectroscopy & Tunable Cavity

7.1 Introduction

Materials that possess both (anti)ferromagnetic and (anti)ferroelectric order are called multiferroics. While materials that have a coupling between their magnetic and electric properties are called magnetoelectric [87]. Materials belonging to both of these classes offer a huge technological advantage by allowing control of their magnetic property by external electric field and vice-versa. Magnetoelectric multiferroics offer a wide range of possibility in realization of next generation devices. They can be exploited for electric and magnetic field sensors, transducers, non-volatile memory devices, voltage controlled phase-shifters used in antenna arrays, electric field controlled magnetic tunnel junctions, etc. [88–90]. From a technical standpoint, switching magnetization with electric field is easier to accomplish than with magnetic field. Usually a high electric current is required to produce a reasonable magnetic field, on the contrary a decent electric field can be produced by applying a moderate voltage across a thin film. This enables miniaturization of voltage controlled magnetic devices with multiferroics.

Bismuth orthoferrite, BiFeO_3 (BFO), is a room temperature magnetoelectric multiferroic. This material is the topic of numerous research papers and has vast potential applications [10–12]. Owing to the electromagnon excitations in sub-THz range, BFO lends itself as a candidate for studying strong THz light-matter coupling. Placing BFO in a high Q cavity, we intend to investigate the coherent coupling of cavity-photons and BFO magnons. Cavity-magnon-polaritons (CMPs) are efficient transducer between spin and

photon systems; they can play an important role in quantum information technology, spintronics, coherent perfect absorption, etc. [91–98], see section 7.2. In the THz range, using THz-TDS in recent years, cavity polaritons with (meta)material excitations have been observed [17, 99, 100]. Investigation in THz-CMP is still a novel field during this research project. In order to detect THz CMP in BFO, we analyze the properties of BFO and examine the controllability of its resonance frequencies. In addition, we explore the design aspects of a tunable THz cavity optimized for BFO magnons. Utilizing the findings and tools developed in this chapter, discovery of CMP in BFO would be the subject of a future project.

7.2 Strong Light-Matter Coupling

Based on the coupling strength between material excitations and photons and their decay rates, there can be different regimes of light-matter coupling. In an optical cavity, if the rate of energy transfer between photons and excitations is greater than the dissipation rates of individual sub-systems, the strong coupling regime can be reached where coherent, reversible energy exchange between the sub-systems take place. At that point, cavity photons and excitations can not be considered as separate particles, rather they give rise to a hybrid polaritonic system that possesses the properties of both constituents. Strong coupling can alter material properties like chemical reaction rates, electrical conductivity, optical and energy transfer properties, etc. and is of great interest in basic science [16, 15]. The Polariton that forms due to coupling of cavity-photon and magnon is called cavity-magnon-polariton (CMP).

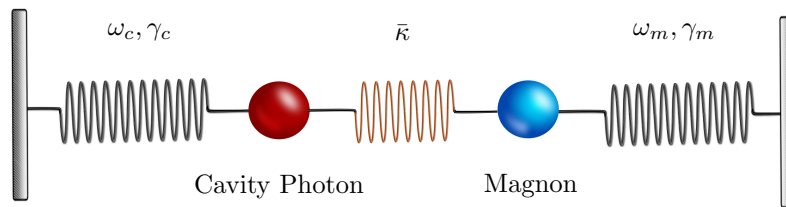


Fig. 7.1: Two harmonic oscillators coupled together by spring of coupling strength $\bar{\kappa}$

Formation of CMP can be explained by both classical and quantum mechanical framework. Although formally studied under cavity quantum electrodynamics, we can illustrate the important features of the polariton modes using two coupled classical harmonic oscillators [101, 102]. The following derivation is adapted from [103] and can be applied to any

material excitation other than magnon. As illustrated in fig. 7.1, we assume cavity photon and magnon are each harmonic oscillators of unit mass with characteristic frequency ω_c, ω_m and damping factor γ_c, γ_m , respectively. These oscillators are connected via a spring of coupling strength $\bar{\kappa}$, where the bar is used to distinguish the quantity from extinction coefficient, κ . For simplicity we will assume that the cavity mode ω_c is fixed while magnon resonance ω_m may be varied. Furthermore, the quantities $\gamma_c, \gamma_m, \bar{\kappa}$ are made dimensionless by normalizing by ω_c . The equation of motion for the coupled system where the cavity is driven by a harmonic force, $F(t) = fe^{-i\omega t}$ is given below:

$$\begin{aligned} \ddot{x}_1 + \omega_c^2 x_1 + 2\gamma_c \omega_c \dot{x}_1 - \bar{\kappa}^2 \omega_c^2 x_2 &= F(t) \\ \ddot{x}_2 + \omega_m^2 x_2 + 2\gamma_m \omega_c \dot{x}_2 - \bar{\kappa}^2 \omega_c^2 x_1 &= 0 \end{aligned} \quad (7.1)$$

The normal modes of the coupled system can be calculated by solving relevant eigenvalue problem, which has a non-trivial solution when $\det(\mathbf{\Omega}) = 0$. From the following matrix we see that the eigenmodes are independent of the driving force.

$$\mathbf{\Omega} = \begin{pmatrix} \omega^2 - \omega_c^2 + 2i\gamma_c \omega_c \omega & \bar{\kappa}^2 \omega_c^2 \\ \bar{\kappa}^2 \omega_c^2 & \omega^2 - \omega_m^2 + 2i\gamma_m \omega_c \omega \end{pmatrix} \quad (7.2)$$

Near the matching frequency, $\omega_m = \omega_c$, the dispersion relations that solve $\det(\mathbf{\Omega}) = 0$ can be simplified by defining complex angular frequencies, $\tilde{\omega}_c = \omega_c - i\gamma_c \omega_c$ and $\tilde{\omega}_m = \omega_m - i\gamma_m \omega_c$, that help derive eq. (7.3) [103]. The real and imaginary parts of $\tilde{\omega}_{\pm}$ represent, respectively, the frequency dispersion and line-width of upper (ω_+) and lower (ω_-) polariton branches. We define a detuning factor, $\Delta = \omega_c - \omega_m$, which is used to illustrate the behavior of $\tilde{\omega}_{\pm}$ near $\Delta = 0$, fig. 7.2. Due to coupling, a gap opens between the hybrid modes, fig. 7.2 (a), which is a signature of strong light-matter interaction. This phenomenon is variously termed as anticrossing, avoided crossing, level repulsion. We define Rabi gap, $\Omega_R = \omega_+ - \omega_-$ at $\Delta = 0$. For the condition $|\gamma_c - \gamma_m| \ll \bar{\kappa}^2$, it can be shown $\Omega_R = \bar{\kappa}^2 \omega_c$, a relation that underscores the role of $\bar{\kappa}$ in experimental observation of distinct polariton branches.

$$\tilde{\omega}_{\pm} = \frac{1}{2} \left[\tilde{\omega}_m + \tilde{\omega}_c \pm \sqrt{(\tilde{\omega}_m - \tilde{\omega}_c)^2 + \bar{\kappa}^4 \omega_c^2} \right] \quad (7.3)$$

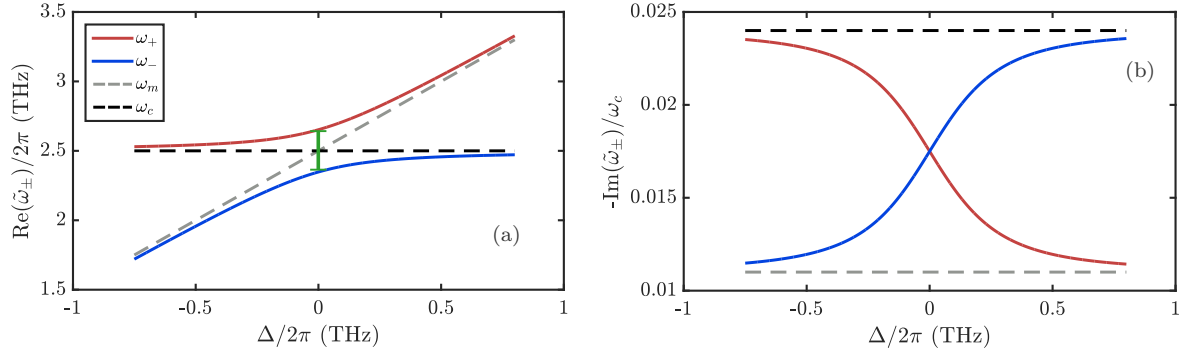


Fig. 7.2: Assuming $\omega_c/2\pi = 2.5$ THz, we vary the magnon mode so that both resonances may coincide. Calculation was performed using eq. (7.3) with parameters, $\bar{\kappa} = 0.35$, $\gamma_m = 0.011$, $\gamma_c = 0.024$. Polariton modes are represented by solid lines, while uncoupled photon, magnon modes are depicted using dashed lines. (a) Anticrossing polariton branches can be observed. Ω_R is shown with green line. (b) Evolution of mode line width with Δ . Line widths are bound by uncoupled line widths γ_c, γ_m and cross at $\Delta = 0$.

In the quantum mechanical description of strong coupling between N coupled oscillators and smaller number of photons in a cavity of mode volume V , the Rabi splitting follows the relation 7.4 [16, 103]. Since magnons are collective oscillation of spins, by controlling the sample filling factor (V_{smp}/V), we may verify the splitting behavior. Here sample volume, V_{smp} , is related to number of spins, $N \propto V_{\text{smp}}$. Additionally, it is useful to define a dimensionless parameter, cooperativity, $C = g^2/\gamma_m\gamma_c$ where g defines the coupling strength and satisfies $g = \Omega_R/2\omega_c$. If the coupled system satisfies $C > 1$, it is in the strong coupling regime, but if $C < 1$ it is said to be in the weak coupling regime.

$$\Omega_R \propto \sqrt{\frac{N}{V}} \propto \sqrt{\frac{V_{\text{smp}}}{V}} \quad (7.4)$$

We, therefore, need to satisfy the following prerequisites for observing CMP in BFO:

- Investigate BFO magnon resonance tuning
- Investigate cavity construction and resonance tuning
- Find conditions that would lower losses in both systems, since $C \propto 1/\gamma_m\gamma_c$

7.3 BFO

7.3.1 Basic Properteis

BiFeO₃ or BFO has relatively high Curie and Neel temperature $T_C \sim 1100$ K, $T_N \sim 640$ K, respectively, above which the ferroelectric and antiferromagnetic properties vanish [14]. Its distorted perovskite structure gives rise to the large spontaneous electric polarization along $\langle 111 \rangle$ directions of magnitude $\sim 100 \mu\text{C}/\text{cm}^2$ [14, 104]. It is a G-type antiferromagnet and has spins aligned ferromagnetically in (111) planes while spins between adjacent (111) planes are antiferromagnetically aligned [105]. The presence of Dzyaloshinskii-Moriya interaction between neighboring spins causes spin canting and a relatively long range (~ 62 nm) spiral spin structure, called spin cycloid [106, 107].

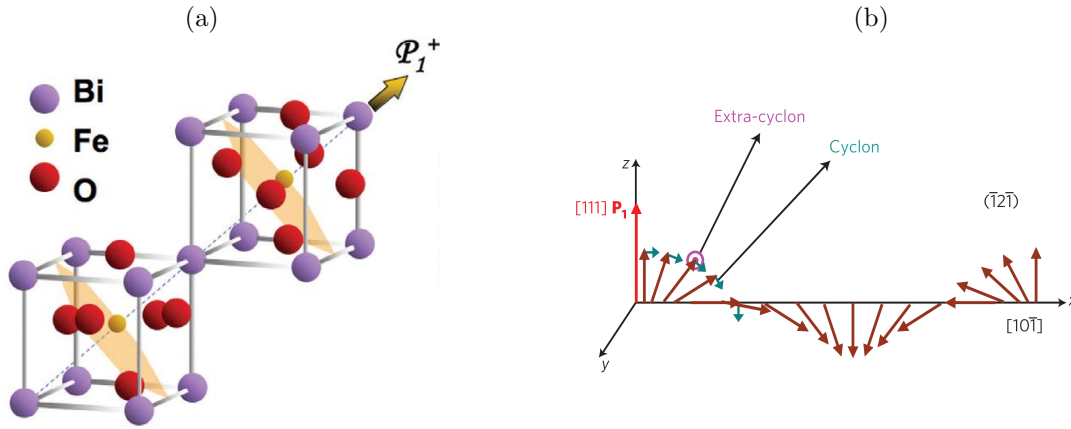


Fig. 7.3: (a) Crystal structure with ferroelectric polarization along $\langle 111 \rangle$ shown by the arrow and (111) planes containing spins are shaded, reprinted from [105] with permission from Elsevier, (b) Spin Cycloid structure, reprinted from [108] with permission from Nature Materials

The $(\bar{1}2\bar{1})$ plane contains the spin-cycloid which propagate along $[10\bar{1}]$ [14]. The cycloidal structure can have two types of oscillations: parallel and perpendicular to the cycloidal plane, as verified by inelastic Raman scattering in [14] and called Cyclon, extra Cyclon modes. Notationally, according to [106, 109], the in and out of plane modes of the structure are labeled as Φ , Ψ . The spin cycloid resonance (SCR) modes appear as a result of the coupling between the magnons and optical phonons inside the crystal [104] and can be excited by the electric field of incident light which happens to fall in the far-infrared range, so they are termed as electromagnons. The lowest transverse optical phonon mode is located ~ 2 THz [110]. Due to the presence of an electric dipole moment, the electromagnons are not pure spin waves [111].

7.3.2 THz spectroscopy on BFO

We received a polycrystalline BFO sample which was cut to a thickness of 1.58 ± 0.07 mm. The sample is substantially lossy in the THz range as can be seen in the time and frequency domain measurements in figs. 7.4 and 7.5. THz-TDS performed on BFO single crystal has been reported in [13] by reducing temperature from 400 K to 10 K. Following measurements were performed in room temperature in N_2 purged environment.

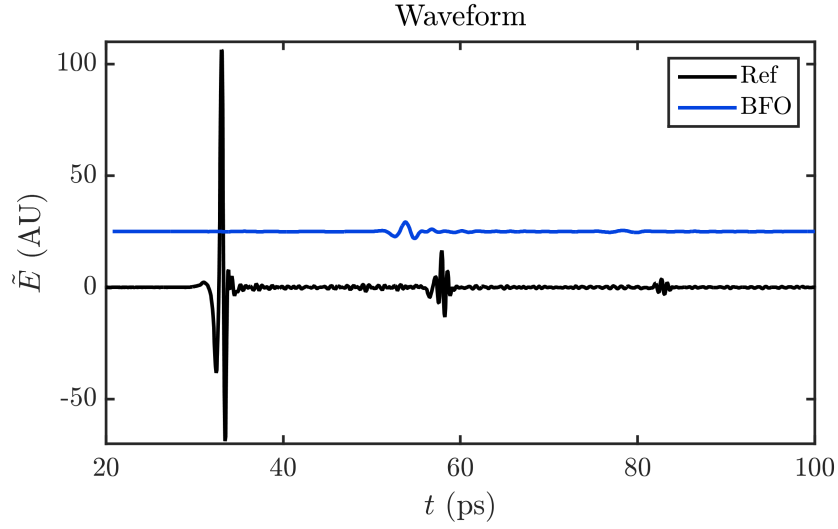


Fig. 7.4: Waveforms are offset along y axis for clarity.

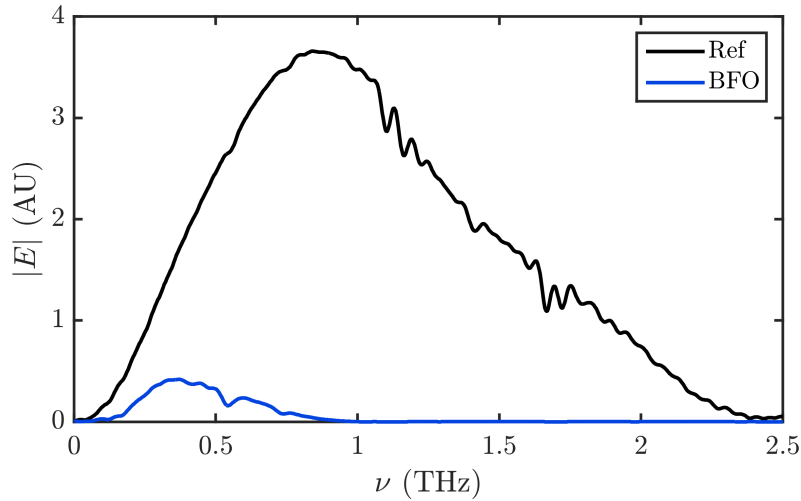


Fig. 7.5: Spectra from time trace before detector reflection to avoid oscillations. Dips after 1 THz are due to weak water vapor absorptions present even after N_2 purging.

Observing the transmitted spectra from 20 ps long scan we can see clear resonances at

0.54, 0.73 THz. Additionally, there are features at 0.35, 0.41, 0.47 THz. By the virtue of AR coating on the detector EO crystal, which significantly reduces the FP oscillations arising from the detector crystal, we could resolve the closely spaced SCR modes at around 0.5 THz by performing 200 ps scan after the pulse-peak. According to [106, 109] these modes are labeled as $\Psi_1^{(2)}$, $\Psi_1^{(1)}$, Φ_2 and our measurement locates them at 0.53, 0.56, 0.73 THz respectively, see fig. 7.6. In this chapter, sub-THz BFO excitation is variously called magnon, SCR, electromagnon emphasizing respectively that the magnon mode is a collective spin precession, related to the spin cycloidal magnetic ordering of BFO, and that the magnon is coupled to the electric order of BFO due to its magnetoelectric multiferroic nature.

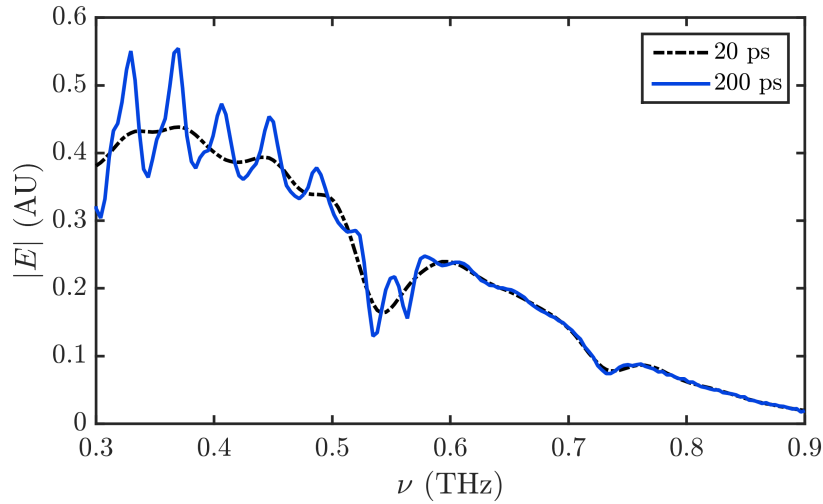


Fig. 7.6: Low and high resolution spectroscopy. Time in legend indicates the time length after the 1st peak in time domain. 200 ps trace contains many detector reflection which are highly reduced in the region around 0.7 THz due to the AR coating on GaP.

The index of the polycrystalline sample, $n \sim 5$ with high extinction coefficient, can be seen in figs. 7.7 and 7.8, which was analyzed using techniques developed in [47] using data collected in this project. In addition to the material absorption, the high index is responsible for transmission loss at the air-sample interfaces. Since the sample is a pressed pellet, there are scattering losses which we have been ignored [42, 112]. The index of the polycrystalline sample is in agreement with [107], where they also show the huge birefringence present in crystalline BFO. The loss in BFO may present a challenge in observing the CMP.

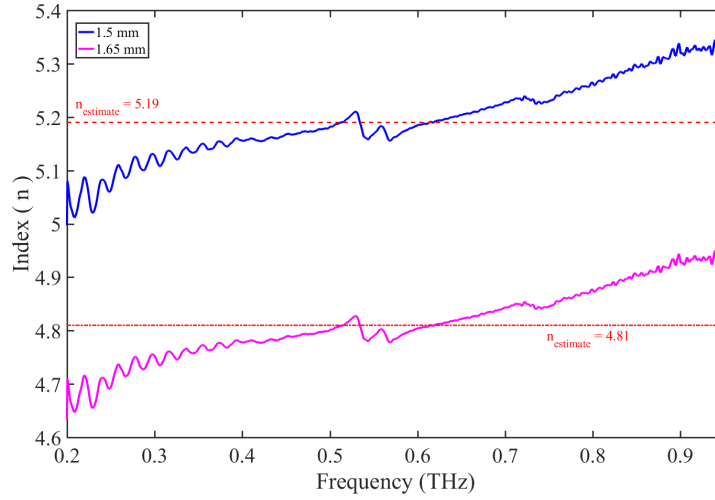


Fig. 7.7: BFO index estimated for two extreme sample thicknesses using etalon reduction technique, from [47] with permission

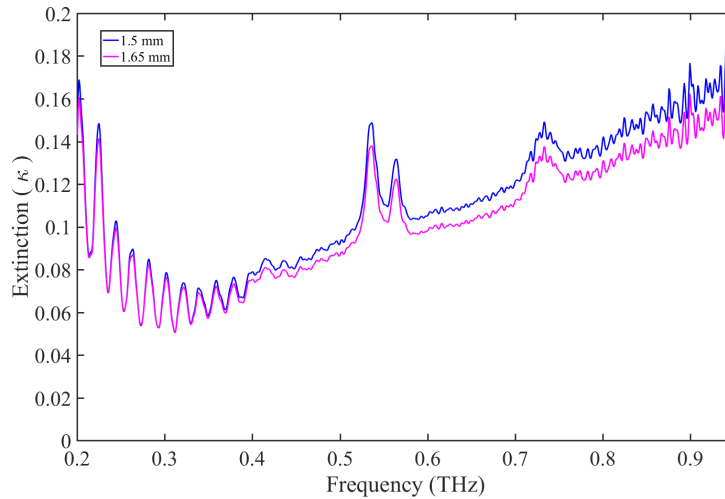


Fig. 7.8: BFO extinction estimated for two extreme sample thicknesses using etalon reduction technique, from [47] with permission

7.3.3 Electric Field Tuning

The SCR modes in single crystal BFO thin film were reported to be tuned via an external electric field in [108] verified by Raman scattering. We applied external DC electric field on our polycrystalline sample from a high-voltage (HV) power-supply. Appropriate dielectric mount was built for this measurement, see fig. 7.9. We went up to 12.5 kV potential difference between a gap ~ 5 mm, where the sample was placed which results in an electric

field ~ 25 kV/cm. Estimating from the result from [108], we expected the magnons to move by ~ 40 GHz. Unfortunately we did not see any change in the response of our sample.

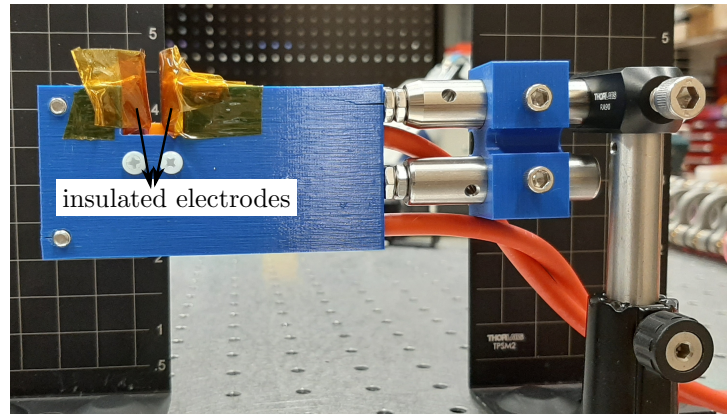


Fig. 7.9: Polyimide (kapton) tape used to insulate HV electrodes to prevent breakdown. Sample is placed between the electrodes.

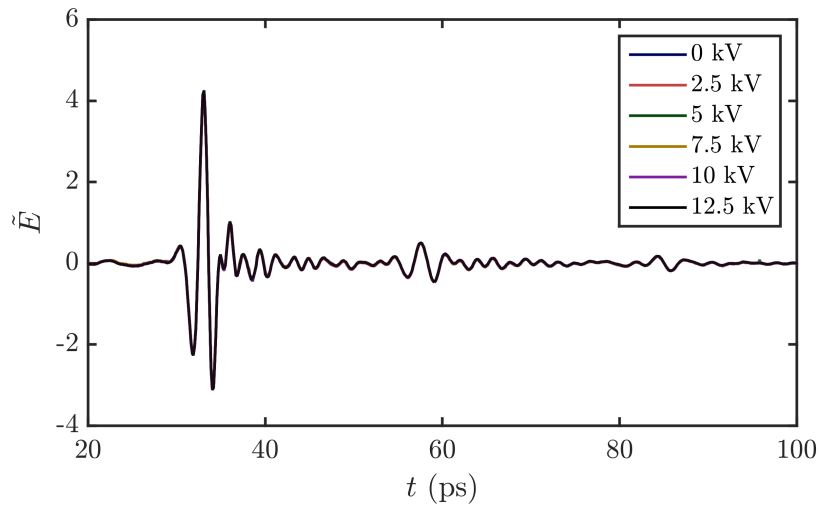


Fig. 7.10: Time traces were taken up to 200 ps after the peak. No meaningful change in waveform could be observed.

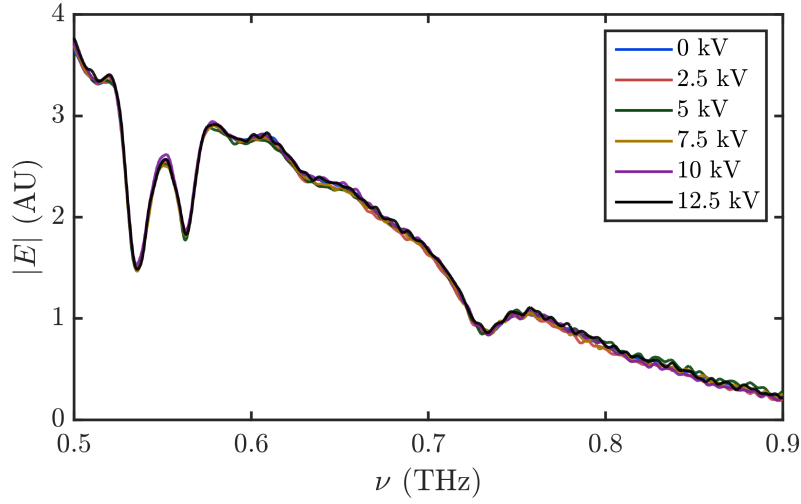


Fig. 7.11: Transmitted spectrum

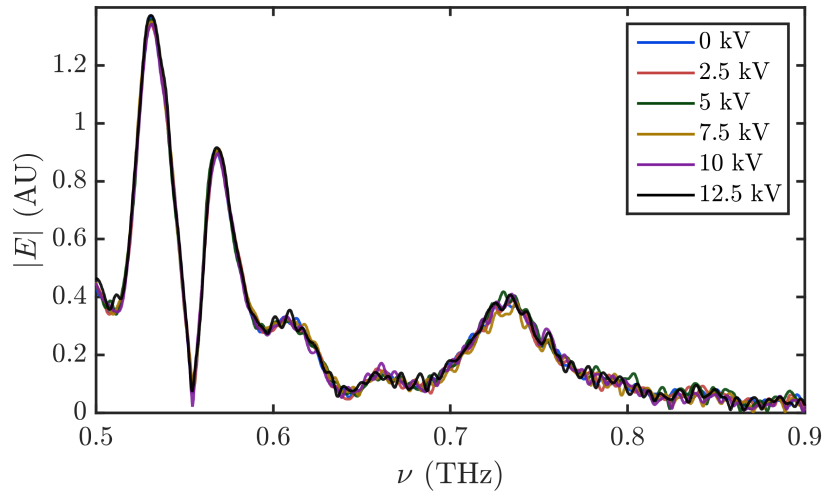


Fig. 7.12: Spectrum of the free induction decay (FID) which correspond to the emission of the magnon modes. FWHM of the FID peaks at the modes $\nu \approx 0.53, 0.56, 0.73$ THz are $\Delta\nu \approx 26, 23, 60$ GHz respectively.

The absence of electric field tuning suggests that the BFO sample was not poled, or its poling was destroyed by arcing from the HV electrodes which occurred a few times. Thus controlling resonance frequency by electric field could not be utilized for the study of light-matter coupling. However, BFO can be poled by applying high DC electric fields (~ 100 kV/cm) across it [113].

7.3.4 Temperature Tuning

In the literature we find many reports of tuning the SCR modes by varying temperature of BFO sample [13, 109, 111]. The reports suggest that reducing temperature reduces absorptions in BFO and significantly helps in electromagnon detection. Unfortunately we did not have any equipment for precise temperature control at the time, so we resorted to changing the BFO temperature by optical heating via laser diodes. We varied the diode laser power by limiting the current responsible for lasing, which provided a coarse method of changing the sample temperature.

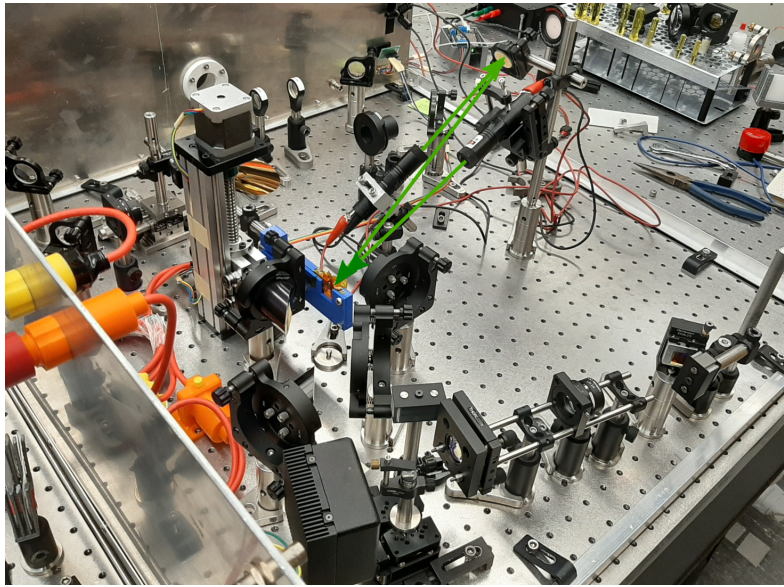


Fig. 7.13: Two green laser pointers were used to optically heat the BFO sample. The laser diodes were connected in parallel to an external current limiting power supply for controlled lasing.

Long time-domain traces of 220 ps after main peak were measured and analyzed. Due to optical heating we can observe the increase in index and absorption directly from time-domain, fig. 7.14. We also show the temperature tuning of the magnons around 0.5 THz in fig. 7.16, where the temperature increases with higher laser current. Using curve fitting based on [106], [47] estimates the temperature of BFO sample from 300–345 K.

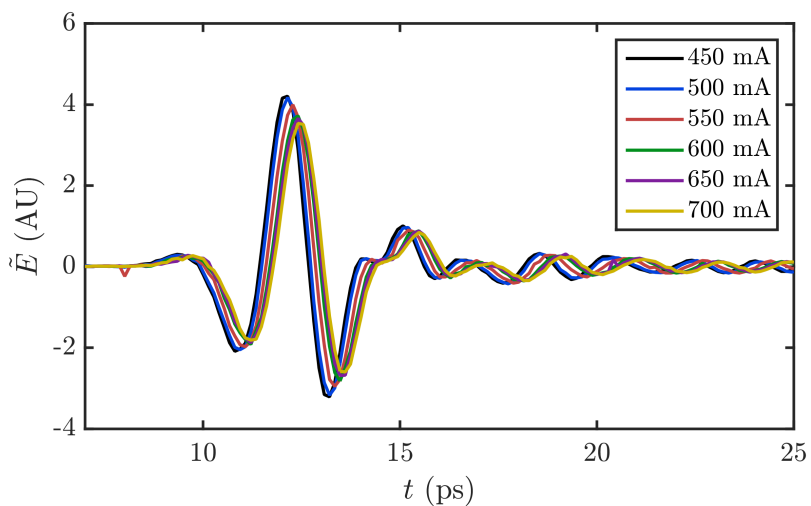


Fig. 7.14: Legend indicates total current supplied to two laser diodes in parallel. Higher current implies higher sample temperature.

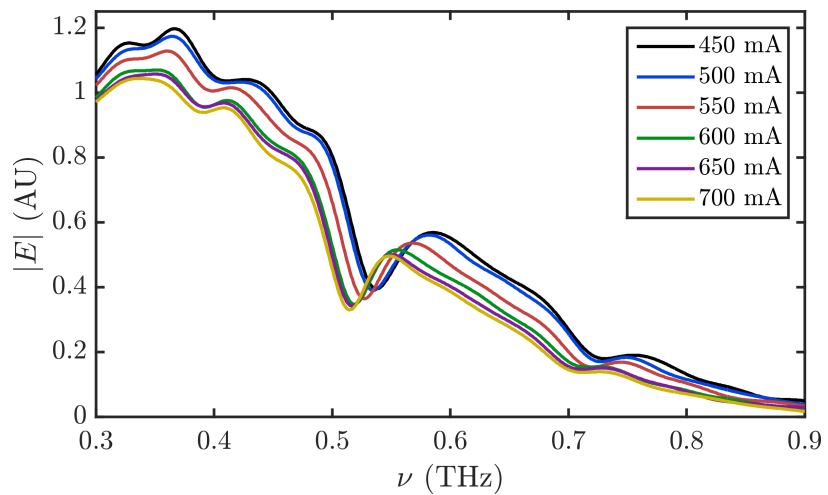


Fig. 7.15: Spectra using time-trace before echo from detector crystal appears. Increasing temperature is resulting in an increase in transmission loss and decrease in magnon frequency.

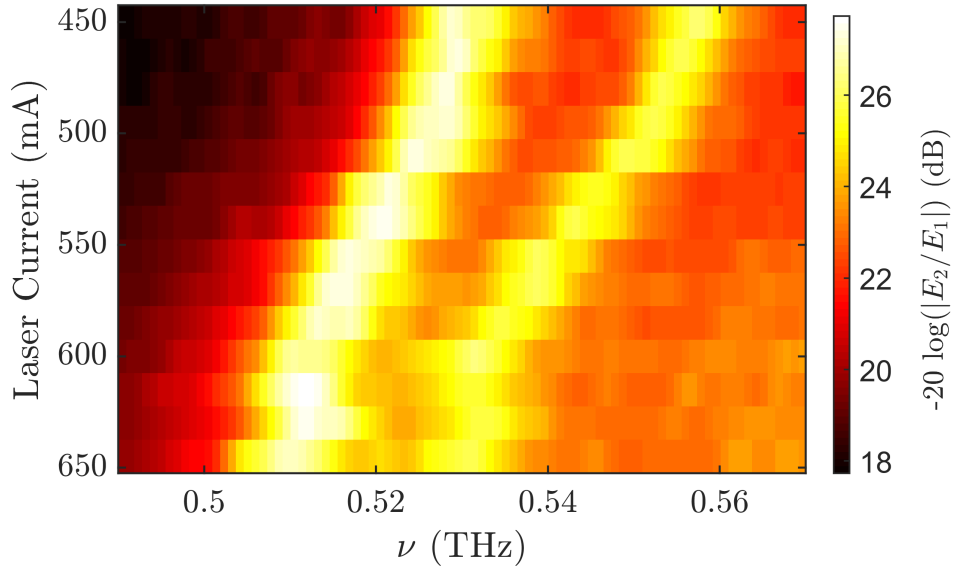


Fig. 7.16: Ψ_1 modes tuned by changing diode laser current that induce optical heating in the sample. Frequency shift of 25–30 GHz is observed.

Due to the relatively high sample index ~ 5 , the rectangular slab of BFO can be assumed to operate as a low Q , Fabry-Pérot (FP) etalon cavity. A study of the coupling between the temperature controlled electromagnon modes and etalon cavity modes from this sample can be found in [47], where CMP could not be identified. As indicative of our finding and literature reports, [13, 109, 111], we see that to lower BFO losses, we require to decrease sample temperature.

Therefore, to conduct further studies in room temperature, we are led to the construction of a high Q THz resonator that would enable detection of strong cavity photon-magnon coupling. In the following sections we will explore planar FP cavity, emphasizing on the calculation side of the device.

7.4 Fabry-Pérot Resonator

High Q resonators are commonly used in microwave and optical frequencies, but not so frequently exploited in the sub-mm wavelengths. A requisite for the cavity is a low loss mirror which has a high reflectance but low transmission. It is difficult to make a metallic mirror that would transmit THz light due to the Drude absorptions, which require depositing very thin metal layer on the order of few nanometers [100, 114]. Alternatively,

one can use layered dielectrics to make mirrors with variable reflection coefficients, called distributed Bragg reflector (DBR). We present calculations for the design of a high Q scanning FP cavity with DBRs and their response in both frequency and time domain.

7.4.1 Basic Principle

The simplest type of interferometer can be built by placing two parallel mirrors with high reflectivity at some adjustable spatial separation.

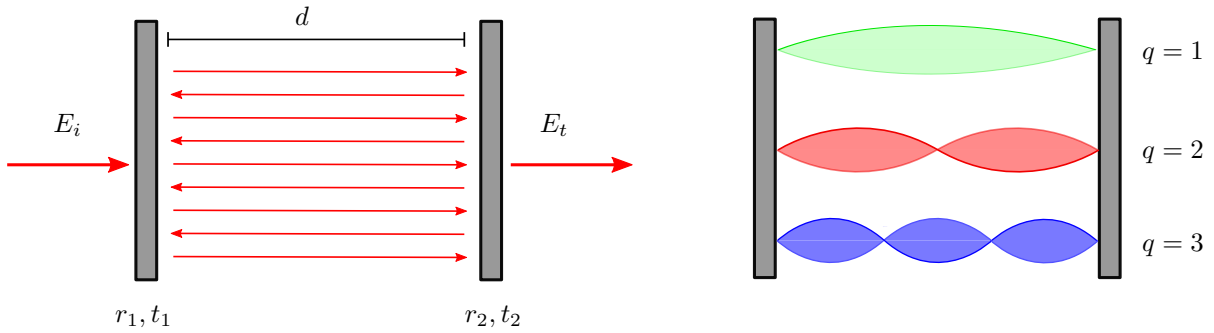


Fig. 7.17: Reflection and transmission coefficients shown for the mirror surface close to the cavity. The other surface is assumed to have no Fresnel loss.

We define round-trip time $t_r = \frac{2nd}{c}$. Since there can be phase change due to reflection, particularly in metallic reflectors, we have $r_1 r_2 = |r_1 r_2| \exp(i\phi_r)$. We additionally define the following, round-trip attenuation factor r_L and phase-factor due to a single round-trip ϕ :

$$\begin{aligned} r_L &= |r_1 r_2| \exp(-\alpha d) \\ \phi &= 2\pi\nu t_r - \phi_r \end{aligned} \tag{7.5}$$

The field at a point right after the first mirror inside the cavity, $E_{cav}(\nu)$, can be written in terms of the incident plane wave field on the first mirror $E_i(\nu)$, eq. (7.6). Inside the cavity, there are two waves going in opposite directions, both of which will interfere to produce the final spatio-temporal field distribution which would result in a standing wave with nodes and anti-nodes. In eq. (7.6), we consider only circulating waves traveling in

one direction.

$$\begin{aligned}
 E_{cav} &= E_i t_1 \sum_{m=0}^{\infty} (r_L \exp(-i\phi))^m \\
 &= \frac{1}{1 - r_L \exp(-i\phi)}
 \end{aligned} \tag{7.6}$$

After each round-trip only waves that add in phase, $\phi = 2m\pi, m \in \mathbb{Z}$ will grow, while others will decay. As a result, we have modes, called the resonance modes of a cavity, that satisfy, $\nu_q = q\nu_{fsr}, q \in \mathbb{N}$. As $r_L \rightarrow 1, E_{cav} \rightarrow \infty$, thus a huge enhancement of the field is possible in the cavity. Additionally, the points of peak electric field, i.e., the anti-nodes will oscillate at the resonance frequency ν_q , while the nodes will have zero intensity. The free spectral range of a cavity ν_{fsr} is the spacing between two adjacent modes of a cavity. Since for most low-loss mirrors in normal incidence $\phi_r \approx 2\pi$ we could define ν_{fsr} as eq. (7.7). By changing the length of the cavity we can change ν_{fsr} and thus the mode frequencies. This is the basic principle of scanning Fabry-Pérot interferometer.

$$\nu_{fsr} = \nu_{q+1} - \nu_q = \frac{1}{t_r} = \frac{c}{2nd} \tag{7.7}$$

The intensity of the circulating field inside the cavity is given by eq. (7.9), where the maximum intensity, $I_{max} = \frac{I_i |t_1|^2}{(1+r_L)^2}$. We define finesse of the cavity system, \mathcal{F} , entirely in terms of the absolute value of the round-trip attenuation factor, eq. (7.8). \mathcal{F} is a number which provides a measure of the sharpness of the resonance modes and one desires to construct a cavity with high \mathcal{F} , which correspond to a high Q cavity, see fig. 7.19 and eqs. (7.10) and (7.15).

$$\mathcal{F} = \frac{\pi \sqrt{r_L}}{1 - r_L} \tag{7.8}$$

$$I_{cav} = |E_{cav}|^2 = \frac{I_{max}}{1 + (2\mathcal{F}/\pi)^2 \sin^2(\pi\nu/\nu_{fsr})} \tag{7.9}$$

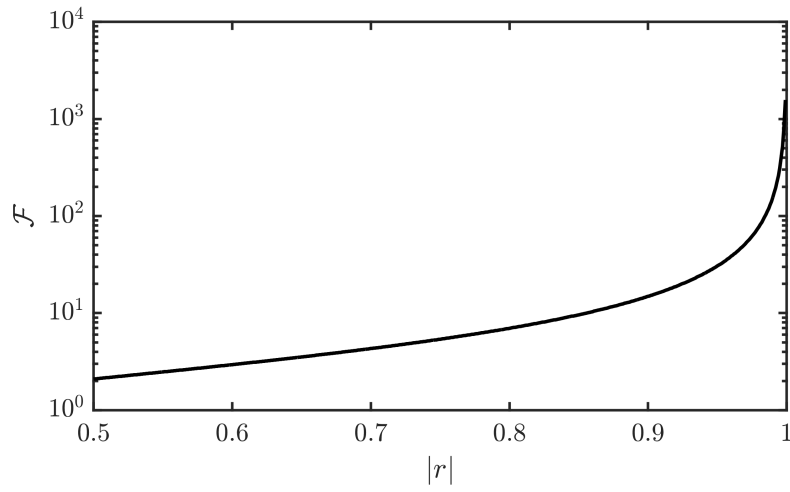


Fig. 7.18: Finesse for an empty cavity made of mirrors with identical reflection coefficients, r

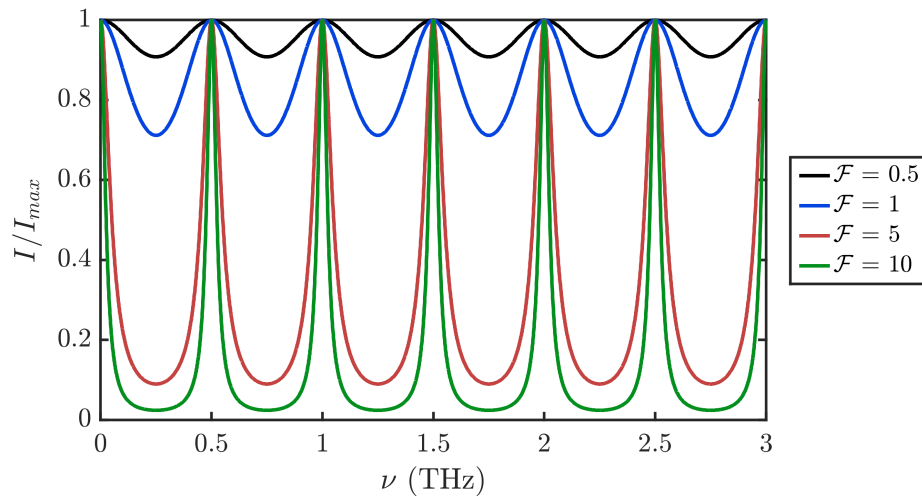


Fig. 7.19: For a cavity with $d = 300\mu\text{m}$, varying \mathcal{F}

For $\mathcal{F} \gg 1$, it can be shown that the FWHM of the resonance peaks satisfy [23]:

$$\Delta\nu \approx \frac{\nu_{fsr}}{\mathcal{F}} \quad (7.10)$$

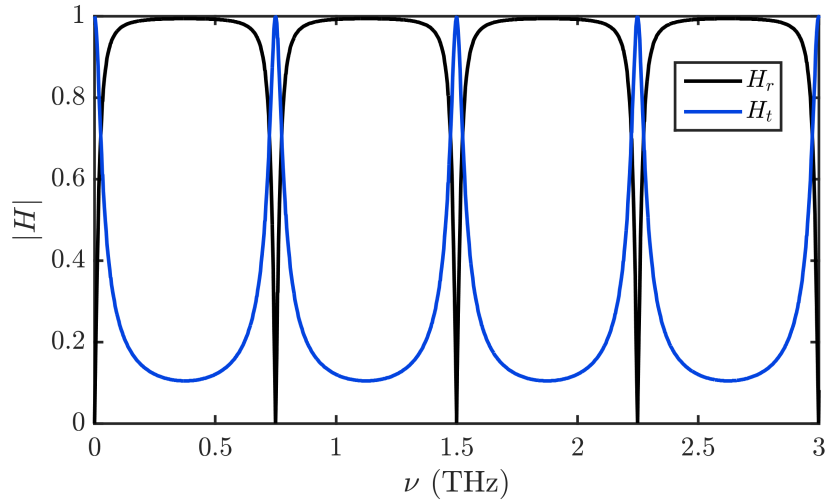


Fig. 7.20: Magnitude of amplitude transfer functions for reflected and transmitted light for a typical high- \mathcal{F} cavity

7.4.2 Loss and Photon Lifetime

From eq. (7.5), we could define total cavity round-trip power attenuation factor per unit length α_{cav} as:

$$r_L^2 = R_1 R_2 \exp(-2\alpha d) = \exp(-\alpha_{cav}(2d)) \quad (7.11)$$

Which can be written as:

$$\alpha_{cav} = \frac{1}{2d} \ln \left(\frac{1}{R_1 R_2} \right) + \alpha \quad (7.12)$$

We define photon lifetime, τ , as power attenuation per unit time. Therefore, resonance FWHM, $\Delta\nu$ can also be represented by τ [23]:

$$\tau = \frac{1}{c\alpha_{cav}}, \quad \Delta\nu \approx \frac{1}{2\pi\tau} \quad (7.13)$$

To quantify the performance of a resonant cavity, there is another parameter called the quality factor, Q , which describes the photon storage capability of a particular cavity. It is desirable to have a high Q cavity corresponding to long photon lifetime. Q is defined

for a particular frequency as follows:

$$Q = 2\pi \frac{\text{energy stored}}{\text{energy lost per period of oscillation}} \quad (7.14)$$

We can write the following relationship between Q and other parameters defined earlier, from [23]:

$$Q(\nu_0) = 2\pi\nu_0\tau \approx \frac{\nu_0}{\Delta\nu} \approx \frac{\nu_0}{\nu_{fsr}} \mathcal{F} \quad (7.15)$$

As a consequence of eq. (7.15), we can see that longer cavity length and thus a shorter ν_{fsr} would correspond to higher Q . In time-domain this would mean that the electric field will decay like $\exp(-\frac{t}{2\tau})$. As a result one is required to scan time domain signal for a significantly long time, which is challenging for standard THz-TDS set-up. We can also conclude that lowering cavity loss is equivalent to increasing the Q value, which helps enhance magnon-photon coupling, since cooperativity, $C \propto 1/\Delta\nu \propto Q$.

7.4.3 Angle Tuning Fabry-Pérot Modes

The simple planar scanning cavity described above is called conditionally stable, meaning it is very prone to misalignment, even if the mirror diameters are infinite. For a finite mirror diameter, the effect of misalignment increases with the mirror spacing, d . Thus it is worth while to examine a cavity with fixed spacing, where d is considerably small. Small d ensures tighter light confinement, i.e., smaller mode volume, which increases Ω_R , see eq. (7.4). Moreover as $\nu_{fsr} \propto 1/d$, we can increase the spacing between resonance modes by lowering d , this would help better resolve the CMP modes. Now it is also possible to tune the cavity modes by varying the incidence angle.

We consider an FP cavity of infinite mirror diameter operating in off-axis mode. By changing the angle of incidence to a non-zero value, for plane waves, the round-trip phase factor becomes $\phi(\theta) = 2\pi\nu t_r \cos(\theta)$ [23]. Consequently, keeping d constant, we can increase the mode frequency by increasing the angle of incidence as in eq. (7.16). Since in actual experiments, we work with finite sized mirrors, it is obvious that light will escape the cavity after many round trips, which may be modeled by appropriate ray tracing. This would result in lowering the Q of cavity modes with increase in incidence angle. Nevertheless,

this technique has been exploited in discovering cavity-polaritons [115, 116] and can be utilized if required.

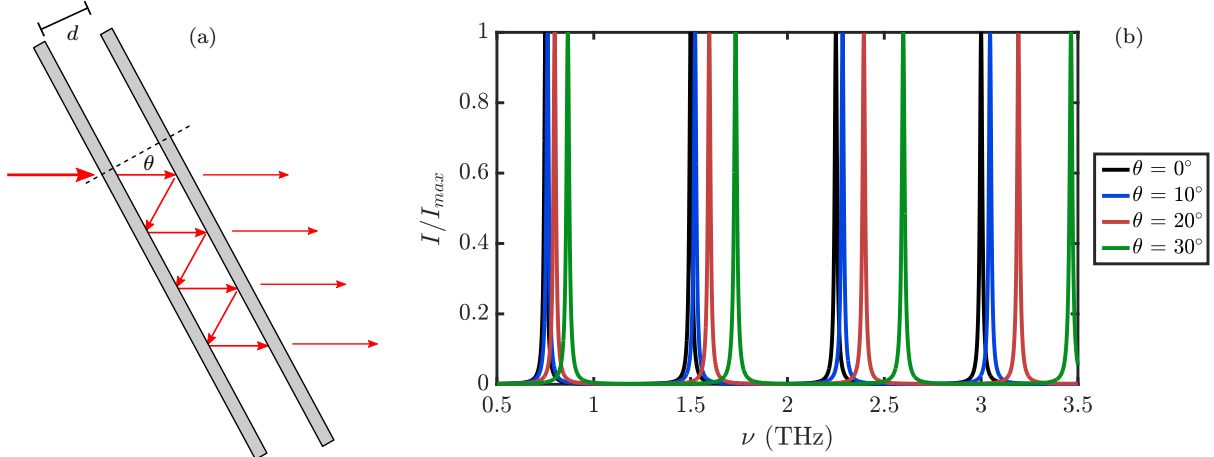


Fig. 7.21: Angle tuning ideal resonator with infinite mirror diameter and fixed d

$$\nu_q(\theta) = \frac{q\nu_{fsr}}{\cos(\theta)}, \quad \nu_{fsr} = \frac{c}{2nd} \quad (7.16)$$

7.5 Distributed Bragg Reflector

7.5.1 Basic Construction

From our discussion of FP resonator, we can see the importance of high performance reflectors. Distributed Bragg Reflectors (DBRs) or quarterwave stacks can be simply constructed by a periodic array of high ($n_>$) and low ($n_<$) index materials of $\lambda/4$ thicknesses for a target wavelength and incidence angle, an early development of such multilayered structure can be found in [117]. As a result, the frequency response of the layered system, which is also referred to as 1D photonic crystal, exhibits stop bands and pass bands [73]. The frequency range that fall in the stop band are not allowed to transmit and they are almost entirely reflected. The magnitude of this reflectance can be altered by changing the number of layers used in the periodic structure. This is particularly useful for construction of FP resonator, since we want some transmission through each mirror. Moreover, one can tune the central frequency for the stop-bands by changing layer thicknesses d_1, d_2 .

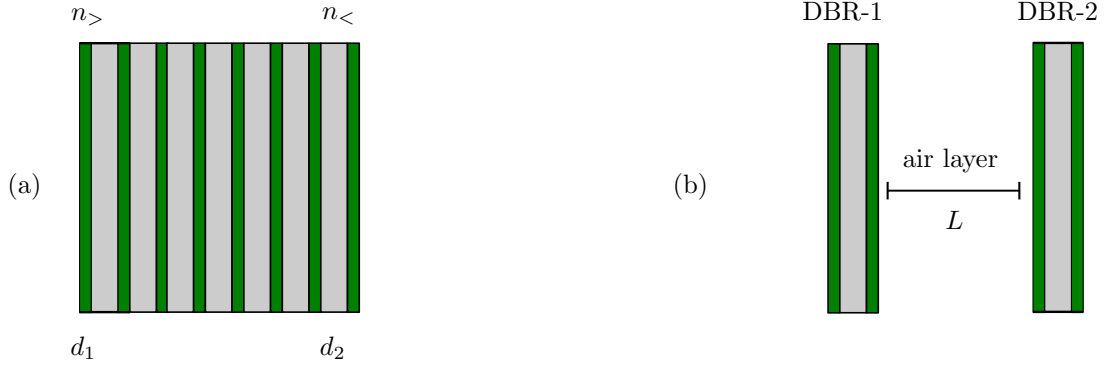


Fig. 7.22: (a) Periodic alteration of high (green) and low (grey) index dielectric constituting a DBR, (b) resonant cavity made with two DBRs

Our DBR is composed of alternating high-index dielectric and air layers, where the dielectric constitute the initial and final layers, i.e., we do not have any substrate material. Each layer is required to satisfy $nd = (2m + 1)\frac{\lambda_0}{4}$, $m \in \mathbb{N}_0$, for a target wavelength λ_0 at normal incidence. The widest bandwidth can be achieved when the optical thicknesses are truly a quarter-wavelength, i.e., $m = 0$. Moreover, the bandwidth of operation can be increased by increasing the ratio $n_{>}/n_{<}$. At oblique incidence, the optical path length difference between waves from adjacent layers decrease and consequently the stop-bands shift toward higher frequencies. A detailed calculation on various DBR structures can be found in [73]. For BFO magnon resonance, we set our target frequency at 0.55 THz, which correspond to $\lambda_0/4 \approx 136 \mu\text{m}$.

7.5.2 Polyimide DBR

For $\nu < 1$ THz Polyimide (PI) is a suitable candidate for high-index layer due to its availability as films and higher index ($n \sim 1.85$) compared to other polymers. Although even higher index material is desirable for broader-bandwidth. We attached 3 Mil thick PI films to each-other using double-sided tape which has a thickness of $\sim 100 \mu\text{m}$. The biggest issue in working with thin plastic films is that keeping each film flat and parallel to each-other is challenging. Ergo, we did not get desirable performance. Measurements in fig. 7.24 were taken without nitrogen purging.

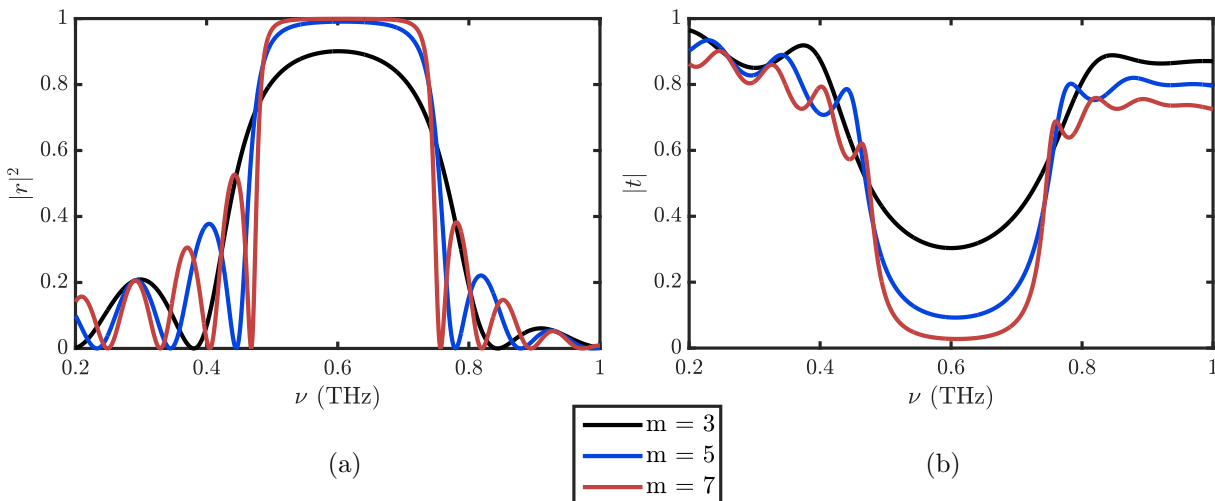


Fig. 7.23: Calculated response of PI DBR varying film number (a) Power reflectance from lossless films (b) amplitude transmission coefficient from lossy films

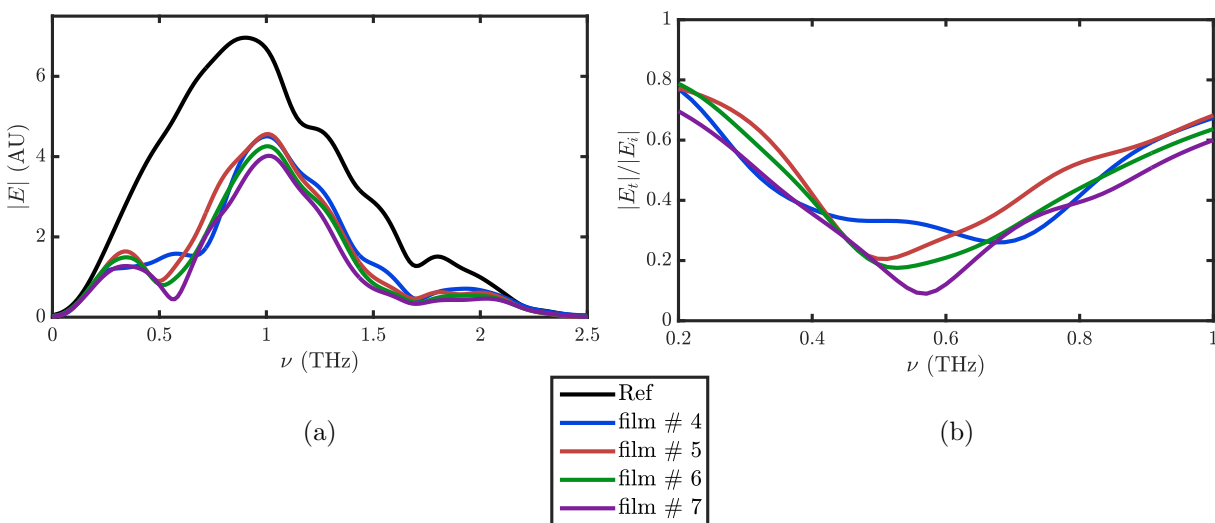


Fig. 7.24: Measured transmission response of PI DBR varying stack number. (a) amplitude spectra, (b) ratio with respect to reference.

7.5.3 Silicon DBR

In the THz range, High resistivity float zone silicon (HRFZ-Si) is known to have one of the lowest losses while also possessing high index of refraction ($n \approx 3.42$). This makes Si an excellent material for DBR. The only issue that arises is requiring a very thin wafer for broad-band operation. In fig. 7.25 we can see how the reflection bandwidth changes with thickness. Since Si wafers of thickness of the order of few 10s of microns would be fragile

and expensive, we decided to use a thicker wafer of $280\ \mu\text{m}$.

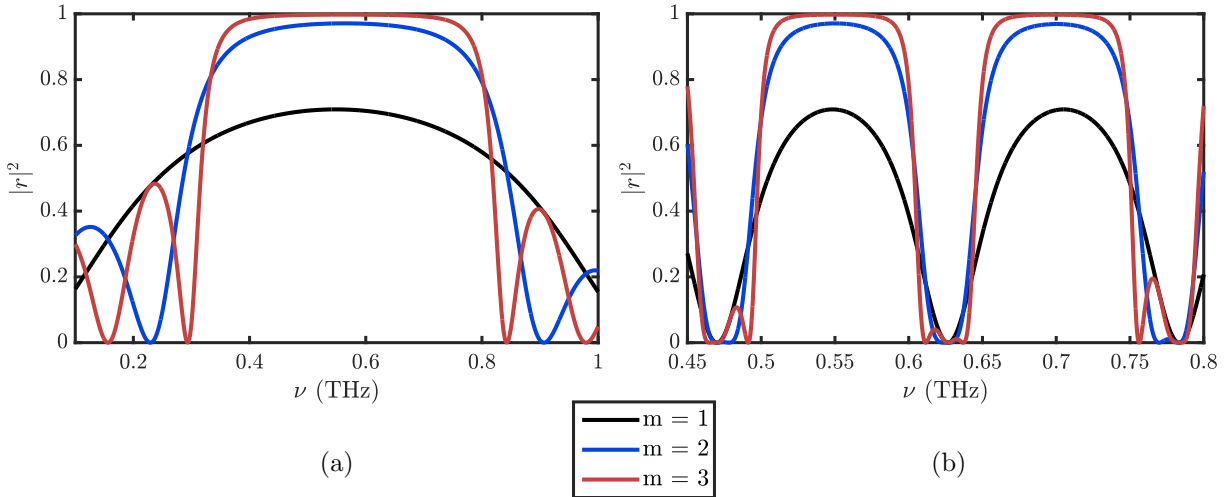


Fig. 7.25: Calculated response of Si DBR varying wafer number (a) $40\ \mu\text{m}$ thick Si with $127\ \mu\text{m}$ spacer, (b) $280\ \mu\text{m}$ thick Si with $127\ \mu\text{m}$ air spacer. It is possible to make a DBR that may be utilized to study BFO magnons-polaritons at $\sim 0.55, 0.73\ \text{THz}$.

In unpurged environment we measured the transmission of DBR consisting two wafers, each $280\ \mu\text{m}$ thick. For a three wafer DBR, we barely observed any transmission in the stop-bands, so we would present the data on FP cavity made with symmetrical pair of both types of DBR in section 7.8.

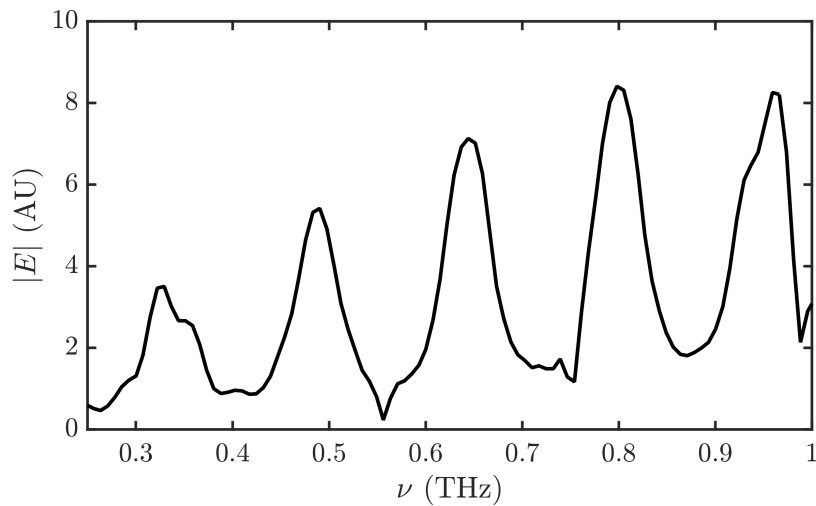


Fig. 7.26: Measured transmission spectrum from Si DBR consisting two wafers of thickness $280\ \mu\text{m}$ spaced by $127\ \mu\text{m}$, sharp absorption dips around $0.55, 0.75\ \text{THz}$ correspond to water vapor absorption

7.6 Pulse in Ideal FP Cavity

Fabry-Pérot interferometry is based on multi-beam interference where the input light may be assumed to be quasi-monochromatic or possessing a coherence time significantly longer than the characteristic time-scale, round-trip time (t_r), of the cavity. But for our purposes, we want to investigate the time-domain response of a simple broad-band cavity to an incident THz pulse. A valuable discussion on this topic can be found in [118], we further explore the implications for our setup.

An incident pulse, recorded with our apparatus, is shown in fig. 7.27 which has a pulse duration $t_p \sim 1.4$ ps. For calculation, we assume that the lossless mirrors used in the cavity have $r = 0.95$ and are of infinitesimal thickness. We also stipulate that a single pulse is incident on the cavity, i.e., equally spaced pulse train is not involved, which is reasonable as our pulses are spaced in time by $\sim 1 \mu\text{s}$ and no two pulses can noticeably interact due to the damping present in our devices. Later we will examine the performance of the prescribed DBR FP cavity. For the output signal, in subsequent calculations, we present the following:

- (a) Amplitude spectrum $|E_2|$
- (b) Waveform \tilde{E}_2
- (c) Short-time windowed amplitude spectrum or spectrogram

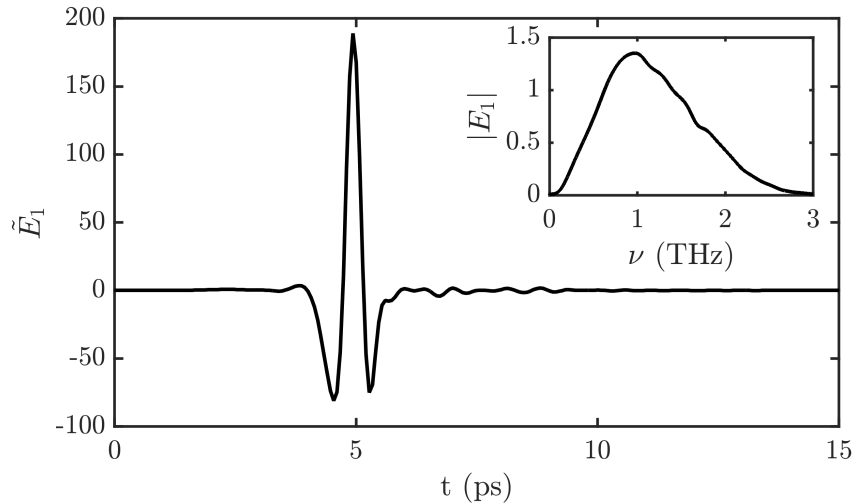


Fig. 7.27: Incident Pulse

We can see from eq. (7.15), that $Q \propto \frac{1}{\nu_{fsr}} = t_r$, therefore we expect to reach higher Q

by increasing cavity length or round trip time. But as can be seen in fig. 7.28 having $t_r > t_p$, the cavity will only have echoing pulses spaced-out in time which do not get to overlap and thus interfere. As a result, field enhancement at the anti-nodes inside the cavity would not be possible. One may be misled looking at $|E_2|$ alone. To show that in time and frequency domains there is actually no local resonance mode present, we performed spectrogram using a window of width 3.5 ps, where the window is moved along the waveform and only the region within the window is used to calculate spectrum. One possible disadvantage of small ν_{fsr} is that the output spectrum can get too populated with cavity modes that makes resolving spectral details challenging.

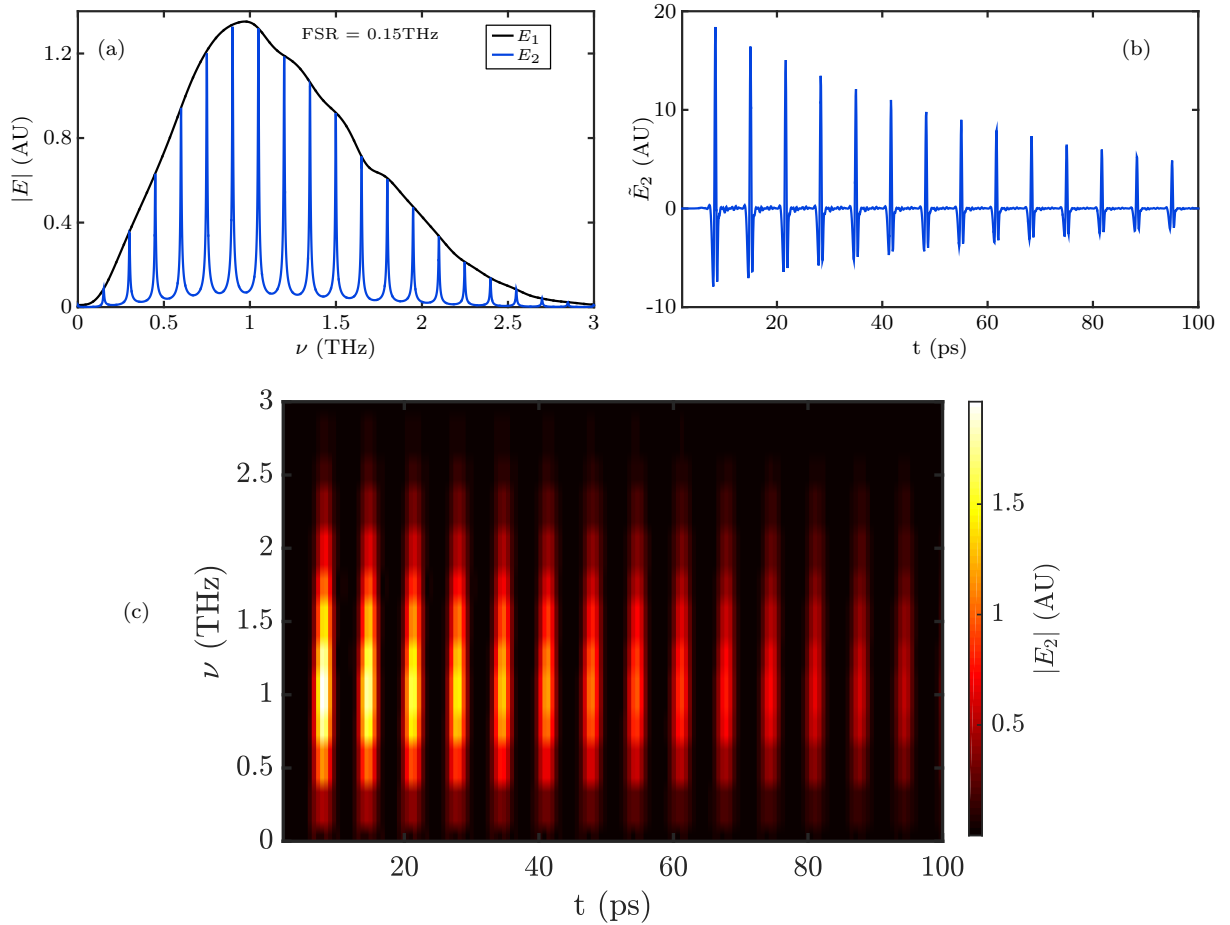


Fig. 7.28: Cavity length, $d = 1000 \mu\text{m}$, corresponding to $t_r \approx 6.7 \text{ ps}$. Cavity modes are present in output spectrum (a), but that does not imply we have multiple constructively interfering frequencies (b),(c).

In fig. 7.29 we have $t_r < t_p$ and ν_{fsr} is within the bandwidth of input pulse. We can clearly observe the cavity ring-down at the resonant frequency. The spectrogram further bolsters this fact. But since to observe this effect we had to reduce t_r , we ended up with a low Q

resonator for the input pulse. On a positive technical note, due to the lower Q , one does not have to record long time trace to approach the theoretical Q value. Also, having a single tunable cavity mode, it would be easier to resolve spectral features that are spaced further than the mode linewidth.

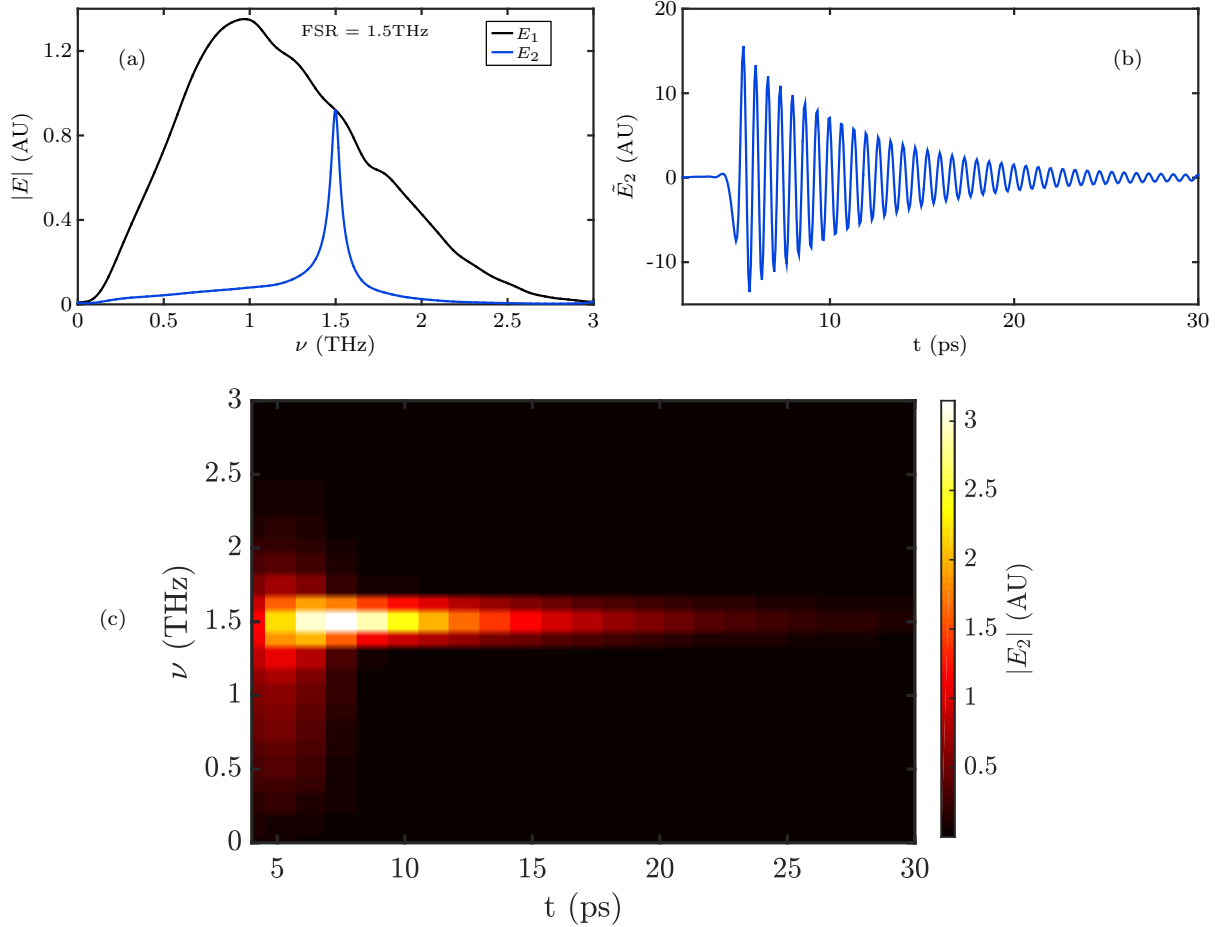


Fig. 7.29: Cavity length, $d = 100 \mu\text{m}$, corresponding to $t_r \approx 0.67$ ps

Finally, in fig. 7.30 although we satisfy $t_r < t_p$, ν_{fsr} falls beyond the bandwidth of the incident pulse. Thus, there is no cavity mode that can be detected with our pulse even though they exist due to the physical construction of the cavity. Consequently, we only have a rapidly decaying output pulse. In this case, almost all of the signal is reflected toward the source.

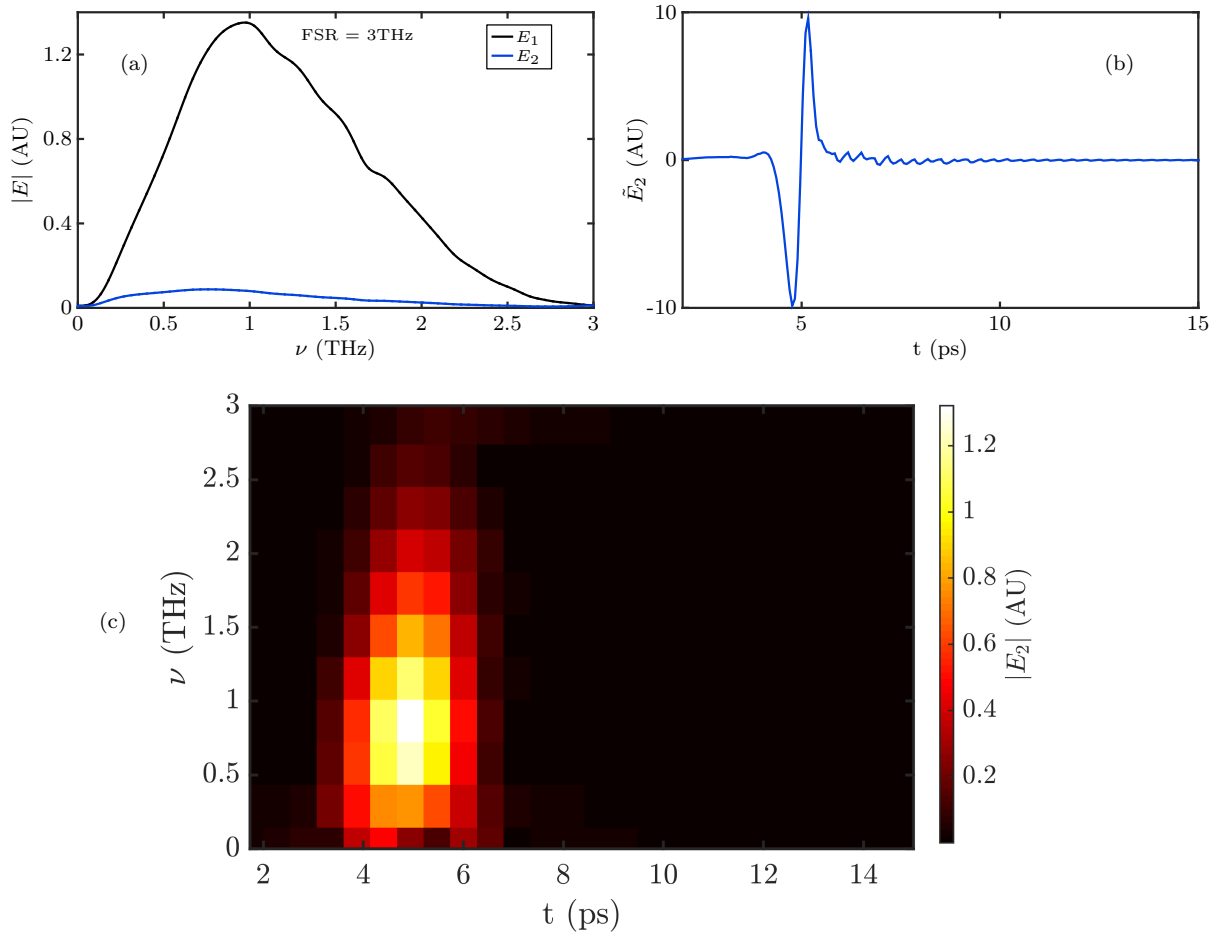


Fig. 7.30: Cavity length, $d = 50 \mu\text{m}$, corresponding to $t_r \approx 0.33$ ps

This section would be useful for qualitative understanding of the behavior a single pulse in FP cavity. Based on this we can analyze or explore more complex setups.

7.7 Response of DBR FP Cavity

Inserting a defect layer in a periodic array of dielectrics, say a DBR, one can achieve a 1D photonic crystal cavity, where instead of a stop-band there appears a sharp transmission peak in the frequency domain and spatially light is confined in the defect layer. This is an equivalent description of an FP cavity made with identical DBRs. For the following sections, the length of the defect layer will be denoted by L . Given a pair of DBR, we can calculate the frequency and time-domain behavior of the resonator using [3, 73]. A similar calculation was employed in chapter 5.

7.7.1 Transmission Transfer Function

We assume there is no misalignment in the optics and light as plane wave is normally incident on the photonic structure. For 280 μm thick HRFZ-Si wafers, using $\alpha \approx 0.05$ 1/cm, we calculated \mathcal{F} for cavities made of identical DBRs on both end, when each consists:

- (a) two Si wafers
- (b) three Si wafers

The corresponding Finesse, $\mathcal{F} \approx 100,920$ for (a), (b). The cavity transmission transfer functions due to two different DBRs are shown in fig. 7.31. Ignoring the effect of input spectrum on the Q value of the output, we find that for $L = 525 \mu\text{m}$, the theoretical quality factor for $Q \approx 240,2795$ for (a), (b). A similar scanning interferometer was reported using various thicknesses and resistivities of Si wafer in [119], a photonic crystal cavity was reported in [99, 120].

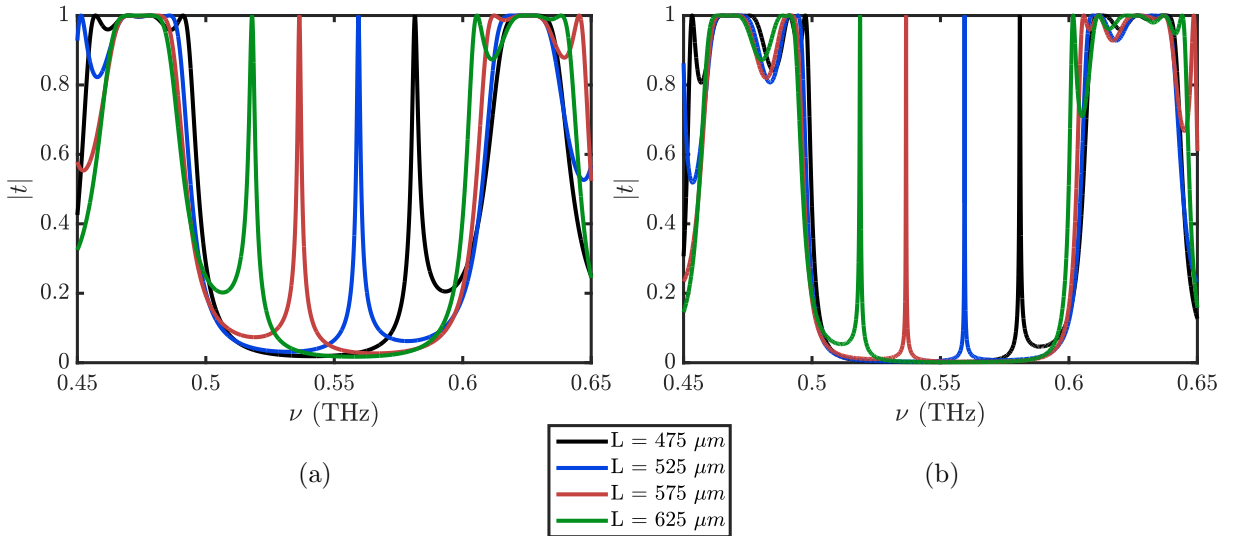


Fig. 7.31: Tuning cavity modes by varying L . (a) Each DBR consisting two Si wafers, (b) each DBR consisting three Si wafers.

From a technical point of view, as discussed in section 7.4.3, it may be advantageous to construct a fixed cavity and tune the modes by changing the angle of incidence. Here we calculate the theoretical response of angle tuning of a cavity made with a pair of two Si wafer DBR. For this case we set $L = 280 \mu\text{m}$, which slightly lowers the Q value but confines light in a shorter space, a condition that increases the Rabi splitting in observing cavity-polaritons, since $\Omega_R \propto \sqrt{1/V}$. It can be seen that the response is polarization

dependent. Since, for angles below Brewster's angle Fresnel reflectance increases for s-polarized light and decreases for p-polarized, we can see \mathcal{F} of the cavity change accordingly. Here we have not considered the effect of finite DBR diameter, which will allow light to leak out after many round trips.

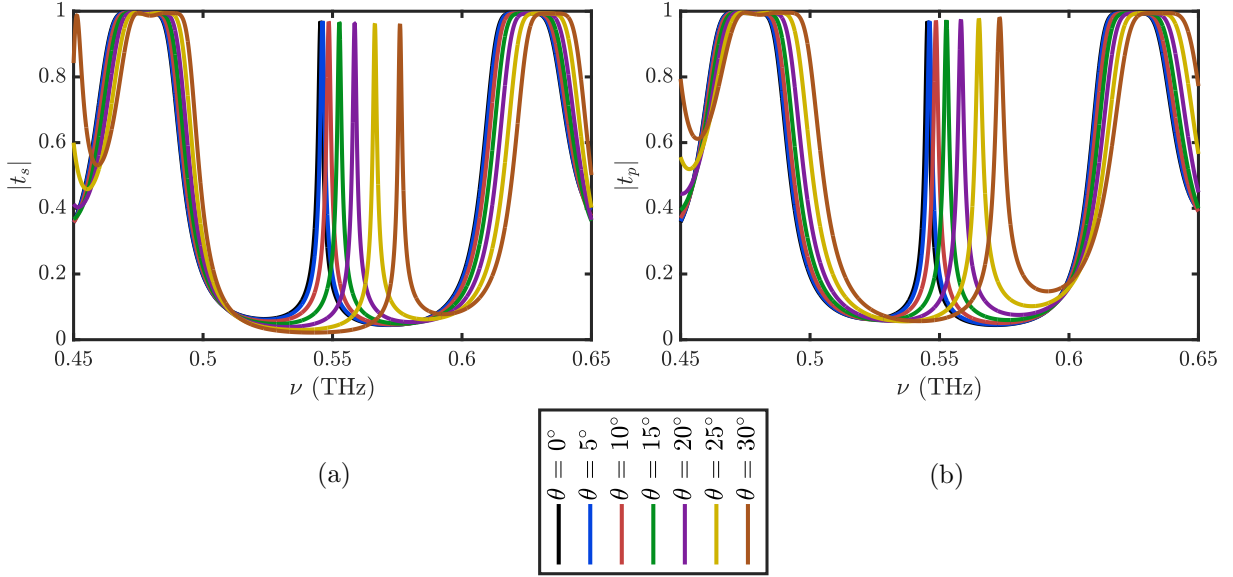


Fig. 7.32: Air gap, $L = 280 \mu\text{m}$. (a) s-polarization, (b) p-polarization

Assuming that the input spectrum is flat across the stop-band, we can determine the theoretical Q value of the calculated output signal. At normal incidence $Q \approx 188$. At $\theta = 30^\circ$, $Q \approx 240, 110$ for s, p polarizations respectively.

7.7.2 Time-domain Response

Given an input THz pulse, we can calculate the frequency and time-domain response of the DBR based cavity to the pulse. In subsequent calculations for the cavity, we will use two identical DBRs each constructed with two Si wafers of $280 \mu\text{m}$ thickness spaced by 5 Mil ($127 \mu\text{m}$). We assume normal incidence and $L = 550 \mu\text{m}$, which allows a cavity mode $\sim 0.55 \text{ THz}$, close to room temperature BFO magnon. The reference and output signal is shown in fig. 7.33. The reference signal is taken from experiment and rest is calculated.

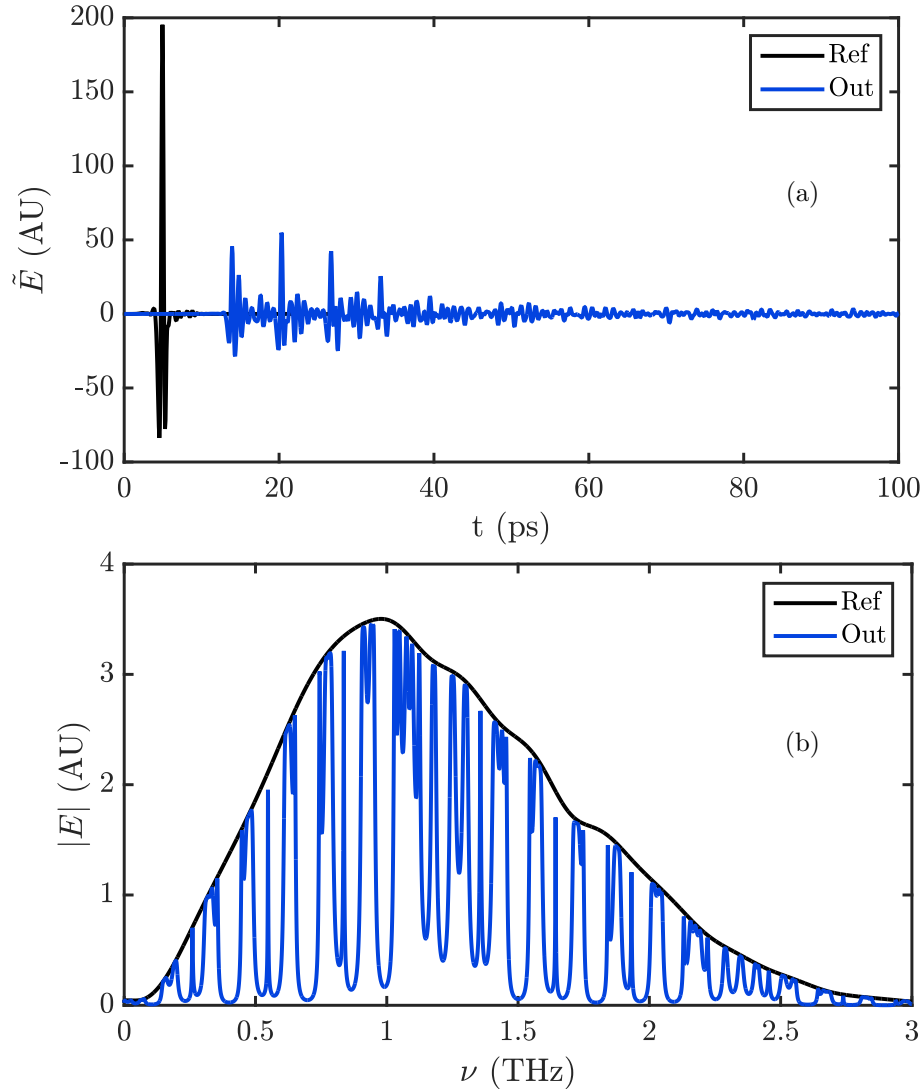


Fig. 7.33: $L = 550 \mu\text{m}$, Ref is from experiment and Out is calculated. (a) time domain, (b) frequency domain

Due to the cavity's smaller bandwidth of operation, indicated by the dips in above output spectrum, compared to the input pulse, it becomes difficult to identify the cavity's time-domain performance. Hence, we illustrate in the following calculations, how the resonator would respond to a narrow-band signal. In both following cases the time-duration of the input waveform is significantly larger than the round-trip time of the cavity.

In fig. 7.34 we can observe how the transmitted signal grows due to the resonator that allows one output mode. The spectrogram in fig. 7.35 further illustrates the long photon-lifetime at large time scales.

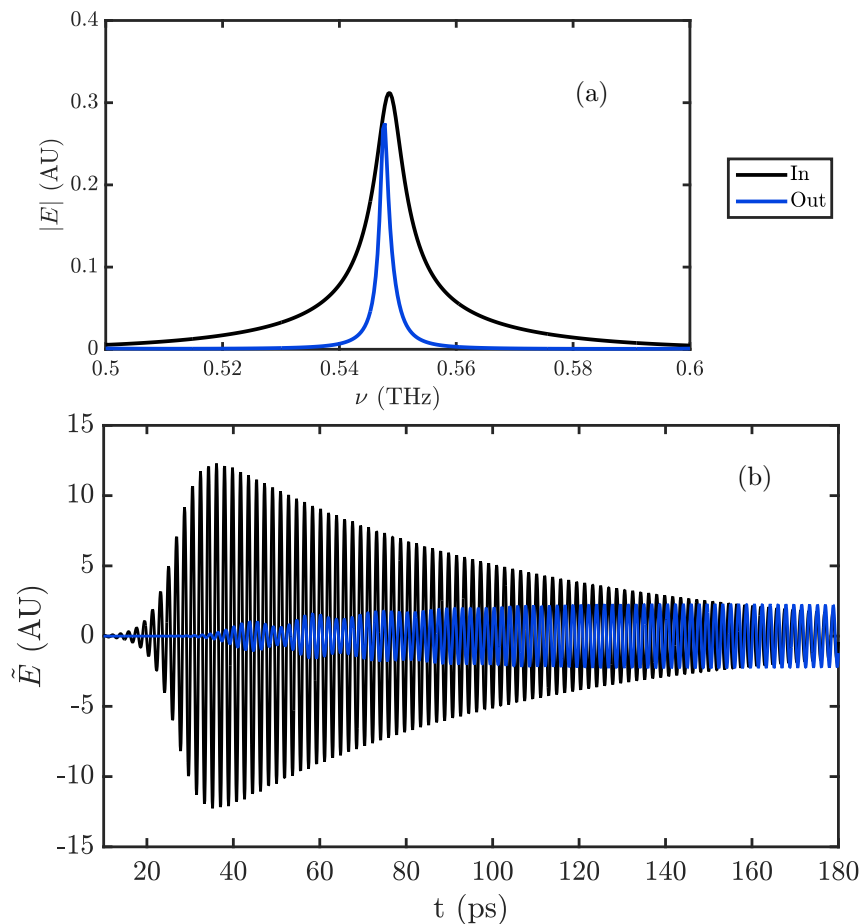


Fig. 7.34: Calculation with $L = 550 \mu\text{m}$. (a) spectra, (b) waveform.

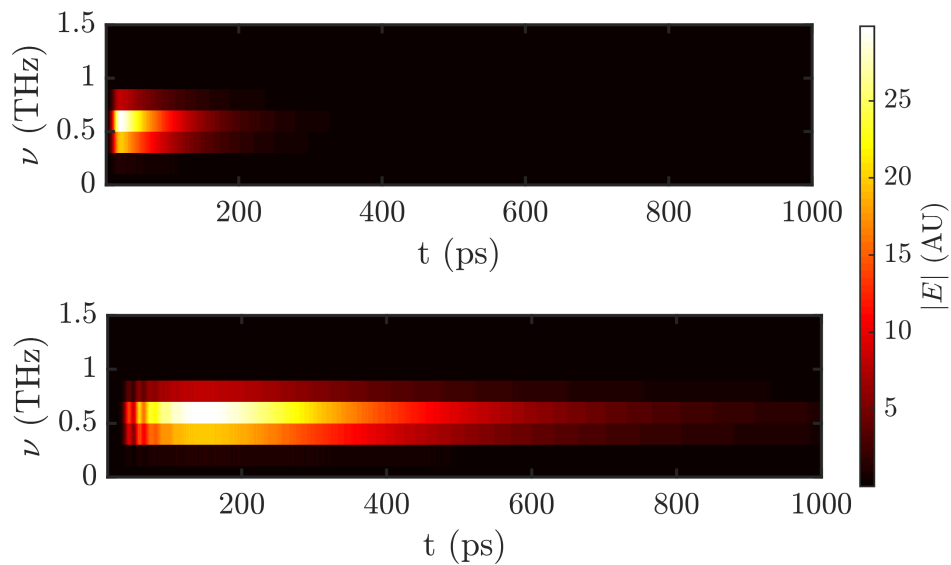


Fig. 7.35: Spectrogram performed on fig. 7.34 (b) with 50 ps moving window. Top and bottom panels correspond to input and output signals respectively.

By increasing the length of the cavity, the resonator would allow multiple modes. For a broader input bandwidth that would allow two modes to persist, we can see closely spaced frequencies beating in time-domain, figs. 7.36 and 7.37. Such phenomenon is also observed if one detects cavity-polaritons, but in that case the beating would be between two frequencies that are higher and lower than the cavity mode, see eq. (7.3).

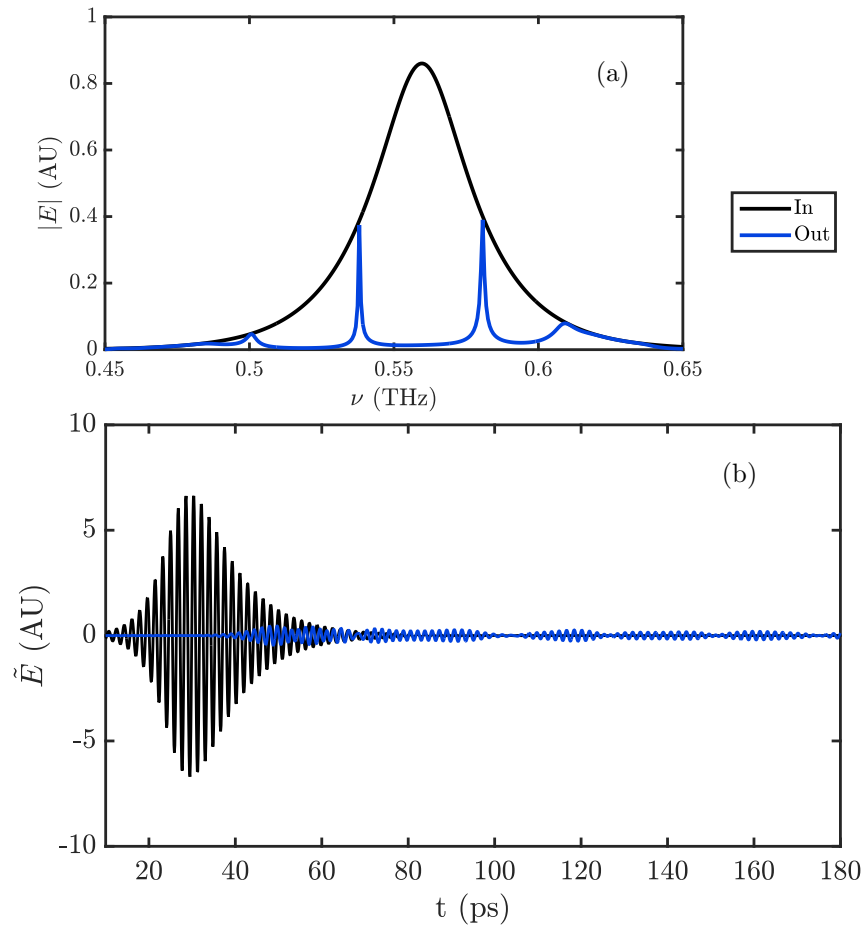


Fig. 7.36: Calculation with $L = 2800 \mu\text{m}$. (a) spectra, (b) waveform.

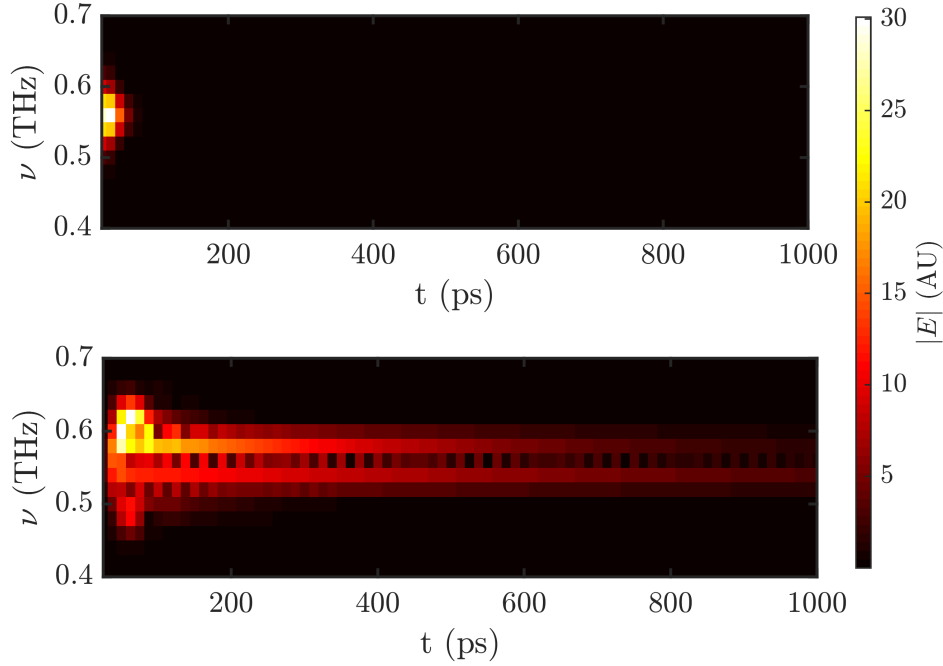


Fig. 7.37: Spectrogram performed on fig. 7.36 (b) with 50 ps moving window. Top and bottom panels correspond to input and output signals respectively.

One must note that a high Q cavity mode would correspond to a long damped oscillation, which implies that we require a long time trace to make sense of the Q value. Thus using THz-TDS, it is crucial to scan for a long time in measurements involving high Q resonators. But standard TDS setups are usually not employed for such long scan times. Therefore, one may incline to design a cavity with reasonable Q that can be measured and tested with available apparatus.

To illustrate this effect, we can consider the above DBR cavity with spacing $L = 2.8$ mm, a distance that is easy to incorporate in experimental scanning cavity. Since our data is recorded in time-domain prior to Fourier transformation (FT), we can calculate the output spectrum by considering certain initial segment of the waveform and windowing out the rest that follows, see section 3.4. Fig. 7.38 shows the effect of time-duration on the measured mode linewidth. Time in legend correspond to the time length after the 1st peak in output waveform (not shown). Calculations suggest, given there are no misalignments, a time trace of the order of nanoseconds would be required to satisfactorily extract the theoretical Q value. We would like to comment that the Q of the cavity is independent of our length of time-trace. The time-trace is only used to determine the Q value, which may be limited by apparatus.

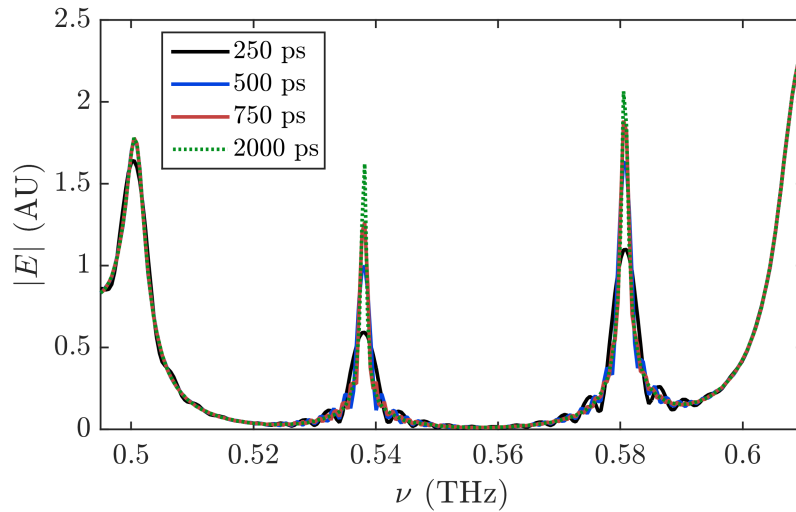


Fig. 7.38: Calculated transmission spectra with $L = 2.8$ mm, varying output waveform length that is used for FT.

7.8 Result from Cavity Measurement

Based on the calculations presented, a prototype of the planar Fabry-Pérot cavity was constructed. To make each DBR, 3D printed mounts were used to hold Si wafers of thickness $280 \mu\text{m}$ which were spaced by a 5 Mil shim. When the DBRs are in contact we have $L_{min} \sim 550 \mu\text{m}$. One DBR was fixed on the optical table, while the other was connected to a linear stage to vary L . Results are presented below. Following plots are offset along y-axis for clarity.

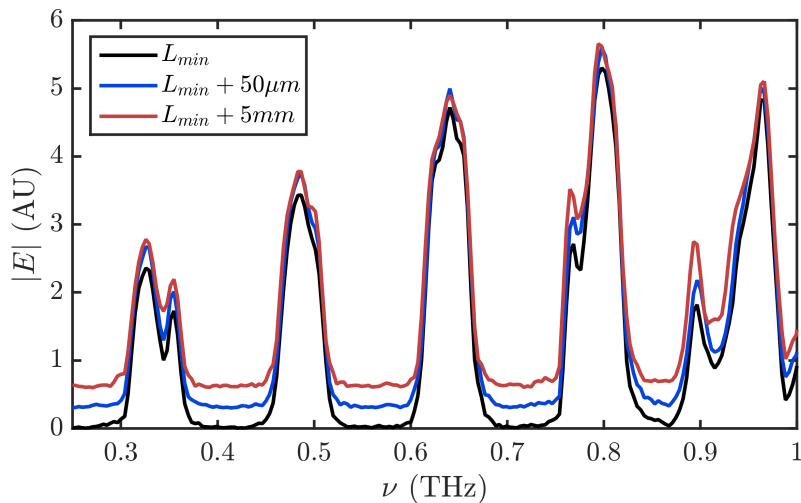


Fig. 7.39: Cavity made of DBRs consisting three Si wafers each. Due to very low transmission, we could not detect any resonance modes as distance between DBRs are increased.

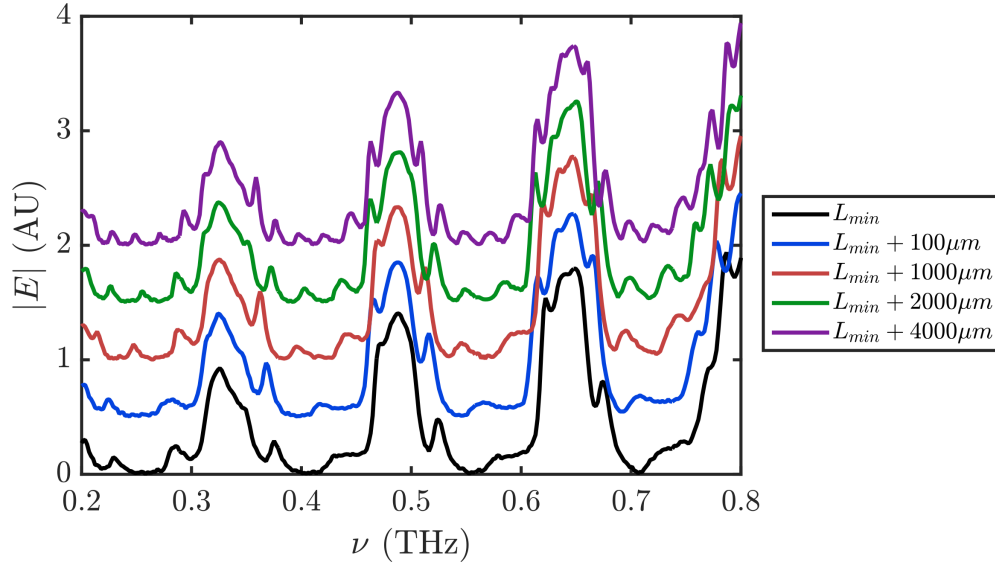


Fig. 7.40: Cavity made with pair of DBRs each consisting two Si wafers. As cavity length is increased, the number of weak cavity modes can be seen to increase in the reflection region. Due to alignment issues, the modes are not prominent.

The prototype scanning FP cavity did not perform satisfactorily and is being improved upon in a future project by another student employing more stable machined metal mounts.

7.9 Discussion

Motivated by the prospective discovery of room temperature strong THz cavity photon and BFO electromagnon coupling, we examined the relevant experimental aspects. For the spectral investigation on BFO sample we exploited anti-reflection (AR) coating on GaP detector crystal for resolving the closely spaced magnon modes. From the condition for CMP formation, we realize the need for a mechanism to tune the resonance of either the magnon or the cavity. Since we could not efficiently control BFO resonances without optically heating the sample, which increases loss, we resorted to the construction of a scanning FP cavity built with multilayered dielectrics, DBR. To increase the chance for CMP detection, we require light to be spatially confined but temporally long lived. This implies building a high Q cavity with small spacing between the mirrors. We performed both time and frequency domain analysis on the interaction of a THz pulse with an empty cavity for better understanding the physics and its implication for recording waveform using THz-TDS. A prototype cavity was built; but due to its inefficiency, an improved version for the study of CMP will be pursued in a future research project.

7.10 Conclusion

Room temperature magnetoelectric multiferroics are of great interest for their wide range of possible applications. BFO falls in this category and possesses magnon modes that can be excited by the electric field of THz light. Due to its sub-THz resonances, BFO can be studied for strong light-matter coupling, which can play a vital role in quantum information technology and spintronics. To explore this untrodden territory, we investigated the requirements for observing CMP in BFO. We performed time-domain spectroscopy on polycrystalline BFO sample and located the dominant electromagnon modes that fall in the range 0.5–0.75 THz, in room temperature. The AR coating developed in chapter 5 were utilized in our endeavor to high spectral resolution. We could not tune BFO magnons with external electric field, hence poling of the sample and examination of its ferroelectric behavior is required. We could tune the resonances via optical heating but that involves unwanted increase of absorption. We explored the design aspects of a high Q tunable cavity so that we may observe the dispersion relation of CMP by tuning the cavity modes. We calculated the performance of the proposed DBR and FP cavity and mentioned the possibility of angle tuning the cavity modes. The prototype cavity did not meet required standard, so an improvement in cavity construction is demanded. The calculations performed in this chapter would guide in the right direction for building a tunable cavity optimized for discovering CMP in BFO using THz-TDS.

The constructed spectrometer, analysis techniques, spectroscopy of low loss materials, AR coatings, DBR—have all been exploited to some capacity for the study of light-matter coupling in BFO. With an upgraded experimental setup, further investigation will be pursued in another project.

Chapter 8

Conclusions

Time domain spectroscopy is a powerful technique in characterizing materials and complex systems. It allows one to directly observe the temporal dynamics of the system under study. We have constructed a terahertz time domain spectrometer (THz-TDS) exploiting optical nonlinearity in electro-optic crystals. We generate short single-cycle THz pulses that have a broad bandwidth, which is utilized in spectral investigations of dielectrics and multilayered polymer film based optics. As a developing technological field, commercial THz optics seldom provides cost effective solutions. In this project, we make use of thin low loss polymer films and adhesives in the construction of economic, easy to apply THz optics. Equipped with the tools developed in this project, we investigate the strong light-matter coupling between THz cavity photons and electromagnons in room temperature magnetoelectric multiferroic BiFeO₃ (BFO). The cross coupling between electric and magnetic lattice in BFO offers tremendous versatility in device applications.

Chapter 2 highlights the theory of generation and phase resolved detection of THz pulses. Due to high optical non-linearity (d_{eff}) and band gap, we chose LiNbO₃ (LNB) as our generation crystal. For efficient THz output via optical rectification (OR), we require that the THz phase velocity match the IR group velocity in the electro optic (EO) crystal. Due to the huge mismatch between refractive indices for IR and THz in LNB, $v_g(\omega_0)/v(\Omega) \sim 2.2$, we accomplished phase matching by pulse-front-tilt (PFT) of IR pulses in LNB [27]. Using the inverse process of OR, we exploit Pockels effect and EO sampling in a GaP crystal in a collinear geometry to coherently detect the THz waveform. Appendices A and B would serve as resources for a step-by-step procedure in reconstruction of the apparatus from the ground up. The fully functional apparatus incorporates micro-controller operated

translation stages for multi-sample characterization and a planned scanning Fabry-Pérot (FP) cavity in a N₂ purged environment.

Built on the foundation of Fourier transformation, in chapter 3, we illustrate the basic mathematical techniques employed in extracting optical parameters from thick samples, i.e., samples where internally reflected pulses can be clearly distinguished from main transmitted pulse. Harnessing the connection between time and frequency domains, we develop analysis tools which are applied in later chapters to simulate time-domain signals from complex multilayered structures. Applying our THz-TDS in the characterization of low loss dielectrics that possess no resonances in the bandwidth 0.3–2.5 THz, in chapter 4 we extract optical parameters of commercially supplied HRFZ-Si, ceramic alumina, quartz glass. These materials have found various uses in the THz range and our purpose was to identify the material properties of these samples for future device fabrication. Moreover, this allowed us to test the performance of our spectrometer. From careful observation of the absorption spectra, $\alpha(\nu)$, we can identify negative value of $\alpha(\nu)$ in the lower frequency end. We attribute this unrealistic effect to insufficient sample thickness compared to the wavelength of light.

Using the optical parameters of examined dielectrics, we develop very low-cost multilayered antireflection coatings (ARCs) for them in chapter 5. We explored the possibility of utilizing commercially available pressure sensitive adhesive tapes (PSATs) and films in creating the ARCs centered around a specific frequency. Although a similar technique was employed in [66, 67] by gluing Polyimide film on substrate, we extend its applicability by exploring the effectiveness of various polymer films and their combinations in configurations up to four layers. Moreover, we demonstrate that our approach can create practical wide-band ARCs. Based on [73], we develop code to analyze and model the behavior of the dielectric layers both in frequency and time domains. The mathematical tools developed in chapter 3 were applied in comparing experiment to calculation for both the transmitted and internally reflected pulses from AR coated substrates. With our analysis tools we can propose polymer layer assemblies tailored for certain frequency region for a given substrate. Since our coatings are removable, one can apply a different ARC designed for another frequency of interest on the same substrate. This gives flexibility in reducing Fresnel loss and FP effect in transmission and can significantly enhance the performance of THz optical components. Our findings can positively impact the advancements in THz technology.

By appropriate application of ARCs, we show the possible enhancement of non-collinearly

generated THz pulse power from LiNbO₃. Such a detailed treatment for improvement exploiting commercial polymers has not yet been reported. Empirical validation of the proposed generation setup must still be undertaken to confirm this. In addition, we have applied an ARC on both faces of a GaP EO crystal to significantly reduce FP effect in free space EO sampling. This facilitates performing high resolution spectroscopy at certain spectral regions with EO crystal of finite thickness. The ARC on GaP was chosen to operate around the region 0.75 THz, close to which we have resonance modes of BiFeO₃.

Employing multilayered polymers, we propose the construction of economic, relatively narrowband linear polarizers with high extinction ratio and low insertion loss, in chapter 6. We made a prototype low performance polarizer with polyethylene (PE) shrink wraps for qualitative testing of the Brewster's angle pile-of-plates design. The technique is similar to the more expensive, broader band and bulky one reported in [86], where the spacing between Si wafers are large enough to prevent inter-wafer reflections to transmit forward. On the contrary, in our upgraded design, we exploit polarization based interference effect arising from closely spaced polymer layered structure. As a result, when operated at the Brewster's angle, the p-polarized light transmits through the layers without any reflection, while the s-polarized light is strongly reflected at certain frequency bands. By varying the thickness of PE films, inter-film spacing, and number of layers, we can control the location and bandwidth of operation alongside the extinction ratio. With appropriate calculation, this design can be adapted to a cheap THz beam splitter with a specific splitting ratio. We have constructed a prototype of the latest design that is awaiting further performance testing.

The apparatus and optical components described in this work were primarily developed in order to investigate the coupling of THz light to magnetic materials. Cavity enhanced light-matter coupling is of great interest in fundamental science and for various future technologies. Strong coupling has been reported to alter the properties of material under study, which gave birth to an emerging field, polariton chemistry [16, 121, 122]. When the energy transfer rate between cavity photons and material excitations is greater than their dissipation rates, strong coupling regime can be reached when the constituent sub-systems hybridize to form a polariton quasi particle. Cavity techniques in the THz regime are still not so well established compared to microwave and optical frequencies. Only in recent years, we have seen an upswing in publications on the coupling between THz cavity photons and material excitations [17, 99, 100]. In chapter 7 we briefly describe the formation of cavity magnon polariton (CMP) using coupled harmonic oscillators based on [103].

The signature of the coupling is manifested by the Rabi splitting or anti-crossing of the polariton branches, which occurs when the resonance frequencies of the sub-systems match. We noted the importance of lowering the losses in both THz cavity and material excitation for the observation of polariton modes. Moreover, to enhance coupling strength one should increase the filling factor of the sample-loaded cavity. This suggests employment of a high Q cavity with low mode volume.

In this project, we concentrate on the sub-THz excitation in a polycrystalline BFO sample. Electric field of THz pulse can couple to the collective spin cycloid resonance (SCR) modes in BFO, which is why these modes are also called electromagnons. In order to perform high resolution spectroscopy of BFO magnons, we made use of ARC on GaP EO crystal. Owing to the magnetoelectric coupling, it has been reported that the electromagnon resonances could be tuned via external electric field in BFO thin film [108]. Unfortunately, our attempt with electric field tuning of a slab of the sample did not come to fruition. Nonetheless, as reported by [13, 109, 111], we could tune BFO magnons by varying its temperature via optical heating. In room temperature the BFO sample showed noticeable loss, which only increased with temperature. Therefore, we investigated on the design of a tunable high Q Fabry-Pérot (FP) THz cavity for the discovery of room temperature CMP in BFO.

We explored the design of distributed Bragg reflectors (DBRs) using carefully layered low loss dielectrics. Applying our analysis techniques, we simulated the time and frequency domain responses of FP cavities built with a pair of identical DBRs. We outlined the possible implications of various cavity systems for our THz-TDS apparatus. We highlighted the feasibility of angle tuning cavity modes of a fixed FP cavity. This technique can be advantageous because in a fixed cavity construction, there is little room for misalignment and the spacing between the DBRs can be made reasonably small which reduces mode volume and consequently enhances coupling strength. Using HRFZ-Si wafers, we constructed two DBRs that are incorporated in a prototype scanning FP cavity. Due to the subpar performance of the prototype, the design and construction of a revised version of this apparatus with a more stable mounting structure has formed the basis of another project with the objective to detect room temperature THz CMP in BFO.

We hope that the work done in this project will pave the way to future discoveries of THz cavity polaritons and the developed tools and techniques will facilitate numerous future research projects. The low-cost and easy-to-apply optics innovated during this thesis may find various applications in days to come.

Appendix A

Alignment Procedure

We describe step by step procedure for THz generation and detection using respectively pulse front tilt in LiNbO₃ and electro-optic sampling using GaP. For a schematic ray diagram see fig. 2.8 in chapter 2.

A.1 Pre-generation Considerations

One has to bear in mind that the same pulse pair produced after the 1st beam splitter (BS) is used for both generation and detection. Therefore, the pump and probe lengths have to be of equal optical path length. Hence, when laying out optics on optical table, one has to have a foresight concerning this. Since a delay stage is used to finely match/change path length differences, one does not need to be very precise in measuring lengths. We used a combination of ruler and thin adhesive tape to measure distances between optics. It is also worth noting that placing irises along the beam path would help in future alignment work.

A.2 Generation

Once the lens combination for 4f telescope and angles for diffraction grating are determined, we can start working on alignment. We remind that α, β are respectively the incidence and diffraction angle measured from grating normal. The most challenging part is to optimally align pump IR on the LNB prism, for this purpose we used a 3D printed alignment tool,

see fig. A.1 (a), such technique was implemented using cardboard by [123]. For ease of alignment we use a 5 axis prism holder shown in fig. A.1 (b). Following order of operation will guide one to easy and optimal alignment.

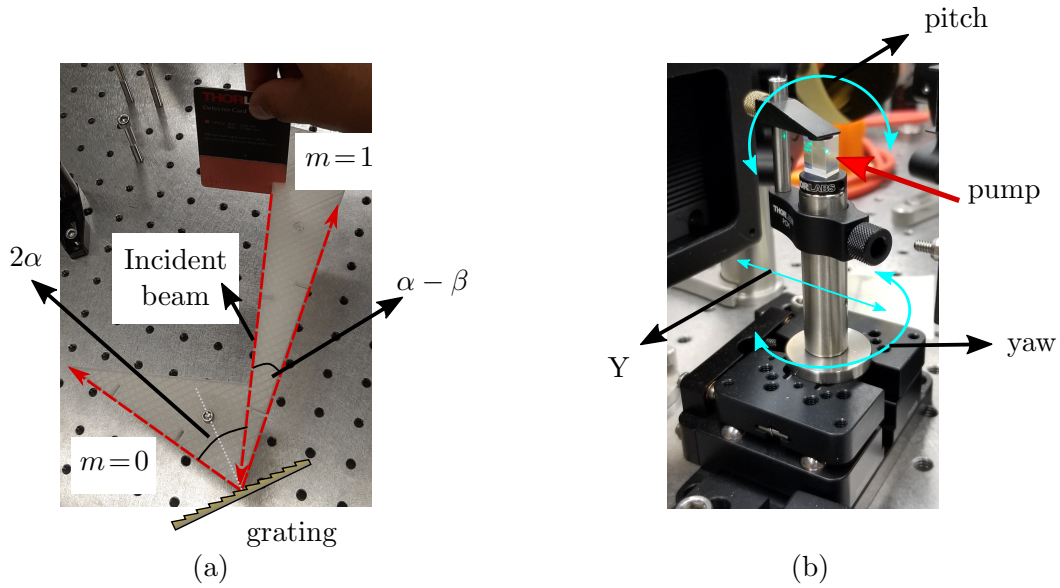


Fig. A.1: (a) 3D printed alignment tool, m denotes the order of diffraction, $m = 1$ is used to pump LNB. (b) 5 axis translation stage PY005 from Thorlabs is used to mount LNB prism. 3 vital axes are labeled according manufacturer specification.

- Verify the polarization of beam incident on diffraction grating. Make sure the polarization is parallel to the plane containing incident and diffracted beams, for maximal energy reflection. Use a $\lambda/2$ wave plate to that end, if required.
- align the diffracted beam with the alignment tool shown in fig. A.1 (a). Use both $m = 0, 1$ order reflections for alignment. Make sure the beams are also horizontally parallel to the table. Make use of the kinematic mount of the diffraction grating for adjustments. If the $m = 0$ beam is not utilized, it is best to block it with a beam block.
- Determine the optic axis of LNB crystal. In fig. A.1 (b) , it is along the vertical axis. We have to align the diffracted IR polarization along the LNB optic axis. This may require placing a $\lambda/2$ wave plate inside the 4f telescope where the beam intensity is not so high.
- We used a cage system to assemble the 2 lenses used in 4f telescope. The focused beam after the last lens should be closer to the output face of LNB prism. Upto this

point laser alignment can be performed with low power.

- Put a big beam block to block the IR after LNB. Increase the laser power to ~ 10 W. Manually adjust the location of the prism mount so that maximal green generation is observed by eye. Usually for the shape of our prism, one should notice 2 green dots shining from within LNB.
- Prepare thermopile power detector for operation and connect its output to lock-in amplifier. Use chopper at 23 Hz.
- Place thermopile detector right next to the output face of THz light, and scan the region to find THz signal. One should notice a jump in detector signal when THz power is incident on it.
- To make sure the detected power is indeed coming from THz and not via optical heating of some sort, rotate the IR polarization by rotating $\lambda/2$ waveplate. If THz is indeed responsible for the signal, then rotating IR polarization parallel to LNB optic axis will not produce any THz, thus no signal will be recorded. We note that THz polarization would be parallel to LNB optic axis.
- After crude detection of THz light. We have to optimize output power and beam direction. With the same power detector check if THz is coming out of LNB perpendicular to output face. Since the THz beam would be diverging, we have to roughly determine the central axis of transmission. Now to keep the beam horizontal to table use the pitch adjustment on prism mount.
- In order to keep THz exiting perpendicular to LNB face, we have to use the yaw adjustment in the mount. At the same time we have to slightly tweak the kinematic mount of grating. Adjusting both of them, one can optimize generated THz power exiting normal to prism.
- One may also make use of the y-axis marked in fig. A.1 (b), to get a higher generation. The other 2 axes, X, Z (not shown above), only have a little effect once coarse alignment is done.

A.3 Detection

After generating THz, one has to guide the beam and finally focus on GaP for EO sampling. We use unprotected gold coated off-axis parabolic mirrors (OAPM) for collimating and focusing THz. Before using these mirrors, one has to pay attention to the orientation of each OAPM, since orientation for receiving collimated light is not the same as receiving diverging light, see fig. 2.8.

- Using a visible laser pointer adjust the kinematic mounts of each OAPM. Careful alignment with visible light is necessary to prepare the OAPMs for THz alignment.
- It should be noted that using a small effective focal length OAPM, one can focus beam tighter and have higher electric field but as a drawback attain a lower Rayleigh range. The location of both THz focus at the sample and GaP should be identified. To mark the sample location, one can use a set-screw affixed to a post and mount the post such that the tip of the set-screw defines the THz focus. To locate the GaP focus, one can leave the power detector at the point of maximum THz power, at the focus. This would mark the location where IR should go through GaP. Do not yet place the GaP.
- After THz alignment is done with the help of above mentioned power detector, we need to concentrate on the probe beam. Block THz beam with a piece of metal. We pay attention to the operational power of the balanced-detector, for our Nirvana photo-detector (Model 2007), each photo-diode can accept power < 1 mW. Keeping this in mind we use a combination of beam-splitters and neutral density filters to reduce the probe power.
- Use a Glan-Taylor prism to allow only the probe polarization parallel to THz (vertical) to transmit. This is useful since EO sampling is polarization sensitive.
- With the help of a telescope, collimate probe beam to a spot size comparable to THz spot and align the probe onto the thermopile detector aperture, which was left at the THz focus where GaP should go. This makes sure both THz and IR are overlapped on the same spot. Now remove the detector and place the GaP crystal at the THz focus.
- Use Wollaston prism to check the polarization of IR exiting from GaP. It should be same as right after Glan-Taylor polarizer. Now introduce a $\lambda/4$ waveplate and

rotate it appropriately so that the Wollaston prism equally splits the probe into 2 components. This process makes sure that IR now is circularly polarized. Now remove the Wollaston and further align probe beam toward balanced detector.

- It should be noted that only at low IR intensity, GaP would be optically isotropic. So one should try to keep probe power low for EO sampling. It helps to place a long focal length convex lens before the balanced detector, we use $f = 200$ mm, to focus the 2 components of IR through the narrow apertures of balanced detector.
- The IR power before the wollaston prism should be ~ 1.5 mW, i.e., after splitting the 2 components each would be ~ 0.75 mW, lower than the damage threshold of the photo detectors. With the help of 2 mirrors the decomposed beams should be sent to Ref and Signal apertures of Nirvana. The 2 mirrors play a key role in the optimization process. Placing big irises before each aperture helps to further block stray reflections from the pump beam, this may help reduce background offset signal from the Nirvana.
- Attach the balanced output of Nirvana to an oscilloscope and operate the device in balanced mode. One does not have to worry about Loop Bandwidth settings since that is primarily for Auto-balanced mode.
- Block one aperture of Nirvana and with the help of oscilloscope and respective adjustment mirror optimize the signal in oscilloscope. THz should be kept blocked until instructed. Once both of the beams are adjusted, they should each read the same value in oscilloscope. Now keeping both apertures open, one should get nearly zero reading from oscilloscope.
- Unblock THz beam and increase chopper frequency to a high value, we use 1 KHz. Connect the output from balanced detector to lock-in and run the script `Find_THz_Peak_Quick.m` given in appendix B. This will move the delay stage and measure THz waveform. Once a peak is found, the code moves the stage to the point that correspond to peak THz signal.
- At this point, one may adjust the last OAPM before GaP to maximize peak signal. Slightly moving the GaP back or forth using a translation stage would help further maximize signal. Finally one can very finely, with caution, tweak the grating angles for more signal. At this stage, each optic can be optimized and the above mentioned script should be run frequently to locate the new point in time where THz peak is.

Appendix B

Matlab Codes

Codes for THz-TDS apparatus control used in this project are listed below.

Listing B.1: Quickly find THz peak signal from waveform

```
%% Script file: Find_THz_Peak_Quick.m
% This code is used to detect the peak of THz waveform in a
  crude fashion
% For actual measurements use codes: setup_1.m ,
  THz_TDS_for_kids_v2.m
clc
clear all
close all
%% MUST PROVIDE THE FOLLOWING VARIABLE VALUES
  =====
step_size = 2; %
start_step = 500;
end_step = 1500;
%% GLOBAL variables
global shift_delay device_name dq calibration_factor

shift_delay = 50 / 1000; % 5 times the time-constant of lock
  -in;
calibration_factor = 1; % since we want signal VS step (not
  sig vs time-delay) graph
```

```

%% Start DAQ
daq.getDevices;
daq_rate = 250000; % change it if needed; 250 000 --->
    default
daq_sample = 3000; % change it if needed; 5000 ---> default
daq_channel = 'ai2';
duration_daq = (daq_sample/daq_rate);

%set daq parameters
dq = daq.createSession('ni');
addAnalogInputChannel(dq,'Dev1', daq_channel, 'Voltage');
dq.Rate = daq_rate;
dq.DurationInSeconds = duration_daq;
%% Start/detect Stage
device_name = detect_stage(); % provided by linear stage
    manufacturer
%% Show Current Position
device_id = open_stage(device_name); % Modified by Akif
[current_step_pos, current_ustep_pos] = current_position(
    device_id); % shows current position before move
fprintf('\n current position of stage:\t step_pos: %d, \t
    ustep_pos: %d \n',current_step_pos, current_ustep_pos);
close_stage(device_id);
%% Sweep to find peak
% following line is for microstepping
%[data_mat] = microstep_stage_and_measure(total_sweeps ,
    start_step, end_step, u_step_size);

% following line is for stepping
[data_mat] = step_stage_and_measure(1 , start_step, end_step
    , step_size);
%% find the max signal
[~,ind] = max(abs(data_mat(:,2))) ;
fprintf(['\n\nthe peak may be at step position :\t %d \n'...
    'the signal is %.2f \n' ], data_mat(ind,1),

```

```

        data_mat(ind,2));
%% Move stage to peak position
device_id = open_stage(device_name);
move_stage( device_id,  data_mat(ind,1), 0);
disp('Stage has moved to the Peak');
close_stage(device_id);

```

Listing B.2: Function for stepping stage and measuring

```

function [ data_matrix, raw_data_sweeps ] =
    step_stage_and_measure( total_sweeps, start_step, end_step
        , step_size )
% Only stepping. NO microstepping here
% streamlined by Akif
% Function outputs:
% data_matrix:  time and signal respectively in 1st and 2nd
    col
% raw_data_sweeps: signal for each sweeps in coloumns
global shift_delay callibration_factor device_name dq
step_count = ceil(abs(end_step-start_step) / step_size);
array_size =  step_count + 1;
array_step_pos = NaN(total_sweeps, array_size);
array_signal    = NaN(total_sweeps, array_size);

device_id = open_stage(device_name);
for j = 1: total_sweeps % total number of forward sweeps by
    delay stage

    fprintf('\n\n starting forward-sweep:%d \n\n',j)
    %  device_id = open_stage(device_name);
    move_stage( device_id, start_step , 0);
    [current_step, ~] = current_position(device_id);

    array_step_pos(j,1) = current_step;
    % close_stage(device_id)
    pause(shift_delay);

```

```

% measure
data_daq = dq.startForeground;
array_signal(j,1) = mean(data_daq);

% open a figure handle and do not number it
figure
for i = 1: step_count
    % device_id = open_stage(device_name);
    move_to_step = current_step + step_size;
    move_stage( device_id, move_to_step , 0);

    [current_step, ~] = current_position(device_id);
    array_step_pos(j, i+1) = current_step;
    % close_stage(device_id)
    pause(shift_delay);

% measure
data_daq = dq.startForeground;
array_signal(j,i+1) = mean(data_daq);
    plot(array_step_pos(j,:), array_signal(j, :), '.');
%line(final_array_position,final_array_signal);
% put the line in if necessary
title('THz Waveform')
% ['Signal at ', num2str(par.
    ps_after_peak_for_noise),'ps after peak']
xlim([start_step, end_step]);
ylim([-10 10]);
ylabel('Au')
xlabel('Steps')
legend(['sweep #', num2str(j)])
grid on;
end
end

```

```

close_stage(device_id);
time_ps = callibration_factor * array_step_pos(1, :);
raw_data_sweeps = [time_ps; array_signal]';
mean_array_signal = mean(array_signal,1) ; % this is a row
    array
data_matrix = [time_ps ; mean_array_signal]';

end

```

Listing B.3: Function for microstepping stage and measuring

```

function [data_matrix] = microstep_stage_and_measure(
    total_sweeps, start_step, end_step, u_step_size)
%% Description
% coded by Akif. Still some room for improvement.
% Output:
% data_matrix: 1st col --> time; 2nd col--> mean signal from
    all sweeps
global shift_delay callibration_factor device_name dq
step_count = abs(end_step-start_step); % not measuring on the
    last step. Step_size is 1 by default
% total physical steps travelled (1 less than
    total_step_positions)

%u_steps_in_single_step = fix(256 / u_step_size); % total
    physical usteps in one step
u_steps_in_microstepping_loop = fix(255 / u_step_size); %
    disregarding ustep==0. this will be less than total
    physical usteps as ustep==256 is not allowed
uuu_in_step = u_steps_in_microstepping_loop + 1; %
    ustep_positions_in_single_step. including ustep==0.
% total ustep positions in a single step.

% arrays (row vectors or matrix built of concatenated rows)

```

```

final_array_size = (uuu_in_step * step_count ) + 1;           %
    adjust arrays accordingly
final_array_step_pos = NaN(total_sweeps , final_array_size);
    % FINAL STEP positions go here
final_array_signal = NaN(total_sweeps , final_array_size);
    % FINAL SIGNALS GO HERE
%% Forward Sweeps
device_id = open_stage(device_name);
for j = 1: total_sweeps

    array_signals_in_single_step = NaN(1, uuu_in_step); %
        signals in a given step
    fprintf('\n\n starting forward-sweep:%d \n\n',j)
    % device_id = open_stage(device_name);
    move_stage( device_id, start_step , 0);
    % close_stage(device_id)
    pause(shift_delay);
    % open a figure handle and do not number it
    figure
    for i = 1:step_count

        % take data at this (step,0 u_step)
        data_daq = dq.startForeground;
        array_signals_in_single_step(1, 1) = mean(data_daq);

        array_ustep_pos_within_step = zeros(1, uuu_in_step);
        array_ustep_pos_within_step(1,1) = 0;
        % move to the next step after micro-stepping (i.e.,
            after next loop)

        % do microstepping now
        for u = 1: u_steps_in_microstepping_loop

            % device_id = open_stage(device_name);
            % first microstep then take voltage

```

```

    [current_step , current_u_step] =
        current_position(device_id);

    move_to_u_step = current_u_step + u_step_size;

    move_stage(device_id, current_step,
        move_to_u_step);
    [current_step , current_u_step] =
        current_position(device_id);

    array_ustep_pos_within_step(1, u+1) =
        current_u_step;
    % close_stage(device_id)
    pause(shift_delay)

    % this will be a function input-parameter

    % take voltage measurement now
    data_daq = dq.startForeground;
    array_signals_in_single_step(1, u+1) = mean(
        data_daq);
    % deal with arrays and calculation

end

array_current_step = current_step * ones(1 ,
    uuu_in_step); % initialized as ones
array_steps_usteps = array_current_step +
    array_ustep_pos_within_step /256;

final_array_step_pos(j , uuu_in_step * (i - 1) + 1 :
    uuu_in_step * i ) = array_steps_usteps;
final_array_signal(j , uuu_in_step * (i - 1) + 1 :
    uuu_in_step * i ) = array_signals_in_single_step;
% Plot a figure of the above data

```

```

plot(final_array_step_pos(j,:), final_array_signal(j,
    :),'.'');
%line(final_array_position,final_array_signal);
% put the line in if necessary
title('THz Waveform')
xlim([start_step, end_step]);
ylim([-5 10]);
ylabel('Au')
xlabel('Steps')
grid on;

% now move to the next step
% device_id = open_stage(device_name);
[current_step, ~] = current_position(device_id);
move_to_step = current_step + 1;
move_stage( device_id, move_to_step , 0);
% close_stage(device_id)
pause(shift_delay);

    % this will be a function input-parameter

end
% this is the last step pos.
data_daq = dq.startForeground;

% device_id = open_stage(device_name);
[current_step, ~] = current_position(device_id);
% close_stage(device_id)

final_array_step_pos(j ,end) = current_step;
final_array_signal(j , end) = mean(data_daq);
% take voltage measurement now for the (last step, 0

```

```

        ustep) position
end % for total_sweeps
close_stage(device_id)
% plot all the data together
fig_all_sweeps = figure    ;
hold on
for jj = 1: total_sweeps
    sweep_str = strcat('sweep# ', num2str(jj));
    plot(final_array_step_pos(jj, :), final_array_signal(jj,
        :), '-', 'DisplayName', sweep_str)

end
hold off
title('THz Waveform')
xlim([start_step, end_step]);
ylim([-5 10]);
ylabel('Au')
xlabel('Steps')
legend('show')
grid on;

mean_array_signal = mean(final_array_signal ,1);
data_matrix = [ calibration_factor * final_array_step_pos(1,
    :); mean_array_signal]';

end

```

Listing B.4: Script for sample stage control

```

% Script file: setup_4sample_mount
% Used for 4 sample characterization without opening purge
    box.
% requires function 'sm_4sample_mm' that controls stepper
    motor
clearvars -except ard shield sm_4sample
global sm_4sample

```

```

%% Initialize Arduino
if ~exist('ard','var')
    ard = arduino('COM4','Uno','Libraries','Adafruit/
        MotorShieldV2');
    shield = addon(ard,'Adafruit/MotorShieldV2');
    sm_4sample = stepper(shield, 1, 200,'StepType', 'Double',
        'RPM',2);
end
%% Move stages
target = 117; % Find other 4 heights where samples go.
% Default sample locations are given in smp_pos
% go to 117 for ref
sm_4sample_mm(target); % sample will be at THz focus
%% Some guidelines

smp_pos = [32.5:20:92.5] ; % measured in mm from the table to
    the bottom of the aluminum plate that has 2 slots
smp_no = [1:4];
mat = [smp_no ; smp_pos];

fprintf('\n Your target position for sample %d is: %d\n',mat)
fprintf('\n for ref go to %d\n', smp_pos(end)+23)
%release(sm_4sample);
% uncomment the above if you want to re-adjust the stage by
    hand the comment it back again

```

Listing B.5: Function for stepper motor control

```

function final_pos = sm_4sample_mm(new_position)
%% know the current position
% you have to define a position by some number, say 100mm.
    you
% have to store that position somewhere so that you can
    always refer back to
% that position as your current position before moving. We
    will store positions in a text file called

```

```
% sm_4sample_mount.txt in motion_control folder
% The physical position is measured from the table to the
    bottom of the
% plate that moves
%% Linear stage info
% steps to lengths
% Amazon stage has pitch 20 microns/step
% following is lengthss in terms of steps

% sub_mm = 5;
% one_mm = 50;
% one_cm = 500;
%% global var
global sm_4sample
%% address for text file for storing current position
file_dir = 'F:\Delay Stage Matlab\motion_control';
file_name = 'sm_4sample_mount.txt';
file_info = fullfile(file_dir, file_name);

%% Limit Switches
if new_position < 25
    disp('Linear Stage will go LOW: LIMIT SWITCH ACTIVATED');
    return
end

if new_position > 118
    disp('Linear Stage will go HIGH: LIMIT SWITCH ACTIVATED')
    ;
    return
end
%% Read Current Position from Text file
fileID = fopen(file_info, 'r');
current_position = fscanf(fileID, '%f');
fclose(fileID);
%% Calculate Steps for height in mm
```

```

height = new_position-current_position;
rounded_height = round(height, 1); % 0.1mm precision
step = round(rounded_height * 50,0);

%% Move Stage
move(sm_4sample,step);
%% Save New Current Position to Text File
current_position = round(new_position,1);
fileID = fopen(file_info,'w+');
fprintf(fileID,'%0.2f',current_position);
fclose(fileID);
%% Output Current Position from Function
final_pos = current_position;
end

```

Listing B.6: Script for controlling cavity length

```

% Script file: cavity_motor_10um.m
% Used to control stepper motor for tuning cavity length
% Requires the function: sm_cavity_um
clearvars -except ard shield sm_cavity
global sm_cavity
%% Initialize Arduino
% use StepType --> Interleave to give you twice resolution.
% The amazon
% stepper motor has the following spec:
% 1 step = 20 microns IN REGULAR OPERATION
% 1 step = 10 microns, IN INTERLEAVE SEETING, IN THEORY

if ~exist('ard','var')
ard = arduino('COM4','Uno','Libraries','Adafruit/
    MotorShieldV2');
shield = addon(ard,'Adafruit/MotorShieldV2');
sm_cavity = stepper(shield, 1, 200,'StepType', 'Interleave',
    'RPM',2);
end

```

```

%% Move stages
test_pos = 3000;
% following function moves the stepper motor in micrometer
cavity_length = sm_cavity_um(test_pos - 50); % argument has
    to be a multiple of 10 microns

```

Listing B.7: Function for controlling cavity stepper motor

```

function final_length = sm_cavity_um(new_length)
%% know the current position
% you have to define a position by some number, call it 100um
    . you
% have to store that position somewhere so that you can always
    refer back to
% that position as your current position before moving. We
    will store positions in a text file called
% sm_cavity.txt in motion_control folder
%% Linear stage info
% steps to lengths
% Amazon stage has pitch 20 microns/step in REGULAR OPERATION
% In INTERLEAVE mode: 1 step = 10 microns, in theory
%% Important for experiment
% For the first measurement, you need to calibrate your
    initial separation
% between mirrors with a calipers so that you know the cavity
    length
% in multiple of 10 microns.
% save this initial calibrated value in sm_cavity.txt in
    motion_control folder
%% Restriction on lengths
if mod(new_length, 10) ~= 0
fprintf('length has to be multiple of 10, in microns\n\n')
return;
end

%% global var

```

```
global sm_cavity
%% address for text file for storing current position
file_dir = 'F:\Delay Stage Matlab\motion_control';
file_name = 'sm_cavity.txt';
file_info = fullfile(file_dir, file_name);

%% Limit Switches
if new_length < 5000          %
    disp('Linear Stage will go LOW: LIMIT SWITCH ACTIVATED');
    return
end

if new_length > 31250        %
    disp('Linear Stage will go HIGH: LIMIT SWITCH ACTIVATED')
    ;
    return
end

%% Read Current Position from Text file
fileID = fopen(file_info, 'r');
current_length = fscanf(fileID, '%f');
fclose(fileID);
%% Calculate Steps for height in mm
length = new_length - current_length;
step    = length / 10;

%% Move Stage
move(sm_cavity, step);
%% Save New Current Position to Text File
current_length = new_length;
fileID = fopen(file_info, 'w+');
fprintf(fileID, '%.2f', current_length);
fclose(fileID);
%% Output Current Position from Function
final_length = current_length;
end
```

Listing B.8: Parameters for initializing THz-TDS measurement

```

function par = setup_1()
%% Used for assigning parameter values for measurement

% Laser Settings
par.laser_amp_percentage = '97 %';
par.laser_power = '~14 Watts';
par.laser_steps = '100 Steps';
par.laser_rep_rate = '3 MHz';
% Lock-in Settings
par.ref_freq = '1000 Hz';
par.time_constant = '100 ms';
par.roll_off = '24 dB';
par.sensitivity = '2 mV';
% Delay stage IMP settings
par.peak_step = -8376;
par.sample_material = 'BFO' ;
par.purge_start_time = '1500'; % 24 hours
par.voltage = '17.5 kV'; %
par.step_size = 4; % ref: 2 steps & BFO: 4 steps
par.sweeps = 1; % Number of sweeps, Natural numbers only.

% How many picoseconds?
start_scan_for_waveform = 8 ; % ps before peak.
%start_scan_for_waveform_after_peak = 4;
end_scan_for_waveform = 300; % ps after peak.
%DEFAULT: 22ps for longer scan.Reflection comes at 23ps
par.comments = 'Put any other comments here. All parameters
    get printed to a text file';
%% Stage movement
par.shift_delay = 500 / 1000;
% set shift-delay ~5 times the time-constant of lock-in
par.u_step_size = 128; % do not change it
par.cal = 0.033356409519815; % multiply step positions to
    convert to time delay in pico sec.

```

```

%% DAQ info
par.daq_rate = 250000; % change it if needed DEFAULT: 250000
par.daq_rate_noise = 500;
par.daq_sample = 5000; % change it if needed ; Default: 20000
par.daq_sig_channel = 'ai2'; % see NI DAQ
par.daq_pwr_channel = 'ai7'; % see NI DAQ
par.duration_daq = (par.daq_sample/par.daq_rate);
%% detecting background 'DC' signal /' 0Hz offset
scan_for = 4; % scan for 5ps [default value 5]
start_scan = 16; % ps before peak [default value 12]
par.start_step_scan_background = time_delay_to_step_pos(
    start_scan, par.peak_step);
[~, par.end_step_scan_background]= time_delay_to_step_pos(
    scan_for, par.start_step_scan_background);
%% parameters for measuring actual waveform
par.step_start = time_delay_to_step_pos(
    start_scan_for_waveform, par.peak_step); % start_step
    before peak
[~, par.step_end] = time_delay_to_step_pos(
    end_scan_for_waveform, par.peak_step); % end_step after
    peak
%% Data folder
par.data_folder = fullfile('F:\Delay Stage Matlab', 'Data_THz
    ');
end

```

Listing B.9: Script for THz-TDS measurement

```

%% Script file: THz_TDS_for_kids_v2.m
% Main code for THz TDS
% Streamlined by AKIF
%% Clean up
clc
clear all
close all
%% Global variables

```

```

global shift_delay callibration_factor device_name dq ;
%% Import parameters for the measurement
par = setup_1();
shift_delay = par.shift_delay;
callibration_factor = par.cal;
%% Move Magnet to Position
% magnet_step_motor(par.magnet_position);
% fprintf('Magnet Moving Now... ..\n\n');
% fprintf('MAGNET MOVED TO: %d \n', par.magnet_position);
%% Start DAQ
daq.getDevices;
%set daq parameters
dq = daq.createSession('ni');
addAnalogInputChannel(dq,'Dev1', par.daq_sig_channel, '
    Voltage');
dq.Rate = par.daq_rate;
dq.DurationInSeconds = par.duration_daq;
%% Start/detect Stage
device_name = detect_stage();
%% create data folder if not created already
if ~exist(par.data_folder, 'dir')
mkdir(par.data_folder)
end
%% create data and plot folder for todays date (not time)
dt_folder = datestr(now, 'yyyy_mm_dd');
folder_info = fullfile(par.data_folder,dt_folder);
if ~exist(folder_info, 'dir')
mkdir(folder_info)
end
%% Show Current Position
device_id = open_stage(device_name);
[current_step_pos, current_ustep_pos] = current_position(
    device_id); % shows current position before move
fprintf('\n current position of stage:\t step_pos: %d, \t
    ustep_pos: %d \n\n',current_step_pos, current_ustep_pos)

```

```

;
close_stage(device_id)
%% Step or micro-step?
% s_or_m = step_or_microstep(); % uncomment for completeness
s_or_m = 0; % Forcing to stepping
%% Detect background offset by stepping
tic;
data_mat_background = step_stage_and_measure(1 , par.
    start_step_scan_background , par.end_step_scan_background ,
    par.step_size);
background = mean( data_mat_background(:,2));
%% Step OR Microstep --- and measure THz waveform
if s_or_m == 1
data_matrix_uncorrected = microstep_stage_and_measure(par.
    sweeps , par.step_start , par.step_end , par.u_step_size);

elseif s_or_m == 0
[data_matrix_uncorrected , raw_data_sweeps ] =
    step_stage_and_measure( par.sweeps , par.step_start , par.
    step_end , par.step_size );
end
time_taken_for_measurement_mins = toc / 60; % measurement
    time
%% close daq
release(dq);
%% Post-measurement calculations
time_delay = data_matrix_uncorrected(:,1);
signal_uncorrected = data_matrix_uncorrected(:,2);
no_of_data_points = length(signal_uncorrected);
% find current time after measurement
time_now = datestr(now, 'HH_MM');
% raw data
file_name_uncorrected = strcat(time_now, '_', par.
    sample_material, '_raw.txt');
file_info_uncorrected = fullfile(folder_info,

```

```

    file_name_uncorrected);
file_name_uncorrected_sweeps = strcat(time_now, '_', par.
    sample_material, '_raw_sweeps.txt');
file_info_uncorrected_sweeps = fullfile(folder_info,
    file_name_uncorrected_sweeps);
% print raw data
dlmwrite(file_info_uncorrected, data_matrix_uncorrected , '
    delimiter', '\t', 'precision', 10)
% print raw data from all the sweeps
dlmwrite(file_info_uncorrected_sweeps, raw_data_sweeps , '
    delimiter', '\t', 'precision', 10)

raw_fig = figure;
plot(time_delay, signal_uncorrected, '.')
title('THz Waveform - uncorrected')
    %xlim([]);
    xlim([time_delay(1)-0.1, time_delay(end)+0.1]);
    ylim([-5 10]);
    ylabel('Au')
    xlabel('Pico sec')
    grid on;
%% correct the offset in the signal
% corrected data
file_name_corrected = strcat(time_now, '_corrected.txt');
file_info_corrected = fullfile(folder_info,
    file_name_corrected);
signal_corrected = signal_uncorrected - background;
data_matrix_corrected = [time_delay, signal_corrected];
% print corrected data
dlmwrite(file_info_corrected, data_matrix_corrected , '
    delimiter', '\t', 'precision', 10)
fig_file_name = strcat(time_now, '_', par.sample_material, '
    _waveform');
fig_file_info = fullfile(folder_info, fig_file_name);

```

```

corrected_fig = figure;
plot(time_delay,signal_corrected, 'k')
title('THz Waveform - corrected')
    xlim([time_delay(1)-0.1, time_delay(end)+0.1]);
    ylim([-10 10]);
    ylabel('AU')
    xlabel('ps')
    grid on;
    legend(par.sample_material);
print(corrected_fig , fig_file_info, '-djpeg', '-r400')
%% Quick FFT
n = 4*(2^nextpow2(no_of_data_points)) ;
[freq_amp, ~, fig_fft ] = fun_fft(time_delay,
    signal_corrected , n);
fig_fft_file_name = strcat(time_now, '_',par.sample_material,
    '_fft');
fig_fft_file_info = fullfile(folder_info,fig_fft_file_name);
print(fig_fft , fig_fft_file_info, '-djpeg', '-r400')
%% print parameters file that has the experiment info
print_parameters(time_now, folder_info,par.sample_material,
    par.laser_amp_percentage,par.laser_power,par.laser_steps,
    par.laser_rep_rate,par.ref_freq,par.time_constant,par.
    roll_off,par.sensitivity,par.purge_start_time,par.voltage,
    par.sweeps, no_of_data_points,
    time_taken_for_measurement_mins, par.comments )

```

Listing B.10: Basic function for plotting FFT

```

function [freq_amp, Fs, fig_fft ] = fun_fft(time, signal , n)
% This function will calculate FFT of the supplied arrays
    time and signal.
% We will do custom zero padding with 'n'
% The output will be an 'N X 2' matrix with 1st col being
    freq and 2nd
% amplitude
%% FFT Calculations

```

```
% # of samples/ pico-sec (sampling freq)
Fs = 1 / (time(2) - time(1) );
% frequency array
freq = ((0:(n/2)) * (Fs/n))';
% spectrum amplitudes
Y = fft(signal,n);
P = abs(Y/n);           % power spectrum (2 sided)
amp = P(1: n/2 +1);    % single sided
freq_amp = [freq , amp];
fig_fft = figure;
plot(freq, amp, 'DisplayName', 'FFT');
xlabel('THz')
ylabel('A.U.')
xlim([0 4])
legend('show');
grid on
end
```

References

- [1] I. Newton, *Opticks, or, a treatise of the reflections, refractions, inflections & colours of light*. Courier Corporation, 1952.
- [2] M. W. Jackson, “Fraunhofer and his spectral lines,” *Annalen der Physik*, vol. 526, no. 7-8, pp. A65–A69, 2014.
- [3] E. Hecht, *Optics*, 4th ed. Reading, Mass: Addison-Wesley, 2002.
- [4] Y. S. Lee, *Principles of Terahertz Science and Technology*. Springer, 2009.
- [5] K. Kawase, Y. Ogawa, and Y. Watanabe, “Non-destructive terahertz imaging of illicit drugs using spectral fingerprints,” *Optics express*, vol. 11, no. 20, pp. 2549–2554, 2003.
- [6] Y. C. Shen, T. Lo, P. F. Taday, B. E. Cole, W. R. Tribe, and M. C. Kemp, “Detection and identification of explosives using terahertz pulsed spectroscopic imaging,” *Applied Physics Letters*, vol. 86, no. 24, p. 241116, 2005.
- [7] T. Kleine-ostmann and T. Nagatsuma, “A Review on Terahertz Communications Research,” *Journal of Infrared, Millimeter, and Terahertz Waves*, pp. 143–171, 2011.
- [8] D. D. Arnone, C. M. Ciesla, A. Corchia, S. Egusa, M. Pepper, J. M. Chamberlain, C. Bezant, E. H. Linfield, R. Clothier, and N. Khammo, “Applications of terahertz (thz) technology to medical imaging,” in *Terahertz Spectroscopy and Applications II*, vol. 3828. International Society for Optics and Photonics, 1999, pp. 209–219.
- [9] P. H. Siegel, “Terahertz Technology in Biology and Medicine,” *IEEE transactions on microwave theory and techniques*, vol. 52, no. 10, pp. 2438–2447, 2004.
- [10] G. Catalan and J. F. Scott, “Physics and applications of bismuth ferrite,” *Advanced Materials*, vol. 21, no. 24, pp. 2463–2485, 2009.

- [11] J. Wu, Z. Fan, D. Xiao, J. Zhu, and J. Wang, “Multiferroic bismuth ferrite-based materials for multifunctional applications: Ceramic bulks, thin films and nanostructures,” *Progress in Materials Science*, vol. 84, pp. 335–402, 2016.
- [12] N. Wang, X. Luo, L. Han, Z. Zhang, R. Zhang, H. Olin, and Y. Yang, “Structure, Performance, and Application of BiFeO₃ Nanomaterials,” *Nano-Micro Letters*, vol. 12, no. 1, 2020.
- [13] D. Talbayev, S. A. Trugman, S. Lee, H. T. Yi, S. W. Cheong, and A. J. Taylor, “Long-wavelength magnetic and magnetoelectric excitations in the ferroelectric anti-ferromagnet BiFeO₃,” *Physical Review B - Condensed Matter and Materials Physics*, vol. 83, no. 9, pp. 1–5, 2011.
- [14] M. Cazayous, Y. Gallais, A. Sacuto, R. De Sousa, D. Lebeugle, and D. Colson, “Possible observation of cycloidal electromagnons in BiFeO₃,” *Physical Review Letters*, vol. 101, no. 3, pp. 2–5, 2008.
- [15] D. S. Wang, T. Neuman, J. Flick, and P. Narang, “Weak-to-strong light-matter coupling and dissipative dynamics from first principles,” *arXiv*, no. February, 2020.
- [16] D. S. Dovzhenko, S. V. Ryabchuk, Y. P. Rakovich, and I. R. Nabiev, “Light-matter interaction in the strong coupling regime: Configurations, conditions, and applications,” *Nanoscale*, vol. 10, no. 8, pp. 3589–3605, 2018.
- [17] P. Sivarajah, A. Steinbacher, B. Dastrup, J. Lu, M. Xiang, W. Ren, S. Kamba, S. Cao, and K. A. Nelson, “THz-frequency magnon-phonon-polaritons in the collective strong-coupling regime,” *Journal of Applied Physics*, vol. 125, no. 21, 2019.
- [18] G. Grüner and C. Dahl, *Millimeter and submillimeter wave spectroscopy of solids*. Springer, 1998, vol. 200.
- [19] R. W. Boyd, *Nonlinear optics*, 3rd ed. London: Academic, 2008.
- [20] G. New, *Introduction to Nonlinear Optics*. Cambridge: Cambridge University Press, 2011.
- [21] M. C. Hoffmann, K.-L. Yeh, J. Hebling, and K. A. Nelson, “Efficient terahertz generation by optical rectification at 1035 nm,” *Opt. Express*, vol. 15, no. 18, pp. 11 706–11 713, Sep 2007.
- [22] A. Weiner, *Ultrafast optics*. John Wiley & Sons, 2011.

- [23] B. E. Saleh and M. C. Teich, *Fundamentals of Photonics*, 3rd ed. John Wiley & Sons, Inc, 2019.
- [24] K. Ravi, W. R. Huang, S. Carbajo, E. A. Nanni, D. N. Schimpf, E. P. Ippen, and F. X. Kärtner, “Theory of terahertz generation by optical rectification using tilted-pulse-fronts,” *Optics Express*, vol. 23, no. 4, p. 5253, 2015.
- [25] W. R. Huang, “High Field , High Efficiency Terahertz Pulse Generation by Optical Rectification,” Master’s thesis, Massachusetts Institute of Technology, 2014.
- [26] J. Hebling, A. G. Stepanov, G. Almási, B. Bartal, and J. Kuhl, “Tunable THz pulse generation by optical rectification of ultrashort laser pulses with tilted pulse fronts,” *Applied Physics B: Lasers and Optics*, vol. 78, no. 5, pp. 593–599, 2004.
- [27] J. Hebling, K.-L. Yeh, M. C. Hoffmann, B. Bartal, and K. A. Nelson, “Generation of high-power terahertz pulses by tilted-pulse-front excitation and their application possibilities,” *Journal of the Optical Society of America B*, vol. 25, no. 7, p. B6, 2008.
- [28] J. A. Fülöp, L. Pálfalvi, G. Almási, and J. Hebling, “Design of high-energy terahertz sources based on optical rectification,” *Opt. Express*, vol. 18, no. 12, pp. 12 311–12 327, Jun 2010.
- [29] M. Unferdorben, Z. Szaller, I. Hajdara, J. Hebling, and L. Pálfalvi, “Measurement of refractive index and absorption coefficient of congruent and stoichiometric lithium niobate in the terahertz range,” *Journal of Infrared, Millimeter, and Terahertz Waves*, vol. 36, no. 12, pp. 1203–1209, 2015.
- [30] M. Nakamura, S. Higuchi, S. Takekawa, K. Terabe, Y. Furukawa, and K. Kitamura, “Optical damage resistance and refractive indices in near-stoichiometric MgO-doped LiNbO₃,” *Japanese Journal of Applied Physics, Part 2: Letters*, vol. 41, no. 1 A/B, pp. 2–5, 2002.
- [31] L. Tokodi, J. Hebling, and L. Pálfalvi, “Optimization of the Tilted-Pulse-Front Terahertz Excitation Setup Containing Telescope,” *Journal of Infrared, Millimeter, and Terahertz Waves*, vol. 38, no. 1, pp. 22–32, 2017.
- [32] H. Hirori and K. Tanaka, “Nonlinear optical phenomena induced by intense single-cycle terahertz pulses,” *IEEE Journal of Selected Topics in Quantum Electronics*, vol. 19, no. 1, pp. 8 401 110–8 401 110, 2012.

- [33] K. Ravi, W. R. Huang, S. Carbajo, X. Wu, and F. Kärtner, “Limitations to THz generation by optical rectification using tilted pulse fronts,” *Optics Express*, vol. 22, no. 17, p. 20239, 2014.
- [34] C. A. Palmer and E. G. Loewen, *Diffraction grating handbook*, 5th ed. Thermo RGL, 2002.
- [35] B. Pradarutti, G. Matthäus, S. Riehemann, G. Notni, S. Nolte, and A. Tünnermann, “Highly efficient terahertz electro-optic sampling by material optimization at 1060 nm,” *Optics Communications*, vol. 281, no. 19, pp. 5031–5035, 2008.
- [36] S. R. Systems, *MODEL SR830 DSP Lock-In Amplifier*, Stanford Research Systems, 1290-D Reamwood Avenue Sunnyvale, California 94089, 2011.
- [37] H. C. B. Skjeie, “Terahertz Time-Domain Spectroscopy,” Master’s thesis, Norwegian University of Science and Technology, 2012.
- [38] M. Naftaly and R. Dudley, “Methodologies for determining the dynamic ranges and signal-to-noise ratios of terahertz time-domain spectrometers,” *Optics Letters*, vol. 34, no. 8, p. 1213, 2009.
- [39] P. U. Jepsen and B. M. Fischer, “Dynamic range in terahertz time-domain transmission and reflection spectroscopy,” *Optics Letters*, vol. 30, no. 1, p. 29, 2005.
- [40] R. Lyons, *Understanding Digital Signal Processing*. Pearson Education, 2010.
- [41] T. Butz, *Fourier transformation for Pedestrians*. Springer, 2006.
- [42] M. Naftaly, *Terahertz metrology*. Artech House, 2015.
- [43] J. Neu and C. A. Schmuttenmaer, “Tutorial: An introduction to terahertz time domain spectroscopy (THz-TDS),” *Journal of Applied Physics*, vol. 124, no. 23, 2018.
- [44] W. Withayachumnankul, B. M. Fischer, and D. Abbott, “Material thickness optimization for terahertz time-domain spectroscopy,” *Optical Society of America*, vol. 16, no. 10, pp. 7382–7396, 2008.
- [45] L. Duvillaret, F. Garet, and J.-L. Coutaz, “Highly precise determination of optical constants and sample thickness in terahertz time-domain spectroscopy,” *Applied Optics*, vol. 38, no. 2, p. 409, 1999.

- [46] W. Withayachumnankul, B. Ferguson, T. Rainsford, S. P. Micken, and D. Abbott, "Simple material parameter estimation via terahertz time-domain spectroscopy," *Electronics Letters*, vol. 41, no. 14, pp. 800–801, 2005.
- [47] N. Refvik, "Time Domain Analysis of Material Properties in THz Cavity Systems," Honour's thesis, University of Manitoba, 2020.
- [48] T. R. Sjørgård, "Terahertz Time-Domain Spectroscopy of Thin Material Samples," Master's thesis, Norwegian University of Science and Technology, 2015.
- [49] M. Fox, *Optical Properties of Solids*, 2nd ed., ser. Oxford master series in condensed matter physics. Oxford: Oxford University Press, 2010.
- [50] J. Dai, J. Zhang, W. Zhang, and D. Grischkowsky, "Terahertz time-domain spectroscopy characterization of the far-infrared absorption and index of refraction of high-resistivity, float-zone silicon," *Journal of the Optical Society of America B*, vol. 21, no. 7, p. 1379, 2004.
- [51] M. N. Afsar and H. Chi, "Millimeter wave complex refractive index, complex dielectric permittivity and loss tangent of extra high purity and compensated silicon," *International Journal of Infrared and Millimeter Waves*, vol. 15, no. 7, pp. 1181–1188, 1994.
- [52] Y. Kim, M. Yi, B. G. Kim, and J. Ahn, "Investigation of THz birefringence measurement and calculation in Al_2O_3 and LiNbO_3 ," *Applied Optics*, vol. 50, no. 18, pp. 2906–2910, 2011.
- [53] K. Z. Rajab, M. Naftaly, E. H. Linfield, J. C. Nino, D. Arenas, D. Tanner, R. Mitra, and M. Lanagan, "Broadband dielectric characterization of aluminum oxide (Al_2O_3)," *Journal of Microelectronics and Electronic Packaging*, vol. 5, no. 1, pp. 2–7, 2008.
- [54] M. Naftaly and R. E. Miles, "Terahertz time-domain spectroscopy: A new tool for the study of glasses in the far infrared," *Journal of Non-Crystalline Solids*, vol. 351, no. 40-42, pp. 3341–3346, 2005.
- [55] D. Grischkowsky, S. Keiding, M. van Exter, and C. Fattinger, "Far-infrared time-domain spectroscopy with terahertz beams of dielectrics and semiconductors," *Journal of the Optical Society of America B*, vol. 7, no. 10, p. 2006, 1990.
- [56] P. D. Cunningham, N. N. Valdes, F. A. Vallejo, L. M. Hayden, B. Polishak, X. H.

- Zhou, J. Luo, A. K. Jen, J. C. Williams, and R. J. Twieg, "Broadband terahertz characterization of the refractive index and absorption of some important polymeric and organic electro-optic materials," *Journal of Applied Physics*, vol. 109, no. 4, pp. 1–5, 2011.
- [57] K. M. Mølster, "THz time domain spectroscopy of materials in reflection and transmission," Master's thesis, Norwegian University of Science and Technology, 2017.
- [58] A. Dinovitsler, D. G. Valchev, and D. Abbott, "Terahertz time-domain spectroscopy of edible oils," *Royal Society Open Science*, vol. 4, no. 4, pp. 170 275–170 284, 2017.
- [59] M. Walther, B. M. Fischer, and P. U. Jepsen, "Noncovalent intermolecular forces in polycrystalline and amorphous saccharides in the far infrared," *Chemical Physics*, vol. 288, no. 2-3, pp. 261–268, 2003.
- [60] W. Withayachumnankul, B. M. Fischer, and D. Abbott, "Material thickness optimization for terahertz time-domain spectroscopy," *Optical Society of America*, vol. 16, no. 10, pp. 7382–7396, 2008.
- [61] P. Kužel, H. Němec, F. Kadlec, and C. Kadlec, "Gouy shift correction for highly accurate refractive index retrieval in time-domain terahertz spectroscopy," *Optics Express*, vol. 18, no. 15, p. 15338, 2010.
- [62] I. Hosako, "Multilayer optical thin films for use at terahertz frequencies: Method of fabrication," *Applied Optics*, vol. 44, no. 18, pp. 3769–3773, 2005.
- [63] J. Kröll, J. Darmo, and K. Unterrainer, "Metallic wave-impedance matching layers for broadband terahertz optical systems," *Optics Express*, vol. 15, no. 11, p. 6552, 2007.
- [64] B. Cai, H. Chen, G. Xu, H. Zhao, and O. Sugihara, "Ultra-broadband THz antireflective coating with polymer composites," *Polymers*, vol. 9, no. 11, pp. 1–9, 2017.
- [65] C. Brückner, T. Käsebier, B. Pradarutti, S. Riehemann, G. Notni, E. B. Kley, and A. Tünnermann, "Broadband antireflective structures for the THz spectral range fabricated on high resistive float zone silicon," *33rd International Conference on Infrared and Millimeter Waves and the 16th International Conference on Terahertz Electronics, 2008, IRMMW-THz 2008*, vol. 17, no. 5, pp. 281–282, 2008.

- [66] J. Lau, J. Fowler, T. Marriage, L. Page, J. Leong, E. Wishnow, R. Henry, E. Wollack, M. Halpern, D. Marsden, and G. Marsden, “Millimeter-wave antireflection coating for cryogenic silicon lenses,” *Applied Optics*, vol. 45, no. 16, pp. 3746–3751, 2006.
- [67] K. Kawase and N. Hiromoto, “Terahertz-wave antireflection coating on Ge and GaAs with fused quartz,” *Applied Optics*, vol. 37, no. 10, p. 1862, 1998.
- [68] D. J. Kinning and H. M. Schneider, “Release coatings for pressure sensitive adhesives,” *Adhesion Science and Engineering*, pp. 535–571, 2002.
- [69] E. V. Fedulova, M. M. Nazarov, A. A. Angeluts, M. S. Kitai, V. I. Sokolov, and A. P. Shkurinov, “Studying of dielectric properties of polymers in the terahertz frequency range,” *Saratov Fall Meeting 2011: Optical Technologies in Biophysics and Medicine XIII*, vol. 8337, p. 83370I, 2012.
- [70] I. E. Khodasevych, C. M. Shah, S. Sriram, M. Bhaskaran, W. Withayachumnankul, B. S. Ung, H. Lin, W. S. Rowe, D. Abbott, and A. Mitchell, “Elastomeric silicone substrates for terahertz fishnet metamaterials,” *Applied Physics Letters*, vol. 100, no. 6, pp. 8–11, 2012.
- [71] Y. S. Jin, G. J. Kim, and S. G. Jeon, “Terahertz dielectric properties of polymers,” *Journal of the Korean Physical Society*, vol. 49, no. 2, pp. 513–517, 2006.
- [72] S. Alfihed, M. H. Bergen, A. Ciocoiu, J. F. Holzman, and I. G. Foulds, “Characterization and integration of terahertz technology within microfluidic platforms,” *Micromachines*, vol. 9, no. 9, pp. 1–9, 2018.
- [73] H. A. Macleod, *Thin-Film Optical Filters*, 5th ed., ser. Series in optics and optoelectronics. CRC Press, 2017.
- [74] F. D. Brunner and T. Feurer, “Antireflection coatings optimized for single-cycle THz pulses,” *Applied Optics*, vol. 52, no. 16, pp. 3829–3832, 2013.
- [75] X.-j. Wu, J.-l. Ma, B.-l. Zhang, S.-s. Chai, Z.-j. Fang, C.-Y. Xia, D.-y. Kong, J.-g. Wang, H. Liu, C.-Q. Zhu, X. Wang, C.-J. Ruan, and Y.-T. Li, “Highly efficient generation of 02 mJ terahertz pulses in lithium niobate at room temperature with sub-50 fs chirped Ti:sapphire laser pulses,” *Optics Express*, vol. 26, no. 6, p. 7107, 2018.
- [76] H. Lin, S. Yu, C. Shi, X. Lv, P. Lv, Z. Xie, G. Zhao, and S. Zhu, “Extended Sellmeier

- equation for the extraordinary refractive index of 5% MgO-doped congruent LiNbO₃ at high temperature,” *AIP Advances*, vol. 7, no. 9, p. 095201, 2017.
- [77] X. Zhang, J. Qiu, X. Li, J. Zhao, and L. Liu, “Complex refractive indices measurements of polymers in visible and near-infrared bands,” *Appl. Opt.*, vol. 59, no. 8, pp. 2337–2344, Mar 2020.
- [78] R. French, J. Rodríguez-Parada, M. Yang, R. Derryberry, and N. Pfeifferberger, “Optical properties of polymeric materials for concentrator photovoltaic systems,” *Solar Energy Materials and Solar Cells*, vol. 95, no. 8, pp. 2077–2086, 2011.
- [79] S. Ando, Y. Watanabe, and T. Matsuura, “Wavelength dependence of refractive indices of polyimides in visible and near-ir regions,” *Japanese journal of applied physics*, vol. 41, no. 8R, p. 5254, 2002.
- [80] F. Yan, C. Yu, H. Park, E. P. Parrott, and E. Pickwell-Macpherson, “Advances in polarizer technology for terahertz frequency applications,” *Journal of Infrared, Millimeter, and Terahertz Waves*, vol. 34, no. 9, pp. 489–499, 2013.
- [81] D. T. Rampton and R. W. Grow, “Economic infrared polarizer utilizing interference effects in films of polyethylene kitchen wrap,” *Applied Optics*, vol. 15, no. 4, p. 1034, 1976.
- [82] A. Mitsuishi, Y. Yamada, S. Fujita, and H. Yoshinaga, “Polarizer for the Far-Infrared Region,” *Journal of the Optical Society of America*, vol. 50, no. 5, p. 433, 1960.
- [83] D. J. Griffiths, *Introduction to Electrodynamics*, 4th ed. Boston: Pearson, 2014.
- [84] F. X. Canning, “Corrected fresnel coefficients for lossy materials,” in *2011 IEEE International Symposium on Antennas and Propagation (APSURSI)*. IEEE, 2011, pp. 2123–2126.
- [85] H. Weber, “The Fresnel equations for lossy dielectrics and conservation of energy,” *Journal of Modern Optics*, vol. 61, no. 15, pp. 1219–1224, 2014.
- [86] A. Wojdyla and G. Gallot, “Brewster’s angle silicon wafer terahertz linear polarizer,” *Optics Express*, vol. 19, no. 15, p. 14099, 2011.
- [87] N. A. Spaldin, “Multiferroics: Past, present, and future,” *MRS Bulletin*, vol. 42, no. 5, pp. 385–389, 2017.

- [88] H. Palneedi, V. Annapureddy, S. Priya, and J. Ryu, “Status and perspectives of multiferroic magnetoelectric composite materials and applications,” *Actuators*, vol. 5, no. 1, 2016.
- [89] J. F. Scott, “Room-temperature multiferroic magnetoelectrics,” *NPG Asia Materials*, vol. 5, no. 10, pp. 1–11, 2013.
- [90] J. F. Scott, “Applications of magnetoelectrics,” *Journal of Materials Chemistry*, vol. 22, no. 11, pp. 4567–4574, 2012.
- [91] E. Abe, H. Wu, A. Ardavan, and J. J. Morton, “Electron spin ensemble strongly coupled to a three-dimensional microwave cavity,” *Applied Physics Letters*, vol. 98, no. 25, p. 251108, 2011.
- [92] I. Chiorescu, N. Groll, S. Bertaina, T. Mori, and S. Miyashita, “Magnetic strong coupling in a spin-photon system and transition to classical regime,” *Physical Review B*, vol. 82, no. 2, p. 024413, 2010.
- [93] Y. Kubo, F. Ong, P. Bertet, D. Vion, V. Jacques, D. Zheng, A. Dréau, J.-F. Roch, A. Auffèves, F. Jelezko *et al.*, “Strong coupling of a spin ensemble to a superconducting resonator,” *Physical review letters*, vol. 105, no. 14, p. 140502, 2010.
- [94] D. Schuster, A. Sears, E. Ginossar, L. DiCarlo, L. Frunzio, J. Morton, H. Wu, G. Briggs, B. Buckley, D. Awschalom *et al.*, “High-cooperativity coupling of electron-spin ensembles to superconducting cavities,” *Physical review letters*, vol. 105, no. 14, p. 140501, 2010.
- [95] L. Bai, M. Harder, Y. Chen, X. Fan, J. Xiao, and C.-M. Hu, “Spin pumping in electro-dynamically coupled magnon-photon systems,” *Physical Review Letters*, vol. 114, no. 22, p. 227201, 2015.
- [96] H. Maier-Flaig, M. Harder, R. Gross, H. Huebl, and S. T. Gönnenwein, “Spin pumping in strongly coupled magnon-photon systems,” *Physical Review B*, vol. 94, no. 5, p. 054433, 2016.
- [97] L. Bai, M. Harder, P. Hyde, Z. Zhang, C.-M. Hu, Y. Chen, and J. Q. Xiao, “Cavity mediated manipulation of distant spin currents using a cavity-magnon-polariton,” *Physical review letters*, vol. 118, no. 21, p. 217201, 2017.
- [98] D. Zhang, X.-Q. Luo, Y.-P. Wang, T.-F. Li, and J. You, “Observation of the

- exceptional point in cavity magnon-polaritons,” *Nature communications*, vol. 8, no. 1, pp. 1–6, 2017.
- [99] F. Meng, M. D. Thomson, B. Klug, D. Cibiraite, Q. Ul-Islam, and H. G. Roskos, “Ultrastrong coupling of plasmonic metamaterials and photons in a terahertz photonic crystal cavity,” *International Conference on Infrared, Millimeter, and Terahertz Waves, IRMMW-THz*, vol. 2019-Sept, no. 17, pp. 24 455–24 468, 2019.
- [100] R. Damari, O. Weinberg, D. Krotkov, N. Demina, K. Akulov, A. Golombek, T. Schwartz, and S. Fleischer, “Strong coupling of collective intermolecular vibrations in organic materials at terahertz frequencies,” *Nature Communications*, vol. 10, no. 1, pp. 1–8, 2019.
- [101] L. Novotny, “Strong coupling, energy splitting, and level crossings: A classical perspective,” *American Journal of Physics*, vol. 78, no. 11, pp. 1199–1202, 2010.
- [102] S. R. K. Rodriguez, “Classical and quantum distinctions between weak and strong coupling,” *European Journal of Physics*, vol. 37, no. 2, p. 25802, 2016.
- [103] M. Harder, “Cavity Spintronics Foundations and Applications of Spin-Photon Hybridization,” Ph.D. dissertation, University of Manitoba, 2018.
- [104] A. Kumar, J. F. Scott, and R. S. Katiyar, “Electric control of magnon frequencies and magnetic moment of bismuth ferrite thin films at room temperature,” *Applied Physics Letters*, vol. 99, no. 6, pp. 2–4, 2011.
- [105] Y. H. Chu, L. W. Martin, M. B. Holcomb, and R. Ramesh, “Controlling magnetism with multiferroics,” *Materials Today*, vol. 10, no. 10, pp. 16–23, 2007.
- [106] C. Caspers, V. P. Gandhi, A. Magrez, E. De Rijk, and J. P. Ansermet, “Sub-terahertz spectroscopy of magnetic resonance in BiFeO₃ using a vector network analyzer,” *Applied Physics Letters*, vol. 108, no. 24, pp. 106–111, 2016.
- [107] M. Białek, T. Ito, H. Rønnow, and J. P. Ansermet, “Terahertz-optical properties of a bismuth ferrite single crystal,” *Physical Review B*, vol. 99, no. 6, pp. 25–31, 2019.
- [108] P. Rovillain, R. De Sousa, Y. Gallais, A. Sacuto, M. A. Méasson, D. Colson, A. Forget, M. Bibes, A. Barthélémy, and M. Cazayous, “Electric-field control of spin waves at room temperature in multiferroic BiFeO₃,” *Nature Materials*, vol. 9, no. 12, pp. 975–979, 2010.

- [109] M. Białek, A. Magrez, A. Murk, and J. P. Ansermet, “Spin-wave resonances in bismuth orthoferrite at high temperatures,” *Physical Review B*, vol. 97, no. 5, pp. 1–5, 2018.
- [110] R. De Sousa and J. E. Moore, “Optical coupling to spin waves in the cycloidal multiferroic BiFeO_3 ,” *Physical Review B - Condensed Matter and Materials Physics*, vol. 77, no. 1, pp. 3–6, 2008.
- [111] M. K. Singh, R. S. Katiyar, and J. F. Scott, “New magnetic phase transitions in BiFeO_3 ,” *Journal of Physics Condensed Matter*, vol. 20, no. 25, 2008.
- [112] T. Bardon, R. K. May, P. F. Taday, and M. Strlič, “Influence of particle size on optical constants from pellets measured with terahertz pulsed spectroscopy,” *IEEE Transactions on Terahertz Science and Technology*, vol. 6, no. 3, pp. 408–413, 2016.
- [113] T. Rojac, M. Kosec, B. Budic, N. Setter, and D. Damjanovic, “Strong ferroelectric domain-wall pinning in BiFeO_3 ceramics,” *Journal of Applied Physics*, vol. 108, no. 7, 2010.
- [114] S. A. Jewell, E. Hendry, T. H. Isaac, and J. R. Sambles, “Tuneable Fabry-Perot etalon for terahertz radiation,” *New Journal of Physics*, vol. 10, 2008.
- [115] D. G. Lidzey, D. Bradley, M. Skolnick, T. Virgili, S. Walker, and D. Whittaker, “Strong exciton–photon coupling in an organic semiconductor microcavity,” *Nature*, vol. 395, no. 6697, pp. 53–55, 1998.
- [116] A. Dunkelberger, B. Spann, K. Fears, B. Simpkins, and J. Owrutsky, “Modified relaxation dynamics and coherent energy exchange in coupled vibration-cavity polaritons,” *Nature communications*, vol. 7, no. 1, pp. 1–10, 2016.
- [117] A. Turner, “Some current developments in multilayer optical films,” *J. phys. radium*, vol. 11, no. 7, pp. 444–460, 1950.
- [118] C. Roychoudhuri, “Response of fabry–perot interferometers to light pulses of very short duration,” *JOSA*, vol. 65, no. 12, pp. 1418–1426, 1975.
- [119] J. W. Cleary, C. J. Fredricksen, A. V. Muravjov, J. Enz, M. V. Dolguikh, T. W. Du Bosq, R. E. Peale, W. R. Folks, S. Pandey, G. Boreman, and O. Edwards, “Scanning Fabry-Perot filter for terahertz spectroscopy based on silicon dielectric mirrors,” *Terahertz and Gigahertz Electronics and Photonics VI*, vol. 6472, p. 64720E, 2007.

- [120] X. Shi and Z. Han, “Enhanced terahertz fingerprint detection with ultrahigh sensitivity using the cavity defect modes,” *Scientific Reports*, vol. 7, no. 1, pp. 1–8, 2017.
- [121] R. F. Ribeiro, L. A. Martínez-Martínez, M. Du, J. Campos-Gonzalez-Angulo, and J. Yuen-Zhou, “Polariton chemistry: controlling molecular dynamics with optical cavities,” *Chemical science*, vol. 9, no. 30, pp. 6325–6339, 2018.
- [122] J. Yuen-Zhou and V. M. Menon, “Polariton chemistry: Thinking inside the (photon) box,” *Proceedings of the National Academy of Sciences*, vol. 116, no. 12, pp. 5214–5216, 2019.
- [123] C. Ekström, “Generation of Short Intense Terahertz Pulses Through Optical Rectification,” Diploma Project, Lund University, 2015.